Final report on
Venus Data Analysis Program grant number NAGW-3497
"Plasma Waves in the Magnetosheath of Venus"
Robert J. Strangeway, Principal Investigator.
Funding period: 3/15/93–3/14/96

Publications supported by grant NAGW-3497

1. Intriligator, D. S., L. H. Brace, P. A. Cloutier, J. M. Grebowsky, R. E. Hartle, W. T. Kasprzak, W. C. Knudsen, and R. J. Strangeway, Evidence for ion transport and molecular ion dominance in the Venus ionotail, *J. Geophys. Res.*, *99*, 17,413–17,420, 1994.

2. Ho, C.-M., R. J. Strangeway, and C. T. Russell, Spatial distribution of plasma wave activity in the nightside ionosphere of Venus, *Planet. Space Sci.*, *42*, 813–823, 1994.

3. Strangeway, R. J., and G. K. Crawford, VLF waves in the foreshock, *Adv. Space Res.*, *15*, (8/9)29–(8/9)42, 1995.

4. Greenstadt, E. W., G. Le, and R. J. Strangeway, ULF waves in the foreshock, *Adv. Space Res.*, *15*, (8/9)71–(8/9)84, 1995.

5. Strangeway, R. J., and G. K. Crawford, Comparison of upstream phenomena at Venus and Earth, *Adv. Space Res.*, *16*, (4)125–(4)136, 1995.

6. Strangeway, R. J., Plasma wave evidence for lightning on Venus, *J. Atmos. Terr. Phys.*, *57*, 537–556, 1995.

7. Ho, C.-M., R. J. Strangeway, and C. T. Russell, Venus nightside ionospheric irregularities and their relationship to VLF bursts, *J. Geophys. Res.*, *100*, 9697–9705, 1995.

8. Perez-de-Tejada, H., D. S. Intriligator, and R. J. Strangeway, Intermediate transition in the Venus ionosheath, *J. Geophys. Res.*, *100*, 14,523–14,535, 1995.

9. Mihalov, J. D., and R. J. Strangeway, Large solar wind disturbances during late May and early June 1991, *Solar Physics*, *160*, 363–370, 1995.

10. Greenstadt, E. W., G. K. Crawford, R. J. Strangeway, S. L. Moses, and F. V. Coroniti, Spatial distribution of electron plasma oscillations in the Earth's foreshock at ISEE 3, *J. Geophys. Res.*, *100*, 19,933–19,939, 1995.

11. Strangeway, R. J., Collisional Joule dissipation in the ionosphere of Venus: The importance of electron heat conduction, *J. Geophys. Res.*, *101*, 2279–2295, 1996.

12. Strangeway, R. J., and C. T. Russell, Plasma waves and field-aligned currents in the Venus plasma mantle, *J. Geophys. Res.*, *101*, 17,313–17,324, 1996.

Presentations supported by grant NAGW-3497

1. Strangeway, R. J., The plasma wave evidence for lightning on Venus, XXIVth General Assembly of the International Union of Radio Science, Kyoto, Japan, 1993. INVITED

2. G. K. Crawford, R. J. Strangeway, and C. T. Russell, Plasma waves observed above the dayside ionopause of Venus: evidence for an additional transition layer, *Eos, Trans. AGU, 74(43)*, 375, American Geophysical Union Fall Meeting, San Francisco, 1993.

3. H. Perez-de-Tejada, D. S. Intrigator, and R. J. Strangeway, Evidence for changes in ion composition across the intermediate transition of the Venus ionosheath, *Eos, Trans. AGU, 74(43)*, 376, American Geophysical Union Fall Meeting, San Francisco, 1993.

4. E. W. Greenstadt, S. L. Moses, F. V. Coroniti, G. K. Crawford, and R. J. Strangeway, Electron plasma oscillations in the foreshock: comparison of occurrence at PVO and ISEE 3, *Eos, Trans. AGU, 74(43)*, 493, American Geophysical Union Fall Meeting, San Francisco, 1993.

5. Strangeway, R. J., Comparison of upstream phenomena at Venus and Mars, 30th COSPAR Scientific Assembly, p143 (abstract), Hamburg, Germany, 1994. INVITED

6. Strangeway, R. J., VLF waves in the foreshock, 30th COSPAR Scientific Assembly, p167 (abstract), Hamburg, Germany, 1994. INVITED

7. Perez-de-Tejada, H., D. S. Intriligator, and R. J. Strangeway, Magnetic field profiles across the intermediate transition of the Venus ionosheath, *Eos, Trans. AGU, 75(44)*, 410, American Geophysical Union Fall Meeting, San Francisco, 1994.

8. Strangeway, R. J., and C. T. Russell, Joule dissipation in planetary ionospheres: Implications for planetary lightning, *Eos, Trans. AGU, 75(44)*, 410, American Geophysical Union Fall Meeting, San Francisco, 1994.

9. Strangeway, R. J., C. T. Russell, C. M. Ho, and J. G. Luhmann, Structure of the nightside ionosphere and near-Venus magnetotail as a function of solar activity, Venus II, Tucson, 1995.

10. Strangeway, R. J., C. T. Russell, and G. K. Crawford, Plasma waves observed above the dayside Venus ionopause, Venus II, Tucson, 1995.

11. Strangeway, R. J., and C. T. Russell, Collisional Joule dissipation of lightning generated plasma waves in planetary ionospheres, *Eos, Trans. AGU, 76(17), Supplement*, S192, American Geophysical Union Spring Meeting, Baltimore, 1995.

12. Strangeway, R. J., Interaction of the solar wind with the non-magnetized planets, International Union of Geodesy and Geophysics, XXI General Assembly, Boulder (abstract), p.A89, 1995. INVITED

13. Strangeway, R. J., and C. T. Russell, Collisional Joule dissipation of plasma waves in planetary ionospheres, International Union of Geodesy and Geophysics, XXI General Assembly, Boulder (abstract), p.A89, 1995.

14. Strangeway, R. J., and C. T. Russell, Plasma waves are not a heat source for the dayside ionosphere of Venus, *Eos, Trans. AGU, 76(46), Supplement*, F339, American Geophysical Union Fall Meeting, San Francisco, 1995.

Summary of research supported by grant NAGW-3497

It can be seen frpm th elist of publications and presentations that this grant has supported a large amount of work in a variety of topics. The research supported by this grant can be divided into three basic topics: 1) Plasma waves in the Venus magnetosheath; 2) Plasma waves in the Venus foreshock and solar wind; 3) Plasma waves in the Venus nightside ionosphere and ionotail. We will briefly describe the major results in each of these areas here.

1) Plasma waves in the Venus magnetosheath

This topic is the major research are supported by this grant. The main issues to be addressed were: a) What are the wave modes observed in the magnetosheath and upper ionosphere? b) Are the waves a significant source of heating for the topside ionosphere? and c) what is the source of the waves?

There is still considerable debate within the scientific literature concerning the possible wave modes. However, the consensus appears to be that the waves are not whistler-mode waves propagating through the magnetosheath from the bow shock [*Strangeway and Russell*, 1996], as originally hypothesized [*Scarf et al.*, 1979; *Taylor et al.*, 1979]. Instead the waves appear to be generated in situ. They therefore appear to be an important element in the coupling of the solar wind to the planetary ionosphere, acting to transfer momentum from one species to the other.

We have also found that the waves mainly occur above the ionosphere, in a region known as the plasma mantle [*Strangeway and Russell*, 1996]. In this region the magnetic field is mainly draped over the ionopause. This therefore makes it unlikely that the waves transfer energy from the magnetosheath to the ionosphere [*Strangeway and Crawford*, 1993]. Moreover, the waves occur in a region where the magnetic field rotates to a more flow aligned direction. It is possible that the field-aligned currents associated with the field rotation generate the waves. On the other hand, because this is a region of mixed magnetosheath and ionospheric plasma, some form of "pick-up" ion instability could operate.

In pursuing the nature of the field-aligned currents, we have found that the rotation of the magnetic field is such that the field is more flow-aligned at lower altitudes. This strongly implies that the flow is significantly reduced at lower altitudes due to mass-loading. Since mass-loading

is the most likely cause of the field-aligned currents, the waves are almost certainly a consequence of the interaction of the two plasmas (either current driven, or pick up ions), and not a source of the currents.

The region of field-aligned current and plasma waves is therefore an additional transition region, besides the bow shock and ionopause. Upstream of the bow shock we have undisturbed solar wind, while in the ionosphere, of course, the plasma is primarily of planetary origin. It is possible that the transition region we have found above the dayside ionosphere evolves to become the "Intermediate Transition" observed further downstream of the planet [*Perez-de-Tejada et al.*, 1995]. Such a suggestion can be addressed through more data analysis, but perhaps the most useful tool is three-dimensional mass-loaded magnetohydrodynamic simulation.

Recently, collisional Joule dissipation has been invoked as another means for absorbing wave energy in the ionosphere of Venus [*Cole and Hoegy*, 1996]. However, we have shown that the Joule dissipation at the altitudes where the waves occur is essentially zero, and again the waves are not a significant source of heat for the dayside ionosphere [*Strangeway*, 1996].

With the support of this grant we have advanced our under the waves in the dayside magnetosheath of the planet.. We have demonstrated that the waves do not supply heat to the ionosphere. Moreover, it is apparent that mass-loading of the solar wind is occurring near where the waves are observed, and it is possible that the waves act to transfer momentum from the solar wind to plasma of planetary origin.

2) Plasma waves in the Venus foreshock and solar wind

In addition to the research on waves in the magnetosheath we have also carried out some research on waves observed upstream of the planetary bow shock in a region known as the foreshock. The foreshock and bow shock modify the ambient magnetic field and plasma, and we should understand this region if we are to also understand the magnetosheath.

One of the most interesting results we have found was made possible by mapping the plasma waves observed in the electron foreshock, using data acquired over several years [*Crawford et al.*, 1993; *Strangeway and Crawford*, 1995a; *Strangeway and Crawford*, 1995b]. We found that the electron plasma oscillations did not begin at the point where the field lines in the upstream solar wind are tangential to the bow shock (this is the at which electrons can begin to be accelerated and reflected at the shock). Instead the waves peak in amplitude some distance away from the shock. In addition the waves fade away about 15 Venus radii away from the shock. A similar result was found at the Earth, except that the distances where about a factor of ten greater [*Greenstadt et al.*, 1995]. This indicates that the energy acquired by the electrons at the shock depends on shock size, in that the decrease in wave amplitude upstream of the shock implies that no electrons have sufficiently high energy to travel upstream to the location where the waves weaken. Instead the electrons are convected downstream by the solar wind. Since the electrons gain energy by drifting along the shock, it is reasonable for the amount of energy gained to be determined by the shock radius of curvature.

On the other hand, the maps of the foreshock wave emissions at Venus did show a difference with respect to the Earth, at least with regard to the ion foreshock. We found that the ion acoustic waves, which were thought to be driven by ions reflected at the bow shock, were observed further downstream than the ULF waves, also though to be driven by ions from the shock [*Strangeway and Crawford*, 1995a; *Strangeway and Crawford*, 1995b]. This implies that the ion acoustic waves have a different source than the ULF waves. The source for the VLF ion acoustic waves has yet to be determined.

3) Plasma waves in the Venus nightside ionosphere and ionotail

Although most of the research supported by this grant was directed to wave observations on the dayside of the planet, we also analyzed data from the nightside. The plasma waves observed by the Pioneer Venus Orbiter in the nightside ionosphere of Venus continue to be of considerable interest, primarily because they have been cited as evidence for lightning on Venus [*Strangeway*, 1995]. The lightning hypothesis has been further strengthened since a recent study [*Ho et al.*, 1995] has shown that the waves are not associated with gradients within the plasma, which would be expected if a local instability were to be the source of the waves.

Recently, the lightning hypothesis has come under attack from a new direction. If the waves observed in the low altitude ionosphere are indeed due to lightning, then they must propagate through the highly collisional bottomside ionosphere. The collision frequency is so high at the lowest altitudes ($\approx$ 130 km) that the waves will heat the ionosphere. It has been argued [*Cole and Hoegy*, 1996] that the amount of heating will be so great that the ionosphere will be significantly perturbed by the waves. Since the ionosphere is not perturbed, then Cole and Hoegy argue that we must reject the lightning hypothesis.

However, it has been pointed out [*Strangeway*, 1996] that at higher altitudes, the collision frequency is small enough that electron heat conduction can carry the heat away, even with relatively large conduction scale lengths. At lower altitudes the heat conduction is weaker, and so some local heating does occur. However, because the heat conduction is weak, the region of enhanced temperatures is thermally isolated. Thus, even though there is some local heating in the bottomside, there is no evidence for this heating in the topside ionosphere.

At higher altitudes in the nightside we have discovered ion acoustic waves that appear to be a signature of flowing ions of ionospheric origin [*Intriligator et al.*, 1994], while in the tail lobes we have observed bursts of waves at 5.4 kHz [*Ho et al.*, 1994]. Through comparison with Langmuir probe data, and polarization analysis, we deduce that the waves are plasma oscillations, indicating that the lobe density can be as low as 0.36 cm^{-3}.

References (papers supported by this grant are indicated thus: [NAGW-3497])

Cole, K. D., and W. R. Hoegy, Joule heating by ac electric fields in the ionosphere of Venus, *J. Geophys. Res*, *101*, 2269–2278, 1996.

Crawford, G. K., R. J. Strangeway, and C. T. Russell, VLF imaging of the Venus foreshock, *Geophys. Res. Lett.*, *20*, 2801–2804, 1993.

Greenstadt, E. W., G. K. Crawford, R. J. Strangeway, S. L. Moses, and F. V. Coroniti, Spatial distribution of electron plasma oscillations in the Earth's foreshock at ISEE 3, *J. Geophys. Res.*, *100*, 19,933–19,939, 1995. [NAGW-3497]

Ho, C.-M., R. J. Strangeway, and C. T. Russell, Spatial distribution of plasma wave activity in the nightside ionosphere of Venus, *Planet. Space Sci.*, *42*, 813–823, 1994. [NAGW-3497]

Ho, C.-M., R. J. Strangeway, and C. T. Russell, Venus nightside ionospheric irregularities and their relationship to VLF bursts, *J. Geophys. Res.*, *100*, 9697–9705, 1995. [NAGW-3497]

Intriligator, D. S., L. H. Brace, P. A. Cloutier, J. M. Grebowsky, R. E. Hartle, W. T. Kasprzak, W. C. Knudsen, and R. J. Strangeway, Evidence for ion transport and molecular ion dominance in the Venus ionotail, *J. Geophys. Res.*, *99*, 17,413–17,420, 1994. [NAGW-3497]

Perez-de-Tejada, H., D. S. Intriligator, and R. J. Strangeway, Intermediate transition in the Venus ionosheath, *J. Geophys. Res.*, *100*, 14,523–14,535, 1995. [NAGW-3497]

Scarf, F. L., W. W. L. Taylor, and I. M. Green, Plasma waves near Venus: Initial observations, *Science*, *203*, 748–750, 1979.

Strangeway, R. J., Plasma wave evidence for lightning on Venus, *J. Atmos. Terr. Phys.*, *57*, 537–556, 1995. [NAGW-3497]

Strangeway, R. J., Collisional Joule dissipation in the ionosphere of Venus: The importance of electron heat conduction, *J. Geophys. Res.*, *101*, 2279–2295, 1996. [NAGW-3497]

Strangeway, R. J., and G. K. Crawford, On the instability and energy flux of lower hybrid waves in the Venus plasma mantle, *Geophys. Res. Lett.*, *20*, 1211–1214, 1993.

Strangeway, R. J., and G. K. Crawford, Comparison of upstream phenomena at Venus and Earth, *Adv. Space Res.*, *16*, (4)125–(4)136, 1995a. [NAGW-3497]

Strangeway, R. J., and G. K. Crawford, VLF waves in the foreshock, *Adv. Space Res.*, *15*, (8/9)29–(8/9)42, 1995b. [NAGW-3497]

Strangeway, R. J., and C. T. Russell, Plasma waves and field-aligned currents in the Venus plasma mantle, *J. Geophys. Res.*, *101*, 17,313–17,324, 1996. [NAGW-3497]

Taylor, W. W. L., F. L. Scarf, C. T. Russell. and L. H. Brace, Absorption of whistler mode waves in the ionosphere of Venus, *Science*, *205*, 112–114, 1979.

JOURNAL OF GEOPHYSICAL RESEARCH, VOL. 101, NO. A8, PAGES 17,313–17,324, AUGUST 1, 1996

Plasma waves and field-aligned currents in the Venus plasma mantle

R. J. Strangeway and C. T. Russell

Institute of Geophysics and Planetary Physics, University of California, Los Angeles

Abstract. Plasma waves, observed above the dayside Venus ionosphere by the Pioneer Venus Orbiter (PVO) plasma wave instrument, have been attributed to whistler mode waves, lower hybrid waves, or ion acoustic waves. In order to clarify the nature of the waves, we have performed both case study and statistical analyses of the plasma wave and magnetic field data. We find that the plasma wave data are well ordered by altitude with respect to the location where the PVO Langmuir probe, or orbiter electron temperature probe (OETP), measures a density of 100 cm^{-3}, known as the OETP ionopause. The dominant signature in the wave data appears to be a change in the instrument noise level because of changes in the plasma Debye length. However, there is a burst of wave activity near the OETP ionopause. Also, we find that there is a rotation in the magnetic field at or near this location. By casting the magnetic field data into a coordinate system ordered by the presumed magnetosheath flow, we find that the rotation of the field tends to orient the field in a more flow-aligned direction at lower altitudes. We attribute this to mass loading at lower altitudes. We further suggest that the field-aligned current associated with the field rotation corresponds to a shear Alfvén wave standing in the magnetosheath flow. The field-aligned currents are present because of boundary conditions imposed on the flow, and it is not clear if the waves are actually associated with the field-aligned currents or are simply coincidental. Since the waves are observed at the OETP ionopause, further progress in understanding these waves will be made though determining what underlying plasma structure, if any, is related to the OETP ionopause, which is defined by a specific instrument threshold. Nevertheless, our study confirms that the wave activity, field-aligned currents, and OETP ionopause all occur within the plasma mantle above the ionosphere. As such, the plasma waves are not an energy source for the dayside ionosphere.

1. Introduction

The ionosphere forms the principal obstacle to the solar wind for an unmagnetized planet, allowing direct interaction between the solar wind and ionospheric plasma. At Venus, part of this interaction occurs in a region known as the plasma mantle [*Spenner et al.*, 1980], which lies above the dayside ionopause of Venus. The mantle contains a mixture of ionospheric and solar wind plasma. VLF and ELF plasma waves are observed in this region by the Pioneer Venus Orbiter (PVO) [*Crawford et al.*, 1993], and it appears likely that these waves are a consequence of the mixed plasmas. A similar region is found at Mars [*Nagy et al.*, 1990; *Sagdeev et al.*, 1990], although it is referred to as the planetosphere rather than the mantle, and plasma waves are also observed within this region [*Grard et al.*, 1991].

At Venus the VLF and ELF waves were originally thought to be whistler mode waves generated at the bow shock, propagating through the magnetosheath to be absorbed within the ionosphere [e.g., *Scarf et al.*, 1979, 1980a; *Taylor et al.*, 1979]. However, *Szegö et al.* [1991] pointed out that the magnetic field near the ionopause (in the mantle) is draped over the ionopause. Since whistler mode waves tend to carry energy parallel to the ambient magnetic field, very little wave energy is consequently transported to the ionosphere. Instead, *Szegö et al.* [1991] suggested that the waves were lower hybrid waves generated by the relative drift between ions of planetary and solar wind origin.

Unfortunately, lower hybrid waves also carry most of their wave energy flux parallel to the ambient field [*Strangeway and Crawford*, 1993]. Moreover, thermal effects, such as ion and electron Landau damping, were neglected by *Szegö et al.* [1991]. Thus *Strangeway and Crawford* [1993] concluded that an ion acoustic-like instability [*Taylor et al.*, 1981] may best explain the waves. *Huba* [1993] followed up on this suggestion and found that an ion-acoustic instability could be generated by the relative drift between shocked solar wind electrons and cold planetary oxygen ions. The group velocity of these waves is $\approx(n_i T_e/n_e m_i)^{1/2} \approx 10$ km s^{-1} for typical mantle values, where n_i is the oxygen ion density, T_e is the magnetosheath electron temperature, n_e is the electron density, and m_i is the ion mass. Electrostatic ion acoustic waves have lower energy density than electromagnetic whistler mode waves for the same electric field amplitude. This, combined with the low group velocity, implies that ion acoustic waves would not transport significant energy from the mantle to the ionosphere.

More recently, however, *Shapiro et al.* [1995] have argued that cold electrons of planetary origin would tend to quench the ion acoustic instability discussed by *Huba* [1993]. Instead, they suggested that the modified two-stream instability generates waves in two branches. One, the lower hybrid (or hydrodynamic) branch, is below the lower hybrid resonance

Paper number 96JA00927.
0148-0227/96/96JA-00927$09.00

frequency and is not detectable by the Pioneer Venus wave instrument. The other, which they refer to as the kinetic branch (absent in the earlier analysis of *Szegö et al.* [1991]) would be detectable by PVO. It should be noted, however, that this so-called kinetic branch appears to be simply the whistler mode resonance cone. Inspection of equation (11) and Figure 6 of *Shapiro et al.* [1995] shows that for this branch, $\omega \approx \omega_{lh}(m_p/m_e)^{1/2}(k_{||}/k) \approx \Omega_e \cos\theta$, where ω is the wave frequency, m_p and m_e are the proton and electron masses, respectively, Ω_e is the electron gyrofrequency, ω_{lh} is the lower hybrid frequency ($= \Omega_e(m_e/m_p)^{1/2}$), k is the wave vector, θ is the angle of the wave vector with respect to the magnetic field, and $k_{||} = k\cos\theta$. For this mode the assumption that $\omega << \Omega_e$ is no longer valid, and kinetic effects due to gyroresonance, as well as Landau damping by the cold (planetary) electrons, should be included. The group velocity of both wave modes considered by *Shapiro et al.* [1995] is primarily along the magnetic field and hence mainly tangential to the ionopause.

It therefore appears unlikely that the waves observed in the Venus plasma mantle are a significant source of energy for the dayside Venus ionosphere, regardless of the wave mode considered. However, the waves may play an important role within the mantle. If they are generated by the relative drift between magnetosheath and planetary ions, they may provide momentum coupling and also cause local heating of the planetary ions. On the other hand, *Crawford et al.* [1993] showed that the waves are often associated with field-aligned currents within the mantle region. It is therefore possible that the waves are generated by the field-aligned currents and may be a source of anomalous resistivity within the plasma. It is the purpose of this paper to determine, from a statistical viewpoint, where the waves occur within the mantle and what other phenomena are associated with the waves. This will hopefully provide an initial step in constraining the various hypotheses put forward to explain the waves.

In section 2 we will discuss the different definitions of the ionopause at Venus. We will show that the ionopause as defined by the Langmuir probe (the orbiter electron temperature probe (OETP) ionopause) orders the plasma wave data. Of the various ionopause definitions the OETP ionopause is at highest altitude and generally lies within the plasma mantle, as defined by *Spenner et al.* [1980]. In section 3 we will describe a coordinate system used to order the magnetic field data. This coordinate system, which is aligned along the radial and assumed magnetosheath flow directions, allows us to show that the magnetic field is deflected above the ionosphere, in a manner consistent with mass loading at lower altitudes. In section 4 we will present a statistical analysis that further supports the results of sections 2 and 3, that the waves tend to occur at the OETP ionopause and that a field-aligned current is often observed near this ionopause. In section 5 we will study the observed magnetic field rotation in more detail, showing that the rotation can be explained as being due to field lines that are convected to lower altitudes in the subsolar region, where they are transported more slowly to the nightside than at higher altitudes. We will further show that the field rotation can be interpreted as a shear Alfvén wave standing in the magnetosheath flow. Last, in section 6 we will summarize our results. The OETP ionopause clearly orders the data, but it is not yet obvious what is the ultimate source for the waves. The next step appears to be determining the nature of the OETP ionopause.

2. OETP Ionopause

One possible source of confusion concerning the nature of the plasma waves observed on the dayside of Venus is due to different definitions of the ionopause. *Phillips et al.* [1988] show in their Figure 4 the altitude of the ionopause using different definitions. The four definitions discussed by *Phillips et al.* [1988] are (1) the altitude at which the PVO Langmuir probe (orbiter electron temperature probe, OETP) measures a density of 100 cm^{-3} (the OETP ionopause); (2) the altitude at which the retarding potential analyzer (ORPA) measures 100 cm^{-3} (the ORPA ledge); (3) the altitude where plasma thermal pressure equals magnetic pressure (the pressure balance ionopause); and (4) the altitude where the ORPA observes a break in the density profile (the ORPA top). These different "ionopauses" are usually encountered in the order given when passing from high to low altitude. At low solar zenith angles they are close together in altitude, but they can be hundreds of kilometers apart at the terminator.

Crawford et al. [1993] noted that the wave bursts detected by the orbiter electric field detector tended to occur at or near the OETP ionopause. This can be seen clearly in Figure 1. In Figure 1 we show the 100-Hz wave amplitude plotted using a gray-scale representation as a function of altitude and local time. The data are taken from the Unified Abstract Data System (UADS) database for orbits 125–248, with Figure 1a showing the inbound leg for each orbit and Figure 1b showing the outbound leg. UADS was originally designed as an on-line data system [*Ferandin et al.*, 1980], using a common 12-s format for all instrument data. Later, the on-line system was discontinued, and UADS data were subsequently submitted by experimenters to the National Space Science Data Center, as described in the appendix to *Brace and Kliore* [1991]. The circles in Figure 1 give the location of the OETP ionopause (L. H. Brace, personal communication, 1993) for each orbit.

In the UADS database the wave amplitude is given as both a peak and an average, and we have used the peak in Figure 1. The peak amplitude allows us to more clearly discern the association between the waves and the underlying plasma structure, but some caution should be employed in interpreting the data. In particular, both the peaks and averages are calculated using a 24-s window with 12-s spacing. Thus there is a potential for aliassing of the data, especially in point-by-point comparisons. However, statistical studies will be less prone to aliassing, and Figure 1 shows that statistically the wave amplitude tends to peak at or near the OETP ionopause. Thus we will use altitude with respect to the OETP ionopause to order the data, rather than altitude from the surface of the planet. While subsequent analysis presented in this paper will show that the OETP ionopause is a useful reference altitude for ordering the data, this methodology is also supported by *Crawford* [1993]. He showed that for a sample of some 30 orbits the OETP ionopause altitude ordered the plasma wave data better than the $\beta = 1$ altitude, which tended to occur always below the wave intensity peak altitude. Since the other ionopause definitions discussed earlier usually occur below the $\beta = 1$ altitude, they will similarly be less useful in ordering the plasma wave data.

In the introduction we stated that the waves are observed within the plasma mantle. Although we refer to the altitude at which the Langmuir probe measures a density of 100 cm^{-3} as the OETP ionopause, we consider this as occurring within the

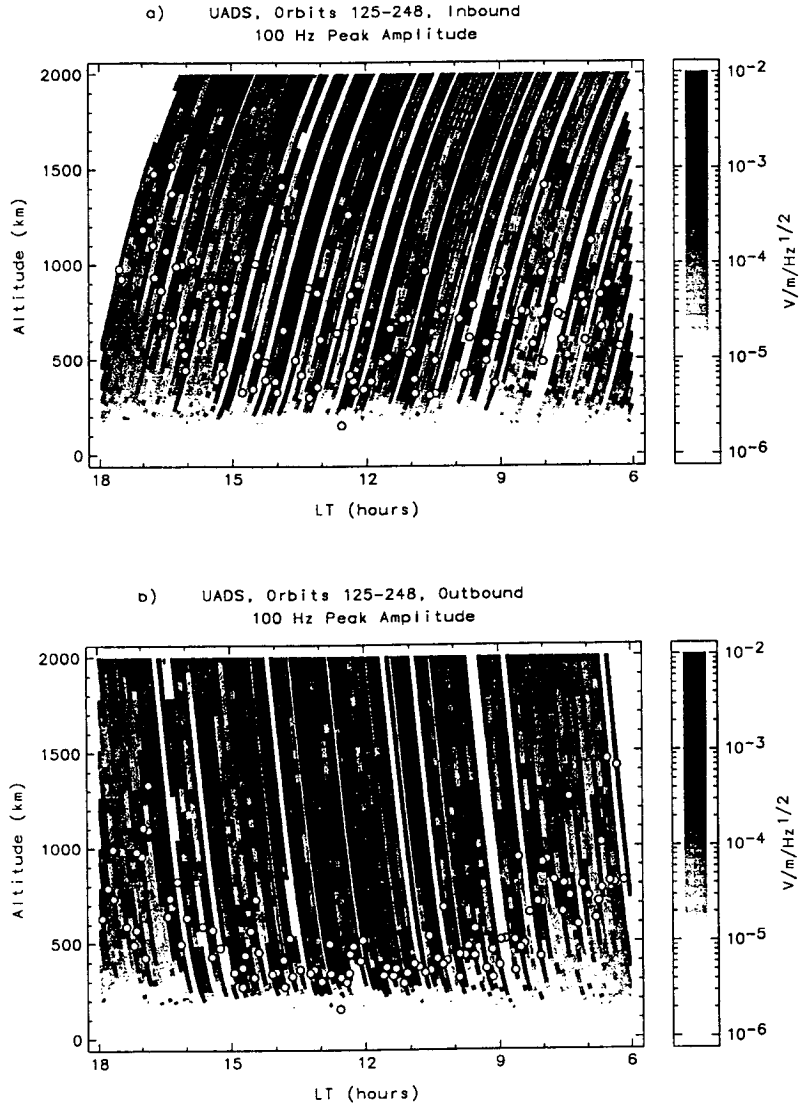

Figure 1. 100 Hz peak amplitude as a function of altitude and local time for orbits 125–248. The data are shown for (a) inbound and (b) outbound portions of each orbit. The gray scale indicates the peak amplitude per 24-s interval, with 12-s spacing between samples. The circles indicate the altitude of the orbiter electron temperature probe (OETP) ionopause.

plasma mantle. At higher altitudes the plasma is essentially shocked solar wind plasma. At much lower altitudes the plasma is ionospheric in origin. The OETP ionopause is therefore probably within a region of mixed plasmas. Whether or not the OETP ionopause corresponds to a sharp boundary, or is simply a point on a more gradual transition, requires further analysis.

Before discussing the magnetic field and plasma wave signatures at the OETP ionopause in more detail, we note that the other striking feature in Figure 1 is the relatively low level of plasma wave noise at lower altitude. We will discuss this later. However, our main conclusion concerning the low level of wave noise is that this is mainly an instrument artifact associated with the changes in the plasma Debye length and is not due to the absorption of waves as postulated by *Scarf et al.* [1980a].

3. Flow-Aligned Coordinates

Besides using the OETP ionopause as a reference altitude, we will also use a coordinate system for the magnetic field data that is based on the assumed flow direction within the magnetosheath. This coordinate system, which is similar to radial-east-north coordinates, is shown in Figure 2. In deriving the coordinate system we have assumed that the magnetosheath flow is symmetric about the Venus-Sun line and is mainly tangential to the obstacle, which we further assume is spherical in shape. Thus most of the flow is assumed to be along the direction labeled "flow," with very little or no radial component, except at the subsolar point. The direction labeled "perp" completes the triad and is perpendicular to both the radial and assumed flow direction. The transformation from the Venus solar orbital (VSO) coordinate system to the "radial-flow-

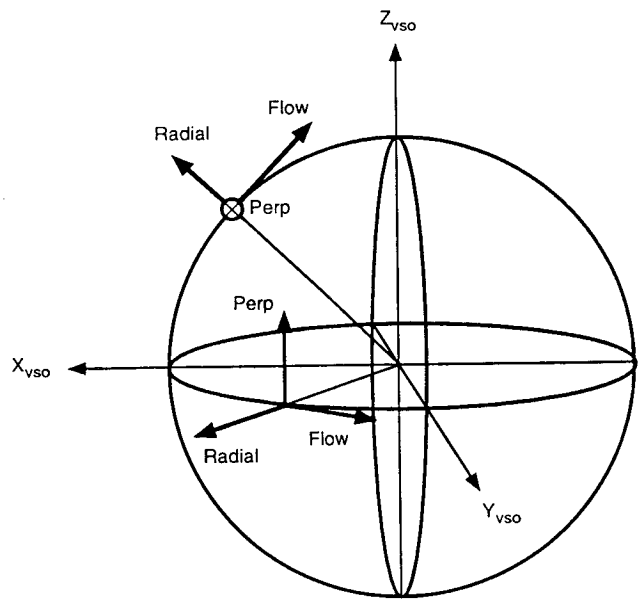

Figure 2. Relationship between flow-aligned coordinates and Venus solar orbital (VSO) coordinates.

perp" system can be obtained as follows: If the spacecraft position is given by **R** in VSO, then the perpendicular direction $\hat{\mathbf{p}} = \hat{\mathbf{x}} \times \mathbf{R}/|\hat{\mathbf{x}} \times \mathbf{R}|$, where $\hat{\mathbf{x}}$ is the unit vector along the X_{VSO} axis. The flow direction is given by $\hat{\mathbf{f}} = \hat{\mathbf{p}} \times \mathbf{R}/|\mathbf{R}|$. The radial direction is of course given by $\hat{\mathbf{r}} = \mathbf{R}/|\mathbf{R}|$. The dot product of any vector in VSO with the unit vectors $\hat{\mathbf{r}}$, $\hat{\mathbf{f}}$, and $\hat{\mathbf{p}}$ gives the vector in the radial-flow-perp coordinates. A similar coordinate system was employed by *Law and Cloutier* [1995] in their study of the magnetic field structure.

The usefulness of this coordinate system can be seen in Figure 3, where we present high-resolution plasma wave and magnetic field data for the outbound portion of orbit 169. This orbit was also shown by *Crawford et al.* [1993]. The top four panels show the wave intensity for the four wave channels, while the bottom four channels show the magnetic field rotated into radial-flow-perp coordinates. The vertical line in each panel indicates the location of the OETP ionopause.

Before discussing the magnetic field data, we will repeat some of the points made by *Crawford et al.* [1993] concerning the plasma wave data. First, the dominant change in intensity, especially at 100 Hz, is the change in instrument background. This is due to the change in plasma Debye length, which is short (a few centimeters) within the ionosphere and long (a few meters) within the magnetosheath. The antenna length is 0.76 m [*Scarf et al.*, 1980b], while the spacecraft is 2.54 m in diameter. Hence the antenna is within the Debye sphere of the spacecraft when the spacecraft is in the magnetosheath, and the wave instrument is sensitive to noise caused by photoemission of electrons from the spacecraft and antenna elements. In the ionosphere the antenna is effectively shielded from photoemission noise. Thus any analysis of the wave data near the dayside ionopause should take into account the change in background. In particular, the decrease in wave intensity as the spacecraft enters the ionosphere cited by *Scarf et al.* [1980a] is not evidence for whistler mode absorption in the ionosphere but is simply the result of the change in instrument background. However, in addition to the change in background, Figure 3 shows a wave burst at all four channels at the OETP ionopause. This burst does not display any of the characteristics of the background noise and is probably due to plasma waves generated at or near the OETP ionopause.

Turning now to the magnetic field data, Figure 3 shows that the field is quite large near the OETP ionopause. The magnetic barrier [*Elphic et al.*, 1980] extends to altitudes well below the OETP ionopause. Throughout this region the radial component is small, and the field is mainly draped over the obstacle. However, the field direction changes just below the OETP ionopause. Above the OETP ionopause the field has large components both parallel and perpendicular to the assumed flow direction. Below the OETP ionopause the field rotates to a direction parallel to the assumed magnetosheath flow. *Luhmann* [1988] discussed the presence of a magnetic field rotation within the mantle region. In her model the rotation of the field was due to convection of the field to lower altitudes, where the horizontal plasma flow was reduced. This velocity shear causes the magnetic field to be more flow-aligned at lower altitudes, resulting in the "weathervaning" of the field described by *Law and Cloutier* [1995] in their analysis of magnetic field data from the dayside of Venus.

Since there is little or no change in magnetic field magnitude, the current in the magnetic shear layer is mainly field-aligned. The magnetic field is mainly horizontal, and hence the field-aligned currents are horizontal. At lower altitudes the magnetic field is shielded from the ionosphere by perpendicular currents, which also flow horizontally. We therefore assume that there are only vertical gradients in the field, and the variation of the horizontal components of magnetic field as a function of altitude will be used to calculate the current density.

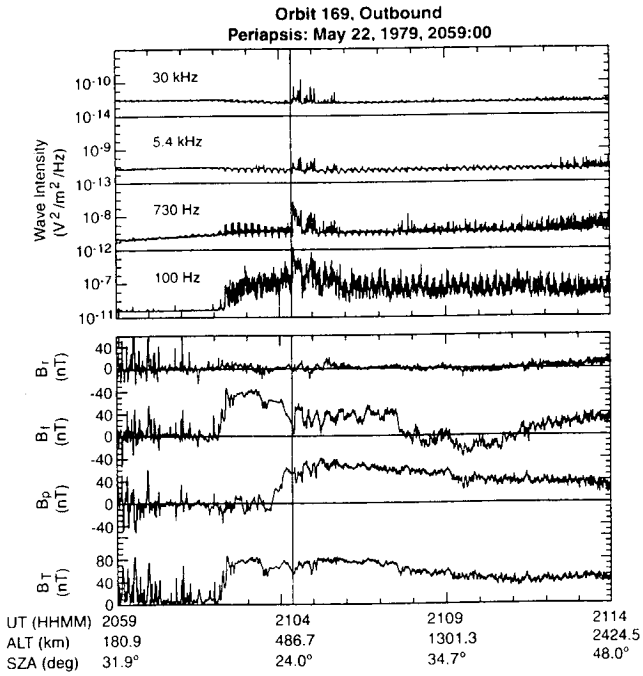

Figure 3. High resolution plasma wave and magnetic field data from orbit 169 outbound. Fifteen minutes of data are shown, with the top four panels showing wave intensity for the four wave channels, using a logarithmic scale. The bottom four panels show the magnetic field, cast into radial-flow-perp components. The vertical line in Figure 3 marks the OETP ionopause.

Additional examples of high resolution wave and field data are given in Figures 4, 5, and 6. Each of Figures 4, 5, and 6 show a wave burst near the altitude of the OETP ionopause. In all the examples the burst is detected at 100 Hz, but sometimes the burst extends to higher frequencies. This argues against a lower hybrid wave mode and for an acoustic mode [*Taylor et al.*, 1981; *Strangeway and Crawford*, 1993; *Huba*, 1993], since the lower hybrid resonance frequency is typically only a few tens of Hertz. Because lower hybrid waves are thought to be in resonance with ions of planetary origin, there would be little or no Doppler shift of the waves when observed in the spacecraft frame, which moves relatively slowly with respect to the planet. The spacecraft speed is $\approx$10 km s^{-1}, while the shocked solar wind speed is $\approx$100 km s^{-1}.

In each of the examples shown in Figures 3–6 the magnetic field deflects to a more flow-aligned direction at lower altitude. The tendency for the field to become more flow aligned below the OETP ionopause will be a conclusion of the statistical analysis presented in sections 4 and 5. However, it should be noted that not every orbit displays this behavior. There are orbits in which the field rotation is in the opposite sense, becoming transverse to the assumed flow direction at lower altitudes. This could be because the actual magnetosheath flow is not as assumed or because the interplanetary magnetic field changes direction. Clearly, these exceptions should be investigated, but we will defer such analysis to future studies.

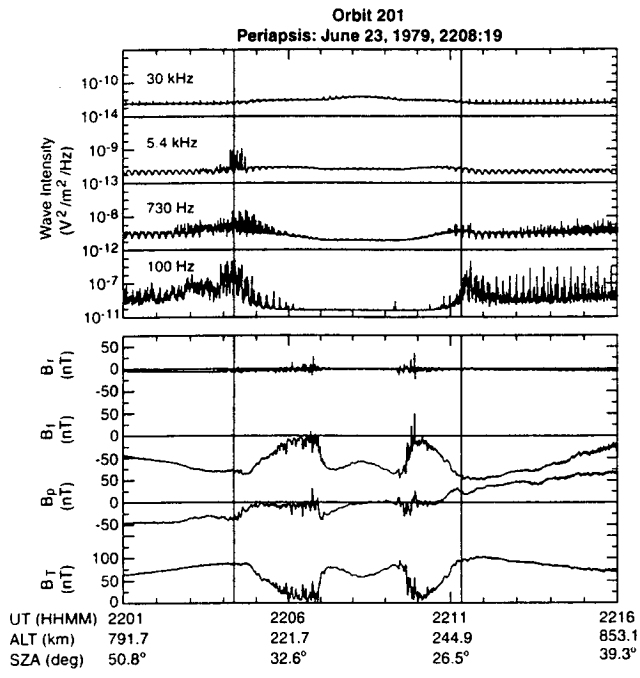

Figure 5. Wave and magnetic field data for the periapsis portion of orbit 201. Similar in format to Figure 3. This orbit was also discussed by *Luhmann* [1988].

4. Wave Occurrence Statistics

In Figure 7 we show UADS data from the first three dayside periapsis seasons of the Pioneer Venus Orbiter (i.e., orbits 125–248, 345–475, and 570–700). In Figure 7 we have restricted the data to solar zenith angles (SZA) < 30°. The top panel of Figure 7a shows the peak wave amplitude binned as a function of altitude with respect to the OETP ionopause, using 25-km bins. For each channel the symbols indicate the median peak amplitude per bin, with the shaded area indicating the upper and lower quartile. Clearly, the largest signal is measured at 100 Hz, but both the 730-Hz and 5.4-kHz channels also observe a wave burst at the OETP ionopause. However, as noted earlier, the major signature associated with the OETP ionopause appears to be a change in the instrument back-

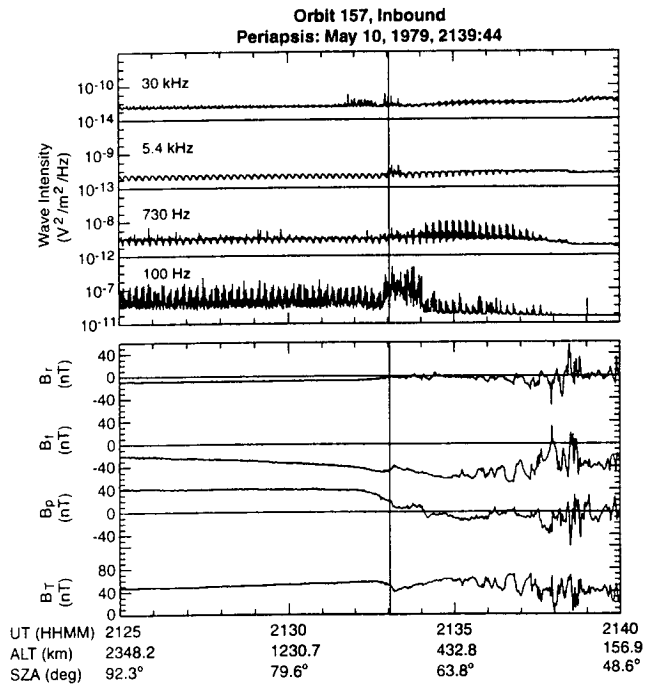

Figure 4. Wave and magnetic field data for the inbound portion of orbit 157. Similar in format to Figure 3.

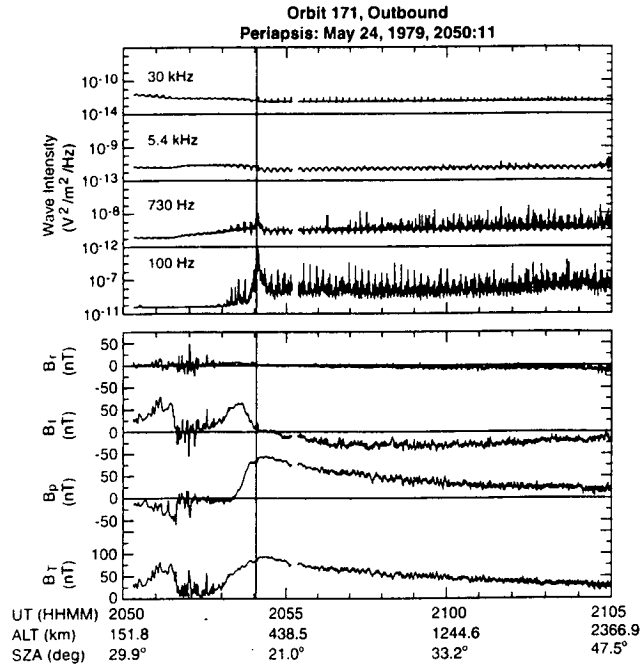

Figure 6. Wave and magnetic field data for the outbound portion of orbit 171. Similar in format to Figure 3. This orbit was also discussed by *Law and Cloutier* [1995].

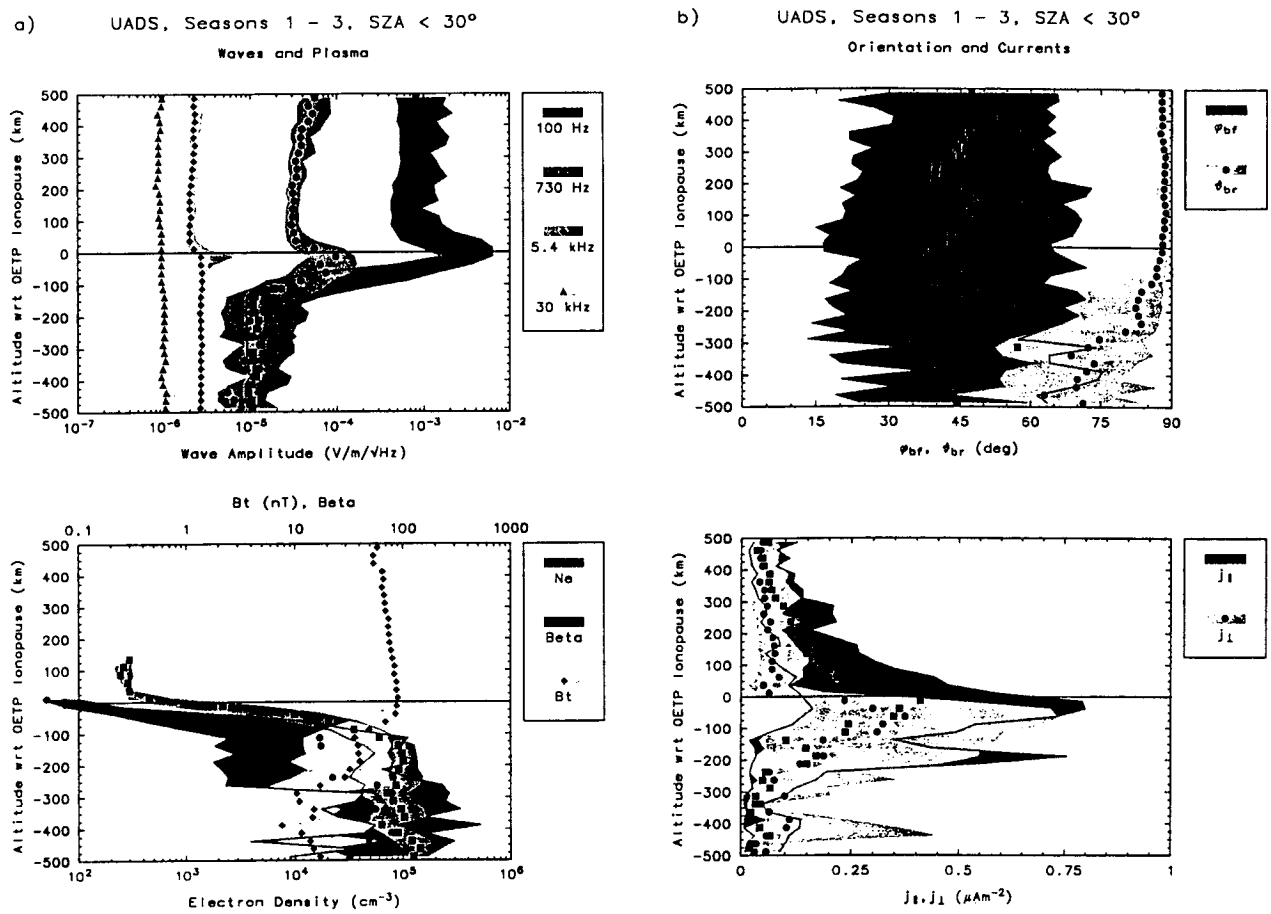

Figure 7. Wave and plasma variations as a function of altitude with respect to the OETP ionopause for solar zenith angles (SZA) <30°. In Figure 7 and subsequently (Figures 8 and 9) we have used data from the Unified Abstract Data System database for the first three seasons of dayside periapsis. The wave data are peak amplitudes. The plasma data are from the Langmuir probe. In calculating the plasma beta we assume that the ion temperature (T_i) = T_e/1.8 for altitudes > 350 km, where T_e is the electron temperature. The top panel of Figure 7a shows the wave amplitude for the four wave channels, while the bottom panel shows magnetic field strength, electron density, and plasma beta. The symbols show the median values per 25-km-altitude bin, while the shaded regions mark the upper and lower quartiles per bin. In Figure 7b we show the angle the magnetic field makes with the presumed flow direction (ϕ_{bf}) and the angle the field makes with respect to the vertical (θ_{br}). Both angles have been folded into the range 0°–90°. The bottom panel of Figure 7b shows the parallel and perpendicular current density, calculated assuming horizontal currents and neglecting the vertical component of the magnetic field.

ground. For example, apart from the peak at the OETP ionopause, we would conclude that the 100-Hz background changed from $\approx 10^{-5}$ V m^{-1} Hz$^{-1/2}$ within the ionosphere to $\approx 10^{-3}$ V m^{-1} Hz$^{-1/2}$ within the magnetosheath. At the OETP ionopause the peak wave amplitude is $\approx 10^{-2}$ V m^{-1} Hz$^{-1/2}$.

The bottom panel of Figure 7a shows the ambient magnetic field strength and plasma parameters. From the magnetic field profile we deduce that the OETP ionopause is probably within the magnetic barrier region; there is little change in field strength across the OETP ionopause.

The plasma beta is deduced from the electron data, assuming that the ion temperature is related to the electron temperature. *Miller et al.* [1984] presented average profiles of the electron and ion temperature for the dayside ionosphere of Venus, and we have used a function attributable to J. L. Phillips to model the temperature ratio. For altitudes >350 km the ratio is constant, with the ion temperature (T_i) = T_e/1.8, where T_e is the electron temperature. The peak temperature ratio (T_e/T_i) is ≈4 at 200 km altitude. For reference, the electron temperature increases with increasing altitude, with $T_e \approx 0.1$ eV at altitudes ≈160 km, ≈0.3 eV at 250 km, and then gradually increasing up to the OETP ionopause altitude, where T_e as measured by the Langmuir probe ≈1 eV. At lowest altitude the deduced ion temperature T_i ≈0.06 eV. Because of the enhanced T_e/T_i ratio at ≈200 km, T_i does not begin to increase until ≈250 km altitude. At 350 km altitude, $T_i \approx 0.2$ eV, increasing to around 0.5 eV at the OETP ionopause. It should be remembered, however, that the ion temperature is deduced from the electron temperature and does not take into account the presence of superthermal ions often detected at or above the ionopause [*Taylor et al.*, 1981]. Beta is generally <1 at the OETP ionopause.

By definition the density at the OETP ionopause is 100 cm^{-3}, and no electron data are included in the UADS data for lower values, when the spacecraft is in sunlight. However, electron data from higher altitudes may be included if the density is >100 cm^{-3}. Thus the apparent ledge in the density pro-

file could simply be an effect of the density threshold for the Langmuir probe.

Figure 7b shows the magnetic field orientation and the current densities as a function of altitude with the respect to the OETP ionopause. From the top panel of Figure 7b we see that the field is mainly horizontal at and above the OETP ionopause. However, the orientation with respect to the presumed flow direction shows no preferred orientation as a function of altitude for this SZA range, with median value around 45° and the lower and upper quartiles at ≈25° and 65°. Because the top panel of Figure 7b does not show how the field changes direction along an individual orbit, we show the current density in the bottom panel of Figure 7b. As noted earlier, we assume only vertical gradients in the field. The field-aligned current indicates regions where the field rotates but does not change magnitude, while the perpendicular currents indicate where the field is shielded from the lower ionosphere. In presenting current densities in Figure 7b we have excluded data for which the vertical separation used to compute the current density is less than 20 km. This is done to exclude data near periapsis, where the spacecraft is traveling mainly horizontally, and the assumption that the observed gradients are vertical is probably not valid. At these low altitudes, fine-scale structures known as flux ropes tend to occur, further invalidating the assumption of vertical gradients.

From Figures 7a and 7b we therefore conclude that the OETP ionopause orders the wave data, with the largest-amplitude wave bursts occurring at the OETP ionopause. Furthermore, the OETP ionopause marks a region where the magnetic field rotates and field-aligned currents flow. The causal relationship, if any, between the waves and the currents has yet to be determined, but at this stage we would conclude that the currents flow in response to the magnetic field geometry imposed by the different flow regimes within the magnetosheath and ionosphere.

The peak current density in Figure 7b is 1 $\mu A\ m^{-2}$. This corresponds to a relative drift velocity of 60 $km\ s^{-1}$ for an electron density of 100 cm^{-3}, which is the nominal plasma density at the OETP ionopause. This velocity is much smaller than the thermal velocity of the shocked solar wind protons (temperature ≈100 eV) and the ambient electrons, be they hot shocked solar wind (≈50 eV) or cold planetary (≈1 eV) electrons. In order to drive an instability, we expect the drift velocity of the current-carrying species to be larger than its thermal velocity. If the current is to be the source of an instability, this suggests that cold planetary electrons are the current carriers, and these electrons are a small fraction of the total density. If, for example, we assume that the electrons of planetary origin are only 3% of the total density, then the electron drift velocity ≈1800 $km\ s^{-1}$, which is much larger than the cold electron thermal speed. This current could generate an obliquely propagating acoustic mode with phase speed of the order of the shocked solar wind sound speed but with parallel phase velocity of the order of the electron drift velocity. However, such an instability will be subject to Landau damping by the solar wind protons, unless the protons are cooler than the solar wind electrons. This is usually not thought to be the case, although *Shapiro et al.* [1995] do present an example of one orbit in which the electron temperature is ≈100 eV. Clearly, determining whether or not the currents are a source of the waves requires detailed knowledge of the ambient ion and electron populations.

Figures 8 and 9 show plasma and field data for SZA in the range 30° < SZA < 60° and 60° < SZA < 90°, respectively. The format of Figures 8 and 9 is similar to Figure 7, and again, current density data obtained for vertical separations less than 20 km have been excluded. As the SZA increases, the vertical scale of the plasma and field gradients also increases. Thus the current densities tend to be smaller at higher SZA. At higher SZA the change in orientation of the magnetic field becomes more clear, with the lowest ϕ_{bf} occurring at the OETP ionopause. Figures 8 and 9 therefore reinforce the conclusions drawn from Figure 7.

5. Field Rotation at the OETP ionopause

While the altitude profiles of current density and magnetic field orientation indicate that the magnetosheath magnetic field rotates at or near the OETP ionopause, the data shown in Figures 7, 8, and 9 do not indicate the sense of the rotation. In Figure 10 we show the orientation and the rotation of the magnetic field near the OETP ionopause. The magnetic field orientation just below the OETP ionopause is shown in the top panel of Figure 10. The data are binned in 10° ϕ_{bf} bins, with the solid circles giving the median θ_{br} angle and the error bars marking the upper and lower quartile per bin. Noting that $\theta_{br} < 90°$ means that the field is pointing to higher altitude, Figure 10 shows that when the field is pointing away from the subsolar point ($-90° < \phi_{bf} < 90°$) the field is also pointing to higher altitude. The reverse is the case when the field points toward the subsolar point.

The bottom panel of Figure 10 shows the median and quartiles of the field rotation on passing through the OETP ionopause from above. The angle ϕ_{bf} has been folded into the range 0°–90°, while the angle $\Delta\phi_{bf}$ is defined as <0 if the net orientation of the field is more flow-aligned at lower altitude. Thus, for the majority of the data, the field rotates to a more flow-aligned orientation at lower altitude.

The magnetic field orientation and rotation shown in Figure 10 can be explained in terms of velocity shear across the OETP ionopause. Near the subsolar point the magnetosheath flow tends to transport magnetic flux to lower altitude, where the field is "hung up" on the obstacle, presumably because of the presence of ionospheric plasma. A flux tube that has been convected by the magnetosheath flow will be at lower altitude near the subsolar point and at higher altitude away from the subsolar point where the magnetosheath flow is more nearly tangential to the obstacle. Because the flow at higher altitudes is faster, while the subsolar portion of the flux tube moves more slowly, the flux tube will tend to be aligned along the flow as it is convected away from the subsolar region. This "weathervaning," discussed by *Law and Cloutier* [1995] and modeled by *Luhmann* [1988], is shown schematically in Figure 11.

In Figure 11 the light gray surface marks a layer in which field-aligned currents flow. The solid arrows show the magnetosheath flow above this layer. The dark gray curves are magnetosheath flux tubes. When the flux tubes pass through the current layer, indicated by becoming darker gray, they encounter a region of reduced flow. As the flux tubes are transported away from the subsolar region, the shear in the flow causes the bend in the field to become larger, and the flux tube immediately below the current layer tends to be flow-aligned. In passing, we note that a similar process has been invoked for the formation of flux ropes [e.g., *Luhmann and Cravens*, 1991, and references therein], but flux rope formation occurs at lower altitude. Flux ropes are observed deep within the ionosphere below the magnetic barrier.

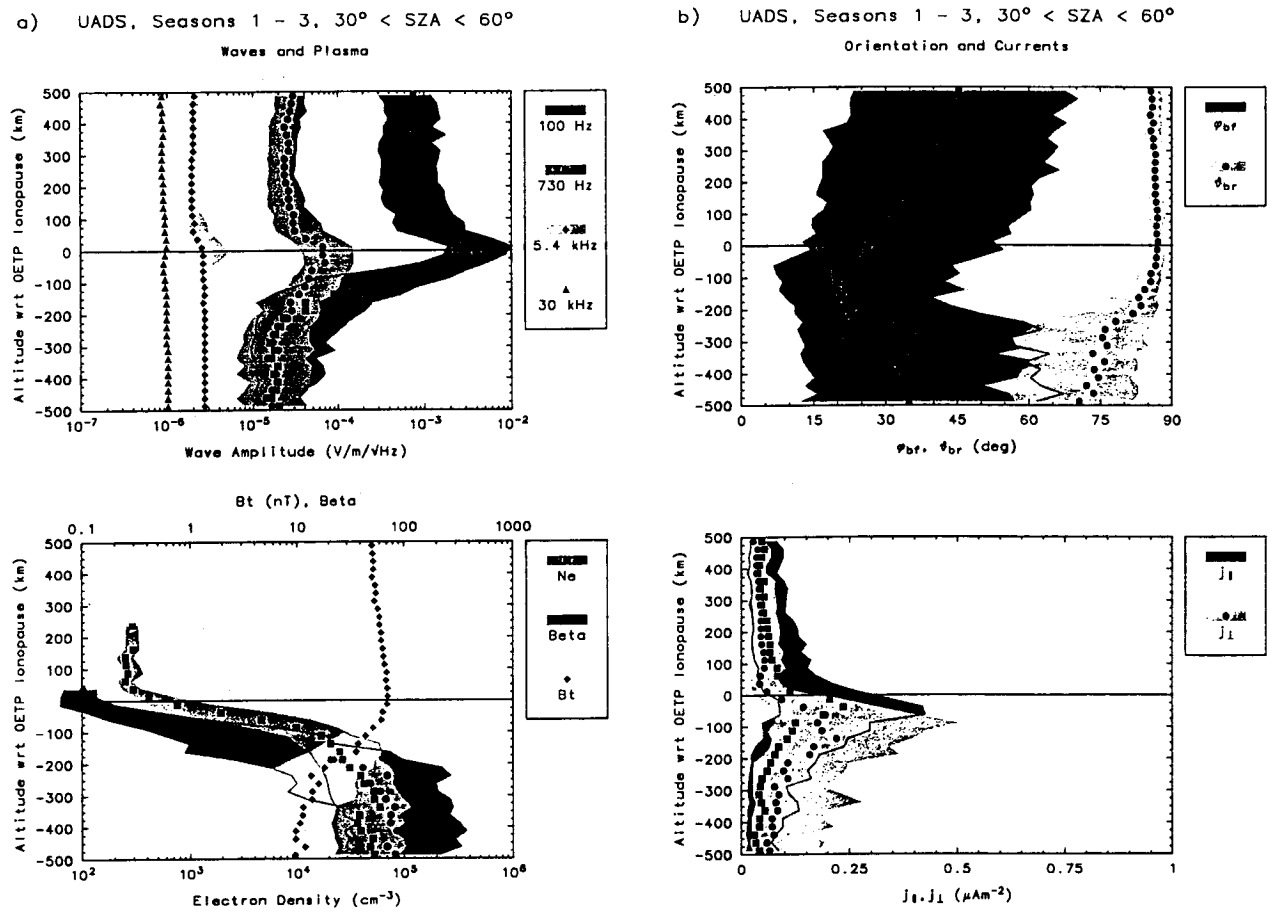

Figure 8. Wave and plasma variations as a function of altitude with respect to the OETP ionopause for 30° < SZA < 60°. Similar in format to Figure 7.

We can explain the field-aligned current layer as a shear Alfvén wave standing in the magnetosheath flow. This is in many ways analogous to the slow-mode standing wave observed in the terrestrial magnetosheath, as reported by *Song et al.* [1992], and discussed theoretically by *Southwood and Kivelson* [1992]. For a shear Alfvén wave the flow perturbation (**u**) is related to the magnetic field perturbation (**b**) by

$$\frac{\mathbf{u}}{V_a} = -\frac{\mathbf{b}}{B_0}\frac{\cos\theta}{|\cos\theta|}$$

where $\mathbf{B}_0$ is the ambient magnetic field, V_a is the Alfvén speed $= B_0/(\mu_0\rho_0)^{1/2}$, μ_0 is the permeability of free space, ρ_0 is the mass density, and θ is the angle between the wave vector (**k**) and $\mathbf{B}_0$. Since the wave is standing in the magnetosheath flow, **k** points upward, and $\theta \approx \theta_{br}$. From Figure 10, if $\mathbf{B}_0$ points away from the subsolar point, then $\mathbf{B}_0$ also has an upward component. Thus $\mathbf{k}\cdot\mathbf{B}_0 > 0$, and **u** is antiparallel to **b**. We illustrate the geometry of this situation in the two left-hand panels of Figure 12 for two orthogonal planes: the plane defined by the radial direction and the flow vector (top) and the horizontal plane (bottom). Since the horizontal component of the flow velocity (**v**) is also away from the subsolar point, $\mathbf{v}\cdot\mathbf{B}_0 > 0$. The direction of **u** is such that the horizontal flow velocity is reduced below the field-aligned current layer. Taking primed vectors as being below the current layer, then $\mathbf{v}' = \mathbf{v} + \mathbf{u}$, $\mathbf{B}_0' = \mathbf{B}_0 + \mathbf{b}$, and to first order $\mathbf{v}'\cdot\mathbf{B}_0' = \mathbf{v}\cdot\mathbf{B}_0 - (\mathbf{u}\cdot\mathbf{v})(\mathbf{k}\cdot\mathbf{B}_0)/(\omega\mu_0\rho_0)$. Since $\mathbf{u}\cdot\mathbf{v} < 0$, $\mathbf{v}'\cdot\mathbf{B}_0' > \mathbf{v}\cdot\mathbf{B}_0$, and the field is more flow-aligned below the current layer. We note that the closer alignment occurs with a change in both the field and the flow. When the magnetic field points toward the subsolar point, $\mathbf{k}\cdot\mathbf{B}_0 < 0$ and $\mathbf{v}'\cdot\mathbf{B}_0' < \mathbf{v}\cdot\mathbf{B}_0$, but $\mathbf{v}\cdot\mathbf{B}_0 < 0$, as illustrated in the two panels on the right-hand side of Figure 12. Again, the field is more flow-aligned below the current layer, and again, both field and flow rotate to accomplish this alignment.

Figure 10 shows that the median rotation of the field is ≈10°, and hence $b/B_0 \approx 0.18$. From Figure 7, $B_0 \approx 100$ nT at the OETP ionopause, while the plasma density is ≈100 cm^{-3}. If protons are the dominant ion, then $V_a \approx 220$ km s^{-1}. Thus $u \approx 40$ km s^{-1}, which should be compared with a nominal sheath flow speed of 100 km s^{-1}, and the flow velocity can be significantly reduced across the current layer. Increasing the amount of O^+ present reduces V_a and hence u. However, an increase in O^+ density would suggest that some slowing of the magnetosheath flow will have already occurred, and the flow velocity above the shear layer could be lower than 100 km s^{-1}. Nevertheless, even if the flow is reduced because of mass loading at higher altitudes, our discussion here indicates that there is a marked reduction in flow below the OETP ionopause, presumably because of higher planetary ion densities.

6. Conclusions

Through analysis of data from individual orbits and also from statistical studies we find that the plasma wave data are well ordered by altitude with respect to the OETP ionopause,

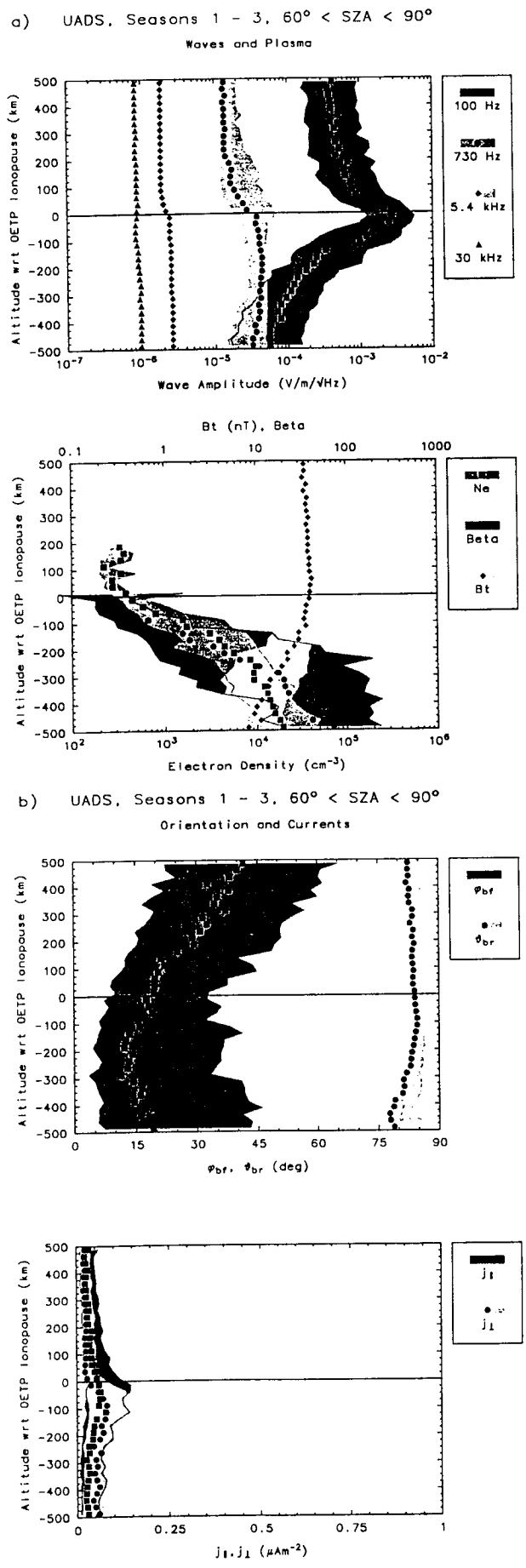

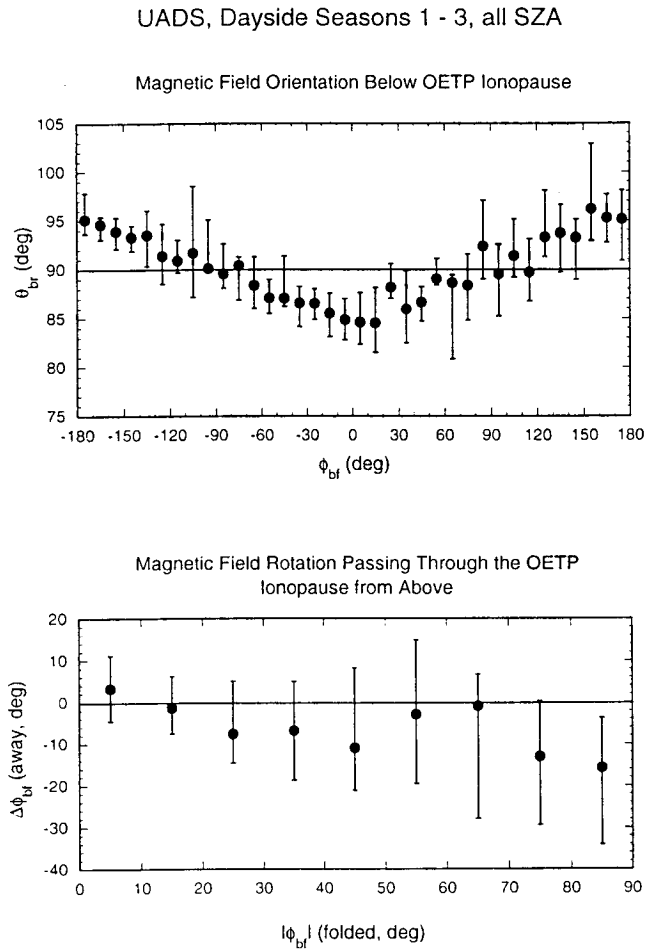

Figure 10. Magnetic field orientation and rotation at the OETP ionopause. The solid circles indicate the median, while the error bars mark the upper and lower quartile.

which is the altitude at which the Langmuir probe on PVO measures an electron density of 100 cm^{-3}. Of the various definitions of the ionopause the OETP ionopause is usually at highest altitude. The dominant signal in the wave data is a change in the background noise of the instrument, which we attribute to changes in the plasma Debye length. At low altitudes, within the ionosphere, the wave instrument is shielded from noise due to photoelectron emission from the spacecraft. At higher altitudes, in the magnetosheath, the antenna is within the Debye sphere of the spacecraft and is probably more sensitive to photoelectron emission noise and other sources of noise on the spacecraft. Inspection of the high-resolution plasma wave data does suggest that the wave burst often observed near the OETP ionopause is due to naturally occurring waves, since the data are qualitatively different. However, some caution may be warranted since the Debye length is ≈0.74 m when n_e = 100 cm^{-3} and T_e = 1 eV, this density and temperature being appropriate for the plasma at the OETP ionopause. Since the antenna separation is 0.76 m, a resonance between the antenna and the Debye sheath is possible.

Figure 9. Wave and plasma variations as a function of altitude with respect to the OETP ionopause for 60° < SZA < 90°. Similar in format to Figure 7.

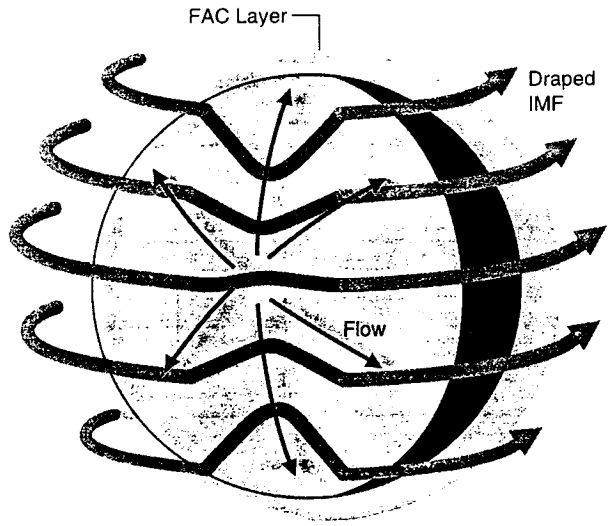

Figure 11. Schematic of the magnetic field geometry in the mantle and upper ionosphere.

The statistical studies show that field-aligned currents flow at or perhaps slightly below the OETP ionopause. These field-aligned currents occur above the topside density gradient and well above the perpendicular currents which mark the bottom of the magnetic barrier. On comparison with the data presented by *Spenner et al.* [1980], this places the OETP ionopause and the field-aligned currents in the mantle.

The field rotation associated with the field-aligned currents tends to align the field more closely with the magnetosheath flow. It appears that the flow alignment occurs because of a shear in the magnetosheath flow [see *Luhmann*, 1988; *Law and Cloutier*, 1995] which is probably due to mass loading by ionospheric plasma at lower altitudes. The magnetic field geometry is hence dictated by the field and flow boundary conditions imposed within the magnetosheath and the ionosphere, and the field-aligned currents occur in response to this imposed geometry. We have suggested that the field-aligned current layer is a shear Alfvén wave standing in the magnetosheath flow. The plasma waves observed at the OETP ionopause may be a consequence of the field-aligned currents but are certainly not a cause.

Recently, *Sauer et al.* [1994] argued that a composition boundary should be present above the ionopause of Venus and Mars. Perhaps the OETP ionopause is this boundary. However, the two-dimensional simulations of *Sauer et al.* [1994] cannot explain the field rotation we have discussed here. This rotation in the field should only be present in three-dimensional simulations. We also note that the composition boundary discussed by *Sauer et al.* [1994], and observed at Mars by *Dubinin and Lundin* [1995], is associated with a decrease in the ambient magnetic field strength. At Venus the magnetic field strength tends to decrease at altitudes below the location of the field-aligned currents. The field rotation discussed here strongly suggests that the magnetosheath magnetic field passes into a region dominated by plasma of planetary origin (i.e., below the composition boundary), as the increased mass density

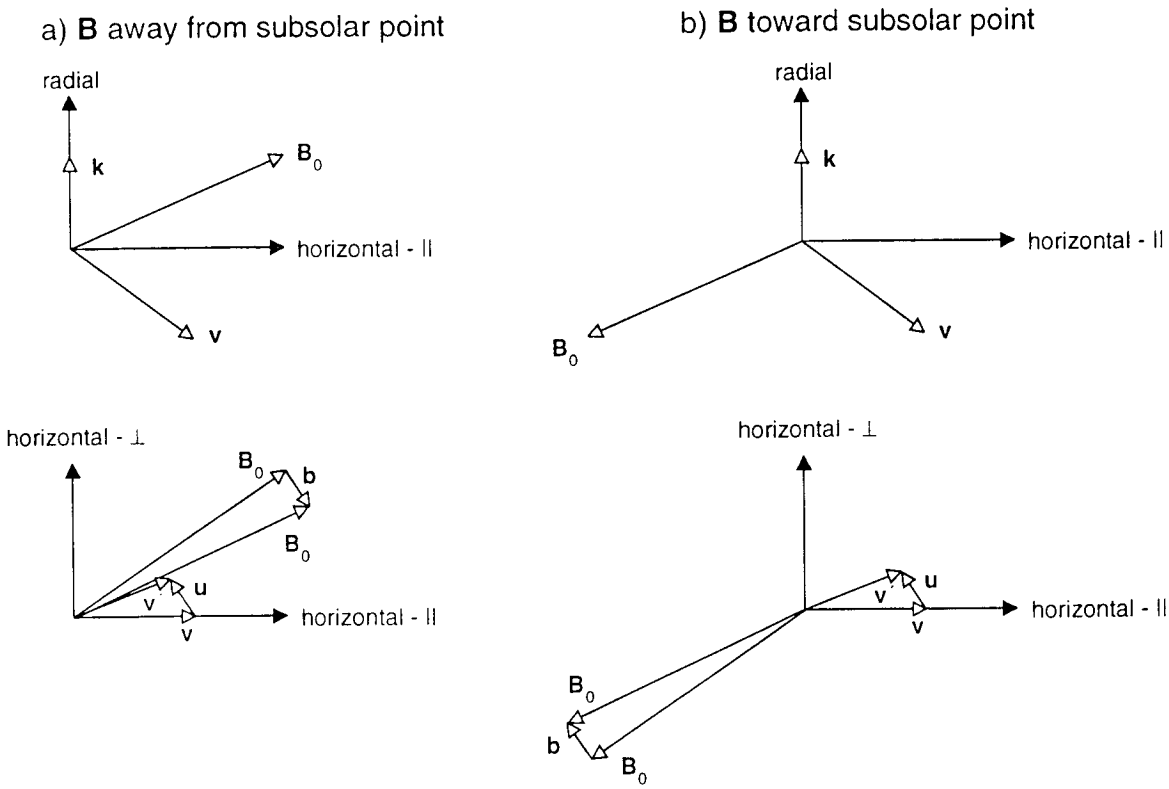

Figure 12. The relationship between the magnetic field perturbation and velocity perturbation for a shear Alfvén wave standing in the magnetosheath flow. Figure 12 shows (a) magnetic field pointing away from the subsolar point, and (b) magnetic field pointing toward the subsolar point. The unprimed vectors are above the current layer, while the primed vectors are below. For each case the upper plot shows the projection in the radial-flow plane, with the lower plot showing the projection in the horizontal plane.

would result in a velocity shear across the composition boundary.

An additional complication in determining the relationship between the various signatures observed in the mantle is the "intermediate transition" (IT) [*Pérez-de-Tejada et al.*, 1991, 1993, 1995]. The IT is usually observed above the ionopause near or behind the terminator and is often associated with both a reduction of the magnetic field strength and a rotation of the field to a more Venus-Sun-aligned orientation. *Sauer et al.* [1994] suggested that the IT is an example of the composition boundary found in their simulations. We suggest here that the transition within the field and plasma observed on the dayside evolves downstream, ultimately becoming the IT. Whether the OETP ionopause, which may be a plasma boundary, or the field-aligned current, which may mark a shear in the flow, evolves into the IT has yet to be determined.

Indeed, the relationship between the OETP ionopause and the field-aligned current is unclear. Both occur within the mantle. The mantle provides the transition from magnetosheath to ionosphere which requires a change in magnetic field orientation, marked by the field-aligned current, and a change in plasma density and composition, perhaps corresponding to the OETP ionopause. Near the subsolar point we might expect these two transitions to be close together, since a change in the plasma mass density could introduce the velocity shear that results in the Alfvén wave. However, further downstream these two signatures could separate, since the shear is carried by a standing Alfvén wave, while a mass density change could be carried by a slow-mode wave.

In conclusion, while the OETP ionopause clearly orders the magnetic field and plasma wave data, the relationship between each of these is not yet obvious. It is possible that the plasma waves are generated by the field-aligned currents which we attribute to a standing Alfvén wave associated with the shear in the plasma flow. On the other hand, if the OETP ionopause is a composition boundary, then we might expect pickup ion related instabilities to be present, be they lower hybrid [*Szegö et al.*, 1991; *Shapiro et al.*, 1995] or ion acoustic [*Huba*, 1993]. Alternatively, if the OETP ionopause corresponds to a density gradient, then perhaps gradient-drift instabilities generate the waves [cf. *Huba*, 1992]. Thus it is necessary to determine the nature of the OETP ionopause, which is an instrument-defined boundary, as being the altitude at which the Langmuir probe measures a density of 100 cm^{-3}. Unfortunately, most of the plasma instrumentation on board the Pioneer Venus Orbiter was designed to operate optimally in a dense cold plasma, the ionosphere, or in a supersonic beam, the solar wind, but not in both. The possible exception is the orbiter retarding potential analyzer (ORPA). Regardless of the ultimate source of the waves, our analysis confirms that the waves occur within the plasma mantle and are hence not a direct source of heating for the topside ionosphere.

Acknowledgments. We wish to thank L. H. Brace for kindly supplying the Langmuir probe data used in this study. We are also grateful to G. K. Crawford, whose initial efforts provided the basis for the present work. This is IGPP publication 4318 and was supported by NASA grants NAG2-485 and NAGW-3497.

The Editor thanks K. Sáuer and J. D. Huba for their assistance in evaluating this paper.

References

Brace, L. H., and A. J. Kliore, The structure of the Venus ionosphere, *Space Sci. Rev.*, *55*, 81–163, 1991.

Crawford, G. K., A study of plasma waves arising from the solar wind interaction with Venus, Ph. D. thesis, Univ. of Calif., Los Angeles, 1993.

Crawford, G. K., R. J. Strangeway, and C. T. Russell, VLF emissions at the Venus dayside ionopause, in *Plasma Environments of Non-Magnetic Planets*, edited by T. I. Gombosi, pp. 253–258, Pergamon, Tarrytown, N. Y., 1993.

Dubinin, E., and R. Lundin, Mass-loading near Mars, *Adv. Space Res.*, *16*, (4)75–4(79), 1995.

Elphic, R. C., C. T. Russell, J. A. Slavin, and L. H. Brace, Observations of the dayside ionopause and ionosphere of Venus, *J. Geophys. Res.*, *85*, 7679–7696, 1980.

Ferandin, J. A., C. L. Weeks, and R. D. Pak, Pioneer Venus unified abstract data library and quick look data delivery system, *IEEE Trans. Geosci. Remote Sens.*, *GE-18*, 19–27, 1980.

Grard, R., C. Nairn, A. Pedersen, S. Klimov, S. Savin, A. Skalsky, and J. G. Trotignon, Plasma and waves around Mars, *Planet. Space Sci.*, *39*, 89–98, 1991.

Huba, J. D., Theory of small-scale density and electric field fluctuations in the nightside Venus ionosphere, *J. Geophys. Res.*, *97*, 43–50, 1992.

Huba, J. D., Generation of waves in the Venus mantle by the ion acoustic beam instability, *Geophys. Res. Lett.*, *20*, 1751–1754, 1993.

Law, C. C., and P. A. Cloutier, Observations of magnetic structure at the dayside ionopause of Venus, *J. Geophys. Res.*, *100*, 23,973–23,981, 1995.

Luhmann, J. G., A three-dimensional diffusion/convection model of the large scale magnetic field in the Venus ionosphere, *J. Geophys. Res.*, *93*, 5909–5914, 1988.

Luhmann, J. G., and T. E. Cravens, Magnetic fields in the ionosphere of Venus, *Space Sci. Rev.*, *55*, 201–274, 1991.

Miller, K. L., W. C. Knudsen, and K. Spenner, The dayside Venus ionosphere, I, Pioneer-Venus retarding potential analyzer experimental observations, *Icarus*, *57*, 386–409, 1984.

Nagy, A. F., T. I. Gombosi, K. Szego, R. Z. Sagdeev, V. D. Shapiro, and V. I. Shevchenko, Venus mantle - Mars planetosphere: What are the similarities and differences?, *Geophys. Res. Lett.*, *17*, 865–868, 1990.

Pérez-de-Tejada, H., D. S. Intriligator, and R. J. Strangeway, Steady-state plasma transition in the Venus ionosheath, *Geophys. Res. Lett.*, *18*, 131–134, 1991.

Perez-de-Tejada, H., D. S. Intriligator, and R. J. Strangeway, Magnetic field properties of the intermediate transition of the Venus ionosheath, *Geophys. Res. Lett.*, *20*, 991–994, 1993.

Perez-de-Tejada, H., D. S. Intriligator, and R. J. Strangeway, Intermediate transition in the Venus ionosheath, *J. Geophys. Res.*, *100*, 14,523–14,535, 1995.

Phillips, J. L., J. G. Luhmann, W. C. Knudsen, and L. H. Brace, Asymmetries in the location of the Venus ionopause, *J. Geophys. Res.*, *93*, 3927–3941, 1988.

Sagdeev, R. Z., V. D. Shapiro, V. I. Shevchenko, A. Zacharov, P. Király, K. Szegó, A. F. Nagy, and R. J. L. Grard, Wave activity in the neighborhood of the bowshock of Mars, *Geophys. Res. Lett.*, *17*, 893–896, 1990.

Sauer, K., A. Bogdanov, and K. Baumgärtel, Evidence of an ion composition boundary (protonopause) in bi-ion fluid simulations of solar wind mass loading, *Geophys. Res. Lett.*, *21*, 2255–2258, 1994.

Scarf, F. L., W. W. L. Taylor, and I. M. Green, Plasma waves near Venus: Initial observations, *Science*, *203*, 748–750, 1979.

Scarf, F. L., W. W. L. Taylor, C. T. Russell, and R. C. Elphic, Pioneer Venus plasma wave observations: The solar wind–Venus interaction, *J. Geophys. Res.*, *85*, 7599–7612, 1980a.

Scarf, F. L., W. W. L. Taylor, and P. V. Virobik, The Pioneer Venus orbiter plasma wave investigation, *IEEE Trans. Geosci. Remote Sens.*, *GE-18*, 36–38, 1980b.

Shapiro, V. D., K. Szegö, S. K. Ride, A. F. Nagy, and V. I. Shevchenko, On the interaction between the shocked solar wind and the planetary ions on the dayside of Venus, *J. Geophys. Res.*, *100*, 21,289–21,305, 1995.

Song, P., C. T. Russell, and M. F. Thomsen, Slow mode transition in the frontside magnetosheath, *J. Geophys. Res.*, *97*, 8295–8305, 1992.

Southwood, D. J., and M. G. Kivelson, On the form of the flow in the magnetosheath, *J. Geophys. Res.*, *97*, 2873–2879, 1992.

Spenner, K., W. C. Knudsen, K. L. Miller, V. Novak, C. T. Russell, and R. C. Elphic, Observation of the Venus mantle, the boundary between solar wind and ionosphere, *J. Geophys. Res.*, *85*, 7655–7662, 1980.

Strangeway, R. J., and G. K. Crawford, On the instability and energy

flux of lower hybrid waves in the Venus plasma mantle, *Geophys. Res. Lett.*, *20*, 1211–1214, 1993.

Szegö, K., V. S. Shapiro, V. I. Shevchenko, R. Z. Sagdeev, W. T. Kasprzak, and A. F. Nagy, Physical processes in the plasma mantle of Venus, *Geophys. Res. Lett.*, *18*, 2305–2308, 1991.

Taylor, H. A., Jr., R. E. Daniell, R. E. Hartle, H. C. Brinton, S. J. Bauer, and F. L. Scarf, Dynamic variations observed in thermal and superthermal ion distributions in the dayside ionosphere of Venus, *Adv. Space Res.*, *1*, 247–258, 1981.

Taylor, W. W. L., F. L. Scarf, C. T. Russell, and L. H. Brace, Absorption of whistler mode waves in the ionosphere of Venus, *Science*, *205*, 112–114, 1979.

C. T. Russell and R. J. Strangeway, Institute of Geophysics and Planetary Physics, University of California, Los Angeles, 405 Hilgard Ave., Los Angeles, CA 90095-1567. (e-mail: ctrussell@igpp.ucla.edu; strange@igpp.ucla.edu)

(Received October 30, 1995; revised March 15, 1996; accepted March 21, 1996.)

JOURNAL OF GEOPHYSICAL RESEARCH, VOL. 101, NO. A2, PAGES 2279–2295, FEBRUARY 1, 1996

Collisional Joule dissipation in the ionosphere of Venus: The importance of electron heat conduction

R. J. Strangeway

Institute of Geophysics and Planetary Physics, University of California, Los Angeles

Abstract. The ionosphere of an unmagnetized planet, such as Venus, is characterized by relatively high Pedersen conductivity in comparison to the terrestrial ionosphere because of the weak magnetic field. Collisional Joule dissipation of plasma waves might therefore be an important source of heat within the Venus ionosphere. However, any assessment of the importance of collisional Joule dissipation must take into account the cooling provided by electron heat conduction due to temperature gradients. Once heat conduction is included we find that collisional Joule dissipation is significant only in the bottomside ionosphere; waves observed at or near the dayside ionopause, or at higher altitudes (> 150 km) within the nightside ionosphere do not cause significant heating through collisional Joule dissipation. However, lightning-generated whistler mode waves propagate through the highly collisional bottomside ionosphere, and we have performed detailed wave propagation calculations where we self-consistently calculate the heating due to Joule dissipation and the cooling due to heat conduction. The heat conduction always exceeds the collisional cooling from elastic collisions. Because the high collision frequency at low-altitude results in a low thermal conductivity, a steep temperature gradient is required to provide the heat flux. However, this gradient thermally decouples the bottomside ionosphere from higher altitudes. Collisional Joule dissipation of lightning generated whistlers is not likely to have any consequences for the global ionospheric energy budget. Cooling by inelastic collisions, specifically the vibrational excitation of CO_2, further reduces the bottomside temperature. It is the inelastic cooling rate that determines the atmospheric heating rate, any excess heat again being carried away through heat conduction. We find that for typical wave field amplitudes of 10 mV/m the bottomside is heated to a few eV, while intense fields (100 mV/m) result in bottomside temperatures of a few tens of eV. This high a temperature may cause electronic excitation of the neutrals, which could result in optical or ultraviolet emissions from the ionosphere due to lightning. This possibility requires further investigation but requires the incorporation of additional inelastic cooling processes, such as electronic excitation of the neutral atmosphere.

1. Introduction

Recently, *Cole and Hoegy* [1995] suggested that collisional Joule dissipation of VLF waves is a significant source of heating within the ionosphere of Venus. Depending on the amount of collisional Joule dissipation, this could have important ramifications for the Venus ionosphere. For sufficiently high Joule dissipation the heating due to VLF waves would have to be included in the energy budget of the ionosphere. Even more significantly, if the heating rate is large enough to cause unrealistically high electron temperatures, then some of the earlier interpretations of the plasma waves observed at Venus may have to be revised, especially the identification of VLF bursts in the nightside ionosphere as being due to lightning-generated plasma waves.

There are two basic VLF wave phenomena observed within or near the Venus ionosphere for which collisional Joule dissipation may be important. The first of these is observed at the dayside ionopause, mainly in the 100-Hz channel of the Pioneer Venus Orbiter electric field detector (OEFD). The OEFD measures plasma waves at four frequencies, 100 Hz, 730 Hz, 5.4 kHz, and 30 kHz [*Scarf et al.*, 1980c]. The 100-Hz waves observed at the dayside ionopause were initially identified as whistler mode waves generated at the bow shock, propagating through the magnetosheath to the ionopause [e.g., *Scarf et al.*, 1980b], and it was argued that the waves were transporting energy, providing heat to the dayside ionopause though Landau damping.

More recently, *Szego et al.* [1991] suggested that the waves were lower hybrid resonance waves generated by the relative drift between O^+ ions of planetary origin and the shocked solar wind. As the waves are generated locally, Landau damping will act to inhibit wave growth, rather than provide a means for energy transport. *Strangeway and Crawford* [1993] pointed out that *Szego et al.* [1991] neglected Landau damping, and the damping of lower hybrid waves argues for an alternative wave mode and instability. *Huba* [1993] suggested that the waves were instead an ion acoustic mode. Thus the mode identification of the waves observed at the dayside ionopause has not been resolved. Nevertheless, we should determine if collisional Joule dissipation is important for these waves, as that may provide an alternative means for transferring wave energy to the plasma, in addition to the dissipation associated with resonant wave-particle interactions.

In the opening paragraph we already alluded to the second wave phenomenon which may be subject to collisional Joule dissipation: the observation of VLF bursts at low altitudes in

Paper number 95JA02587.
0148-0227/96/95JA-02587$05.00

the nightside ionosphere. These waves have been attributed to lightning in the Venus atmosphere [e.g., *Scarf et al.*, 1980a; *Scarf and Russell*, 1983; *Russell*, 1991]. If these waves are indeed due to lightning, then they must propagate through the most dense, and most highly collisional, region of the ionosphere. It is consequently very important that we determine how large the Joule dissipation for these waves may be. In particular, is the heating rate so large that the ionosphere cannot adequately absorb the energy? In which case, we might expect there to be detectable changes in the ionosphere due to lightning. We note that there have been no reports of lightning-related signatures within the ionosphere of Venus, apart from the VLF bursts. Small-scale irregularities were reported by *Grebowsky et al.* [1991], who interpreted the irregularities as being due to a local instability. This instability was identified as a lower hybrid drift instability [*Huba*, 1992; *Huba and Grebowsky*, 1993]. Although initially suggested as an alternative to the lightning interpretation, the lower hybrid drift instability does not explain the majority of the VLF bursts [*Strangeway*, 1995a, b]. If we find that collisional Joule dissipation is significant for the nightside bursts, then perhaps we should revisit the issue of correlation between wave bursts and density fluctuations, as this may explain the 20% correlation between waves and density fluctuations found by *Strangeway* [1995b].

Within the nightside ionosphere two types of wave burst have been attributed to lightning. The first of these occurs at 100 Hz [*Scarf et al.*, 1980a], the second is broad-banded in nature [*Singh and Russell*, 1986], being detected in the higher-frequency channels of the OEFD. Later work [*Russell et al.*, 1988, 1989a], which did not contain telemetry errors apparently included in the analysis of Singh and Russell [*Taylor and Cloutier*, 1988; *Russell and Singh*, 1989] showed that the wideband bursts peaked at low altitudes and that the burst rate was maximum near the dusk terminator. It was consequently argued that lightning at Venus was generated mainly in the dusk local time sector [*Russell*, 1991]. We will not address the Joule dissipation of these wideband signals in this paper, mainly because the source of these high-frequency signals is not understood. They are observed in the propagation stop band between the electron gyrofrequency and the plasma frequency and so cannot be radiation from below the ionosphere [*Strangeway*, 1991a].

On the other hand, there is evidence that the 100-Hz bursts are propagating though the ionosphere from below. The wave burst rates are largest at low altitudes [*Russell et al.*, 1988; *Ho et al.*, 1991]. The waves are polarized perpendicularly to the ambient magnetic field, provided the data are restricted to signals that are within the whistler mode resonance cone under the assumption of vertical propagation [*Sonwalkar et al.*, 1991, *Strangeway*, 1991b]. Furthermore, the burst rate decreases much less rapidly for increasing altitude if the data are restricted to within the resonance cone [*Ho et al*, 1992]. The resonance cone test, which only applies to waves that are propagating from below the ionosphere, is a strong indicator of a subionospheric source such as atmospheric lightning for the 100-Hz waves. Waves that propagate through the ionosphere are likely to be subject to collisional Joule dissipation.

It is the purpose of this paper to determine whether or not collisional Joule dissipation is important for plasma waves observed within the Venus ionosphere. In the next section we discuss the ionospheric heat budget, giving expressions for the different terms within the heat budget and the associated collision frequencies. In section 3 we compare orders of magnitude for the heating and cooling terms. We find that electron heat conduction can easily accommodate the heating due to collisional Joule dissipation, except at very low altitudes within the ionosphere. Thus waves observed near the dayside ionopause of Venus or at higher altitudes (> 150 km) in the nightside ionosphere do not supply any significant heating through collisional Joule dissipation. This finding does not preclude additional dissipation due to resonant wave-particle interactions, but a detailed estimation of this form of dissipation is beyond the scope of the present paper. In section 4 we perform detailed wave propagation calculations, following the methodology of *Huba and Rowland* [1993] but with the added step of iteratively modifying the electron temperature altitude profile so as to balance the heat budget. In section 4 we artificially set the inelastic cooling rate through vibrational excitation of CO_2 equal to zero. This facilitates the demonstration of how the electron temperature profile changes to accommodate the heating by Joule dissipation through heat conduction to higher altitudes. In section 5 we allow vibrational cooling to occur, and we find that this further reduces the electron heating. In addition, we point out that it is the inelastic collision cooling rate that determines how much heat enters the neutral atmosphere, not the Joule dissipation rate. Any excess heat is carried away through heat conduction. Last, we give some concluding remarks in section 6.

2. Heat Budget

The equations given below governing collisions and transport are as given in the work by *Huba*, [1994, pp. 31–39]. A more detailed discussion on collision frequencies and the electron heat budget can be found for example in the work of *Banks and Kockarts* [1973, chaps. 9 and 22], albeit with slightly different numerical constants. Under the assumption of steady state and no relative flow between species the electron heat budget is given by

$$\nabla_{\parallel}\cdot\mathbf{q}_{\parallel} + Q_j + Q_m + Q_v = 0 \tag{1}$$

In (1) we chose the convention that a positive value for each of the terms corresponds to electron cooling. The heat flux $\mathbf{q}_{\parallel}$ is parallel to the ambient magnetic field (unless otherwise stated, the subscripts "$\perp$" and "$\parallel$" indicate direction with respect to the ambient magnetic field). We assume that the electrons are isotropic, and $\mathbf{q}_{\parallel}$ is the collisional heat flux associated with a temperature gradient. The quantity $-Q_j$ is the heating due to Joule dissipation. Q_m is the cooling rate due to elastic collisions between electrons and ions and/or neutral particles, indicated by the subscript "m" as the cooling rate is determined by momentum transfer. As we shall see later, this is a relatively inefficient cooling process. Q_v is the cooling rate due to inelastic collisions. We shall also show later that the dominant inelastic cooling process at low altitudes is the vibrational excitation of CO_2, hence we denote inelastic cooling by the subscript "v."

The temperature gradient heat flux is given by [*Huba*, 1994]

$$\mathbf{q}_{\parallel} = -K_{\parallel}\nabla_{\parallel}k_B T_e = -3.2\,\frac{n_e k_B T_e}{m_e \nu_e}\nabla_{\parallel}k_B T_e \tag{2}$$

In (2), $K_{\parallel}$ is the parallel heat conductivity, k_B is the Boltzmann constant, T_e is the electron temperature, n_e is the electron density, m_e is the electron mass, and ν_e is the total electron collision frequency.

As written, (1) and (2) do not include any heat flux across the ambient magnetic field. At high altitudes, where the electron collision frequencies are low, this is justified since the parallel heat conductivity is much larger than the perpendicular heat conductivity. At low altitudes, where the collision frequencies are much higher, the better assumption is that only vertical gradients are present within the ionosphere. However, when the collision frequency is large with respect to the gyrofrequency, the thermal conductivity is independent of the orientation of the magnetic field, with magnitude given by $K_{\parallel}$ in (2). For high collision frequencies with respect to the electron gyrofrequency, we need no longer consider only the parallel temperature gradient, and we can replace $\nabla_{\parallel}$ by ∇ in (1) and (2).

In a cold plasma the collisional Joule dissipation rate due to a wave electric field which is perpendicular to the ambient magnetic field is given by [*Cole and Hoegy*, 1995]

$$Q_{j\perp} = -\frac{n_e e^2 E_{\perp}^2 \nu_e}{2m_e(\nu_e^2 + \Omega_e^2)} \tag{3}$$

assuming that the wave frequency (ω) $\ll \Omega_e$ or ν_e. In (3), $E_{\perp}$ is the perpendicular wave electric field amplitude, e is the electron charge, and Ω_e is the electron gyrofrequency ($\Omega_e = eB_0/m_e$, where B_0 is the ambient magnetic field strength). The Joule dissipation as given by (3) is the same as the Joule dissipation rate using the Pedersen conductivity, except for the factor of two which arises from the averaging over a wave cycle of the sinusoidally varying electric field. The Joule dissipation rate is smaller for increasing magnetic field strength, and is maximum when $\nu_e = \Omega_e$. Thus, as pointed out by *Cole and Hoegy* [1995], we might expect the Joule dissipation to be larger in the weakly magnetized Venusian ionosphere than in the highly magnetized terrestrial ionosphere.

The collisional Joule dissipation associated with a wave field that is parallel to the ambient magnetic field is similar to (3), except that the electron gyrofrequency is replaced by the wave frequency:

$$Q_{j\parallel} = -\frac{n_e e^2 E_{\parallel}^2 \nu_e}{2m_e(\nu_e^2 + \omega^2)} \tag{4}$$

In the introduction we noted that there is still some uncertainty in the wave mode identification for the waves observed near the dayside ionopause. Three wave modes have been considered: whistler mode; lower hybrid mode; and ion acoustic mode. Of these three, the first two are perpendicularly polarized, while the last is polarized along the magnetosheath flow velocity (i.e., independent of the ambient field direction). Given the uncertainties in mode identification we will use (3) to assess the relative importance of collisional Joule dissipation on the dayside.

In assessing the effect of collisional Joule dissipation we will neglect any kinetic effects such as resonant wave-particle interactions. Clearly, such processes are important in a warm plasma, where wave phase speeds are comparable to electron thermal speeds. For whistler mode waves, kinetic effects are important for $\beta_e \approx 1$, where β_e is the ratio of thermal to magnetic pressure = $2\mu_0 n_e k_B T_e / B_0^2$ (μ_0 is the permeability of free space). We will use the condition $\beta_e = 1$ as an indicator of parameter regimes for which kinetic effects may have to be included.

On the nightside, the mode identification is much more clear cut. If the 100-Hz waves observed at low altitudes are due to atmospheric lightning, they must be whistler mode waves. Moreover, the data indicate that the waves are perpendicularly polarized with respect to the ambient magnetic field [*Strangeway*, 1991b]. Thus (3) is also appropriate for the nightside. With regard to kinetic effects, *Strangeway et al.* [1993a] and *Strangeway* [1995a, b] have shown that the low-altitude 100-Hz wave bursts tend to occur in regions of low β_e. At the lowest altitudes we therefore expect collisional processes to be more important for wave dissipation than resonant wave-particle interactions.

The cooling rate due to elastic collisions is given by

$$Q_m = \sum_{\text{species}} \frac{3m_e n_e k_B (T_e - T_s)\nu_{es}}{m_s} \tag{5}$$

In (5) the sum is over both ions and neutrals, T_s is the species temperature, and m_s is the species mass.

The cooling rate due to vibrational excitation of CO_2 is derived in the appendix. At high temperatures (> 0.3 eV) the vibrational cooling rate, in W/m^3, is given by

$$Q_v = 5.18\times10^{-22} n_e N_{CO2} T_e^{1/2} \tag{6}$$

where N_{CO2} is the neutral CO_2 density, in cm^{-3}, n_e is expressed in cm^{-3}, and T_e is in eV.

The various terms in (1) depend on the electron-ion and electron-neutral collision frequencies. For electron-ion collisions

$$\nu_{ei} = 2.9\times10^{-6} n_e \lambda T_e^{-3/2} \tag{7}$$

where λ is the Coulomb logarithm (≈ 20), densities are in cm^{-3}, and temperatures are again in eV. For electron-neutral collisions

$$\nu_{en} = 4.19\times10^{7} N_n \sigma T_e^{1/2} \tag{8}$$

where N_n is the neutral density in cm^{-3} and σ is the collision cross section in cm^2.

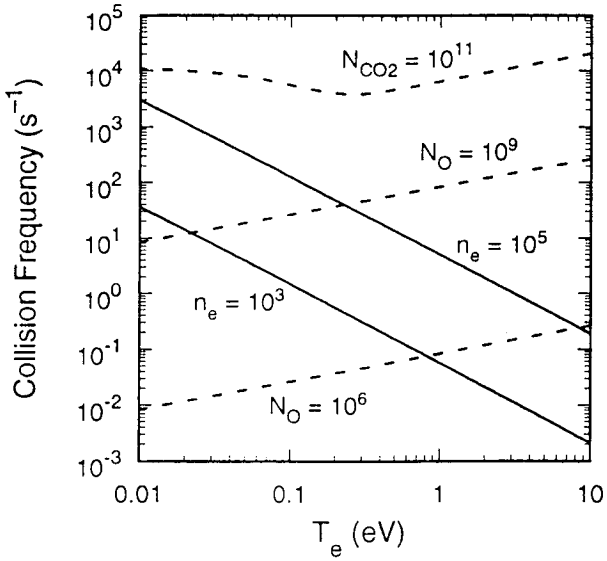

Figure 1. Electron collision frequencies as a function of electron temperature. The electron-ion collision frequency (solid line) is plotted for electron densities of 10^3 and 10^5 cm^{-3}, while the electron-neutral collision frequency (dashed line) is plotted for neutral oxygen densities of 10^6 and 10^9 cm^{-3}, and neutral CO_2 density of 10^{11} cm^{-3}. Ionospheric electron temperatures typically lie in the range 0.1 to 1 eV [*Theis et al.*, 1980].

The dominant neutrals in the nightside ionosphere of Venus are O and CO_2. We will assume the cross section for O is 2×10^{-15} cm^2, giving a collision frequency of $\approx 8.4\times10^{-8} N_O T_e^{1/2}$, similar to the value given by *Banks and Kockarts* [1973, chap. 9], where N_O is the atomic oxygen density. For CO_2 we use the results of *Morrison and Greene* [1978], as discussed in the appendix. At higher temperatures (> 0.3 eV) the cross section has an asymptotic value of $\approx 1.55\times10^{-15}$ cm^2.

The electron-ion and electron-neutral collision frequencies are plotted as a function of electron temperature in Figure 1. The solid lines give the electron-ion collision frequency for electron number densities of 10^3 and 10^5 cm^{-3}. The dashed lines give the electron-neutral collision frequency for neutral densities of 10^6 and 10^9 cm^{-3} for O and 10^{11} cm^{-3} for CO_2. The low electron and O density curves are representative of the high-altitude ionosphere and ionopause, while the high electron density represents the low-altitude ionosphere. The CO_2 curve is representative of the bottomside of the ionosphere ($\approx$ 130 km), while the $N_O = 10^9$ curve is representative of the middle ($\approx$ 150 km) altitude ionosphere (see, e.g., *Theis et al.* [1980] and *Hedin et al.* [1983] for altitude profiles of the electron and neutral densities respectively). Electron temperatures usually lie in the range 0.1 to 1 eV [*Theis et al.*, 1980], although we have extended the temperature range beyond these limits in the figure. Figure 1 shows that at high altitudes, electron-ion collisions will dominate. At lower altitudes, where the electron temperature is lower, electron-ion collisions will still tend to dominate, because of the steep temperature dependence of the electron-ion collision frequency. Only at the very lowest altitudes, i.e., the bottomside ionosphere, do we expect electron-neutral collisions to be important. A similar result was found by *Luhmann et al.* [1984], although they used a slightly lower electron-neutral collision frequency.

Figure 1 and (8) also show that for sufficiently high neutral densities and electron temperatures, the electron-neutral collision frequency can be large, > 10^4 s^{-1}. Within the ionosphere, magnetic field strengths of 30 nT are well above the average, but this only corresponds to $\Omega_e = 5\times10^3$ rad/s. Thus it is possible that $\nu_{en} > \Omega_e$, in which case (3) shows that the Joule dissipation is reduced, and increasing the electron temperature will further reduce the Joule dissipation.

3. Joule Dissipation: Order of Magnitude Estimates

The discussion in the previous section indicates that there are two limits which we can apply to the Venus ionosphere. The first is when electron-ion collisions dominate, while the second is when electron-neutral collisions dominate. As noted earlier, the former is more appropriate for high altitudes, while the latter is more appropriate for the bottomside ionosphere.

When electron-ion collisions dominate, we can rewrite the heating and cooling rates, expressed in W/m^3, as

$$\nabla_{\parallel}\cdot\mathbf{q}_{\parallel} = \frac{0.031\,T_e^{7/2}}{L^2\lambda} \tag{9}$$

$$Q_j = -\frac{1.3\times10^{-12}\,n_e^2\lambda E^2}{B_0^2 T_e^{3/2}\,(1+\nu_{ei}^2/\Omega_e^2)} \tag{10}$$

$$Q_m = \frac{7.6\times10^{-22}\,n_e^2\lambda}{(m_i/m_p)T_e^{1/2}} \tag{11}$$

In (9), L is the scale length for heat conduction, as discussed below, given in kilometers. In (10), E is the wave electric field in volts per meter; B_0 is the ambient magnetic field strength in nanoteslas, and we have assumed that the wave is polarized perpendicularly to the ambient magnetic field. The term in parentheses in (10) ≈ 1 when $\nu_{ei} \ll \Omega_e$, as is usually the case when electron-ion collisions dominate. In (11), m_i and m_p are the ion and proton masses respectively, and we have assumed that $T_e \gg T_i$. In all these equations T_e is in eV, densities are in cm^{-3}, and λ is again the Coulomb logarithm.

In specifying a scaling law for the heat conduction, from (2), $\nabla_{\parallel}\cdot\mathbf{q}_{\parallel} \propto -\nabla_{\parallel}(K_{\parallel}\nabla_{\parallel}T_e) = -(\nabla_{\parallel}K_{\parallel}\nabla_{\parallel}T_e + K_{\parallel}\nabla_{\parallel}^2 T_e)$. When electron-ion collisions dominate, $K_{\parallel} \propto T_e^{5/2}$ and is independent of n_e. Hence the first term in parenthese will always be positive, and we therefore require $\nabla_{\parallel}^2 T_e < 0$ for $\nabla_{\parallel}\cdot\mathbf{q}_{\parallel} > 0$. This condition is not satisfied for a temperature dependence such as $T_e \propto \exp(-x/L)$, but it is for $T_e \propto \exp(-x^2/L^2)$ when $x \approx 0$. In deriving a scaling law we therefore assume that the temperature profile is such that $\nabla_{\parallel}\cdot\mathbf{q}_{\parallel} > 0$, as required for the electron energy budget, and simply take $-\nabla_{\parallel}(K_{\parallel}\nabla_{\parallel}T_e) = K_{\parallel}T_e/L^2$, where L is a heat conduction scale length.

When electron-neutral collisions dominate,

$$\nabla_{\parallel}\cdot\mathbf{q}_{\parallel} = \frac{1.1\,n_e T_e^{3/2}}{N_n(\sigma/\sigma_O)L^2} \tag{9'}$$

$$Q_j = -\frac{1.7\times10^5\,n_e E^2}{N_n(\sigma/\sigma_O)T_e^{1/2}\,(1+\Omega_e^2/\nu_{en}^2)} \tag{10'}$$

$$Q_m = \frac{2.2\times10^{-23}\,n_e N_n(\sigma/\sigma_O)T_e^{3/2}}{(m_n/m_p)} \tag{11'}$$

The symbols have the same meaning as in (9) to (11), and have the same units. In (9'), σ is the electron-neutral collisional cross section, and σ_O is the cross section for oxygen = 2×10^{-15} cm^2. When electron-neutral collisions dominate, the thermal conductivity tends to increase with altitude, and a negative temperature gradient will generally ensure that $\nabla_{\parallel}\cdot\mathbf{q}_{\parallel} > 0$. In (10') the term in parentheses ≈ 1 when $\nu_{en} \gg \Omega_e$. In (11') m_n is the neutral mass, and we have assumed $T_e \gg T_n$.

Turning first to the dayside ionopause, Figure 2 shows the various heating and cooling rates as a function of electron density (Figure 2a) and electron temperature (Figure 2b). We assume that the heat conduction scale (L) is 1000 km, the ambient magnetic field strength (B_0) is 50 nT, and the wave electric field amplitude (E) is 10 mV/m. Also, as noted above, we assume that electron-ion collisions dominate, i.e., we are using (9) to (11), and the ions are O^+ [e.g., *Brace and Kliore*, 1991]. We choose a scale length of 1000 km since the ambient magnetic field is draped over the ionopause, and the important scales are horizontal. These scales will be much longer than vertical scales, and 1000 km is a reasonable order of magnitude estimate. Above the dayside ionopause, wave spectral amplitudes can be as large as 10^{-3} V m^{-1} Hz$^{-1/2}$ [*Strangeway*, 1991a]. We convert the spectral amplitude to a wave electric field amplitude by assuming that the spectral bandwidth is of order the wave frequency. Thus, at 100 Hz a spectral amplitude of 10^{-3} V m^{-1} Hz$^{-1/2}$ corresponds roughly to an electric field amplitude of 10 mV/m.

In Figure 2a we assume that $T_e = 1$ eV, which is large for the ionosphere but is appropriate for the transitional region where the waves are observed. It is clear that for fixed temperature the Joule dissipation is always greater than the elastic collisional cooling. This is because both have the same dependence on the electron-ion collision frequency, and hence on electron

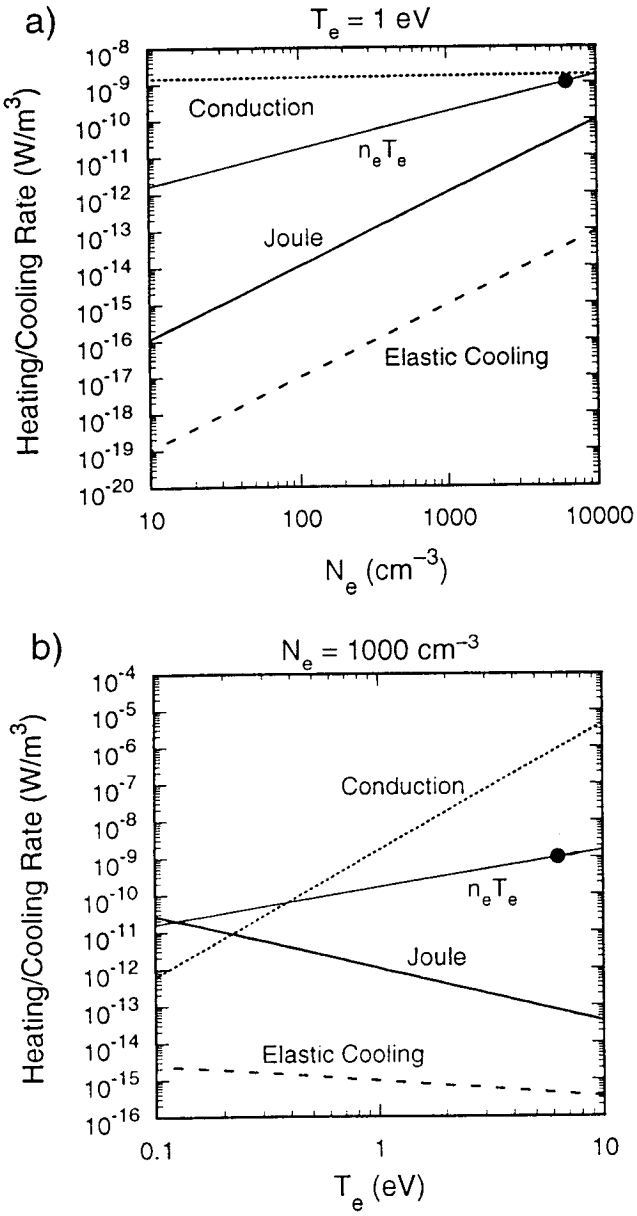

Figure 2. Electron heating and cooling rate estimates for the dayside ionopause. Since electron-ion collisions dominate, the rates are given by (9) to (11). The rates are shown (a) as a function of density for T_e = 1 eV and (b) as a function of temperature for n_e = 1000 cm^{-3}. It is also assumed that L = 1000 km, B_0 = 50 nT, E = 10 mV/m, and the ions are O^+. As an indication of the relative importance of the heating and cooling rates, we include the energy density (n_eT_e). The dot on this line marks β_e = 1, where we expect kinetic effects to be important.

density. More importantly, the electron heat conduction exceeds the Joule dissipation by a sufficiently large factor that we can increase the conduction scale length to 3000 km and still match the Joule dissipation, even for the highest densities shown. For densities of 1000 cm^{-3} the conduction scale could be as large as 30,000 km, about 5 Venus radii.

We also show the energy density of the electrons, n_eT_e, to indicate how important the different heating and cooling terms are, since n_eT_e divided by the cooling or heating rate gives the approximate cooling/heating time constant. It is clear that except at the higher densities the Joule dissipation is relatively weak, with a time constant of more than 100 s. On the n_eT_e curve we mark where β_e = 1, indicated by the dot. Thus at the higher densities we might expect kinetic effects to be more important, possibly enhancing the dissipation rate. However, heat conduction still plays a significant role in the electron heat budget.

Figure 2b shows how the rates depend on electron temperature. For Figure 2b we assume that n_e = 1000 cm^{-3}. For very low temperatures the Joule dissipation can exceed the heat conduction. However, (9) shows that the heat conduction has a strong dependence on temperature, while (10) shows that the Joule dissipation decreases with increasing temperature. Thus even though the Joule dissipation may initially exceed the heat conduction, a small increase in temperature is sufficient to match Joule dissipation by heat conduction. Figures 2a and 2b demonstrate that Joule dissipation through electron-ion collisions is not an important source of heating for the dayside ionopause.

At higher altitudes within the nightside ionosphere electron-ion collisions will usually dominate, except for the lower plasma densities. The heating and cooling rates for this case are shown in Figure 3a. For Figure 3a we assume that L = 10 km, B_0 = 30 nT, T_e = 0.1 eV, and E = 1 mV/m. These parameters have been chosen to correspond to an ionospheric hole [*Brace and Kliore*, 1991]. We have assumed that the ambient ions are O_2^+, which is usually the case at altitudes ≤ 150 km [*Grebowsky et al.*, 1993], while we also assume that the neutrals are atomic oxygen with a density of 4×10^8 cm^{-3}. Since the magnetic field within a hole is generally radial, it is appropriate to consider vertical scales, and we choose a scale of 10 km. Also, since the waves tend to be somewhat weaker in amplitude, we assume a wave electric field of 1 mV/m. This wave amplitude corresponds to a Poynting flux of ~ 3×10^{-6} W/m^2 for a refractive index ≈ 1000, *Russell et al.* [1989b] reported a median Poynting flux of ~ 10^{-7} W/m^2, assuming a 30-Hz bandwidth.

For the particular choice of wave and plasma parameters in Figure 3a, we again find that electron heat conduction can easily match the Joule dissipation within an ionospheric hole. Even though the heat conduction is of the same order as the Joule dissipation for densities of 10^5 cm^{-3}, we do not expect the wave amplitudes to be as high as 1 mV/m for these densities. At these high densities the scaling laws are given by (9) to (11), while at lower electron densities (9′) to (11′) apply. Whistler mode waves tend not to be observed within the high-density regions at higher altitudes, since they are Landau damped and gyrodamped [*Strangeway*, 1992; 1995a]. The conduction scale length can be as large as 50 km for densities of 10^4 cm^{-3}, and the conduction cooling will still exceed the Joule dissipation. Thus similarly to the dayside ionopause, we do not expect collisional Joule dissipation to be important at moderate altitudes (≥ 150 km) within the nightside ionosphere.

In Figure 3b we have chosen wave and plasma parameters corresponding to the bottomside ionosphere. We assume that L = 2 km, B_0 = 5 nT, n_e = 1000 cm^{-3}, E = 10 mV/m, the neutrals are CO_2 and $N_{CO2} = 10^{11}$ cm^{-3}. The wave amplitude corresponds to the wave intensities observed on the very low altitude passes during the Pioneer Venus Orbiter entry phase [*Strangeway et al.*, 1993b]. We have chosen the very short scale length of 2 km, since this is of order the attenuation

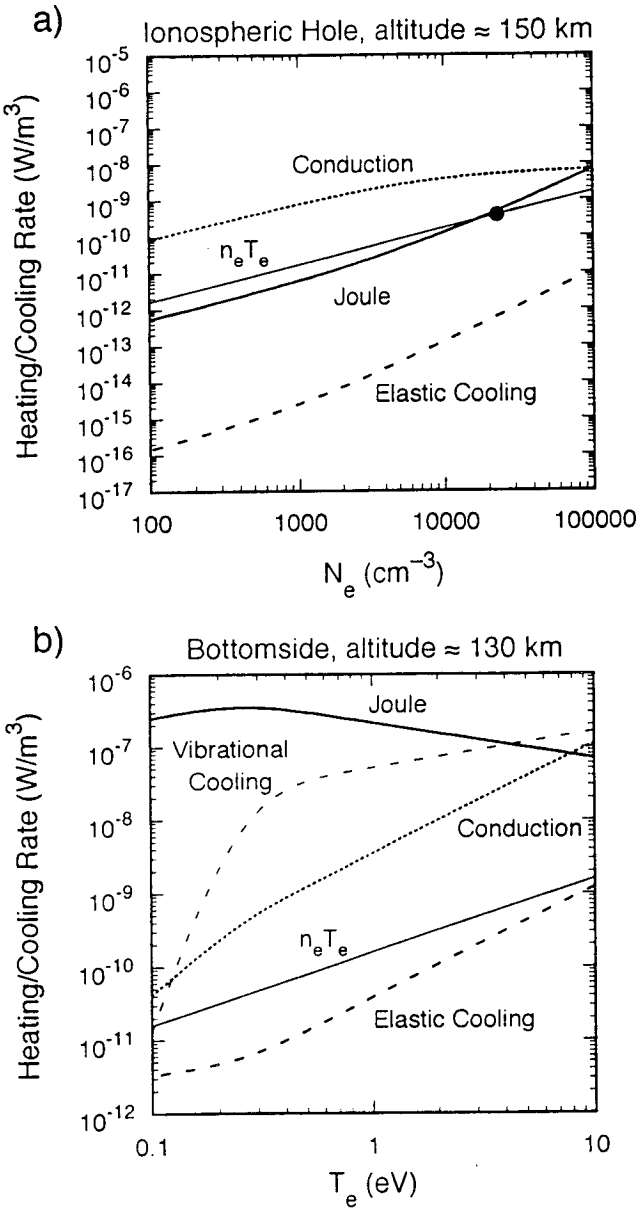

Figure 3. Electron heating and cooling rate estimates for the nightside ionosphere. (a) The rates are shown for an ionospheric hole, altitude ≈ 150 km. We assume that L = 10 km, B_0 = 30 nT, T_e = 0.1 eV, E = 1 mV/m, the ions are O^+, and the neutrals are O with a density of 4×10^8 cm^{-3}. (b) The rates are shown for the bottomside ionosphere, altitude ≈ 130 km, where electron-neutral collisions dominate. We assume that L = 2 km, B_0 = 5 nT, n_e = 1000 cm^{-3}, E = 10 mV/m, the neutrals are CO_2 and $N_{CO2} = 10^{11}$ cm^{-3}. In Figure 3b we have also shown the cooling rate due to vibrational excitation of CO_2 (6).

scale observed for the 100 Hz waves [*Strangeway et al.*, 1993b], and is also of order the density scale height for CO_2 [*Kasprzak et al.*, 1993]. However, Figure 3b shows that even for this short a scale the Joule dissipation exceeds the conduction cooling, except for the higher temperatures. Thus we might expect that collisional Joule dissipation is an important heat source for the bottomside ionosphere.

In addition to the elastic cooling rate, we have also included the cooling rate through vibrational excitation of CO_2 in Figure 3b. This cooling rate often exceeds that due to electron heat conduction, and may in fact be the means for balancing the Joule dissipation at the lowest altitudes. However, as discussed in the appendix, this cooling operates whether or not waves are present, and the cooling rate is so large that it may have important implications for the electron heat budget. In the absence of any other heat source, the vibrational cooling must be balanced by the heat conduction into the volume. Taking the heat conduction curve in Figure 3b as a guide, it is clear that the temperature gradient scale must be very short to supply sufficient heating, and as shown in the appendix, large topside temperatures may be required to provide the downward heat flux necessary to balance the vibrational cooling at the bottomside.

Last, in Figure 3b, $\beta_e > 1$. However, since the collision frequency is $\gg \omega$ and Ω_e, it is by no means clear that resonant wave-particle effects are important. Electron motion is almost certainly dominated by collisions, and it is unlikely that electrons can remain in resonance with waves.

In concluding from Figure 3b that wave Joule dissipation is important for the bottomside we used a fixed wave amplitude and fixed neutral and plasma density. However, all these parameters are changing on very short vertical scales within the bottomside ionosphere. The Joule dissipation that causes electron heating also reduces the wave energy. If the heating rate is high, we would expect that very little wave energy would propagate into the ionosphere. It is therefore necessary to take into account the variation of the waves and the ambient neutrals and plasma if we are to assess realistically the importance of collisional Joule dissipation as a heat source for the ionosphere.

4. Joule Dissipation: Self-Consistent Altitude Dependence

Recently, *Huba and Rowland* [1993] presented an analysis of the VLF wave transmission characteristics of the nightside Venus ionosphere. In their analysis, Huba and Rowland performed a full wave calculation of the wave attenuation for the four frequencies sampled by the Pioneer Venus orbiter electric field detector. In this section we will use the methodology of *Huba and Rowland* [1993] to calculate wave electric field altitude profiles for different ionospheric conditions. However, we will extend the work of Huba and Rowland by calculating the divergence of the Poynting flux (S) of the waves. Since the Joule dissipation is equivalent to minus the divergence of the Poynting flux (i.e., $-Q_j = -\nabla S$), we can use the latter to determine the amount of heating caused by the waves, rather than the approximate form given by (3). In passing, it should be noted that in our calculations Q_j evaluated using (3) and ∇S differ by less than a factor of two. Also, although Huba and Rowland considered all four channels of the OEFD, we will only consider 100 Hz. The Joule dissipation is usually largest for the 100-Hz channel than for the higher frequencies.

The method of *Huba and Rowland* [1993] is to numerically integrate the wave equation

$$\partial^2 E_\pm / \partial z^2 = -k(z)^2 E_\pm \qquad (12)$$

In (12), z is altitude, $E_\pm = E_x \pm iE_y$ is the wave electric field for the cold plasma L (+) or R (−) mode, and $k(z)$ is the wave vector, given by $c^2k(z)^2 = \omega^2 - \omega_{pe}^2\omega/(\omega - i\nu \pm \Omega_e)$, where ω_{pe} is the electron plasma frequency. In this paper we will only solve for the R mode, as this corresponds to the whistler mode. It

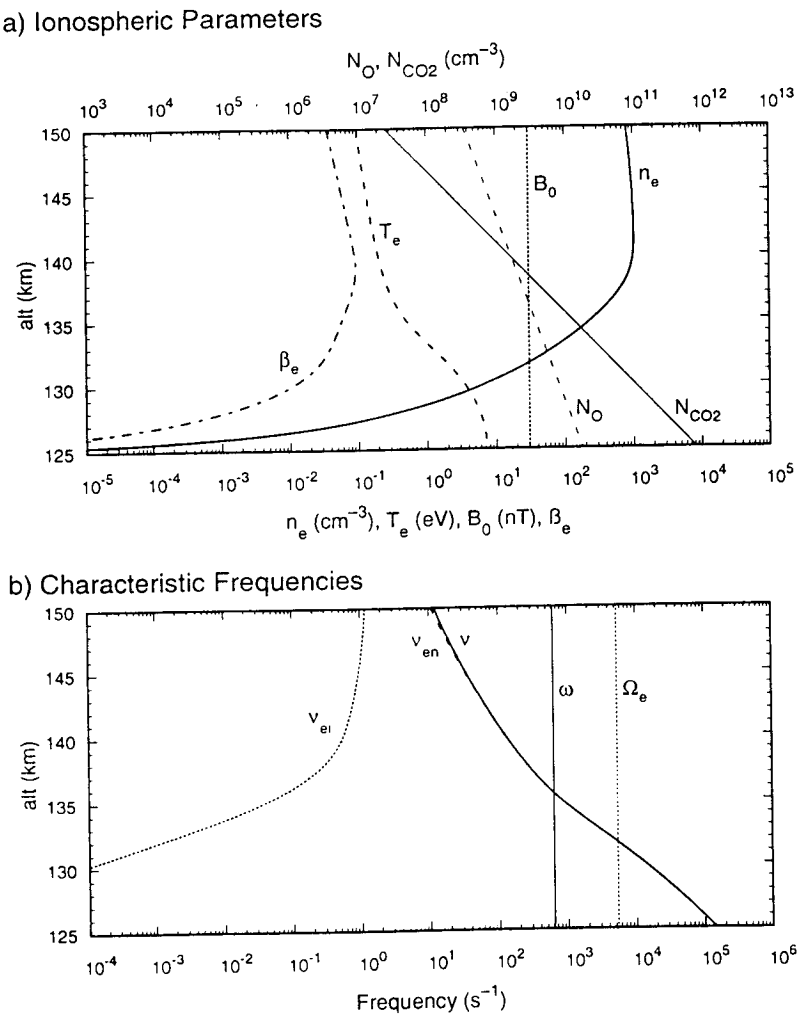

Figure 4. Wave propagation through the nightside Venus ionosphere for weakly attenuated 100-Hz signals. (a) Ionospheric parameters: The peak density is 1000 cm^{-3}, and the ambient magnetic field is 30 nT, corresponding to a deep ionospheric hole. The electron temperature profile has been modified so that (1) is satisfied. (b) Characteristic frequencies: The electron collision frequencies, wave frequency, and electron gyrofrequency are shown. (c) Wave parameters: The wave electric field amplitude and Poynting flux are shown. The real and imaginary parts of the refractive index (μ) are also shown. (d) Heat budget: The Joule dissipation rate, given by minus the divergence of the Poynting flux ($-\nabla S$), the divergence of the heat flux (∇q), and the elastic collision cooling rate (Q_m) are shown. Although not included in the heat budget, we have also included the vibrational cooling rate (Q_v) for reference.

should be noted that for $\nu \gg \Omega_e$ the dispersion relation is essentially the same for both modes.

In order to calculate the transmission characteristics of the ionosphere we need to specify the ambient magnetic field, the electron density, the ion composition, and the neutral density and composition. We will allow the electron temperature to be a variable within the calculation, being adjusted self-consistently so as to balance the heat budget equation (1). The magnetic field is assumed to be vertical and constant, with the magnitude depending on the ionospheric conditions we wish to model.

The neutral density and composition are based on the Pioneer Venus entry phase results of *Kasprzak et al.* [1993]. We assume that the two dominant neutral species are O and CO_2, and we ignore all other neutral species. The O and CO_2 scale height temperatures are 105 K and 109 K respectively [*Kasprzak et al.*, 1993], giving a density scale height of ≈ 6 km for O and ≈ 2 km for CO_2. In (5) we assume that the neutral gas temperature is the scale height temperature.

The electron density profile is modeled using a density profile similar to that used by *Huba and Rowland* [1993], with the modification that we allow the density to equal zero at the bottom of the altitude range under consideration (125 km). Thus the waves are free space modes at the bottom of the ionosphere. The density profile as a function of altitude is given by

$$n_e(z) = n_{e0} \tanh(2z_b) \exp[-(z - z_0)^2/z_t^2]/\tanh(2) \qquad (13)$$

where $z_b = (z - z_1)^5/(z_0 - z_1)^5$, n_{e0} is the density at $z = z_0 \approx$ the altitude of the density peak, z_1 is the minimum altitude, where $n_e(z) = 0$, and z_t is a scale height. Note that since $n_e(z)$ reaches a maximum at an altitude above $z = z_0$, n_{e0} is not exactly the

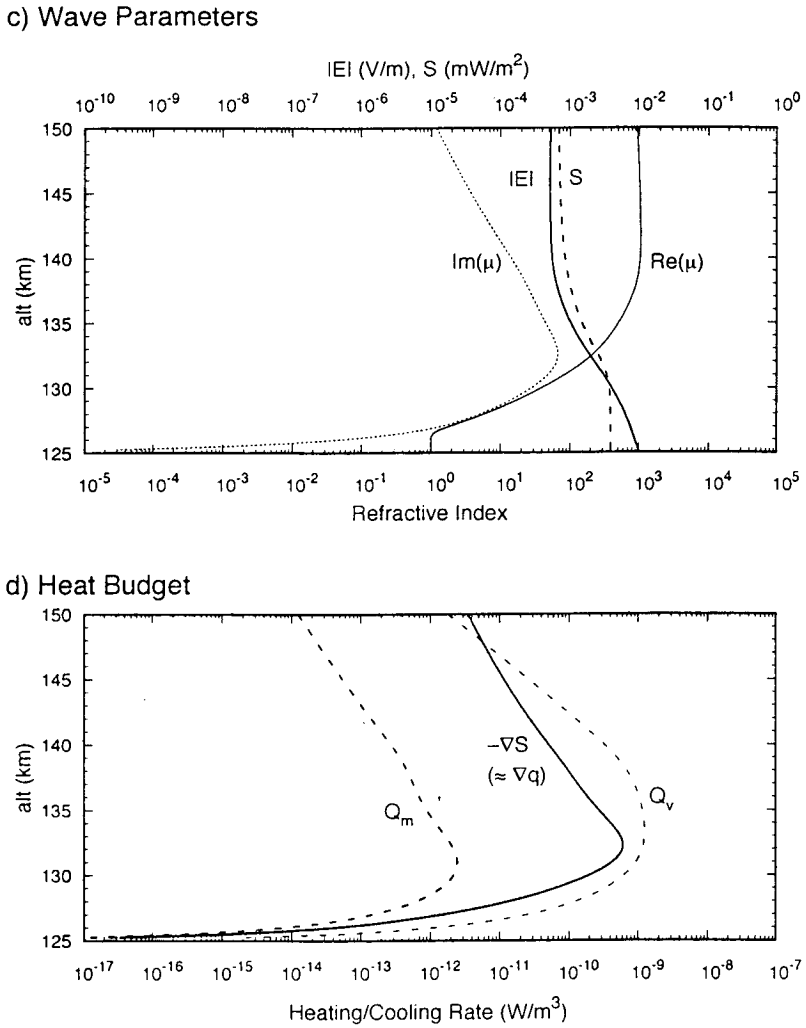

Figure 4. (continued)

peak density, and z_0 is not exactly the peak density altitude. Nevertheless, for convenience, we will refer to n_{e0} as the peak density and z_0 as the peak density altitude. In our calculations we assume z_1 = 125 km, z_0 = 140 km, and z_t = 20 km. The altitude minimum and peak density altitude are consistent with the occultation measurements from the Pioneer Venus Orbiter [*Brace and Kliore*, 1991], although the bottomside density profile is not well known. Indeed, the high vibrational cooling rate suggests that the bottom of the ionosphere could be higher than the assumed 125 km altitude. We vary n_{e0} depending on the ionospheric conditions we wish to model. The ions have the same density profile as the electrons and are assumed to be O_2^+. For the purposes of calculating the electron cooling due to collisions we assume that the ion temperature is equal to the neutral gas temperature in (5).

At this stage we will arbitrarily set the vibrational cooling rate (Q_v) to zero in the heat budget (1). This is done for two reasons. First, as discussed in the appendix, including vibrational cooling requires a source of electron heating. As we shall see later, for an ionosphere which extends down to 125 km altitude, we find that the vibrational cooling always exceeds the heating due to wave dissipation. Thus, including the vibrational cooling in this case results in a temperature profile where the electrons supply heat to the bottomside to offset the cooling, rather than conduct heat away from the region of wave dissipation. Second, by artificially turning off the vibrational cooling, we can more clearly demonstrate how heat conduction acts to balance wave heating.

The first case we analyze models a deep ionospheric hole, with n_{e0} = 1000 cm^{-3} and the ambient magnetic field = 30 nT. The whistler mode waves detected at Venus are primarily detected in ionospheric holes [e.g., *Strangeway*, 1995b]. This is a consequence of both the reduced Landau damping and gyrodamping [*Strangeway*, 1992, 1995a], and the relative transparency of the bottomside ionosphere [*Huba and Rowland*, 1993]. The corresponding ionospheric parameters are shown in Figure 4a. As discussed above, the neutral densities are based on the Pioneer Venus entry phase observations, with the electron density given by (13). The electron temperature profile has been modified self consistently so that the heat budget equation (1) is satisfied, as we discuss below. The electron temperature at the bottom of the ionosphere is ≈ 8 eV.

Figure 4b shows the associated characteristic frequencies. We have assumed an incident wave with frequency 100 Hz. Electron-ion collisions are relatively infrequent, even at 150 km, because of the low ambient density. At 150 km altitude, however, the electron-neutral collision frequency is also very low, ≈ 10 s^{-1}.

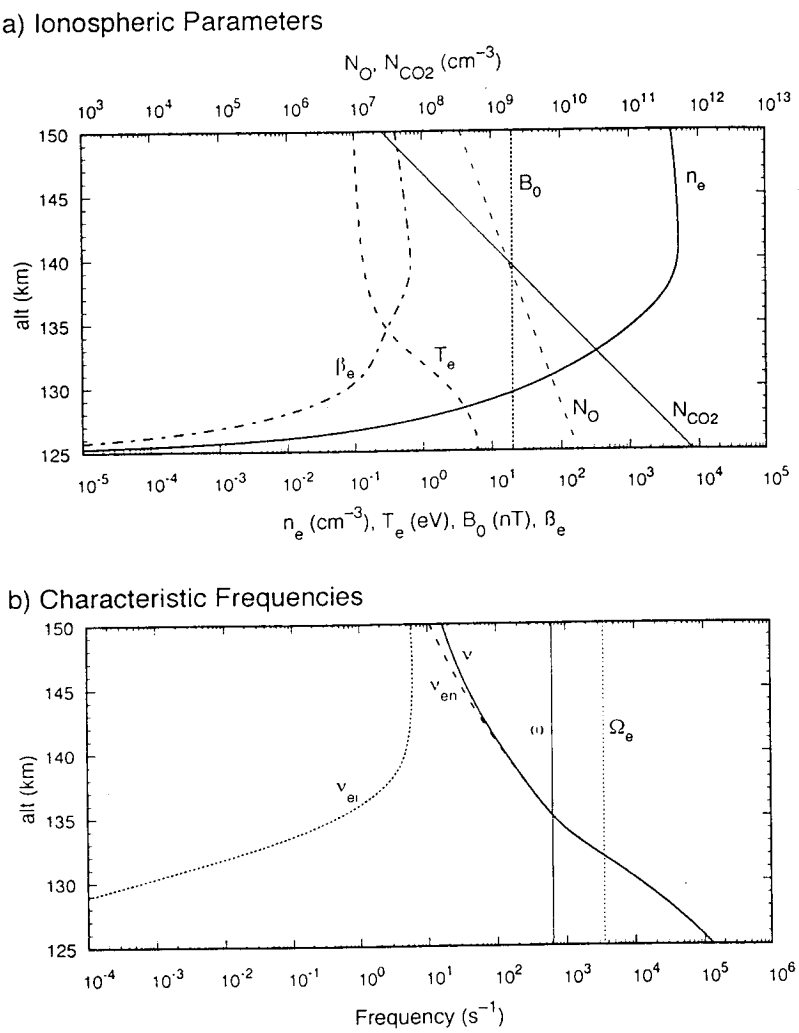

Figure 5. Wave propagation through the nightside Venus ionosphere for moderately attenuated 100-Hz signals. Similar in format to Figure 4. The peak density is 5000 cm^{-3}, and the ambient magnetic field is 20 nT, corresponding to a moderate ionospheric hole.

Figure 4c shows the associated wave parameters. At the bottom of the ionosphere we assume a net applied wave field of 10 mV/m. This wave field is the sum of both incident and reflected waves. The actual incident wave field is ≈ 0.3 V/m. Figure 4c shows that at the top of the model the wave amplitude is 0.5 mV/m, with a Poynting flux (S) of 6×10^{-7} W/m^2, similar to the values cited when discussing Figure 3a. For completeness, we also include the real and imaginary parts of the refractive index (μ). The imaginary part is largest at 132 km, and at this altitude the gradient in the Poynting flux is steepest.

The various terms that enter the heat budget are shown in Figure 4d. Because the elastic collision cooling (Q_m) is so weak, the Joule dissipation, given by $-\nabla S$, is almost completely balanced by the divergence of the heat flux (∇q), which cannot be resolved separately in the figure. Thermal balance has been achieved through iterative modification of the electron temperature profile. Initially, the temperature is assumed to be constant at 0.1 eV, and there is no heat flux. At the start of an iteration loop the wave amplitude is calculated as a function of altitude for the given ionospheric parameters. The ∇q required for energy balance is then calculated from (1), with Q_j replaced by ∇S. ∇q is numerically integrated to specify a new temperature profile, subject to the constraints that $\nabla T_e = 0$ at 125 km, and $T_e = 0.1$ eV at 150 km altitude. The wave propagation and attenuation is then recalculated using the new temperature profile. This iterative procedure is repeated until the residual of the heat budget, summed over all altitudes, is $< 10^{-4}$ of the root square sum of the constituent terms within the heat budget, giving the temperature profile shown in Figure 4a.

In Figure 4d we also plot the vibrational cooling rate, as given by (6), although this cooling has not been included in the heat budget at this stage. As noted earlier, Q_v generally exceeds the Joule heating rate. An additional electron heat source is required to offset this cooling.

Wave propagation through a moderately attenuating ionosphere is shown in Figure 5. For this case the peak density is 5000 cm^{-3}, and the ambient magnetic field is 20 nT. These conditions correspond to a moderate ionospheric hole. Figure 5a shows that for this case the wave absorption again heats the bottomside ionosphere, resulting with a peak electron temperature ≈ 8 eV. Because of the higher ambient density, ν_{ei} is close to ν_{en} at 150 km (Figure 5b). The wave is more

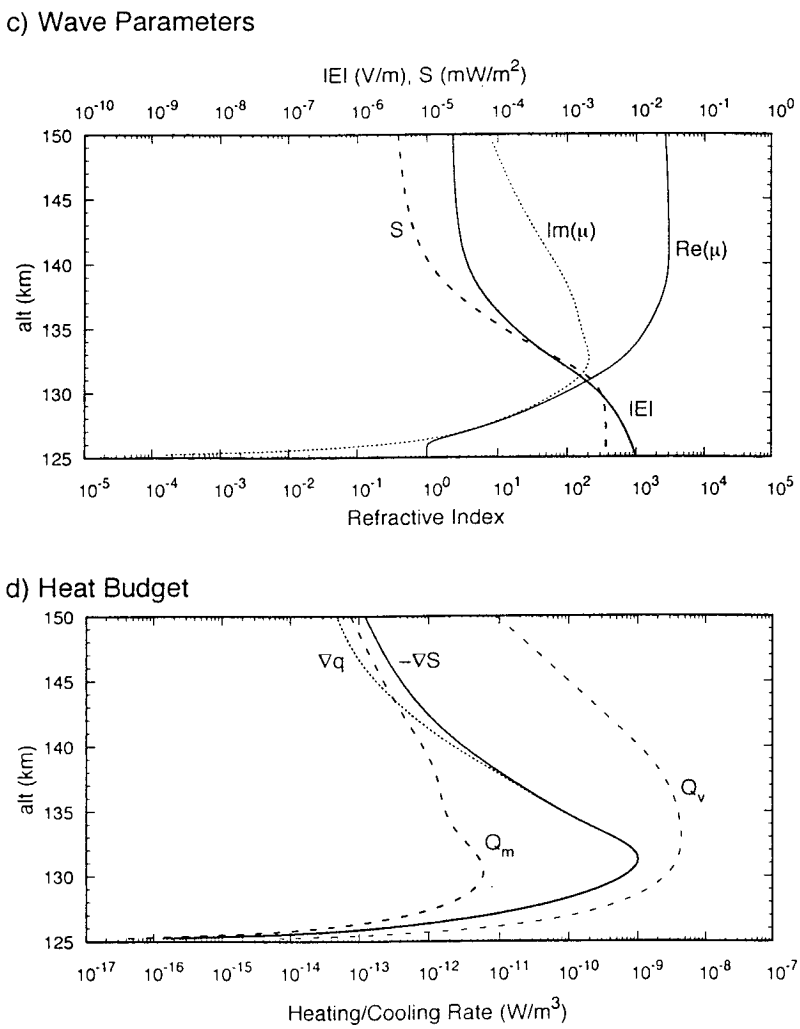

Figure 5. (continued)

strongly attenuated in Figure 5c than in Figure 4c, with an amplitude of 0.03 mV/m, and a Poynting flux of 6×10^{-9} W/m^2 at 150 km.

Solutions for a strongly attenuated 100 Hz wave are shown in Figure 6, where the peak density is 20,000 cm^{-3}, and the ambient magnetic field is 5 nT. These parameters correspond to what is observed in the typical nightside ionosphere. Yet again the self-consistent bottomside temperature is ≈ 8 eV (Figure 6a). In Figure 6b the electron-ion collision frequency is larger than the electron-neutral collision frequency at 150 km. It is clear from Figure 6c that the waves are strongly attenuated, the waves have essentially decayed to background by 135 km altitude. All of the Joule dissipation occurs below 135 km (Figure 6d). At higher altitudes the heat conduction changes sign, providing local heating to offset the elastic cooling.

In Figure 6a, $\beta_e > 1$ throughout the altitude range. However, the collision frequency only drops below the wave frequency for altitudes > 135 km, and at this altitude the waves have essentially vanished. Thus we do not expect resonant wave particle interactions to significantly modify our conclusions.

Figures 4 – 6 show that irrespective of the relative transparency of the ionosphere the net amount of heating is roughly constant. For all three cases the bottomside temperature is increased to about 8 eV. From comparison of (2) and (3), under the assumption that $\nu_{en} \gg \Omega_e$, we find that $T_e \approx 400LE$, where T_e is in eV, L is in kilometers and E is in volts per meter. If we assume that L is given by the neutral density scale height, which appears to be the case in Figures 4a – 6a, then for a net applied field of 10 mV/m and a scale length of 2 km we obtain a temperature of 8 eV, as found from the detailed calculations presented here. Although this temperature is large in comparison to typical ionospheric temperatures, the consequences for the total ionospheric heat budget are probably insignificant. In particular, because the electron-neutral collision frequency is high, the thermal conductivity is low. This allows the ionosphere to support a steep temperature gradient, and the upper ionosphere (> 140 km) is thermally decoupled from the heated region in the bottomside ionosphere. Additionally, we have not included vibrational cooling, which will reduce the electron heating. In the next section we show that the thermal decoupling is still present when we include vibrational cooling.

5. Cooling Through Inelastic Collisions

Figures 4 – 6 show that the electron cooling rate due to the vibrational excitation of CO_2 is about 3 orders of magnitude

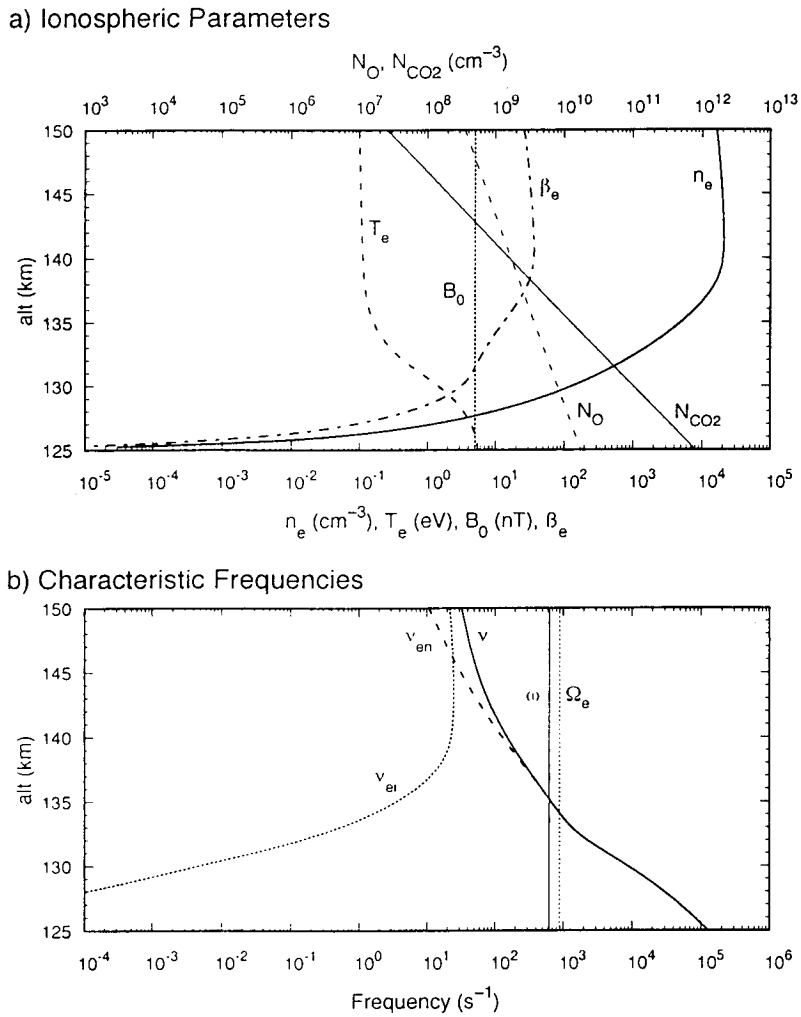

Figure 6. Wave propagation through the nightside Venus ionosphere for strongly attenuated 100-Hz signals. Similar in format to Figure 4. The peak density is 20,000 cm^{-3}, and the ambient magnetic field is 5 nT, corresponding to the typical ionosphere. In Figure 6d the Joule dissipation is so weak at higher altitudes that we also plot $-\nabla q$, as this balances the cooling due to ions.

larger than the cooling due to elastic collisions. As such this cooling should be included in the heat budget. However, as noted in the appendix, the vibrational cooling operates even in the absence of any wave heating, and a downward heat flux is required to offset this cooling. Consequently, unless *Morrison and Greene* [1978] significantly overestimate the cooling rates, the bottom of the ionosphere may be as high as 130 km. In assessing the effect of vibrational cooling we will therefore assume that the z_1 = 130 km, instead of 125 km as used in the previous section. Prior to presenting results of the wave attenuation calculations, however, we note that attempts to obtain solutions for z_1 = 125 km resulted in unrealistically high topside temperatures, unless intense waves ($\approx$ 0.1 V/m amplitude) were applied at the bottomside of the ionosphere. These waves provide enough heat to offset the vibrational cooling, without requiring any additional downward heat flux. Less intense waves did not supply enough heat at the bottomside when z_1 = 125 km.

In Figure 7 we plot solutions of the wave attenuation calculation for four cases: 10 mV/m applied field, weak attenuation (Figure 7a); 100 mV/m applied field, weak attenuation (Figure 7b); 10 mV/m applied field, strong attenuation (Figure 7c); and 100 mV/m applied field, strong attenuation (Figure 7d). For the weakly attenuated waves we assumed a peak electron density of 1000 cm^{-3} and an ambient field strength of 30 nT. For strong attenuation we assumed a peak density of 20,000 cm^{-3} and a field of 5 nT. The wave amplitudes have been chosen to reflect the average and extreme amplitudes expected at the bottomside. Since many of the features of the model have been shown in Figures 4 – 6, we only show the heat budget terms, and the temperature and wave electric field profile in Figure 7.

Figure 7a shows the results for moderate amplitude, weakly attenuated wave field. In this case the vibrational cooling is large enough to offset the Joule dissipation, at least for some of the altitude range. The peak cooling rate is $\approx 5\times10^{-10}$ W/m^3 $\approx 3\times10^3$ eV cm^{-3} s^{-1}. For larger amplitude waves, Figure 7b shows that the vibrational cooling is insufficient to balance the Joule heating. The temperature is therefore elevated, in comparison to Figure 7a. Throughout the altitude range shown Joule heating is balanced by electron heat conduction. Thus only about 10% of the energy released through Joule dissipa-

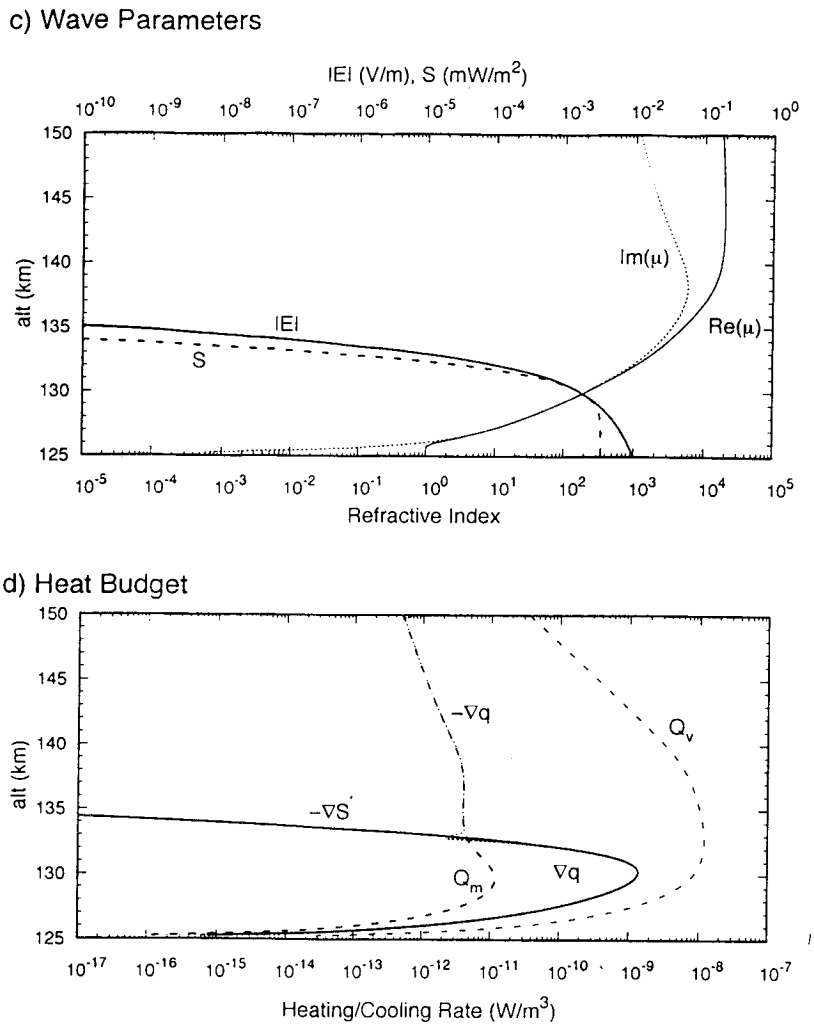

Figure 6. (continued)

tion actually causes vibrational excitation of CO_2, one cannot simply equate the Joule dissipation rate to a neutral atmosphere heating rate. The peak vibrational cooling rate is ≈ 3×10^{-9} W/m^3, roughly an order of magnitude larger than that obtained for a 10 mV/m applied wave field. It should also be noted that the strongest cooling, i.e., the most rapid transfer of heat to the neutrals, does not occur where the electron temperature is highest.

An applied field of 100 mV/m is extremely large, corresponding to the very intense burst observed by the Pioneer Venus Orbiter, at ≈ 128 km on Orbit 5055, assuming a 100 Hz bandwidth. Moreover, most of the incident wave electric field is reflected. For Figures 7b, the incident wave field is ≈ 5 V/m, which is typical for electric fields due to terrestrial lightning at 100 km away from the lightning strike [*Uman*, 1987]. Since the spectral peak of lightning is usually in the few kHz range, we might expect the wave amplitude at 100 Hz to be typically about a factor of 10 less. Furthermore, while wave fields incident on the dayside or dusk ionosphere might be expected to be of this amplitude, since this is the local time range over which lightning appears to occur on Venus [*Russell*, 1991], in the nightside the waves are thought to have traveled some distance in the surface–ionosphere waveguide [*Strangeway*, 1995b], and we expect lower amplitudes. Last, if as we suggest here, the ionosphere is above 130 km altitude, it is possible that the spacecraft was below the ionosphere for the lowest-altitude measurements, and the wave fields measured at ≈ 128 km may include vertical electric fields that are shielded from higher altitudes.

Figures 7c and 7d show the wave attenuation and heat budget for strongly attenuated signals. The decoupling of the bottomside from the topside is shown clearly in Figure 7c, where there is a temperature minimum at ≈ 136 km. At higher altitudes, where the thermal conductivity is higher, a relatively weak positive temperature gradient provides the heat flux necessary to offset the vibrational cooling. At lower altitudes, where the Joule dissipation is occurring and the conductivity is lower, a stronger negative temperature gradient provides the upward heat flux. In Figure 7d, where the applied field is 100 mV/m, the topside electron temperature is slightly elevated. However, in Figures 7c and 7d the maximum vibrational cooling occurs at altitudes above the maximum Joule dissipation.

From Figure 7c one could perhaps come to the somewhat surprising conclusion that a modest amount of wave Joule dissipation is required to offset the vibrational cooling. In Figure A2, where there is no wave heating, we find a topside temperature of 0.5 eV is required to provide the necessary downward heat flux. Because of the wave heating in Figure 7c, less heat

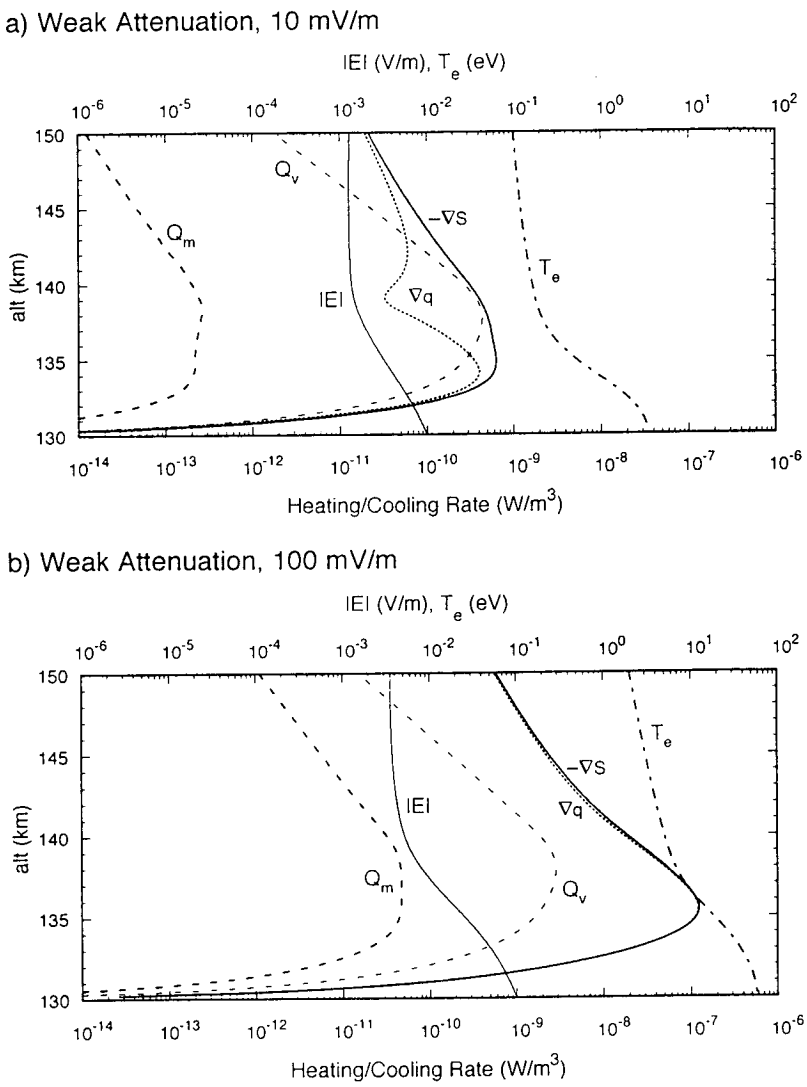

Figure 7. Heat budget, electron temperature, and wave amplitude as a function of altitude, including vibrational cooling in the heat budget. (a) Weakly attenuated, moderate amplitude signal; (b) weakly attenuated, high amplitude signal; (c) strongly attenuated, moderate amplitude signal; (d) strongly attenuated, high amplitude signal.

flux is required from above, and a more reasonable topside temperature of 0.1 eV is obtained.

We can use Figure 7c as a guide for how much heating of the neutral atmosphere is reasonable. The peak cooling rate in Figure 7c is $\approx 10^{-9}$ W/m^3, where the electron density is $\approx$ 20,000 cm^{-3}, and $T_e \approx 0.1$ eV (again in a region where there is no wave Joule dissipation). Unless the vibrational cooling rate is severely overestimated, it seems reasonable to assume that the neutral atmosphere can readily absorb heat supplied at this rate, $\approx 6\times10^3$ eV cm^{-3} s^{-1}, since the plasma parameters are consistent with in situ observations. At 140 km both O and CO_2 have densities of $\approx 2\times10^9$ cm^{-3}, and assuming that the vibrational energy is ultimately converted to thermal energy [*Cole and Hoegy*, 1995], we get a heating rate of 0.04 K s^{-1} atom^{-1}, which for a neutral gas temperature of $\approx$ 100 K, gives a doubling time of 2500 s, a little over 40 min.

Taking an electron cooling rate of 10^{-9} W/m^3 as a rate that does not seriously perturb the atmosphere, only the strongly attenuated large amplitude waves (Figure 7d) appear to be capable of perturbing the atmosphere when we incorporate vibrational cooling in our calculation. Even then, the net heating rate is only ≈ 0.4 K s^{-1} atom^{-1}. However, we have not included other inelastic processes, specifically electronic excitation of CO_2 and O, which are likely to be important when electron temperatures are a few eV. Enhanced ionization may even be possible. Such processes are thought to occur at the Earth [*Taranenko et al.*, 1993a, b] in association with lightning, and it appears reasonable to expect similar effects at Venus for the most intense waves.

6. Conclusions

Through order of magnitude estimates of the relative importance of the different heating and cooling rates we find that collisional Joule dissipation of plasma waves is likely to be important only at low altitudes in the ionosphere of Venus. This conclusion arises from the inclusion of electron heat conduction in the heat budget equation. Except at the lowest

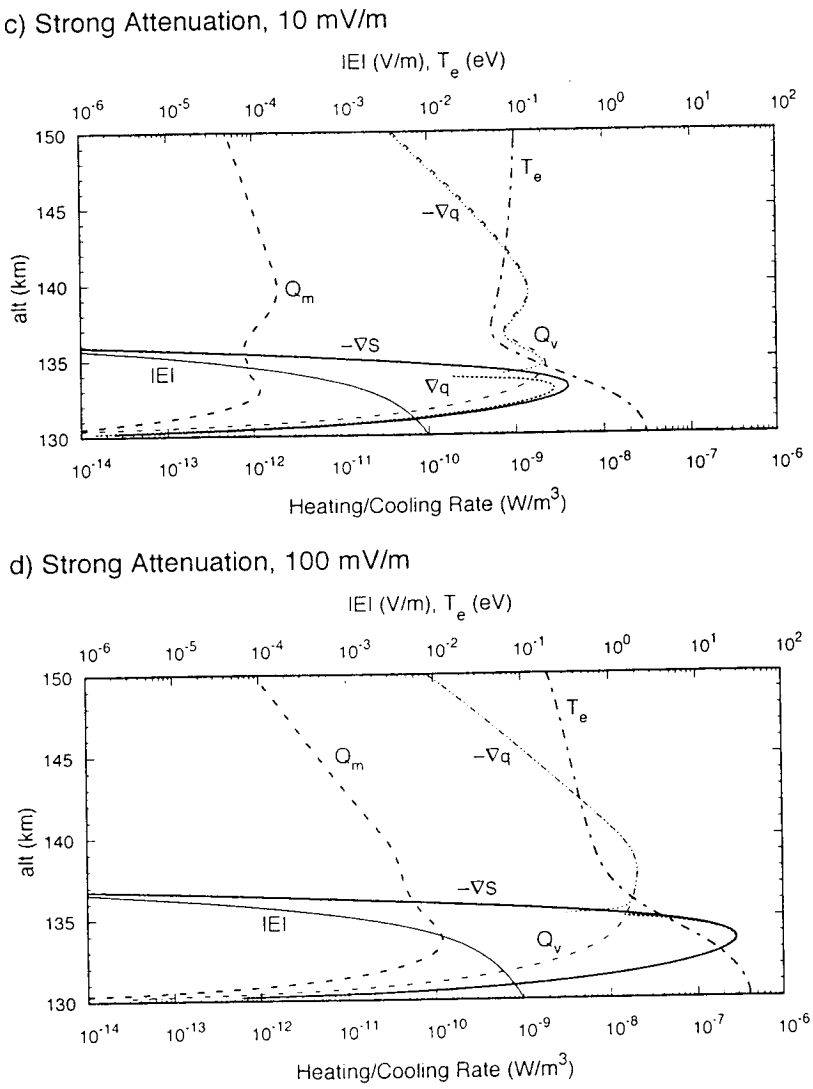

Figure 7. (continued)

altitudes, the heat flux associated with relatively small temperature gradients is sufficient to match the heating from Joule dissipation.

Near the dayside ionopause, temperature gradient scales > 1000 km can provide sufficient heat conduction to offset the Joule dissipation. Waves are mainly observed above the ionopause, where ambient plasma densities are of the order 100 cm^{-3} [*Crawford et al.*, 1993], and the scale lengths can be much longer, several planetary radii. At high altitudes in the nightside (≥ 150 km), temperature gradient scale lengths > 10 km are sufficient for heat conduction to balance Joule dissipation. Even longer scale lengths (> 50 km) are sufficient in the reduced density regions known as ionospheric holes, where the waves are usually detected.

Determining the relative significance of Joule dissipation in the bottomside ionosphere requires detailed wave propagation calculations, because the heating caused by Joule dissipation is a consequence of the attenuation of the wave fields. We have performed wave propagation calculations using the scheme of *Huba and Rowland* [1993], modified to iteratively recalculate the temperature profile until the total heating rate is zero.

During the Pioneer Venus entry phase the OEFD measured 100 Hz waves around 130 km altitude [*Strangeway et al.*, 1993b]. The waves decreased in amplitude with a scale height of the order 1 km, and with a peak amplitude of between 10^{-6} and 10^{-4} V m^{-1} Hz$^{-1/2}$, which corresponds to an electric field amplitude of a few tens of millivolts per meter assuming a bandwidth of 100 Hz. Thus the calculations presented here are consistent with the low altitude entry phase observations, and we might expect bottomside electron temperatures to be elevated to a few tens of eV for the most intense waves. As such, Joule heating by the most intense waves could possibly result in optical or ultraviolet emissions, or even enhanced ionization, which may in turn provide additional evidence for lightning on Venus.

However, while electron heating may be occurring, the high collision frequencies thermally decouple the bottomside ionosphere from higher altitudes, and we do not expect lightning generated heating to have any catastrophic consequences for the global energy budget of the Venus ionosphere and atmosphere. In particular, it is not the Joule dissipation rate, but the inelastic collision cooling rate that determines the amount of heat entering the neutral atmosphere. Electron heat conduc-

tion carries away any excess heat that cannot be absorbed by the neutral atmosphere. Since the inelastic cooling rate, which we have modeled by vibrational excitation of CO_2, is only weakly dependent on temperature above 0.2 eV [*Morrison and Greene*, 1978], the cooling rate is approximately independent of the amount of Joule dissipation, and we find electron cooling rates, and hence neutral atmosphere heating rates, of the order 10^{-9} W/m^3 for typical wave field amplitudes. This rate appears to be well within the bounds of heating rates which can be accommodated by the neutral atmosphere.

Appendix

As noted in the body of the text, CO_2 is the dominant neutral at low altitudes in the Venus ionosphere. *Morrison and Greene* [1978] have investigated the cooling of electrons through collisions with CO_2, and we use their work as a basis for parameterizing the collision cross-section, and vibrational cooling rate. Figure A1 shows the cooling rates from *Morrison and Greene* [1978], as indicated by the symbols. It is assumed that the neutral gas temperature is 200 K. The solid lines in Figure A1 show least squares regression lines through the data. The functional forms for the regression were chosen to best fit the data, with the constraints that the curves approach an asymptotic form at high temperature, and that the functions are positive definite for all temperatures.

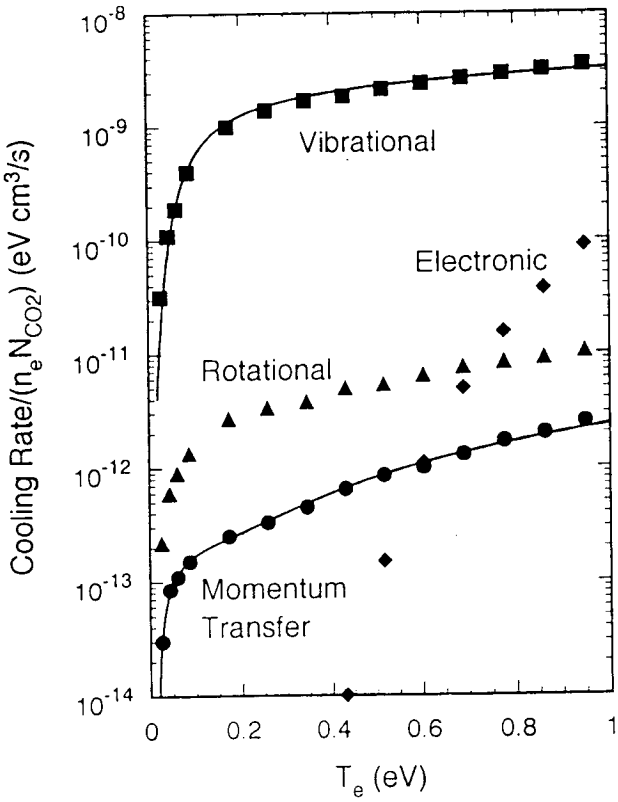

Figure A1. Cooling rates for electron-CO_2 collisions [after *Morrison and Greene*, 1978]. The symbols give the cooling rates for vibrational (squares), electronic (diamonds), and rotational (triangles) excitation of CO_2, and for elastic, momentum transfer (circles), collisions. The solid lines give least squares fits used to parameterize the vibrational cooling rate and momentum transfer collision cross section.

Turning to the momentum transfer cooling rate first, from (5) and (7),

$$Q_m = 3(m_e/m_{CO2})\,4.19\times10^7 \cdot n_e N_{CO2} T_e^{1/2} \sigma (T_e - T_{CO2}) \text{ eV cm}^{-3}\text{ s}^{-1} \quad \text{(A1)}$$

where temperatures are in eV, and densities are in cm^{-3}. Thus the explicit temperature dependence in (A1) is removed prior to performing the fit. Note that (A1) has been expressed in eV cm^{-3} s^{-1}, for direct comparison with Figure A1, 1 eV cm^{-3} s^{-1} = 1.6×10^{-12} erg cm^{-3} s^{-1} = 1.6×10^{-13} W/m^3.

The fit yields a collision cross section for momentum transfer of the form

$$\sigma = 1.55\times10^{-15} + 2.76\times10^{-15} \exp(-11.88\,T_e)/T_e^{1/2} \text{ cm}^2 \quad \text{(A2)}$$

The fit to the vibrational cooling rate curve is

$$Q_v = 3.23\times10^{-9}\, n_e N_{CO2} T_e^{1/2} \cdot \exp(-21.8\exp(-T_e^{1/2}/0.0897)) \text{ eV cm}^{-3}\text{ s}^{-1} \quad \text{(A3)}$$

Thus at high temperatures (> 0.3 eV) $Q_v/Q_m \approx 1.34\times10^3/T_e$ and the vibrational cooling generally exceeds the momentum transfer cooling by about 3 orders of magnitude.

However, while electrons lose most of their energy through inelastic collisions, they lose most of their momentum through elastic collisions. If we denote the effective collision frequency for momentum loss through vibrational excitation of CO_2 as ν_v, then

$$\frac{\nu_v}{\nu_{en}} \approx \frac{m_e}{m_{CO2}} \frac{(T_e - T_{CO2})}{T_e} \frac{Q_v}{Q_m} \quad \text{(A4)}$$

and since $m_{CO2}/m_e = 8\times10^4$, even though $Q_v/Q_m \approx 1.34\times10^3/T_e$, the electron momentum loss collision frequency is essentially that due to elastic collisions. Thus it is the collision frequency for elastic collisions that gives the Joule dissipation rate, while the cooling due to inelastic collisions is the dominant collisional cooling term. This further emphasizes the relative inefficiency of cooling through elastic collisions.

Another consequence of the relative efficiency of vibrational cooling was alluded to in section 4, where we showed that the vibrational cooling rate exceeded the Joule dissipation rate at most altitudes. Even in the absence of waves, the vibrational cooling operates, and may require unrealistically high topside electron temperatures to provide the heat flux required to offset the cooling, depending on the assumed ionospheric density profile. This is shown in Figure A2, where we plot solutions of the heat budget equation (1), but with the Joule dissipation turned off, and cooling through vibrational excitation of CO_2 (A3) turned on. The thick curves to the right of the figure show the temperature and cooling rate profile obtained for the same density profile shown in Figure 6. Since downward heat flux is the only source of heat in the model, (1) requires unrealistically high topside electron temperatures. When obtaining a solution of (1) in this case, we required that the electron temperature at lowest altitude be the same as the neutral gas, and allowed the topside temperature to float.

Because the vibrational cooling rate is proportional to N_{CO2}, while the thermal conductivity is inversely proportional to N_{CO2} (through the collision frequency), small

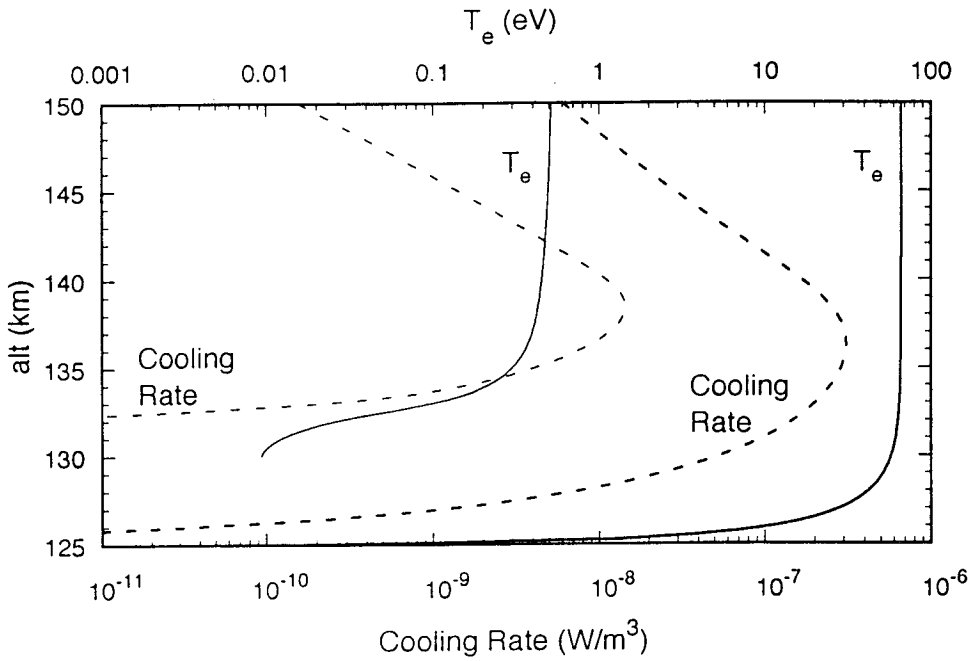

Figure A2. Electron temperature profiles and associated cooling rates for different ionosphere minimum altitudes. The temperature (thick solid line) and collisional cooling rate (thick dashed line) are plotted to the right for an ionospheric density profile that vanishes at 125 km altitude. The peak density is at 140 km, with a value of 20,000 cm^{-3}. The thin lines show the temperature and cooling rate for the same peak density and altitude, but with the ionospheric minimum altitude at 130 km.

changes in the minimum altitude of the ionosphere can have marked changes in the vibrational cooling rate. The thin curves to the left of Figure A2 show the temperature and cooling rate when we assume that the electron density vanishes at an altitude of 130 km. Clearly, while slightly elevated, the temperatures are much more reasonable. Thus in section 5, where we discuss wave transmission including vibrational cooling, we assume the bottom of the ionosphere is at 130 km.

As a last remark on inelastic cooling, we have not included other cooling processes, such as the fine structure excitation of atomic oxygen [*Hoegy*, 1976]. Except at higher altitudes (> 150 km), this cooling is relatively unimportant in comparison to the cooling by CO_2. However, a complete analysis of the electron heat budget should in the future include this and other cooling terms due to inelastic collisions with atomic oxygen.

Acknowledgments. I thank C. T. Russell, K. D. Cole and W. R. Hoegy for many useful discussions. I also thank J. L. Fox and T. E. Cravens who emphasized the importance of inelastic cooling. I am particularly grateful to J. L. Fox for pointing out the work on CO_2 cooling by *Morrison and Greene* [1978]. This work was supported by NASA grants NAG2-485 and NAGW-3497, and is IGPP Publication 4273.

The Editor thanks K. Szegö and another referee for their assistance in evaluating this paper.

References

Banks, P. M., and G. Kockarts, *Aeronomy, Parts A and B*, Academic, San Diego, Calif., 1973.

Brace, L. H., and A. J. Kliore, The structure of the Venus ionosphere, *Space Sci. Rev., 55*, 81–163, 1991.

Cole, K. D., and W. R. Hoegy, Joule heating by ac electric fields in the ionosphere of Venus, *J. Geophys. Res*, in press, 1995.

Crawford, G. K., R. J. Strangeway, and C. T. Russell, VLF emissions at the Venus dayside ionopause, in *Plasma Environments of Non-Magnetic Planets*, edited by T. I. Gombosi, pp. 253–258, Pergamon, New York, 1993.

Grebowsky, J. M., S. A. Curtis, and L. H. Brace, Small-scale irregularities in the nightside Venus ionosphere, *J. Geophys. Res., 96*, 21,347–21,349, 1991.

Grebowsky, J. M., R. E. Hartle, J. Kar, P. A. Cloutier, H. A. Taylor Jr., and L. H. Brace, Ion measurements during Pioneer Venus reentry: Implications for solar cycle variation of ion composition and dynamics, *Geophys. Res. Lett., 20*, 2735–2738, 1993.

Hedin, A. E., H. B. Niemann, W. T. Kasprzak, and A. Seiff, Global empirical model of the Venus thermosphere, *J. Geophys. Res., 88*, 73–83, 1983.

Ho, C.-M., R. J. Strangeway, and C. T. Russell, Occurrence characteristics of VLF bursts in the nightside ionosphere of Venus, *J. Geophys. Res., 96*, 21,361–21,369, 1991.

Ho, C.-M., R. J. Strangeway, and C. T. Russell, Control of VLF burst activity in the nightside ionosphere of Venus by the magnetic field orientation, *J. Geophys. Res., 97*, 11,673–11,680, 1992.

Hoegy, W. R., New fine structure cooling rate, *Geophys. Res. Lett., 3*, 541–544, 1976.

Huba, J. D., Theory of small scale density and electric field fluctuations in the nightside Venus ionosphere, *J. Geophys. Res., 97*, 43–50, 1992.

Huba, J. D., Generation of waves in the Venus mantle by the ion acoustic beam instability, *Geophys. Res. Lett., 20*, 1751–1754, 1993.

Huba J. D., *Naval Research Laboratory Plasma Formulary – Revised 1994*, Nav. Res. Lab., Washington, D. C., 1994.

Huba, J. D., and J. M. Grebowsky, Small scale density irregularities in the nightside Venus ionosphere: Comparison of theory and observations, *J. Geophys. Res., 98*, 3079–3086, 1993.

Huba, J. D., and H. L. Rowland, Propagation of electromagnetic waves parallel to the magnetic field in the nightside Venus ionosphere, *J. Geophys. Res., 98*, 5291–5300, 1993.

Kasprzak, W. T., H. B. Niemann, A. E. Hedin, S. W. Bougher, and D. M. Hunten, Neutral composition measurements by the Pioneer Venus neutral mass spectrometer during orbiter re-entry, *Geophys. Res. Lett., 20*, 2747–2750, 1993.

Luhmann, J. G., C. T. Russell, and R. C. Elphic, Time scales for the

decay of induced large-scale magnetic fields in the Venus ionosphere, *J. Geophys. Res., 89*, 362–368, 1984.

Morrison, M. A., and A. E. Greene, Electron cooling by excitation of carbon dioxide, *J. Geophys. Res., 83*, 1172–1174, 1978.

Russell, C. T., Venus lightning, *Space Sci. Rev., 55*, 317–356, 1991.

Russell, C. T., and R. N. Singh, A re-examination of impulsive VLF signals in the night ionosphere of Venus, *Geophys. Res. Lett., 16*, 1481–1484, 1989.

Russell, C. T., M. von Dornum, and F. L. Scarf, The altitude distribution of impulsive signals in the night ionosphere of Venus, *J. Geophys. Res., 93*, 5915-5921, 1988.

Russell, C. T., M. von Dornum, and F. L. Scarf, Source locations for impulsive electric signals seen in the night ionosphere of Venus, *Icarus, 80*, 390–415, 1989a.

Russell, C. T., M. von Dornum, and R. J. Strangeway, VLF bursts in the ionosphere of Venus: Estimates of the Poynting flux, *Geophys. Res. Lett., 16*, 579–582, 1989b.

Scarf, F. L., and C. T. Russell, Lightning measurements from the Pioneer Venus orbiter, *Geophys. Res. Lett., 10*, 1192–1195, 1983.

Scarf, F. L., W. W. L. Taylor, C. T. Russell, and L. H. Brace, Lightning on Venus: Orbiter detection of whistler signals, *J. Geophys. Res., 85*, 8158–8166, 1980a.

Scarf, F. L., W. W. L. Taylor, C. T. Russell, and R. C. Elphic, Pioneer Venus plasma wave observations: The solar wind–Venus interaction, *J. Geophys. Res., 85*, 7599–7612, 1980b.

Scarf, F. L., W. W. L. Taylor, and P. V. Virobik, The Pioneer Venus orbiter plasma wave investigation, *IEEE Trans. Geosci. Remote Sens., GE-18*, 36–38, 1980c.

Singh, R. N., and C. T. Russell, Further evidence for lightning on Venus, *Geophys. Res. Lett., 13*, 1051–1054, 1986.

Sonwalkar, V. S., D. L. Carpenter, and R. J. Strangeway, Testing radio bursts observed on the nightside of Venus for evidence of whistler-mode propagation from lightning, *J. Geophys. Res., 96*, 17,763–17,778, 1991.

Strangeway, R. J., Plasma waves at Venus, *Space Sci. Rev., 55*, 275–316, 1991a.

Strangeway, R. J., Polarization of the impulsive signals observed in the nightside ionosphere of Venus, *J. Geophys. Res., 96*, 22,741–22,752, 1991b.

Strangeway, R. J., An assessment of lightning or in situ instabilities as a source for whistler mode wave in the night ionosphere of Venus, *J. Geophys. Res., 97*, 12,203–12,215 1992.

Strangeway, R. J., An assessment of plasma instabilities or planetary lightning as a source for the VLF bursts detected at Venus, *Adv. Space Res., 15(4)*, 89–92, 1995a.

Strangeway, R. J., The plasma wave evidence for lightning on Venus, *J. Atmos. Terr. Phys., 57*, 537–556, 1995b.

Strangeway, R. J., and G. K. Crawford, On the instability and energy flux of lower hybrid waves in the Venus plasma mantle, *Geophys. Res. Lett., 20*, 1211–1214, 1993.

Strangeway, R. J., C. T. Russell, C. M. Ho, and L. H. Brace, Plasma waves observed at low altitudes in the tenuous Venus nightside ionosphere, *Geophys. Res. Lett., 20*, 2767-2770, 1993a.

Strangeway, R. J., C. T. Russell, and C. M. Ho, Observation of intense wave bursts at very low altitudes within the Venus nightside ionosphere, *Geophys. Res. Lett., 20*, 2771–2774, 1993b.

Szego, K., V. S. Shapiro, V. I. Shevchencko, R. Z Sagdeev, W. T. Kasprzak, and A. F. Nagy, Physical processes in the plasma mantle of Venus, *Geophys. Res. Lett., 18*, 2305–2308, 1991.

Taranenko, Y. N., U. S. Inan, and T. F. Bell, Interaction with the lower ionosphere of electromagnetic pulses from lightning: Heating, attachment, and ionization, *Geophys. Res. Lett., 20*, 1539–1542, 1993a.

Taranenko, Y. N., U. S. Inan, and T. F. Bell, The interaction with the lower ionosphere of electromagnetic pulses from lightning: Excitation of optical emissions, *Geophys. Res. Lett., 20*, 2675–2678, 1993b.

Taylor, H. A., Jr., and P. A. Cloutier, Telemetry interference incorrectly interpreted as evidence for lightning and present-day volcanism at Venus, *Geophys. Res. Lett., 15*, 729–732, 1988.

Theis, R. F., L. H. Brace, and H. G. Mayr, Empirical models of the electron temperature and density in the Venus ionosphere, *J. Geophys. Res., 85*, 7787–7794, 1980.

Uman, M. A., *The Lightning Discharge*, Academic, San Diego, Calif., 1987.

R. J. Strangeway, Institute of Geophysics and Planetary Physics, University of California, Los Angeles, CA 90024. (e-mail: strange@igpp.ucla.edu)

(Received March 20, 1995; revised August 18, 1995;
accepted August 21, 1995.)

JOURNAL OF GEOPHYSICAL RESEARCH, VOL. 100, NO. A6, PAGES 9697–9705, JUNE 1, 1995

Venus nightside ionospheric irregularities and their relationship to VLF bursts

C. M. Ho,[1] R. J. Strangeway, and C. T. Russell

Institute of Geophysics and Planetary Physics, University of California at Los Angeles

Abstract. The plasma density and magnetic field are highly spatially and temporally variable in the Venus nightside ionosphere. This variability may affect the propagation and the generation of plasma waves. We determine how these irregularities are related to plasma wave activity. Previously, we have found two types of signals in the lower ionosphere, 100-Hz narrow-band signals and high-frequency wideband bursts. We investigate how these two different wave phenomena depend on the structure of the ionosphere. We calculate the ratios of the instantaneous values of electron density, magnetic field, and electron temperature relative to their average (1 min) values, and also their gradient scale lengths. The 5.4-kHz burst activity is related to density depressions and obvious electron temperature enhancements, but varies little with magnetic field strength. The 100-Hz narrow-band signals are often associated with significantly enhanced magnetic field and depressions of electron density. Both higher field strength and lower density result in a lower β (ratio of thermal pressure to magnetic pressure) plasma, which favors the propagation of whistler waves. We find that neither type of signal is associated with gradients of the magnetic field, but the 5.4-kHz wideband signals have higher occurrence rates at higher electron density and temperature gradients, while the 100-Hz narrow-band burst rate increases only slightly for steeper gradients. A local gradient-driven instability cannot explain most of the 100-Hz narrow-band signals, but some 5.4-kHz signals may be associated with pressure gradients.

1. Introduction

The plasma wave instrument on board the Pioneer Venus Orbiter detected many VLF bursts at low altitudes in the nightside ionosphere of Venus. In the initial studies of F. L. Scarf and colleagues, only the bursts detected at 100 Hz were attributed to waves generated by atmospheric lightning [*Scarf et al.*, 1980a; *Scarf and Russell*, 1983], assuming that the 100-Hz bursts were electromagnetic whistler mode waves. Later, *Singh and Russell* [1986] argued that the higher-frequency bursts detected at low altitudes were also lightning related, even though the signals could not propagate to the spacecraft as electromagnetic waves, since they were observed in a propagation stop band between the local electron gyrofrequency and plasma frequency.

The initial studies were at best qualitative. As pointed out by *Taylor et al.* [1987], the initial studies of the 100-Hz bursts were not normalized by observing time, and the analysis of wideband data suffered from the apparent inclusion of artificial bursts due to telemetry errors [*Taylor and Cloutier*, 1988; *Russell and Singh*, 1989]. To correct these defects, two new data sets were derived. One determined the fraction of 30-s intervals within the data set that contained VLF burst activity [e.g., *Russell et al.*, 1988]. The second counted individual bursts, to determine burst rates [e.g., *Ho et al.*, 1991]. Both these data sets allowed normalized rates of activity to be determined, as well as investigation of the dependence of burst activity on parameters such as local time, altitude, and ambient plasma parameters.

With their improved data set, *Russell et al.* [1988] found that both the 100-Hz and wideband wave activity peaked at or near periapsis altitudes. Moreover, the wide-band data tended to peak near the dusk local time sector [*Russell et al.*, 1989a]. This finding was cited as evidence for atmospheric dynamics controlling the burst activity, rather than active volcanism. The altitude and local time dependence was also found in the burst rate study of *Ho et al.* [1991], who further found that the 100-Hz burst activity had a strong dependence on magnetic field strength. In subsequent work, *Ho et al.* [1992] demonstrated that the 100-Hz burst activity could be separated into two classes, one in which 100-Hz bursts are assumed to propagate vertically from below the ionosphere within the whistler mode resonance cone, and the second consisting of non-whistler mode signals. These two classes of signal have markedly different altitude profiles, with the non-whistler mode signal burst rate decreasing much more rapidly with increasing altitude, in a manner similar to the wide-band bursts above the electron gyrofrequency. Estimates of the Poynting flux also suggest a weak falloff with altitude for the 100-Hz signals [*Russell et al.*, 1989b].

However, there is some indication that the burst rates of the high-frequency signals decrease at lowest altitude [e.g., *Ho et al.*, 1992]. Why this occurs has yet to be resolved; it may be due to a change in instrument response to the presumed shortening of the wave pulses at low altitude, or it could be an indication that the higher-frequency waves are only generated above a certain altitude. The latter interpretation does not preclude a lightning source, since there is evidence of direct coupling between lightning and the ionosphere at the Earth [e.g., *Boeck et al.*, 1992; *Burke et al.*, 1992].

[1]Now at Jet Propulsion Laboratory, Pasadena, California.

Paper number 95JA00064.
0148-0227/95/95JA-00064$05.00

It has also been argued that the 100-Hz bursts are generated in situ. From ion mass spectrometer data, *Taylor et al.* [1985] found that ionization troughs were frequently observed in the Venus nightside ionosphere and that 100-Hz plasma waves were often associated with these ion density troughs. Superthermal ions are observed in association with troughs, and through analogy with observations at the dayside ionopause, they suggested that some local plasma instability within the troughs resulted in the burst signals. However, *Scarf* [1986] pointed out that a strong radial magnetic field is a necessary condition to detect whistler mode events. Density troughs are often associated with intensification of the vertical magnetic field [*Brace et al.*, 1982; *Luhmann et al.*, 1981, 1982; *Luhmann and Russell*, 1983]. This phenomenon is conducive to the upward or downward propagation of low-frequency whistler waves, and hence we would also expect a correlation between 100-Hz whistler mode bursts and density troughs.

Recently, *Grebowsky et al.* [1991] have noted that the nightside ionosphere has many small-scale irregularities, as evidenced by anomalous Langmuir probe current-voltage response curves. These perturbations have scale lengths of 0.1–2.0 km. *Grebowsky et al.* [1991] also reported a correlation between the Langmuir probe anomalies and 100-Hz bursts, although they used a somewhat subjective analysis method, with a variable burst threshold and no test for random coincidence. *Strangeway* [1995], using a more objective method, showed that the correlation is only weakly statistically significant and most of the 100-Hz bursts do not appear to be due to electric fields associated with density fluctuations.

However, *Huba* [1992] proposed a lower hybrid drift instability as a possible source for the density fluctuations. Lower hybrid waves also have perpendicular polarization and preferentially occur in low-β plasma regions, as do the whistler mode waves. For sufficiently short wavelengths (≈100 m), the waves could be Doppler shifted to 100 Hz through spacecraft motion. The lower hybrid waves are generated by pressure gradients. Although *Strangeway* [1992] showed examples in which gradients in the field and density tended to bound the regions in which the 100-Hz waves were detected, it is nevertheless important to examine the relationship between 100-Hz waves and ionospheric structure, which can be highly variable at Venus.

Plasma variability in the Venus nightside ionosphere is exhibited in several forms, including large-scale electron density holes [*Brace et al.*, 1980, 1982] and smaller-scale density depressions. The magnetic pressure is usually less than that of the ionospheric plasma. Thus there is much turbulence and distortion in the magnetic field, which is much more irregular in the Venus ionosphere than in the terrestrial ionosphere [*Luhmann and Cravens*, 1991]. These variations may affect the propagation and/or generation of the plasma waves observed in the nightside ionosphere. However, the high variability makes it difficult to establish a criterion to define or measure depressions and enhancements of the ambient plasma parameters. For example, it might be expected that a plasma depression should be accompanied by an enhancement of the magnetic field to maintain pressure balance. But if there are temporal variations, this balance will not be complete, and the variations in magnetic field and density will not necessarily be anticorrelated.

Most investigations of density holes in the nightside ionosphere are case studies. A quantitative definition of holes and statistical methods for studying holes is wanting. For example, while *Taylor et al.* [1987] give identification criteria for ion troughs, some subjectivity is introduced through the estimation of the background profile that would be present in the absence of a trough. Additionally, the method employed by *Taylor at al.* [1987] only specifies the presence or absence of a trough, but not the depth of the trough. Moreover, we have no quantitative definition specifying a magnetic field enhancement. We need an explicit definition of a "hole" or density depression to perform a quantitative statistical study of the magnetic field and plasma and VLF waves in the lower ionosphere of Venus. In the next section we will introduce our methodology to define a depression or enhancement of the field and plasma. Using this definition, we perform statistical studies to determine whether plasma wave activity is associated with ionospheric irregularities in section 3. Our results are summarized in the last section.

2. Methodology

In this study the plasma wave data come from the observations of the Pioneer Venus Orbiter (PVO) electric field detector (OEFD) [*Scarf et al.*, 1980b]. The magnetic field and the electron density are measured separately by the Orbiter magnetometer (OMAG) [*Russell et al.*, 1980] and the Orbiter electron temperature probe (OETP) [*Krehbiel et al.*, 1980]. The OEFD has four narrow-band frequency channels at 100 Hz, 730 Hz, 5.4 kHz, and 30 kHz with ±15% bandwidth. Both electric field and magnetic field data have 0.25-s resolution at the highest data rates. The third PVO eclipse season (orbits 471–570) has low periapsis altitude (141–168 km). For this season, L. H. Brace has provided us with high-resolution (2.0 s) electron density (n_e) and temperature (T_e) data. For comparison, we have consequently used 2.0-s average magnetic field (B_t) data in this study. We have restricted data to below 300 km altitude for the 100 nightside orbits, because we want to emphasize the study of the lower-ionosphere structure and VLF burst signal activity. Under this altitude restriction each orbit has variable time duration (roughly about 6–7 min) depending on the local time of periapsis of the orbit. After surveying all data for season 3, we find that B_t and n_e have larger relative variations than T_e. The magnetic field can vary from a few nanoteslas to 60 nT, while n_e also may change up to 2 orders of magnitude. We find that the irregularity structures generally may be classified as four types according to their dimensions.

First, for 15% of all orbits, the observations show large-scale and relatively static structures in the magnetic field. These static structures are observed for at least 3 min and have a dimension about 2000 km along the orbit. The magnetic field usually is stronger than average. Second, for 15% of the orbits, the observations show semistatic magnetic field structures. Many small-scale structures mix with a few middle-scale (500–2000 km) structures. Third, on about 25% of the orbits, wavelike structures are observed. These orbits mainly are those in the dusk and dawn sides (471–482 and 557–570). The density and temperature have wavelike structures with about 20-s periodicity, but the magnetic field often is highly variable with shorter period, less than 5 s. Thus these wave structures usually have dimensions less than 100 km [*Brace et al.*, 1983]. Last, for the remaining 45% of the orbits, the ionosphere displays irregular rather than periodic structures with dimensions less than 500 km. We should point out that the larger-scale (dimension of >500 km) irregularities are very infrequent, in comparison with the small-scale irregularities. The small-scale irregularities are dominant structures by number in the nightside ionosphere, because 80% of observing time is in regions with variations of less than 500-km scale in the field or plasma. Thus it becomes important for us to determine the rela-

tionship between VLF burst signals and these small-scale irregular structures.

Although these small-scale irregularities can be identified by eye, it is not easy to give them an accurate definition for the purpose of statistical studies. The difficulty comes from their extensive variations in magnitude and time scale. *Taylor et al.* [1987] define an ion trough according to the criteria that the total ion density must decrease by at least a factor 2 relative to the upper envelope of the density profile, with the initial reduction occurring within an interval of 3 s or less, and this depletion must be maintained for at least 10 s. Their definition excludes small and narrow troughs. In addition, any correlation between the magnetic field and plasma cannot be found from their method, because they did not identify magnetic field enhancements. In this study we investigate the variation of both the ambient plasma and magnetic field.

Since a depression or an enhancement must be a variation relative to some background value, we need to find background values for n_e, T_e, and B_t. The nightside ionospheric observations show that the variations from day to day in the field and plasma are very large, so that it is impossible to use a fixed average profile to express them. On two adjacent orbits the electron density may have 1–2 orders of magnitude difference at the same altitude. The Theis model [*Theis et al.*, 1984] is based on statistical average results, and the model does not work well on individual passes. In some days the observed electron density is well above the model everywhere, whereas on many other orbits a much lower density is found, 1–2 orders of magnitude below the model, everywhere along the orbit. Thus we cannot find a general average profile to fit every orbit.

An alternative approach to determining the location of depressions and enhancements is to first obtain the average profile of each orbit from a running average of the instantaneous data, and then use this average value of each quantity ($<B_t>$, $<n_e>$, $<T_e>$) as the background profile. An important task is to choose how large a window over which to average data. The window width of the running average that we used depends on the dimension of the irregularity in which we are interested. A wider window allows the detection of larger-size depressions and enhancements, but the smaller variations occurring inside a large variation will not be identified as a separate feature. When we use a very narrow window, the average profile more nearly follows the instantaneous value inside the larger depressions and enhancements, and large-scale features are not identified. Because we want to focus on the variations with dimension less than 500 km, we use a 60-s window and an arithmetic running average to find and measure these structures, based on the spacecraft speed (10 km/s) around periapsis altitude. Because "disappearing ionospheres" are large density depletion and field enhancements usually lasting for at least half a nightside pass, our criterion cannot identify these structures. Thus in this study, bursts detected for density depressions or magnetic field enhancements are not associated with disappearing ionospheres.

Figure 1 shows a typical orbit of VLF burst signals and the irregularities in magnetic field and electron density in the nightside ionosphere of Venus on orbit 500. The orbit has a periapsis altitude of 150 km at 1055:39 UT. From top to bottom we show electric field wave intensities at 30 kHz, 5.4 kHz, 730 Hz, and 100 Hz. Plasma wave data have 0.25-s resolution. We see that strong impulsive broadband signals appear in all four frequency

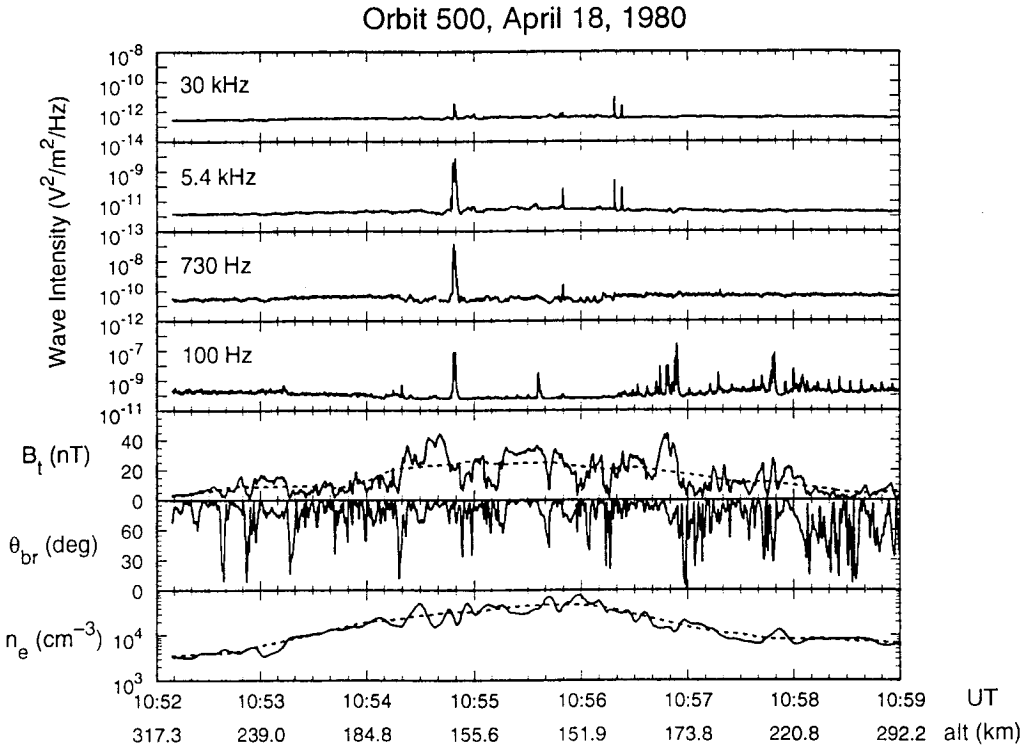

Figure 1. Periapsis pass on orbit 500 showing VLF burst signals and irregularities in the magnetic field and the electron density in the nightside ionosphere of Venus. The upper time series are electric field wave intensities in four narrow-band frequency channels at 30 kHz, 5.4 kHz, 730 Hz, and 100 Hz. The bottom three panels give the total magnetic field, the angle between the magnetic field direction and the radial direction, and the electron density. The dashed lines in the plots of the magnetic field and the density represent their average profiles.

channels. There are some narrow-band signals appearing only in the 100-Hz channel to the right of the plot. The small periodic pulses in the 100-Hz channel after 1057 UT are interference, but the large 100-Hz pulses near 1057 and 1058 UT are real signals. The bottom three panels give the total magnetic field (0.25-s resolution), the angle between the magnetic field direction and the radial direction, and the electron density (2.0-s resolution). The dashed lines in the panels of the magnetic field and the density represent their average respective profiles, which are obtained by using a 60-s running average as discussed above. We can see that there are many irregular enhancements or depressions in the magnetic field and the density. They have different time scales from a few s to some 40 s. The average profiles (dashed lines) follow the general trends of B_t and n_e very well. The burst signals mainly occur in the relatively large and static B_t regions, rather than small-size turbulent regions. In general, when B_t increases, n_e decreases, and vice versa. However, we do not always see a clear anticorrelation between the field and density.

For the study of the relationship between burst activity and irregularities, we calculate the relative variation of B_t, n_e, and T_e, using their instantaneous values over their average profile values ($G/\langle G\rangle$, where G is the instantaneous value and $\langle G\rangle$ is the average). When the ratio is greater than one, and a wave burst occurs, we will say the burst is associated with an enhancement. When the ratio is less than one, any burst signal is associated with a depression. With this variation ratio we may determine the dependence of burst activity on the magnitude of an enhancement or depression of the field and plasma, as we do below, in section 3.1.

We also wish to investigate the relation between burst rates and the magnitude of the gradient or the scale length of the field and plasma. These gradients may be related to either a depression or an enhancement. Because the spacecraft motion near periapsis is mainly horizontal, we detect mostly horizontal gradients in the nightside lower ionosphere. In order to characterize the size of these gradients, we assume that both the field and plasma vary exponentially as a function of horizontal distance. For the magnetic field, we assume $B = B_0 \exp(s/H_B)$, where H_B is the horizontal scale length and s is the displacement in the horizontal direction. Thus

$$\frac{1}{H_B} = \frac{1}{B}\frac{dB}{ds} \approx \frac{\Delta B_j}{B_j \Delta s_j} \tag{1}$$

Here, $\Delta B_j (= B_{j+1} - B_{j-1})$ and $\Delta s_j (= s_{j+1} - s_{j-1})$ approximate dB and ds, where the subscript j refers to the jth measurement in the time series. The electron density and temperature take similar forms with scale length H_n and H_T. We will use these scale lengths to express the magnitude of the gradients in section 3.2. In using (1) we have assumed that there is no significant temporal variation over the time scale of the sample used to determine the scale length, and that the normal altitudinal variation observed in the nightside ionosphere does not greatly affect the deduced gradient scale length.

Because the magnetic field and electron data have 2.0-s resolution, the gradient, as defined in (1), will have 4.0-s resolution. Thus for a gradient in the magnetic field or electron density the minimum scale length we can identify is about 20 km, and the gradient dependence study suffers from this data resolution limitation.

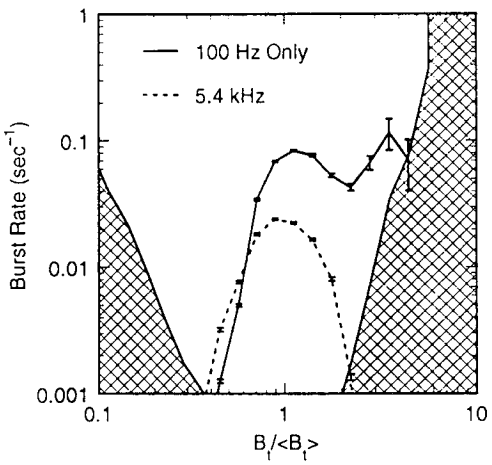

Figure 2. Dependence of the burst rates in the 100-Hz channel only (solid line) and the 5.4-kHz channel (dashed line) on the relative variation of B_t. The rates are plotted on a logarithmic scale. The error bars are given by the rate/$\sqrt{(N-1)}$, where N is the number of 2-s resolution data samples. The hatched region indicates the burst rate for one count per bin. There are no samples in a bin if the hatched region extends to the top of the plot. The narrow-band 100-Hz burst signals have a higher rate mainly in the B_t enhancement region. The 5.4-kHz bursts appear for both enhancements and depressions B_t.

3. Results

Using the method outlined in the previous section, we can find the dependence of burst activity on irregularities through a statistical study. We use the burst identification developed previously [*Ho et al.*, 1991] for high-resolution electric field data and determine whether or not a burst is present at each data interval (0.25 s) and whether burst activity is coincident with the irregularity structure. The lower-resolution (2 s) OETP data are interpolated when merged with the higher-resolution wave data. In addition, we calculate 2-s resolution averages of the magnetic field data, allowing direct comparison with the OETP data. We will examine the dependence of the burst rates on the relative variations in the magnetic field and electrons, as well as with the gradients.

3.1. Effects of Relative Variation on Burst Activity

We use the relative variation of B_t, n_e, and T_e to determine when the different types of burst signals occur. We refer to 100-Hz narrow-band signals as "100 Hz only." We use the 5.4-kHz signals to represent the high-frequency broadband signals, because these broadband signals have a larger amplitude relative to the background noise in the 5.4-kHz channel [*Ho et al.*, 1991, 1992].

Figure 2 shows the relationship between the burst rates in the 100-Hz channel only (solid line) and in the 5.4-kHz channel (dashed line), and the relative variation of B_t. The hatched region in the figure gives the burst rate corresponding to one burst occurring for all the data within the bin (i.e., the inverse of the time spent per bin) and is a measure of the statistical reliability of the calculated rate. There are no samples in a bin when the hatched region extends to the top of the plot. The burst rates (burst number/time spent) have been smoothed by calculating a running average of burst number and time spent separately before calculating the burst rate. Otherwise the smoothed burst rate is biased toward rates that have shorter sample times. Because of

the smoothing it is possible to have a nonzero burst rate less than the inverse sample time. We have also included error bars for the burst rate, given by standard error of the mean = mean/$\sqrt{(N-1)}$, where N is half the time spent per bin. Although the data have been interpolated to obtain burst rates, the underlying data resolution of the OETP data is 2 s, and N therefore roughly corresponds to the number of independent samples within a bin. Thus the error bar gives the 1σ confidence level for the rate. The 100-Hz-only burst signals have higher rates in regions of B_t enhancement, but with little dependence on the size of the enhancement, the falloff for high $B_t/\langle B_t\rangle$ being due to the lack of data samples. The 5.4-kHz burst activity mainly occurs in regions of smaller relative variation. In Figure 2 we used 2.0-s resolution magnetic field data for comparison with the electron data. We also have used 0.25-s resolution magnetic field data, and there is no large difference between the results obtained from the two different data resolutions.

The dependence of the burst rates for the 100-Hz channel only (solid line) and the 5.4-kHz channel (dashed line) on the relative variation of n_e is shown in Figure 3. We see that the 100-Hz-only bursts mainly appear in n_e depressions, but also there is a burst rate peak in n_e enhancements. The 5.4-kHz burst rate peaks in both enhancements and depressions, though there is more burst activity in density depressions. However, the peak in the high density has larger error bars. Although both 100-Hz and 5.4-kHz bursts tend to be detected in the regions of low electron density, the 100-Hz bursts are weakly dependent on density variations. The 100-Hz burst rate tends to be larger for both magnetic field enhancements and density depressions, as we would expect if the plasma β controlled the 100-Hz burst activity.

Figure 4 shows distributions of the burst rates in 100-Hz channel only (solid line) and in the 5.4-kHz channel (dashed line) versus the relative variation of T_e. We see that higher 5.4-kHz burst rates are associated with high T_e relative to the background. The 100-Hz-only signals are less dependent on the relative variation of T_e. The 100-Hz-only signal occurrence rates peak for both T_e enhancements and depressions, with a slightly higher but less statistically significant rate for T_e enhancements. Note that

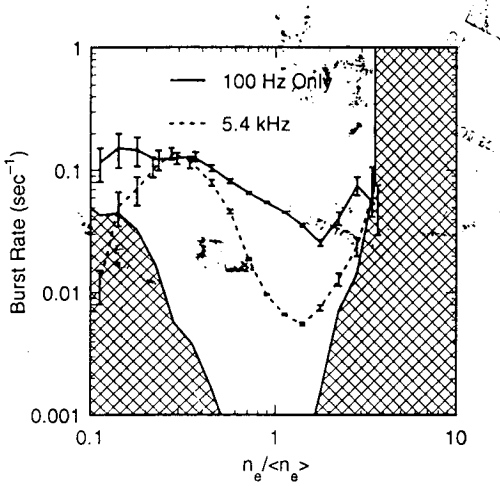

Figure 3. Variation of the burst rates of narrow-band 100-Hz signals (solid line) and 5.4-kHz signals (dashed line) versus the relative variation of n_e. Similar in format to Figure 2. The narrow-band 100-Hz burst signals have a higher rate in the n_e depressions, whereas the 5.4-kHz burst activity mainly depends on the larger variation ratio of n_e relative to its background profile, regardless of enhancement or depression in n_e.

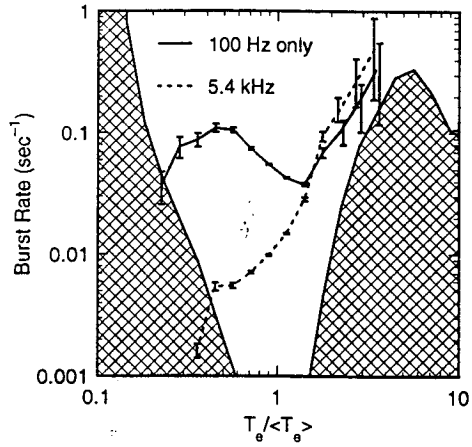

Figure 4. Relationship between the burst rates for narrow-band 100-Hz bursts (solid line) and 5.4-kHz bursts (dashed line) and the relative variation of T_e. Similar in format to Figure 2. The narrow-band 100-Hz burst signals have a slightly higher rate in the T_e enhancement region, but the 5.4-kHz burst activity only appears in the T_e enhancement regions but with large error bars.

although there are samples for the higher temperature ratios, the number is too small to be statistically significant.

Whether or not the 100-Hz narrow-band burst signals appear only inside the density depressions has been argued for several years [*Taylor et al.*, 1985, 1987; *Scarf*, 1986]. Opponents of the lightning hypothesis suggest that the density depression is a sufficient and necessary condition for burst signal appearance. All VLF signals should be associated with these density troughs. Local instabilities around the troughs are the causes of these wave signals. Supporters of the lightning hypothesis argue that lower density and stronger vertical magnetic field inside the trough may act as a wave duct to trap and guide the VLF waves as they propagate from the atmosphere to the ionosphere. However, under this hypothesis, a density depression is not a necessary condition for VLF burst existence. The present study shows that the burst signals do not always occur in the density depression regions. At least 30% of the total 100-Hz-only bursts appear in the n_e enhancement regions, although only 5% of the bursts occur for density ratios greater than 1.26.

The occurrence of bursts within density enhancements appears to indicate that the presence of a trough is not a necessary condition for 100-Hz waves, but it should be noted that our definition of enhancements and depressions is based on a running average, whereas *Taylor et al.* [1985, 1987] define troughs as a reduction in density with respect to an inferred standard density profile. A gradient in the density that is sharp in comparison with the averaging interval could give both an enhancement and a depression according to our definition. Thus the edges of troughs as defined by Taylor et al. may manifest themselves as weak enhancements in our statistics. Nevertheless, there are two mitigating factors that support our statement that a large fraction of 100-Hz bursts are not associated with density troughs. First a trough, as defined by Taylor et al., is most discernible if the density profile is relatively smooth, with the trough being an isolated signature in the profile. In that case, the running average will be a reasonably close approximation to the background profile. It can be shown that for a simple steplike reduction in density from n_1 to n_2, then $n_1/\bar{n} = 1/(1 - f(1 - g))$, and $n_2/\bar{n} = gn_1/\bar{n}$, where $\bar{n}$ is the running average of the density, $g = n_2/n_1$ (< 1), and f is the fraction of time

in the running average for which the density is reduced. If f and g are small, $n_1/\bar{n} \approx 1 + f$, while $n_2/\bar{n} \approx g$. Thus the apparent enhancement is much weaker than the associated depression. If, on the other hand, the density profile is disturbed, then it is not at all clear how one should define an ambient profile. In that circumstance, our method is as appropriate as any other. The second mitigating factor is that in section 3.2 we find that the 100-Hz bursts are not dependent on density gradients, which we would expect if the waves are associated with the edges of density troughs.

We have found some differences between the activity of the 100-Hz narrow-band burst signals and 5.4-kHz high-frequency broadband signals. Although both types of signals often occur in n_e depressions, the 5.4-kHz signals mostly appear in the enhanced T_e regions, whereas the 100-Hz signals mainly are associated with enhanced magnetic field. Thus we infer that the magnetic field variation is a stronger controlling factor for the 100-Hz-only signals. One reason for the magnetic field dependence is that strong magnetic field may enlarge the whistler resonance cone angle, which allows the wave to propagate more nearly parallel to the field. The other reason may be that both stronger magnetic field and lower electron density result in a lower-β plasma than the surrounding medium. Although we have not addressed the β dependence in this study, *Strangeway* [1992] has shown that 100-Hz bursts tends to occur in regions of low β, where the Landau damping of whistler mode waves is small. The correlation of the 5.4-kHz burst activity with enhanced T_e is also relatively important. However, we do not know the source of this correlation. In general, only highly nonlinear plasma waves, such as solitons, are thought to cause changes in the ambient magnetic field or plasma density. On the other hand, plasma waves are often associated with some form of plasma heating. Thus it is not clear which is cause and which is effect in the correlation between the 5.4-kHz waves and enhanced temperatures.

3.2. Gradient Effects on Burst Signals

In order to estimate the possibility of the 100-Hz burst signals being caused by a local source, we study the relationship between the burst signals and gradients of the magnetic field and plasma. Some authors have proposed that the low-frequency waves observed on Venus are caused by a gradient-driven ion acoustic instability [*Taylor et al.*, 1987; *Grebowsky et al.*, 1991]. A more plausible mechanism is the generation of lower hybrid waves through the gradient-driven instability [*Huba*, 1992]. The lower hybrid wave has many similarities to the whistler mode wave. Both of them are polarized perpendicular to the ambient magnetic field as the observations show [*Strangeway*, 1991, 1995]. They preferably occur in low-β plasmas due to weaker attenuation. However, the differences between them also are distinct. A whistler mode wave is an electromagnetic wave and is guided along the ambient magnetic field. A lower hybrid wave is an electrostatic wave and propagates perpendicular to the magnetic field. This wave is driven by the diamagnetic current associated with pressure gradients. *Huba* [1992] has suggested that the irregularities in the lower ionosphere may provide this gradient-driven instability for lower hybrid wave. Furthermore, very short-scale irregularities may also be a consequence of the gradient-driven instability.

In a magnetized plasma, the particle drift velocity $\mathbf{v}_d$ due to a force $\mathbf{F}$ is given by

$$\mathbf{v}_d = \frac{\mathbf{F}\times\mathbf{B}}{qB^2} \tag{2}$$

where q is particle charge. This drift provides the free energy for the lower hybrid wave.

For a force due to a pressure gradient given by a density change, we may represent the drift velocity $\mathbf{v}_{dn}$ by

$$\mathbf{v}_{dn} = \frac{k_B T_e \nabla(n_e)\times\mathbf{B}}{n_e e B^2} \tag{3}$$

If n_e takes an exponential distribution in the horizontal direction $n_e = n_{eo}\exp(s/H_n)$, where H_n is the scale length of density gradient, using the definitions of the electron thermal velocity $v_{th}^2 = k_B T_e/m_e$, and electron gyrofrequency $\Omega_e = eB/m_e$, we have

$$v_{dn} = \frac{v_{th}^2}{\Omega_e H_n} \tag{4}$$

Thus we can see that the drift velocity is proportional to the square of the electron thermal velocity but inversely proportional to the scale length of the density gradient. Ions will have a similar but oppositely directed drift for $T_e \sim T_i$.

The drift velocity associated with a magnetic field gradient is inversely proportional to the scale length of the gradient of the magnetic field:

$$v_{dB} = \frac{2v_{th}^2}{\Omega_e H_B} \tag{5}$$

As noted by *Huba* [1992], the density gradient causes bulk drift of the plasma, while the gradient drift caused by the magnetic field (5) affects the individual particle kinetics. The magnetic field gradient drift opposes the pressure gradient drift in a plasma that is in pressure balance, and the instability can be stabilized for sufficiently high magnetic field gradient drifts. Thus a study of the dependence of the burst rates on the gradients is a crucial test in determining the possible wave source.

In order to examine the dependence of burst activity on gradients, we calculate the burst occurrence rates for different magnetic field and plasma gradients. We have folded negative and positive gradients together. Figure 5 shows these occurrence rates

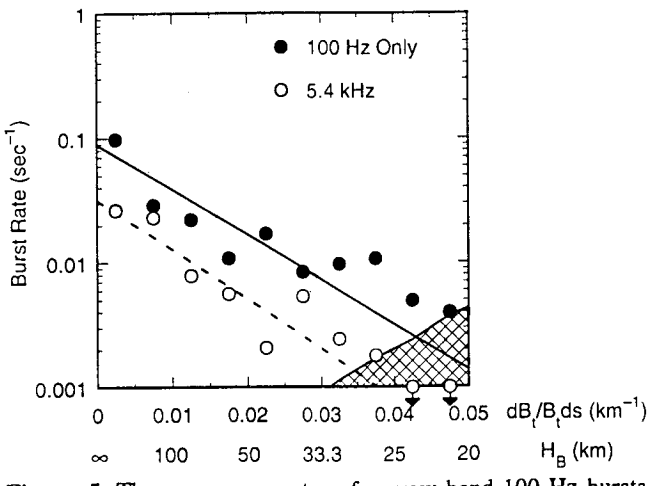

Figure 5. The occurrence rates of narrow-band 100-Hz bursts (solid circles) and 5.4-kHz bursts (open circles) as a function of the gradient of B_t. The hatched region gives the 1-count level, similarly to Figure 2. The straight lines within the plot show regression lines for 100-Hz bursts (solid line) and 5.4-kHz bursts (dashed line), determined by using a weighted least squares method. Both the 100-Hz-only and 5.4-kHz signals are mainly present for smaller gradients ($H_B > 50$ km).

Table 1. Regression Test Statistics for Burst Rate Versus Inverse Gradient Scale Length

Frequency	Gradient	Fit Type[a]	d.f. (n)[b]	Test Statistic[c]	$F_{1,n}$[d]	Slope[e]
100 Hz	B_t	$\log_{10}$	8	31.81	5.32	-36.2 ± 14.8
5.4 kHz	B_t	$\log_{10}$	6	43.85	5.99	-39.6 ± 14.6
100 Hz	n_e	linear	8	5.55	5.32	1.00 ± 0.98
5.4 kHz	n_e	linear	8	41.52	5.32	1.59 ± 0.57
100 Hz	T_e	$\log_{10}$	8	26.93	5.32	10.72 ± 4.77
5.4 kHz	T_e	linear	8	45.15	5.32	2.83 ± 0.97

[a]The regression analysis uses either $\log_{10}$(rate) or rate as the dependent parameter.
[b]Number of degrees of freedom is equal to the number of points used in the regression analysis minus 2.
[c]Ratio of the regression mean square to residual mean square (F test).
[d]Upper 5% point of the $F_{1,n}$ distribution.
[e]Range gives 95% confidence limit.

for burst signals in the 100-Hz-only channel (solid circles) and the 5.4-kHz channel (open circles), as a function of magnetic field gradient (the reciprocal of scale length). In plotting the burst rates we have not smoothed the data, unlike the data shown in previous figures, because we have performed a least squares regression analysis, as indicated by the straight lines in the figure. We also show the error bars for reference and the one burst per bin count rate. At the left side of the figure the scale length goes to infinity, while at the right the scale length H_B decreases to 20 km. We see that the burst rates for two types of signals mainly peak in the small-gradient regions and quickly decrease with increasing gradient (or decreasing scale length). For the 100-Hz-only signals, the burst rate is largest for very small gradients (H_B > 50 km). The 5.4-kHz signals have a similar distribution to the 100-Hz-only signals, with bursts occurring for small gradients, H_B > 50 km. Thus it is obvious that both types of signals are not associated with gradients of the magnetic field.

This is further emphasized on consideration of the regression lines shown in Figure 5. We have used a weighted least squares analysis [e.g., *Pollard*, 1977], since the number of samples in each bin is not uniform. The weight factors, which specify the relative weight applied to the variance of each point, are given by $N-1$, as was used in determining the error bars. Thus much greater weight is given to the points at the left of the figure. In performing the regression analysis we used the $\log_{10}$ of the burst rate, and so the two points at lower right, which correspond to zero burst rate, were not included. Table 1 gives the F test analysis for the regression lines, as well as the slope of the fit. The regression is significant for both 100-Hz and 5.4-kHz burst rates, and Figure 5 shows that the wave bursts preferentially occur when the ambient magnetic field is relatively steady. It should be noted that while we have used 2-s resolution data, a similar result is found if we use the higher-resolution magnetic field data.

Figure 6 shows the variations of burst rates in the 100-Hz channel only (solid circles) and the 5.4-kHz channel (open circles), versus the reciprocal of scale length of electron density. The larger error bars on the right of the plot reflect the very low number of data samples in the steep gradient regions, also indicated by the high 1-count burst rate. In contrast to the magnetic field gradient dependence, the average burst rates for the two types of signals increase for steeper gradients (i.e., smaller scale length, H_n < 30 km). The average 100-Hz-only signal rate gradually increases by about a factor of 2, from 0.05 per second at infinite H_n to ~0.1 per second at H_n = 25 km, although with large fluctuations. The 5.4-kHz burst rate increases by a factor of 4.

The regression analysis shows that the 5.4-kHz bursts have a greater dependence on the density gradient. As shown in Table 1, the fit for the 100-Hz rate is barely significant, whereas the 5.4-kHz fit is highly significant. Note that the rate was used as the dependent parameter in specifying the fit, rather than $\log_{10}$(rate) as used in Figure 5. The regression lines are therefore curved when plotted on a logarithmic scale. It should also be noted that only ~6% of the 100-Hz bursts occur for H_n < 50 km, as opposed to ~10% for the 5.4-kHz bursts. The fraction of bursts increases to ~19% and 34%, respectively, for H_n < 100 km.

The dependence of the burst rates on the electron temperature T_e gradient shown in Figure 7 is similar to that on the electron density n_e. The average 100-Hz burst rate (solid circles) increases gradually from 0.05 s^{-1} to 0.2 s^{-1}. The burst rate for the 5.4-kHz signals (open circles) has an obvious increase from 0.01 s^{-1} to 0.1 s^{-1} when the T_e scale length H_T < 50 km. The F test statistics are given in Table 1. In terms of percent occurrence, 11% of the 100-Hz bursts and 21% of the 5.4-kHz bursts occur for temperature gradient scales H_T < 100 km.

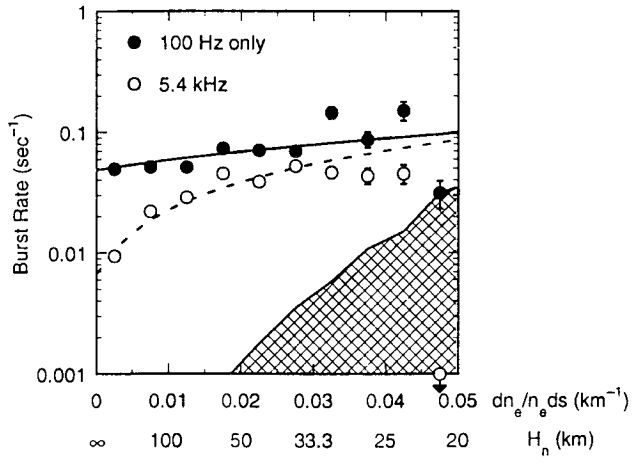

Figure 6. The occurrence rates of narrow-band 1000-Hz bursts (solid circles) and 5.4-kHz bursts (open circles) as a function of the gradient of n_e. Similar in format to Figure 5. The 100-Hz-only burst rate gradually increases for steeper gradients (H_n < 50 km), but the 5.4-kHz signal rate increase appears to be more statistically significant. Both fits use the rate rather than $\log_{10}$(rate) as the dependent parameter in the regression analysis, since this gives a more highly significant fit. The regression lines are therefore curved when plotted on a logarithmic scale.

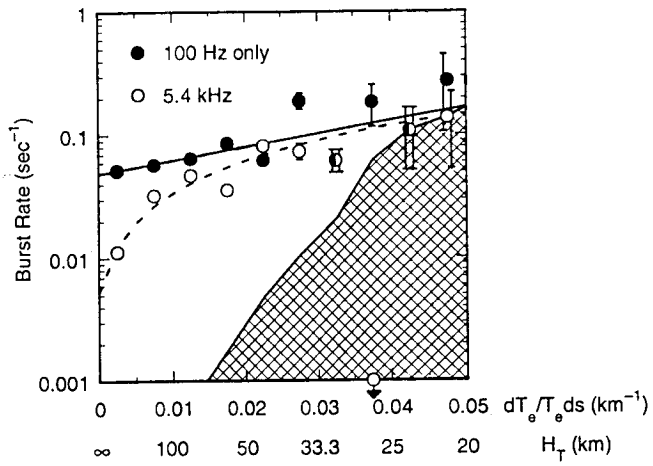

Figure 7. The dependence of the occurrence rate of narrow-band 100-Hz bursts (solid circles) and 5.4-kHz bursts (open circles) on the gradient of T_e. Similar in format to Figure 5. The dependence on temperature gradients is similar to that found for density gradients. Again, a linear fit is used for the 5.4-kHz burst rate, while the 100-Hz fit is specified by using $\log_{10}$(rate).

From the analysis presented in this section we conclude that most signals are not related to local gradients. Both the 100-Hz and 5.4-kHz waves mainly occur in regions with relatively steady magnetic fields. Although both the 100-Hz and 5.4-Hz bursts tend to increase with decreasing density and temperature gradient scale length, the 5.4-kHz bursts show the stronger dependence. Thus while a small fraction of the 100-Hz bursts appear to be associated with density or temperature gradients, most of the signals are not. They are not lower hybrid waves generated by a gradient-driven instability.

4. Discussion and Conclusions

Whether VLF burst signals are caused by the lightning or a gradient-driven instability continues to be a controversial issue. We find that there is no association of bursts with gradients of the magnetic field. Two types of signals mainly appear at large scale lengths (small gradients) in the magnetic field. The 100-Hz burst rates gradually increase with higher gradients of n_e or T_e, but the rate of increase is much less significant than that for the 5.4-kHz bursts. Roughly 95% of the bursts occur in the lower gradient (scale length $H > 50$ km) regions, although the burst rate is lower because of larger time spent in these regions. A few bursts appear in the larger gradient regions, and we do not exclude the possibility that some burst signals are related to a local plasma gradient. Finding that no wave signals are associated with the gradients of the magnetic field or plasma would be highly unexpected in such a variable ionosphere. However, since most of the narrow-band 100-Hz signals observed in the lower ionosphere cannot be generated by gradients, another source, such as atmospheric lightning, or a non-gradient-driven instability, must be involved. With regard to the 5.4-kHz burst signals, there are higher occurrence rates related to steeper temperature gradients. In addition, we find that 5.4-kHz signals mostly appear in the density depressions with higher electron temperature.

Using the data of OETP, from the anomalies of the high-resolution volt-ampere curves, *Grebowsky et al.* [1991] find many small-scale plasma irregularities in the nightside ionosphere. These structures have 0.1 to 2.0-km spatial scale sizes. This scale length in the plasma density may have Doppler-shifted frequency up to 100 Hz in a spacecraft frame moving at 10 km/s. *Huba* [1992] suggests that a lower hybrid wave generated by the gradient-driven instability may cause both electric field and density fluctuations. This short-wavelength mode is most unstable in high-field and low-density plasma regions. The density gradient scale length is a key parameter in the onset of this instability. *Huba* [1992] anticipates that a scale length less than 20 km may excite this mode. Since the largest drift velocity occurs in the steepest gradient region, we expect that the lower hybrid drift instability would be the strongest around the edge of a depression, instead of at the center of the depression. However, for most cases of the 100-Hz-only signals, the waves do not appear in the boundaries of depressions. Because they often occur in the centers of the magnetic field enhancements and density depressions, it is likely that the these structures are acting as ducts to guide the waves.

In summary, through analysis of low-altitude (<300 km) data from orbits 471–570 of the Pioneer Venus Orbiter, we find that the 100-Hz-only burst signals have higher occurrence rates in magnetic field enhancements and the density depressions. The 5.4-kHz burst activity seems to have no dependence on the variation of the magnetic field, but there is a higher rate of occurrence in electron temperature enhancements. Thus magnetic field enhancement is a key factor for 100-Hz signals. Temperature enhancements may be related to 5.4-kHz burst activity, although which is cause and effect has yet to be determined.

Both 100-Hz-only and 5.4-kHz burst signals are observed in the region of low magnetic field gradients. There is an indication that the 5.4-kHz waves occur more frequently for higher gradients of density and temperature. Although there is a gradual increase of the burst rate with increasing gradient steepness for the 100-Hz waves, this is weak. On average, we see that ~95% of the total 100-Hz-only burst signals appear in the small gradient region (scale length of <50 km). Thus most 100-Hz narrow-band signals do not appear to be generated by a local gradient-driven instability.

Acknowledgments. We wish to thank L. H. Brace and R. F. Theis for kindly providing the high-resolution Langmuir probe data. We also thank the referees for many helpful comments. This work is supported by NASA grants NAG2-485, NAG2-501, and NAGW-3497.

The editor thanks J. M. Grebowsky and three other referees for their assistance in evaluating this paper.

References

Boeck, W. L., O. H. Vaughan Jr., R. Blakeslee, B. Vonnegut, and M. Brook, Lightning-induced brightening in the airglow layer, *Geophys. Res. Lett.*, *19*, 99–102, 1992.

Brace, L. H., R. F. Theis, W. R. Hoegy, J. H. Wolfe, J. D. Mihalov, C. T. Russell, R. C. Elphic, and A. F. Nagy, The dynamic behavior of the Venus ionosphere in response to solar wind interactions, *J. Geophys. Res.*, *85*, 7663–7678, 1980.

Brace, L. H., R. F. Theis, H. G. Mayr, S. A. Curtis, and J. G. Luhmann, Holes in the nightside ionosphere of Venus, *J. Geophys. Res.*, *87*, 199–211, 1982.

Brace, L. H., R. C. Elphic, S. A. Curtis, and C. T. Russell, Wave structure in the Venus ionosphere downstream of terminator, *Geophys. Res. Lett.*, *10*, 1116–1119, 1983.

Burke, W. J., T. L. Aggson, N. C. Maynard, W. C. Hoegy, R. A. Hoffman, R. M. Candy, C. Liebrecht, and E. Rodgers, Effects of a

lightning discharge detected by the DE 2 satellite over Hurricane Debbie, *J. Geophys. Res., 97*, 6359–6367, 1992.

Grebowsky, J. M., S. A. Curtis, and L. H. Brace, Small-scale plasma irregularities in the nightside Venus ionosphere, *J. Geophys. Res., 96*, 21,347–21,359, 1991.

Ho, C. M., R. J. Strangeway, and C. T. Russell, Occurrence characteristics of VLF bursts in the nightside ionosphere of Venus, *J. Geophys. Res., 96*, 21,361–21,369, 1991.

Ho, C. M., R. J. Strangeway, and C. T. Russell, Control of VLF burst activity in the nightside ionosphere of Venus by the magnetic field orientation, *J. Geophys. Res., 97*, 11,673–11,680, 1992.

Huba, J. D., Theory of small-scale density and electric field fluctuations in the nightside Venus ionosphere, *J. Geophys. Res., 97*, 43–50, 1992.

Krehbiel, J. P., L. H. Brace, R. F. Theis, J. R. Cutler, W. H. Pinkus, and R. B. Kaplan, Pioneer Venus orbiter electron temperature probe, *IEEE Trans. Geosci. Remote Sens., GE-18*, 49–54, 1980.

Luhmann, J. G., and T. E. Cravens, Magnetic fields in the ionosphere of Venus, *Space Sci. Rev., 55*, 201–274, 1991.

Luhmann, J. G., and C. T. Russell, Magnetic fields in the ionospheric holes of Venus: Evidence for an intrinsic field?, *Geophys. Res. Lett., 10*, 409–411, 1983.

Luhmann, J. G., R. C. Elphic, C. T. Russell, J. A. Slavin, and J. D. Mihalov, Observations of large scale steady magnetic fields in the nightside Venus ionosphere and near wake, *Geophys. Res. Lett., 8*, 517–520, 1981.

Luhmann, J. G., C. T. Russell, L. H. Brace, H. A. Taylor, W. C. Knudsen, F. L. Scarf, D. S. Colburn, and A. Barnes, Pioneer Venus observations of plasma and field structure in the near wake of Venus, *J. Geophys. Res., 87*, 9205–9210, 1982.

Pollard, J. H., *A Handbook of Numerical and Statistical Techniques*, Cambridge University Press, New York, 1977.

Russell, C. T., and R. N. Singh, A re-examination of impulsive VLF signals in the night ionosphere of Venus, *Geophys. Res. Lett., 16*, 1481–1484, 1989.

Russell, C. T., R. C. Snare, J. D. Means, and R. C. Elphic, Pioneer Venus orbiter fluxgate magnetometer, *IEEE Trans. Geosci. Remote Sens., GE-18*, 32–35, 1980.

Russell, C. T., M. von Dornum, and F. L. Scarf, The altitude distribution of impulsive signals in the night ionosphere of Venus, *J. Geophys. Res., 93*, 5915–5921, 1988.

Russell, C. T., M. von Dornum, and F. L. Scarf, Source locations for impulsive electric signals seen in the night ionosphere of Venus, *Icarus, 80*, 390–415, 1989a.

Russell, C. T., M. von Dornum, and R. J. Strangeway, VLF bursts in the night ionosphere of Venus: Estimates of the Poynting flux, *Geophys. Res. Lett., 16*, 579–582, 1989b.

Scarf, F. L., Comment on "Venus nightside ionospheric troughs: Implications for evidence of lightning and volcanism" by H. A. Taylor Jr., J. M. Grebowsky, and P. A. Cloutier, *J. Geophys. Res. 91*, 4594–4598, 1986.

Scarf, F. L., and C. T. Russell, Lightning measurements from the Pioneer Venus Orbiter, *Geophys. Res. Lett., 10*, 1192–1195, 1983.

Scarf, F. L., W. W. L. Taylor, C. T. Russell, and L. H. Brace, Lightning on Venus: Orbiter detection of whistler signals, *J. Geophys. Res. 85*, 8158–8166, 1980a.

Scarf, F. L., W. W. L. Taylor, and P. F. Virobik, The Pioneer Venus orbiter plasma wave investigation. *IEEE Trans. Geosci. Remote Sensing, GE-18*, 36–38, 1980b.

Singh, R. N., and C. T. Russell, Further evidence for lightning on Venus, *Geophys. Res. Lett., 13*, 1051–1054, 1986.

Strangeway, R. J., On the polarization of VLF bursts in the night ionosphere of Venus, *J. Geophys. Res.*, 96, 22,741–22,752, 1991.

Strangeway, R. J., An assessment of lightning or in situ instabilities as a source for whistler mode waves in the night ionosphere of Venus, *J. Geophys. Res., 97*, 12,203–12,215, 1992.

Strangeway, R. J., The plasma wave evidence for lightning on Venus, *J. Atmos. Terr. Phys.*, in press, 1995.

Taylor, H. A., Jr., and P. A. Cloutier, Telemetry interference incorrectly interpreted as evidence for lightning and present-day volcanism at Venus, *Geophys. Res. Lett., 15*, 729–732, 1988.

Taylor, H. A., Jr., J. M. Grebowsky, and P. A. Cloutier, Venus nightside ionospheric troughs: Implications for evidence of lightning and volcanism, *J. Geophys. Res., 90*, 7415–7426, 1985.

Taylor, H. A., Jr., P. A. Cloutier, and Z. Zheng, Venus "lightning" signals reinterpreted as in situ plasma noise, *J. Geophys. Res., 92*, 9907–9919, 1987.

Theis, R. F., L. H. Brace, R. C. Elphic, and H. G. Mayr, New empirical models of the electron temperature and density in the Venus ionosphere with application to transterminator flow, *J. Geophys. Res., 89*, 1477–1488, 1984.

C. M. Ho, Jet Propulsion Laboratory, MS 169-506, 4800 Oak Grove Drive, Pasadena, CA 91109. (email: cho@jplsp.jpl.nasa.gov)

C. T. Russell and R. J. Strangeway, Institute of Geophysics and Planetary Physics, University of California, Los Angeles, 405 Hilgard Avenue, Los Angeles, CA 90024. (email: ctrussell@igpp.ucla.edu; strange@igpp.ucla.edu)

(Received August 23, 1993; revised December 23, 1994; accepted December 27, 1994.)

Pergamon

0273-1177(95)00219-7

Adv. Space Res. Vol. 16, No. 4, pp. (4)125–(4)136, 1995

0273-1177/95 $9.50 + 0.00

COMPARISON OF UPSTREAM PHENOMENA AT VENUS AND EARTH

R. J. Strangeway* and G. K. Crawford**

** Institute of Geophysics and Planetary Physics, University of California at Los Angeles, Los Angeles, CA 90024, U.S.A.*
*** Radio Atmospheric Science Center, Kyoto University, Uji, Kyoto 611, Japan*

ABSTRACT

The region upstream of a planetary bow shock, known as the foreshock, contains a variety of phenomena. Electrons and ions are reflected and energized at the shock. As these stream back upstream they generate both VLF and ULF waves. Studies of the terrestrial foreshock have provided most of our understanding of these phenomena. However, comparisons with other planetary foreshocks are beneficial, even though the instrumentation used to provide the data may be less sophisticated than that flown on Earth orbiting spacecraft. In particular maps of the VLF emissions upstream of the Venus bow shock, using data acquired by the Pioneer Venus Orbiter are particularly illuminating. These maps show that the tangent field line is clearly marked by the presence of plasma oscillations. Of additional interest is evidence that the emissions only extend some 15 Venus radii away from the shock, indicating that the emissions are controlled by the shock scale size. Lower frequency ion acoustic waves are observed deep in the ion foreshock. Only close to the shock do both the ion acoustic waves and ULF waves occur simultaneously. The ULF waves mark the ion foreshock boundary where ion beams should be present. The ion acoustic waves tend to be observed further downstream, where diffuse ion distributions are expected to occur. A similar mapping of the terrestrial foreshock, using data from the ISEE–3 spacecraft shows similar results for the electron foreshock. An extension of this study to include ULF and ion acoustic waves would be helpful.

INTRODUCTION

Most of our understanding of planetary foreshocks comes from studies of the terrestrial foreshock. A variety of wave phenomena occur within the foreshock. The electron foreshock is mainly characterized by electron plasma oscillations /1, 2/ that occur very close to the tangent field line, marking the upstream edge of the electron foreshock. Downstream of the tangent field line, lower frequency VLF waves, known as "down-shifted" plasma oscillations are observed /3, 4/. Further behind the tangent field-line there is a region known as the ion foreshock. In this region a variety of ULF waves are observed, as well as a variety of ion distributions /5/. Ion acoustic waves in the few kHz range are also detected in the ion foreshock /6, 7/.

As a consequence, the foreshock region upstream of a planetary bow shock (or indeed any shock) can in some sense be thought of as a large plasma physics laboratory. In this region we can explore questions concerning particle acceleration at a collisionless shock, investigating, if we wish, either electron or ion acceleration. We can measure and categorize electric field fluctuations in the VLF range, or magnetic field fluctuations in the ULF range. We can investigate beam-plasma instabilities, again either ion or electron associated instabilities, and also resonant or non-resonant. We can also explore pitch angle anisotropy driven instabilities. Such studies can be restricted to the simple linear regime, or investigated in the fully non-linear regime.

*Now at SRI International, Menlo Park, California 94025, U.S.A.

What we cannot do, however, is significantly change the scale size of the foreshock. Also, the terrestrial bow shock is large and most Earth orbiting spacecraft only sample a small region of the foreshock, relatively close to the bow shock. For these reasons, it is worthwhile to study other planetary foreshocks. In this paper we will mainly discuss observations from the Venus foreshock, using data acquired by the Pioneer Venus Orbiter (PVO). In particular we will present maps of the electron and ion foreshock, generated through several hundred passes through the foreshock. With the aid of these maps we will make some inferences concerning electron acceleration at the bow shock. We will also show that the ULF and ion acoustic emissions within the ion foreshock are not necessarily co-located, indicating that the ion acoustic waves are not generated by ion beams, but instead they may be associated with diffuse ion distributions.

The structure of the paper is as follows: First we briefly review the processes responsible for accelerating and reflecting particles at the bow shock. We then present some examples of the VLF waves observed in the Venus foreshock. In the fourth section we show maps of the Venus foreshock, and also some recently generated maps of the terrestrial foreshock. We conclude with a summary of our results.

PARTICLE ACCELERATION AT A BOW SHOCK

Planetary foreshocks are often distinguished by the presence of both VLF and ULF waves. The foreshock boundary is given by the field line that is tangent to the bow shock. Thus the bow shock must be the principal source of the energetic particles responsible for the waves. A note may be in order here concerning the role of magnetosheath leakage. The presence of both VLF and ULF waves in the foreshock of Venus, where there is no magnetosphere acting as a source for leakage particles, suggests that shock acceleration and reflection of particles is necessary in order to populate the foreshock region. We will therefore briefly review some of the processes involved in energizing and reflecting particles at a bow shock.

In many ways, the energization of electrons is more readily understood than ion reflection, primarily because under most circumstances the electrons can be treated as magnetized. Thus, they preserve their magnetic moment. Under these circumstances, electron reflection at the shock is best elucidated through transformation into the de Hoffman-Teller /8/ (HT) frame. In this frame the incoming solar wind flow is aligned along the magnetic field, and there is no $\mathbf{v} \times \mathbf{B}$ electric field. Thus the only forces acting on a particle are the cross-shock electric field and the magnetic mirror forces. For an electron which is reflected by the shock there is consequently no net gain of energy in the HT frame.

The de Hoffman-Teller velocity in the observer's frame (which is assumed to be at rest with respect to the shock surface) is given by

$$\mathbf{v}_{HT} = \frac{\mathbf{n} \times (\mathbf{v}_0 \times \mathbf{b})}{\mathbf{b} \cdot \mathbf{n}} = \mathbf{v}_0 - \mathbf{b} \frac{\cos \theta_{vn}}{\cos \theta_{bn}} v_0 \tag{1}$$

where $\mathbf{n}$ is the shock normal, $\mathbf{v}_0$ is the solar wind velocity in the observer's frame, $\mathbf{b}$ is the unit vector along the magnetic field, θ_{vn} is the angle between the solar wind velocity vector and the shock normal, and θ_{bn} is the angle between the magnetic field and the shock normal /9/. Taking primed vectors to be measured in the HT frame, the transformation from shock frame to HT frame is given by $\mathbf{v}' = \mathbf{v} - \mathbf{v}_{HT}$.

While there is no net energy gain in the HT frame, there is a gain of energy in the shock rest frame. The solar wind "sees" a magnetic mirror moving with a velocity $v_0' = v_0 \cos \theta_{vn} / \cos \theta_{bn}$. Particles are therefore reflected from this mirror with a velocity given by twice the mirror velocity. This reflection by a single moving magnetic mirror has been named "Fast Fermi" acceleration /10/. The velocity of the mirror becomes arbitrarily large as $\theta_{bn} \rightarrow 90°$, implying that electrons could gain relativistic energies at a nearly perpendicular shock. However, the magnetic mirror only reflects particles with sufficiently high pitch angle, outside of the transmission cone (or hyperbola when the cross-shock electric field is taken into account). As the HT velocity increases, more and more of the incident solar wind electron population lies within the transmission cone, and the mirror efficiency $\rightarrow 0$ as $\theta_{bn} \rightarrow 90°$ /9/.

This basic concept of electron acceleration was extended /11/ to include the effects of shock curvature. Shock curvature entered primarily through the variation of the reflected particle energy as a function of θ_{bn} and θ_{vn}. In addition, time-of-flight effects /1/ were incorporated into the model, as well as shadowing of the time-of-flight trajectories by the bow shock itself. The net effect was to produce ring-beam-like distributions, time-of-flight resulting in a cut-off at lower parallel velocities, while the Fast Fermi acceleration gave a hole at lower pitch angles. On integration over perpendicular velocity this resulted in a bump-on-tail distribution, which could generate plasma waves.

Implicit in the HT frame transformation is the assumption that the shock can be treated as planar. It should be noted, however, that in the shock frame there is a motional electric field given by $-\mathbf{v}_0 \times \mathbf{B}$, and it is this field that provides the free energy for acceleration of the electrons. As such, then, the electrons must undergo shock-drift acceleration /12, 13/ in order to gain energy, performing magnetic field gradient drifts along the shock surface. Shock-drift acceleration is usually invoked when considering ion acceleration. The ion Larmor radius is much larger than for electrons, and the assumption of a planar shock is more easily violated by ions. Moreover, the HT frame is less useful for analyzing ion motion since ions are unmagnetized in the shock, and so their trajectories in the shock cannot be studied under the assumption of magnetic moment conservation. Shock-drift acceleration theory follows the exact particle trajectory, and the assumption of adiabaticity is not required. Fast Fermi acceleration can be considered to be shock-drift acceleration, but the reverse need not follow /13/, since the assumptions for Fast Fermi acceleration are more stringent. For sufficiently small radius of curvature shocks, the planar assumption may be invalid, even for electrons.

Bow shock curvature will affect the Fast Fermi process in two ways. First, near the point of tangency, where $\theta_{bn} \rightarrow 90^\circ$, the area of the shock over which reflection occurs becomes vanishingly small. The net flux of reflected particles must also vanish. Second, as noted above, the particles gain energy through gradient drift along the motional electric field. For a solar wind velocity of 400 kms^{-1}, and an upstream magnetic field strength of 10 nT, the motional electric field is $\approx$ 4 mV/m. In drifting along this electric field in the shock ramp, the particle gains ~ 25 keV/R_e. At the Earth, the bow shock the radius of curvature is of the order 20 R_e, and so electrons should be accelerated to high energies before curvature effects become important. At Venus, on the other hand, the shock radius of curvature is $\approx$ 2 R_v (1 R_v = 6052 km, 1 R_e = 6371 km). Shock curvature is consequently more likely to limit the energy gain. Curvature effects are likely to be even more significant at smaller shocks, such as at Mars. As we shall discuss later, there is evidence in the VLF data suggesting that shock curvature limits the electron energy gain at the Venus bow shock.

Ions can also gain energy at a bow shock, through shock-drift acceleration /12, 13/. On the other hand, ions may be reflected without performing any drift along the solar wind electric field, simply undergoing specular reflection /14/. In general it appears that ions perform both shock-drift acceleration, gaining energy in the shock rest frame, and also specular reflection, which requires non-conservation of magnetic moment /5/. These processes result in beam-like distributions of ions, occurring near $\theta_{bn} \approx 45^\circ$. Further downstream, ions are thought to undergo first-order Fermi (or diffusive) acceleration /12, 15/, where particles scatter off wave turbulence upstream and downstream of the bow shock, or even the shock itself. The change in solar wind flow speed across the shock gives the relative velocity between the upstream and downstream wave turbulence.

At present there are two schools of thought concerning the sources and evolution of ions in the foreshock. The first /5/ is that the field-aligned beams generated through specular reflection and/or shock-drift acceleration are unstable to waves which cause the beams to form partially filled rings in phase space, known as intermediate distributions. These distributions then undergo further instability to form complete rings, known as diffuse distributions. The second /15/ is that the diffuse distributions are not directly related to the field-aligned beams and intermediate distributions, but arise from the diffusive acceleration occurring in association with the quasi-parallel shock. Although presented here as completely independent mechanisms, there are points in common. The ULF waves generated by the field-aligned beams may evolve into the turbulence required for first-order Fermi acceleration. Furthermore, the intermediate distributions may form a seed plasma population that is subsequently accelerated through Fermi acceleration.

In this paper we are primarily interested in comparing VLF wave phenomena at the Earth and Venus. We will therefore not specifically discuss the role ULF waves play in modifying the ion foreshock distributions. The brief discussion above shows that the ion foreshock is much more complicated than the electron foreshock. However, we will show that the VLF waves may provide some information, albeit indirect, concerning the nature of the ion distributions in the foreshock.

VLF EMISSIONS IN PLANETARY FORESHOCKS: VENUS DATA

Wave emissions in planetary foreshocks can be best understood if the wave data are analyzed using the foreshock geometry shown in Figure 1 (after /16, 17/). Figure 1 applies to the Venus foreshock, but similar geometries apply to all planetary foreshocks. The figure shows the Interplanetary Magnetic Field (IMF), solar wind, bow shock, and PVO (the observing spacecraft) in aberrated Venus Solar Orbital (VSO) coordinates. VSO coordinates are analogous to Geocentric Solar Ecliptic coordinates. The plane containing the IMF and solar wind is known as the B-v plane, and in Figure 1 we have assumed that both the observing spacecraft and the center of the planet lie in this plane. We refer to the B-v plane that passes through the center of the planet as the equatorial plane. In general the observing spacecraft is not in the equatorial plane, but is in a B-v plane parallel to this. In that case the geometry is still as shown in Figure 1, except that the point of tangency occurs further downstream on the shock, and the shock shape as drawn corresponds to the section of the shock in the B-v plane containing the observing spacecraft.

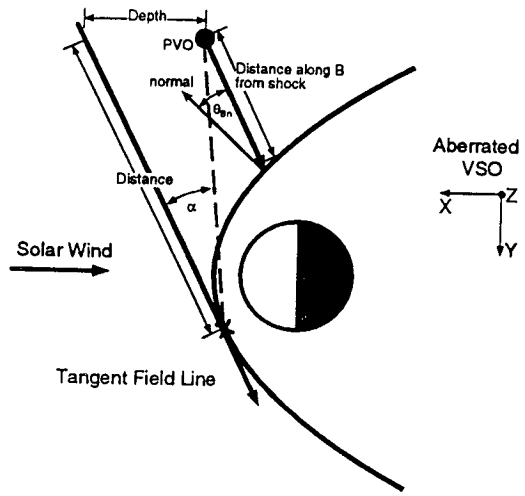

Fig. 1. Foreshock coordinate system at Venus (after /16, 17/).

When considering particle trajectories in the foreshock, the two principal factors are the velocity along the magnetic field, and the convection imposed by the solar wind. Thus we consider distance along and depth behind the tangent field line, as drawn in the figure, to be fundamental parameters. This was first pointed out in discussions of terrestrial observations /1, 18/. An alternative choice of coordinates would be the time-of-flight angle (α), and the distance along the time-of-flight trajectory. This coordinate system was used in studies of the foreshock at Mars /19, 20/. In addition to the depth and distance, other parameters of interest are the shock normal direction with respect to the IMF (θ_{bn}) at the point where the field line passing through the spacecraft intersects the bow shock, and the distance from the spacecraft to the shock along this field line. As drawn in Figure 1 the shock normal lies in the B-v plane, but this is not generally the case.

To show how the wave emissions in the foreshock are related to foreshock geometry, we plot data acquired by PVO in Figure 2 /16, 17/. Throughout the time interval shown (1 hr 45 min) the spacecraft was in the solar wind some 5 R_v behind the terminator and about 7 R_v from the Venus-Sun line. The top four traces in the figure give the wave electric field intensity measured at 30 kHz, 5.4 kHz, 730 Hz and 100 Hz. These are the four wave channels of the Pioneer Venus Orbiter Electric Field Detector (OEFD). The OEFD was restricted to these four channels because of power, weight, and telemetry constraints

/21/. However, within the solar wind the instrument was capable of observing plasma oscillations in the 30 kHz channel, whistler-mode waves in the 100 Hz channel, and Doppler-shifted ion acoustic waves at 5.4 kHz and 730 Hz /22/. The OEFD antenna is very short, 0.76 m effective length, and so is susceptible to interference. This is especially the case when the spacecraft is in the solar wind, where the Debye length is large (~ 7 m), and the spacecraft is emitting photo-electrons. The 100 Hz channel is usually the noisiest, but we have applied a noise reduction scheme based on Bayesian statistical methods /23/ to the data. The middle four panels of Figure 2 show the magnetic field in VSO coordinates. The bottom two panels show the instantaneous depth behind the tangent field line, and the θ_{bn} of the field line connecting the spacecraft to the shock.

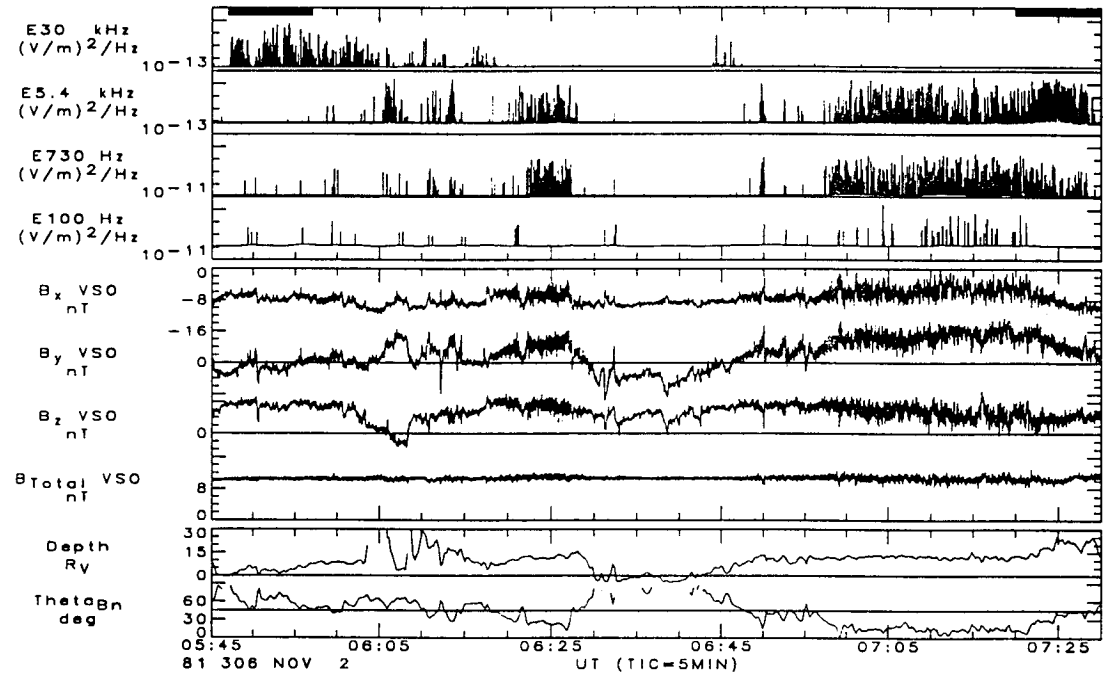

Fig. 2. Example of VLF emissions observed in the foreshock at Venus (after /16, 17/).

In Figure 2 plasma waves are mainly observed in the 30 kHz channel from 0545 to 0605 UT. We have defined depth as positive for locations behind the tangent field line, and during this time depth is small and positive, while θ_{bn} is > 45°. This indicates that the spacecraft is in the electron foreshock. Around 0605 UT there is a rotation in the IMF, and the spacecraft is now further behind the tangent field line. At 0625 UT the spacecraft is in the ion foreshock, since θ_{bn} < 45°. We find that most of the wave activity occurs in the 5.4 kHz and 730 Hz channel, with little or no activity at 30 kHz. These waves are probably Doppler-shifted ion acoustic waves. At the same time, the magnetic field shows considerable variability, indicative of ULF waves. Just prior to 0630 UT the IMF again rotates, but this time so as to place the spacecraft upstream of the tangent field line. When the spacecraft is upstream of the tangent line, depth is negative, and θ_{bn} is not defined. At 0645 UT the IMF changes direction again, and the electron foreshock briefly sweeps over the spacecraft, giving a burst of 30 kHz noise. After 0650 UT until the end of the plot the spacecraft is deep within the ion foreshock, upstream of the quasi-parallel bow shock, and the spacecraft observes intense ion acoustic and ULF waves.

To further assist the mode identification, we have investigated the wave polarization for the 30 kHz waves for the 10 minute interval indicated by the thick horizontal bar to the left of Figure 2, and for the 5.4 kHz emissions for the 10 minute interval indicated by the bar to the right of Figure 2 (after /16, 17/). Figure 3 shows the foreshock geometry (a) and polarization plot (b) for the 30 kHz emissions. In a) we show the equatorial cross-section of the bow shock, as indicated by the dashed curve, together with cross-section of the bow shock in the B-v plane containing the spacecraft, as indicated by the solid curve.

The long straight line which is tangent to the bow shock is the tangent field line. The line parallel to this is the field line passing through the spacecraft. The spacecraft location is indicated by the small dot on this line. As already discussed, at this time (0547:30 UT) the spacecraft is just behind the tangent field line, in the electron foreshock. However, the figure shows that the actual shock intersection point is well behind the terminator. In b) we have plotted the logarithm of the wave intensity as a function of antenna phase with respect to the instantaneous magnetic field, as indicated by the plus symbols. The wave intensity has been scaled so that the maximum intensity observed in the 10 minute interval is given by the radius of the circle, with the minimum corresponding to the center. The actual range in intensities is given in the figure. The almost horizontal line shows the direction of maximum variance through the data points, and we assume that this corresponds to the wave electric field direction. The wave is polarized parallel to the magnetic field, as we expect for plasma oscillations.

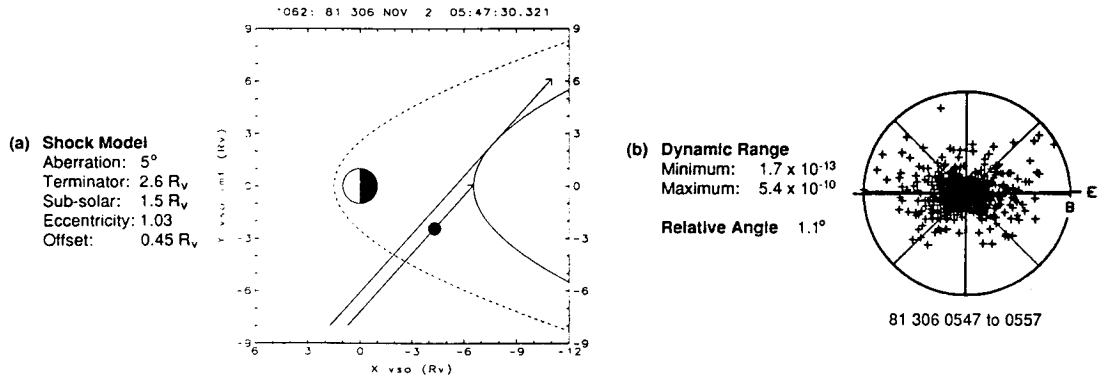

Fig. 3. a) Foreshock geometry and b) 30 kHz polarization plot for waves observed in the electron foreshock (after /17/).

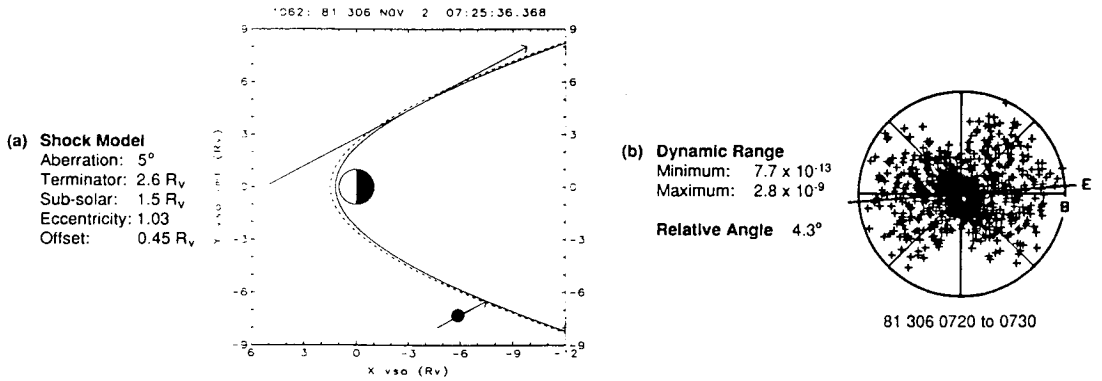

Fig. 4. a) Foreshock geometry and b) 5.4 kHz polarization plot for waves observed in the ion foreshock (after /17/).

In Figure 4 we have performed the same analysis for the 5.4 kHz waves observed towards the end of the interval plotted in Figure 2. The geometry appears to be very different from that shown in Figure 3, but the major change is simply a rotation of the B-v plane, so that the spacecraft now lies in the equatorial plane. Because of this rotation the spacecraft is deep in the foreshock, upstream and close to the quasi-parallel shock. The polarization plot is similar in format to Figure 3. There is more scatter in the data points, but again the wave appears to be polarized parallel to the ambient magnetic field. This sense of polarization is in accord with some terrestrial studies /6/, although others /7/ find that the ion acoustic waves are obliquely polarized, typically about 40° away from parallel. These apparent differences have yet to be reconciled. However, the techniques involved in determining the wave polarization are different. At Venus /16, 17/, and for the earlier terrestrial studies /6/, the polarization is determined through the antenna spin phase at which maxima occur in the wave intensity. The later terrestrial studies /7/ used interference patterns on the long ISEE–1 antenna.

Within the terrestrial ion foreshock the interference pattern of the ion acoustic waves was only observed in wideband spectra obtained with the longer ISEE–1 antenna (215 m), but was absent from the wideband spectra obtained with the ISEE–2 antenna (30 m). Thus the wavelength of the waves is > 30 m, but < 215 m /7/. This conclusion is supported by observations that the wave power spectra are of lower intensity when measured with the 215 m antenna, in comparison to the 30 m antenna /6/. Interestingly, an additional comparison using data from both PVO and the AMPTE/CCE spacecraft revealed wave power levels comparable to the short ISEE–1 antenna power /17/, even though both the PVO and AMPTE/CCE antennas were only 0.76 m effective length. This supports the conclusion that the wavelength of the ion acoustic waves is a few Debye lengths. As noted above, in the solar wind the Debye length (λ_d) ≈ 7 m, and so $k\lambda_d \approx 1.5$, where k is the wave vector ≈ $2\pi/30$.

VLF EMISSIONS AT PLANETARY FORESHOCKS: MAPPINGS

Even though the PVO plasma wave instrument has relatively poor frequency resolution, there are advantages in studying VLF data at Venus. The PVO orbit (period ≈ 24 hr) was much larger than the Venus obstacle, with apoapsis around 12 R_v. Because of this, the spacecraft spent large amounts of time in the solar wind, both upstream of the sub-solar bow shock, and also downstream, near the flanks. The PVO spacecraft was in orbit around Venus for 14 years, and it is possible to carry out large statistical studies. One study /24/, which used data from some 200 orbits (~ one Venus year), showed the usefulness of mapping the foreshock with VLF wave data. This was followed by a more extensive study /16/, using data from a separate 650 orbits. The studies were statistically independent, but had similar results. Some results of the more extensive study are given in Figure 5.

In order to create the maps shown in Figure 5 the data have been restricted to IMF orientations within ± 10° of the nominal Parker spiral angle, which is 35° at Venus. The method used to create the maps /16, 24/ requires that the depth and distance with respect to the point of tangency (Figure 1) of each sample in the data set be computed using the instantaneous IMF. The depth and distance are then converted back to Cartesian coordinates with origin at the point of tangency using the nominal (35°) IMF orientation, rather than the instantaneous direction, so as to prevent "smearing" of the tangent field line. Finally all the data, which come from different B-v planes, are mapped to the equatorial plane, using the point of tangency as the reference point. The data are then accumulated in 1 × 1 R_v bins. Although this mapping mixes subsolar (equatorial) and flank intersections, this does not drastically alter the statistical results /16/.

When determining the depth and distance we not only use the instantaneous IMF, but also use a bow shock whose size has been scaled to the observed shock crossings for each orbit. The shock model is a conic of revolution given by

$$R = \frac{L}{1 + \varepsilon \cos \theta_{sz}} \tag{2}$$

where R is radial distance from the focus, L is the semi latus rectum, ε is the eccentricity, and θ_{sz} is the solar zenith angle with respect to the focus. In modifying the bow shock it is preferable to change L, and keep ε and the focus fixed /25/. This is because the size of the shock close to the planet is specified by L, and it is this size that changes in response to changes in the solar wind. The focus is determined mainly by the obstacle itself, while ε specifies the shape. We have used $\varepsilon = 1.03$, and the focus at 0.45 R_v sunward of the planet /26/ to specify the shock in (2).

The panel at the top left of Figure 5 shows the 9th decile of 30 kHz wave intensity, with the color scale giving the $\log_{10}$ of the wave intensity. The data were accumulated in 1 × 1 R_v bins, but we have interpolated the data in generating the maps. The small black dot is the point of tangency. At the bottom left of the figure we show the data coverage, and throughout most of the distribution we have over 100 samples per bin. We have superimposed the reference shock model on this plot, given by L = 1.69 R_v /17, 27/. It is clear from Figure 5 that the most intense of the 30 kHz emissions lie on the tangent field line, but these emissions only reach a maximum a few R_v away from the point of tangency. More importantly, however, there is a marked decrease in wave intensity some 15 R_v upstream of the point of tangency. We shall return to this point when we discuss terrestrial results.

Besides data from the electron foreshock, Figure 5 shows data from the ion foreshock, as shown in the two right hand panels. The panel at top right shows data from the 5.4 kHz channel, while the panel at bottom right shows the standard deviation of the trace of the magnetic field, using 24 s intervals. This deviation is used as a proxy for the presence of ULF waves. The reference bow shock is super-imposed on both these panels, together with the tangent field line, and a model of the ULF foreshock boundary. The ULF foreshock boundary was determined from terrestrial studies /28/, but modified for the nominal Parker spiral at Venus /17/. As noted above, ion acoustic waves are detected in the 5.4 kHz channel, and Figure 5 shows that the most intense ion acoustic waves occur close to the bow shock, extending out into the ion foreshock. However, the 5.4 kHz waves appear to be confined to locations well downstream of the ULF foreshock boundary. By way of contrast, the model ULF foreshock boundary does appear to mark the upstream extent of the ULF waves. Figure 5 therefore implies that the apparent association of ion acoustic and ULF waves, seen in Figure 2, may be suspect. Both emissions may only be present at the same time when the spacecraft is close to the shock, which is the case for the data in Figure 2, as indicated in the foreshock geometry shown in Figure 4. Also the VLF waves do not appear to be observed in the region close to the ULF foreshock were ion beams are expected to occur. However, it is not clear that the results shown in Figure 5, at Venus, apply to the ion foreshock at the Earth. The smaller shock size at Venus will tend to reduce the Fermi and shock-drift acceleration. Additionally, there is no magnetosphere at Venus, and so there is no reservoir of energetic particles that can leak upstream. Consequently similar mappings of the terrestrial foreshock would be beneficial in determining those features that are specific to Venus, and those which are generally applicable to planetary foreshocks.

Most of the plasma wave data from the terrestrial foreshock were acquired by the ISEE–1 and –2 spacecraft. Unfortunately these spacecraft tended to sample mainly the sub-solar bow shock and foreshock. The ISEE–3 spacecraft, however, did pass through the foreshock sufficiently far from the Earth to permit maps of the VLF emissions to be generated. These passes occurred during the interval in which ISEE–3 was making deep tail passes prior to being sent on an encounter trajectory to Comet Giacobini-Zinner. Results of the foreshock mappings are shown in Figure 6 /29/. The panel at upper left of Figure 6 shows the number of samples on a logarithmic scale. The samples are taken from two passes through the foreshock, one from September 25 to October 1, 1983, the second from December 22 to 27, 1983. In generating the data base, 360 s averages of the magnetic field (from the Jet Propulsion Laboratory magnetometer) are used to determine the foreshock geometry, with the peak intensity per 360 s sample for each channel of the wave instrument being used to characterize the wave emission spectra. Because of the relative paucity of the data, no restriction on the orientation of the IMF is applied to the data, but the maps are drawn using the nominal terrestrial Parker spiral angle (45°). In addition, while the bins in the maps are spaced at 10 R_e intervals, the data are accumulated over 20×20 R_e bins, centered on each 10 R_e grid point.

Unlike the PVO instrument, the ISEE-3 wave instrument has relatively high frequency resolution, with four channels per decade of frequency. The channels of interest for this discussion are the 10-, 17-, 31-, and 56-kHz channels. With this frequency resolution, it is possible to use the observed solar wind density (from the Los Alamos National Laboratory electron detector) to determine the local electron plasma frequency and so make a virtual wave detector, with frequencies related to the electron plasma frequency. This is done by assigning the wave amplitude in the channel whose center frequency lies closest to the plasma frequency (on a log scale) to the "f_{pe}-channel". Wave amplitudes from adjacent channels are assigned to the sub- and super-f_{pe}-channels. The foreshock maps for these virtual channels are shown in Figure 6.

The f_{pe}-channel is shown at the lower left of Figure 6, with the color scale indicating the $\log_{10}$ of the wave amplitude in V/m. The area covered is much lower than in the coverage map, but this is because the 9th decile is not well determined for less than 10 samples. Although less well sampled, there are remarkable similarities between the foreshock maps at the lower left of Figure 6 and the upper left of Figure 5. First, the most intense plasma frequency emissions occur on the tangent field line. Second, the wave intensity peaks some distance away from the point of tangency. Third, the wave emissions upstream of the terrestrial bow shock do not appear to show any decrease up to the edge of the map, extending for distances that are several times the bow shock scale size. Although there is an order of magnitude difference in the absolute scales, the two maps look very similar as drawn, scaled relative to

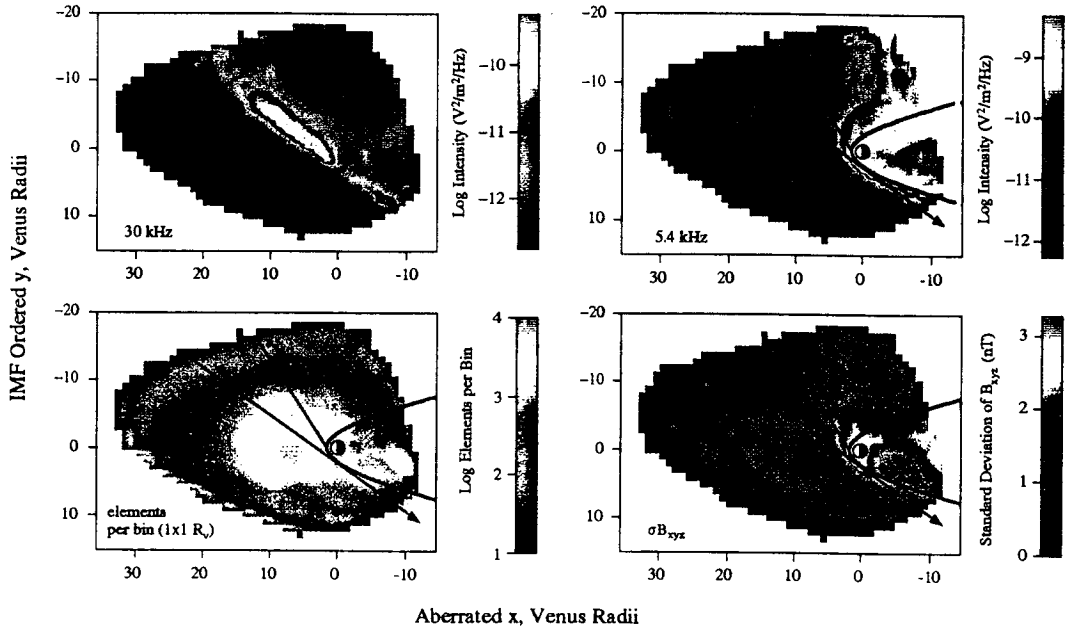

Fig. 5. VLF map of the Venus foreshock for nominal Parker spiral (after /16/).

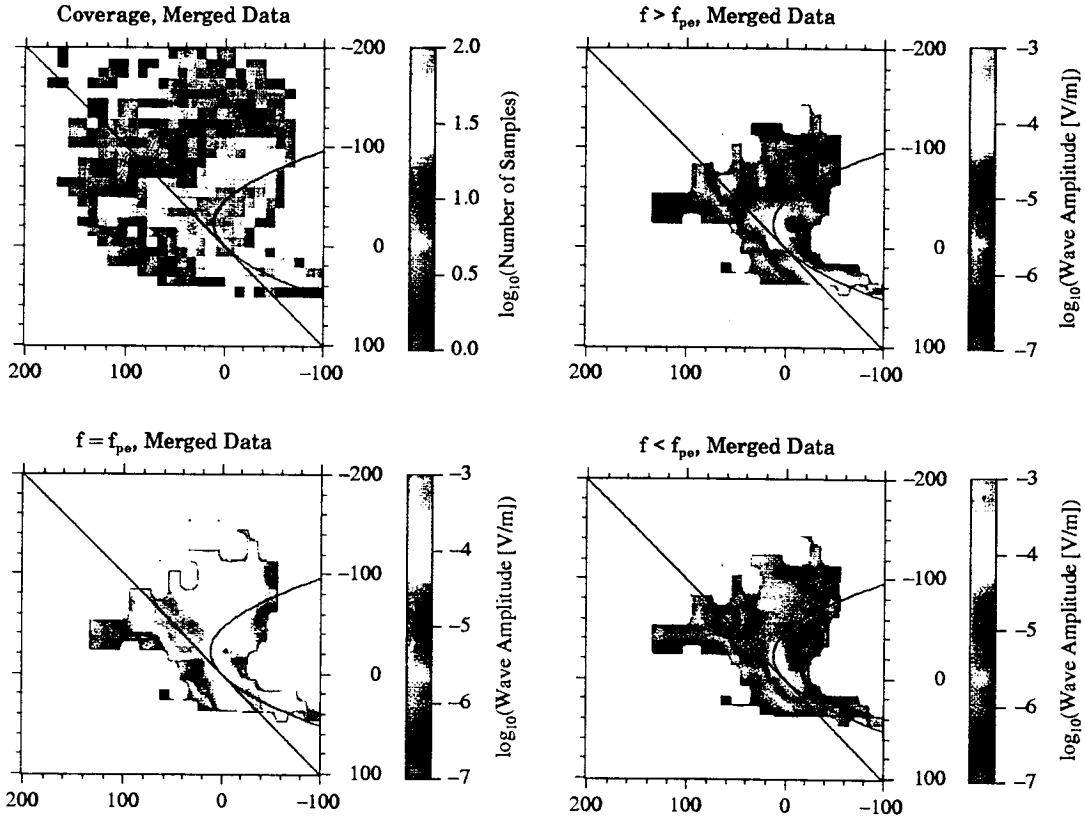

Fig. 6. VLF map of the terrestrial foreshock, using ISEE–3 data (courtesy E. W. Greenstadt /29/).

the bow shock. Thus the drop-off in wave intensity found for the Venus foreshock indicates that the wave emissions are controlled by the bow shock scale size, rather than by some property of the plasma instability itself. In the absence of other geometrical effects, it is usually expected that the spatial extent of the waves is controlled through growth and saturation scales that would be more likely to depend on ambient plasma parameters (e.g., convective growth scales). Since the solar wind at the Earth and Venus are very similar, such scales are comparable. That the cut-off in electron foreshock emissions is controlled by the bow shock scale size is consistent with shock curvature limits to the effectiveness of Fast Fermi acceleration as discussed earlier.

The panels at the right of Figure 6 show the wave amplitudes for the two virtual channels adjacent to the plasma frequency. The super-f_{pe}-channel, at upper right, shows wave emissions at the bow shock, as one might expect because of the enhanced wave noise at the shock. The sub-f_{pe}-channel, at lower right shows some emissions at the shock, but also additional wave noise downstream of the tangent field line. These emissions are much weaker than the plasma frequency emissions. We attribute the sub-f_{pe} emissions to "down-shifted" plasma oscillations /3, 4/. The "down-shifted" plasma oscillations typically have amplitudes of the order 100 μV/m, while the plasma oscillations at the tangent field line have amplitudes of a few mV/m /3/, which is consistent with the relative amplitudes shown in Figure 6.

The relative weakness of the down-shifted plasma oscillations also indicates why the PVO maps show no evidence of these waves. The background colors in Figure 5 correspond to the ambient noise level of the PVO instrument. At 30 kHz (the channel most likely to detect down-shifted plasma oscillations) this level corresponds to ~ 5×10^{-13} $V^2/m^2/Hz$. The peak intensity of the plasma oscillations at the tangent field line is ~ 5×10^{-10} $V^2/m^2/Hz$. Since the down-shifted plasma oscillations are at least an order of magnitude lower in amplitude than the plasma oscillations at the tangent field line, the down-shifted plasma oscillations are close to the PVO instrument background. The Galileo spacecraft flew by Venus in 1990, and the more sensitive plasma wave instrument on this spacecraft detected down-shifted plasma oscillations. The frequency of the emissions depended on depth in a manner very similar to the terrestrial observations /30/.

SUMMARY AND CONCLUSIONS

Particles are reflected and energized at a planetary bow shock, flowing upstream to form a region known as the foreshock. The energization processes include "Fast Fermi" (or electron shock-drift) acceleration for the electrons, shock-drift acceleration and specular reflection for the ion beams, and first order Fermi acceleration as a source of diffuse energetic ions upstream of the quasi-parallel shock. These foreshock distributions generate a variety of VLF and ULF waves.

The electrons generate plasma oscillations on the tangent field line, while further downstream they cause "down-shifted" plasma oscillations. Maps of the plasma frequency emission indicate that there is a finite extent to the tangent field line emissions. We have interpreted this as indicating that the shock scale size controls the energization process. The larger the radius of curvature of the shock, the further along the tangent field line we expect the emissions to occur. This may have implications for foreshock emissions at the outer planets (including Mars), where a variety of shock scale sizes are found, and even for interplanetary shocks, which are much more planar.

The ion foreshock is quite complicated. The maps of the ion foreshock at Venus suggest that the ion acoustic waves are generated some distance downstream of the ion foreshock boundary. The VLF waves appear to be confined to that region where one might expect to find diffuse ion distributions. Previously /31/, ion beam instabilities have been invoked to explain the VLF waves, but this implies that the waves should occur near the ion foreshock boundary where the ion beams occur. Unfortunately the solar wind instrument on board PVO was not designed to provide detailed ion distribution function data, and so we cannot perform direct comparisons between the waves and the ions. Also, the results shown in Figure 5 may only apply to Venus, and extensions of the study shown in Figure 6 to include both ion acoustic and ULF waves would be particularly beneficial. If similar results were to be found for the Earth, then there is the additional implication that the ion acoustic waves are tracers for diffuse distributions, as opposed to ion beam distributions. This inference is highly speculative, and further study is clearly required.

ACKNOWLEDGMENTS

We wish to thank E. W. Greenstadt for kindly allowing us to present the results of his terrestrial foreshock mapping study prior to publication. This work was supported by NASA grants NAG2–485 and NAGW–3497.

REFERENCES

1. Filbert, P. C., and P. J. Kellogg, Electrostatic noise at the plasma frequency beyond the Earth's bow shock, *J. Geophys. Res.* 84, 1369 (1979).

2. Klimas, A. J., The electron foreshock, in *Collisionless Shocks in the Heliosphere: Reviews of Current Research* (eds. B. T. Tsurutani, and R. G. Stone), pp. 237–252, Geophysical Monograph 35, American Geophysical Union, Washington, 1985.

3. Etcheto, J., and M. Faucheux, Detailed study of electron plasma waves upstream of the Earth's bow shock, *J. Geophys. Res.* 89, 6631–6653 (1984).

4. Fuselier, S. A., D. A. Gurnett, and R. J. Fitzenreiter, The downshift of electron plasma oscillations in the electron foreshock region, *J. Geophys. Res.* 90, 3935–3946 (1985).

5. Thomsen, M. F., Upstream suprathermal ions, in *Collisionless Shocks in the Heliosphere: Reviews of Current Research* (eds. B. T. Tsurutani, and R. G. Stone), pp. 253–270, Geophysical Monograph 35, American Geophysical Union, Washington, 1985.

6. Anderson, R. R., G. K. Parks, T. E. Eastman, D. A. Gurnett, and L. A. Frank, Plasma waves associated with energetic particles streaming upstream into the solar wind from the Earth's bow shock, *J. Geophys. Res.* 86, 4493–4510 (1981).

7. Fuselier, S,. A., and D. A. Gurnett, Short wavelength ion waves upstream of the Earth's bow shock, *J. Geophys. Res.* 89, 91–103 (1984).

8. de Hoffman, F., and E. Teller, Magneto-hydrodynamic shock, *Phys. Rev.* 80, 692 (1950).

9. Leroy, M. M. and A. Mangeney, A theory of energization of solar wind electrons by the Earth's bow shock, *Annales Geophysicae* 2, 449–456 (1984).

10. Wu, C. S., A fast Fermi process: Energetic electrons accelerated by a nearly perpendicular bow shock, *J. Geophys. Res.* 89, 8857–8862 (1984).

11. Fitzenreiter, R. J., J. D. Scudder, and A. J. Klimas, Three-dimensional analytical model for the spatial variation of the foreshock electron distribution function: Systematics and comparisons with ISEE observations, *J. Geophys. Res.* 95, 4155–4173 (1990).

12. Forman, M. A., and G. M. Webb, Acceleration of energetic particles, in *Collisionless Shocks in the Heliosphere: A Tutorial Review* (eds. R. G. Stone, and B. T. Tsurutani), pp. 91–114, Geophysical Monograph 34, American Geophysical Union, Washington, 1985.

13. Armstrong, T. P., M. A. Pesses, and R. B. Decker, Shock drift acceleration, in *Collisionless Shocks in the Heliosphere: Reviews of Current Research* (eds. B. T. Tsurutani, and R. G. Stone), pp. 271–285, Geophysical Monograph 35, American Geophysical Union, Washington, 1985.

14. Gosling, J. T., and A. E. Robson, Ion reflection, gyration, and dissipation at supercritical shocks, in *Collisionless Shocks in the Heliosphere: Reviews of Current Research* (eds. B. T. Tsurutani, and R. G. Stone), pp. 141–151, Geophysical Monograph 35, American Geophysical Union, Washington, 1985.

15. Scholer M., Diffusive Acceleration, in *Collisionless Shocks in the Heliosphere: Reviews of Current Research* (eds. B. T. Tsurutani, and R. G. Stone), pp. 287–301, Geophysical Monograph 35, American Geophysical Union, Washington, 1985.

16. Crawford, G. K., *A Study of Plasma Waves Arising from the Solar Wind Interaction with Venus,* Ph. D. Thesis, University of California at Los Angeles, 1993.

17. Crawford, G. K., R. J. Strangeway, and C. T. Russell, VLF emissions in the Venus foreshock: Comparisons with terrestrial observations, *J. Geophys. Res.* 98, 15,305–15,317 (1993).

18. Greenstadt, E. W., and L. W. Baum, Earth's compressional foreshock boundary revisited: Observations by the ISEE 1 magnetometer, *J. Geophys. Res.* 91, 9001–9006 (1986).

19. Skalsky, A., R. Grard, S. Klimov, C. M. C. Nairn, J. G. Trotignon, and K. Schwingenschuh, The Martian bow shock: Wave observations in the upstream region, *J. Geophys. Res.* 97, 2927–2933 (1992).

20. Trotignon, J. G., A. Skalsky, R. Grard, C. Nairn, and S. Klimov, Electron density in the Martian foreshock as a by-product of the electron plasma oscillation observations, *J. Geophys. Res.* 97, 10,831–10,840 (1992).

21. Scarf, F. L., W. W. L. Taylor, and P. V. Virobik, The Pioneer Venus Orbiter plasma wave investigation, *IEEE Trans. Geosci. Remote Sens.* GE-18, 36–38 (1980).

22. Strangeway, R. J., Plasma waves at Venus, *Space Sci. Rev.*, 55, 275–316 (1991).

23. Higuchi, T., G. K. Crawford, R. J. Strangeway, and C. T. Russell, Separation of spin synchronous signals, *Annals of the Institute of Statistical Mathematics* 46, 405–428, 1994.

24. Crawford, G. K., R. J. Strangeway, and C. T. Russell, VLF imaging of the Venus foreshock, *Geophys. Res. Lett.* 20, 2801–2804 (1993).

25. Farris, M. H., and C. T. Russell, Determining the standoff distance of the bow shock: Mach number dependence and use of models, *J. Geophys. Res.* 99, 17,681–17,689 (1994).

26. Slavin, J. A., R. E. Holzer, J. R. Spreiter, and S. S. Stahara, Planetary Mach cones: Theory and observation, *J. Geophys. Res.* 89, 2708–2714 (1984).

27. Crawford, G. K., R. J. Strangeway, and C. T. Russell, Electron plasma oscillations in the Venus foreshock, *Geophys. Res. Lett.* 17, 1805–1808 (1990).

28. Le, G., and C. T. Russell, A study of ULF wave foreshock morphology–1: ULF foreshock boundary, *Planet. Space Sci.* 40, 1203–1213 (1992).

29. Greenstadt, E. W., G. K. Crawford, R. J. Strangeway, S. L. Moses, and F. V. Coroniti, Spatial distribution of electron plasma oscillations in the Earth's foreshock at ISEE–3, in preparation, personal communication, 1994.

30. Hospodarsky, G. B., D. A. Gurnett, W. S. Kurth, M. G. Kivelson, R. J. Strangeway, and S. J. Bolton, Fine structure of Langmuir waves observed upstream of the bow shock at Venus, *J. Geophys. Res.* 99, 13,363–13,371 (1994).

31. Fuselier, S. A., S. P. Gary, M. F. Thomsen, S. J. Bame, and D. A. Gurnett, Ion beams and the ion/ion acoustic instability upstream from the Earth's bow shock, *J. Geophys. Res.* 92, 4740–4744 (1987).

Pergamon

Adv. Space Res. Vol. 15, No. 8/9, pp. (8/9)71–(8/9)84, 1995

0273-1177/95 $9.50 + 0.00

0273-1177(94)00087-5

ULF WAVES IN THE FORESHOCK

E. W. Greenstadt,*,[1] G. Le** and R. J. Strangeway**

** TRW Systems, One Space Park, Redondo Beach, CA 90278, U.S.A.*
*** Institute of Geophysics and Planetary Physics, University of California at Los Angeles, Los Angeles, CA 90024, U.S.A.*

ABSTRACT

We review our current knowledge of ULF waves in planetary foreshocks. Most of this knowledge comes from observations taken within a few Earth radii of the terrestrial bow shock. Terrestrial foreshock ULF waves can be divided into three types, large amplitude low frequency waves (~ 30-s period), upstream propagating whistlers (1-Hz waves), and 3-s waves. The 30-s waves are apparently generated by back-streaming ion beams, while the 1-Hz waves are generated at the bow shock. The source of the 3-s waves has yet to be determined. In addition to issues concerning the source of ULF waves in the foreshock, the waves present a number of challenges, both in terms of data acquisition, and comparison with theory. The various waves have different coherence scales, from ~ 100 km to ~ 1 Earth radius. Thus multi-spacecraft separation strategies must be tailored to the phenomenon of interest. From a theoretical point of view, the ULF waves are observed in a plasma in which the thermal pressure is comparable to the magnetic pressure, and the rest-frame wave frequency can be a moderate fraction of the proton gyro-frequency. This requires the use of kinetic plasma wave dispersion relations, rather than multi-fluid MHD. Lastly, and perhaps most significantly, ULF waves are used to probe the ambient plasma, with inferences being drawn concerning the types of energetic ion distributions within the foreshock. However, since most of the data were acquired close to the bow shock, the properties of the more distant foreshock have to be deduced mainly through extrapolation of the near-shock results. A general understanding of the wave and plasma populations within the foreshock, their interrelation, and evolution, requires additional data from the more distant foreshock.

INTRODUCTION

Ultra low frequency (ULF) magnetic perturbations consist of waves, wave packets, pulses, and any combinations of these, with periods or durations from 1 to 300s, and small to large amplitudes of 0.1 to 100 nT. They are conspicuous constituents of the interactions between the solar wind (SW) and known planetary magnetospheres and ionospheres, including Earth's. ULF waves are observed in the many different regions: the solar wind, foreshock, shock, magnetosheath, magnetopause, and magnetosphere. The waves participate in the phenomenology of wave-particle interactions, as either cause or effect. They are involved in particle thermalization and energization, wave generation, and the transmission of wave energy from one region to another. In the following sections we present an overview of the status of ULF activity in the foreshock, summaries of the best researched properties of the known ULF foreshock, implications from them about the less studied global foreshock, and a few conclusions and recommendations for future investigation.

OVERVIEW

Our knowledge and deductions of ULF phenomenology in the Earth's foreshock have been acquired from both knowledge and theory on two interrelated levels: plasma microphysics on scales of wavelengths and

[1]Retired

growth rates; and global charting on scales of planetary radii. For regions in which detailed observations have been made, our understanding of local and global wave characteristics is proficient, if not entirely complete, because the observations have been used to inspire and validate theoretical calculations and numerical simulations that explain the physics underlying the observed wave phenomenology. For some regions theoretical constructs have been extrapolated from known results but remain unconfirmed because observations have been absent or minimal and measurements at some or all levels of detail are lacking. In yet other regions, large scale patterns of ULF or other activity observed with limited instrumentation suggest extrapolations to detailed microphysics but remain unexplained because they demand theoretical treatments not yet developed or numerical experiments not yet accomplished. Future progress, especially under conditions of restricted support rests on an overall picture of where these various regions lie.

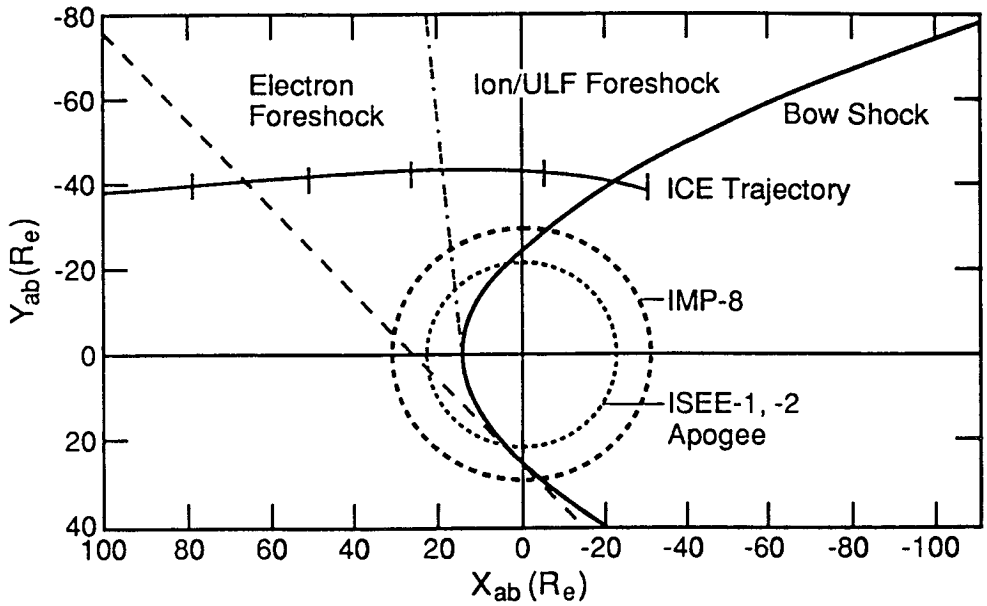

Fig. 1. Schematic of the Earth's bow shock and foreshock regions. The figure also shows the regions sampled by various spacecraft.

Figure 1 offers a rough guide to the state of our knowledge of global ULF in Earth's foreshock, defining regions according to whether and how they are defined by spacecraft observations or by extrapolations from observation. The smaller circle of radius 22 Earth radii (R_e) surrounding the Earth and penetrating the average bow shock represents the approximate apogee of ISEE 1 and 2 as these satellites precessed in their elliptical orbits around the Earth for several years. The pair of spacecraft were well instrumented for field and directional charged particle measurements over a wide spectrum of energies, although not every detector survived the entire life of the project. The area inside the ISEE 1,2 circle may be thought of as defining the region in which the plasma envelope has been sampled by many spacecraft, including Explorers, OGO 5, and AMPTE, at length and in detail to supply most of the existing observational contributions to both the macro- and microphysics of ULF phenomena in the natural extraterrestrial environment.

The larger circle represents the approximate trajectory of IMP 8, a long lived satellite in a nearly circular orbit of radius about half the distance of the moon. IMP 8 was not equipped with as sophisticated a complement of particle experiments as were ISEE and other spacecraft, but it has provided a long record of magnetic field measurements with ample resolution for detecting ULF activity, thereby extending the region of wave recording, and certainly the macroscopic chart, a moderate distance beyond the inner circle. The trajectory segment of the ICE spacecraft (formerly ISEE 3) on its way from a few Earth-gravity-assisted orbits to rendezvous with a comet, is included to emphasize how scarce observations have been in the distant downwind foreshocks outside the IMP 8 territory. The regions marked electron foreshock and ion/ULF foreshock in Figure 1 are, with few exceptions, enlightened extrapolations informed by mea-

surements at or inside the ISEE 1,2 circle. We shall return to a discussion of what we think we know about these extended regions after a description of what we do know within the inner circle.

MORPHOLOGY OF THE KNOWN FORESHOCK REGION

Upstream waves were discovered more than two decades ago /1, 2/. Based on our present understanding of the repeatedly studied inner foreshock region, we have developed a picture of its morphology. In that picture, wave and particle phenomena upstream from the shock arise from kinetic effects occurring in the shock transition region /3, 4, 5, 6, 7/. These effects include: reflection, shock drift acceleration, particle scattering (heating), and first order Fermi acceleration. The effectiveness of the above mechanisms as well as the characteristics of the backstreaming populations (at the shock) are strongly dependent on the direction of the shock normal relative to the plasma flow and the interplanetary magnetic field (IMF) orientation.

Upstream from the Earth's bow shock, we can divide the unshocked plasma into two regions, one magnetically unconnected where no IMF lines connect to or cross the shock, and one the so-called magnetic foreshock region where all IMF lines are connected to the bow shock. The IMF lines tangent to the bow shock form the boundary between those two regions. The superposition of the upstream motion along the magnetic field line and the convection associated with the interplanetary electric field, results in the formation of electron and ion foreshocks within the region of unshocked solar wind connected to the bow shock. Because of the finite velocity of these backstreaming particles and the convection associated with the interplanetary electric field, the electron and proton foreshocks do not fill the entire magnetically connected region, nor are they fully coincident.

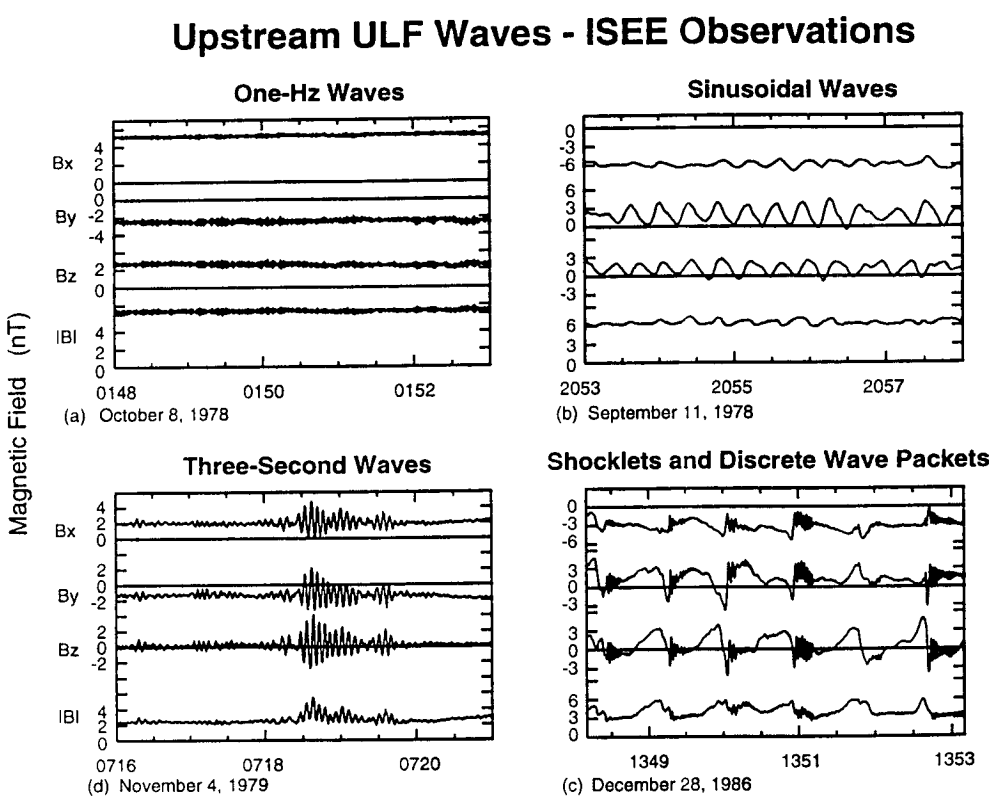

Fig. 2. Observations of different types of ULF waves in the Earth's foreshock region. (a) Upstream propagating whistlers (one-Hz waves); (b) Nearly sinusoidal waves near 30 seconds; (c) Shocklets and discrete wave packets; and (d) Three-second waves.

The electron foreshock boundary is defined by the fastest electrons accelerated along the tangent magnetic field lines. Since the convection velocity is small compared to the typical velocity of escaping electrons

(which can be many times their thermal velocity), the electron foreshock boundary is only slightly displaced downwind from (behind) the IMF tangent lines by the $\mathbf{E} \times \mathbf{B}$ force on the electrons in the Earth's frame of Figure 1. In the electron foreshock, VLF activity and an electromagnetic mode at ULF frequencies has been identified, the so-called upstream propagating whistlers (or "one-Hertz" waves) /8, 9, 10, 11/. Figure 2a shows an example of this type of wave signal.

The ion foreshock boundary in contrast appears to be defined by position-dependent acceleration processes that do not cause protons to move upstream (in the shock frame) until some distance downstream of the electron foreshock. Thus, the ion foreshock boundary is located much deeper in the magnetic foreshock, beginning close to the region called the quasi-parallel part of the bow shock. In the ion foreshock region, several types of waves in the ULF frequencies have been observed. When the IMF cone angle is moderate ($\theta_{Bv} > 40°$), the ULF wave foreshock boundary has been found to correspond to the trajectory of backstreaming ions with a streaming velocity of ~ $1.4V_{sw}$ along the IMF in the Earth's frame and a source point at ~ 50° θ_{Bn} /12, 13/. Among the ULF waves in the ion foreshock, the most frequently observed are the large amplitude waves with periods near 30 seconds /1, 10/. The waveforms of 30-s waves vary from nearly sinusoidal and transverse (e.g., Figure 2b) to highly compressional and steepening, the so-called shocklets (e.g., Figure 2c). Discrete wave packets, which have higher frequency, are often associated with the steepening edges of the shocklets /8/. Recently, a new type of ULF wave with period near 3 seconds was also observed associated with high-β solar wind plasma, as shown in Figure 2d /14/ (β is the ratio of thermal to magnetic energy density).

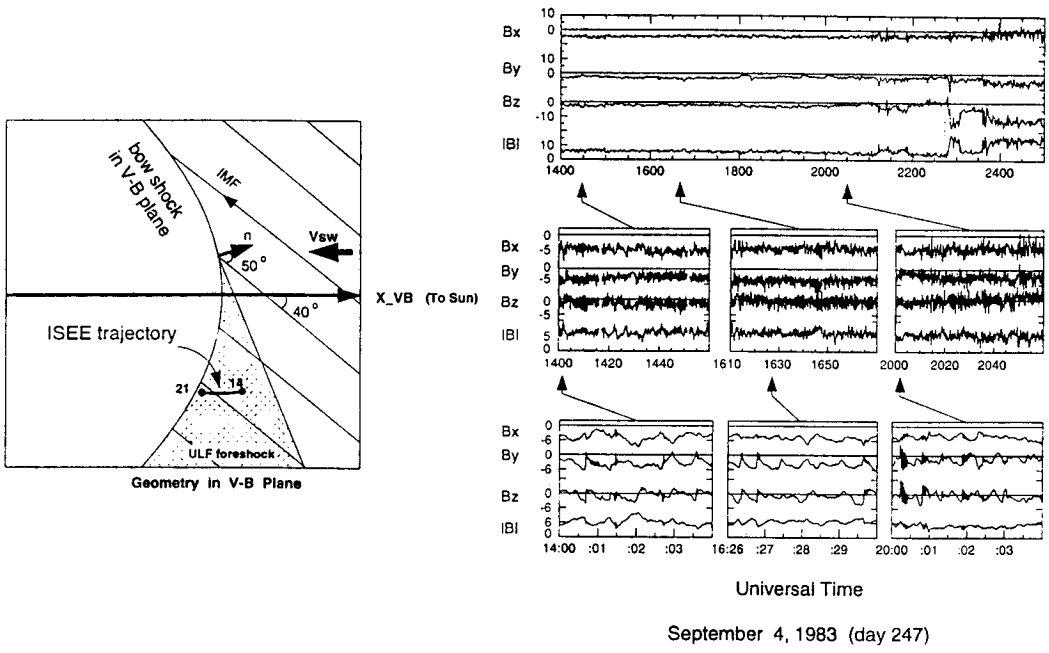

Fig. 3. Variation of upstream waves in the foreshock. The left panel shows the ISEE trajectory in the V-B plane on September 4, 1983 when the IMF cone angle was nearly constant over an extended time period. The right panels are magnetic field observations /15/.

It is commonly known that the properties of upstream waves and particles are position dependent. Figure 3 shows an example of evolution of large amplitude ULF waves in the foreshock region for a long period of steady IMF cone angle and solar wind condition /15/. Under these conditions, the foreshock boundary was steady and any change in wave properties was primarily related to the changing spacecraft location in the foreshock geometry. In this example, the ULF waves change their forms to highly irregular and become stronger, more compressional and more linearly polarized deep into the foreshock. The peak of the ULF power spectrum became broader when the spacecraft was further downstream from the foreshock boundary, as illustrated in Figure 4.

SOURCES OF ULF WAVES

Large Amplitude Waves (30-Seconds Waves)

The most studied waves in the foreshock are the low frequency waves at periods near 30 seconds upstream from the Earth's shock. Their amplitudes can be as large as the background magnetic field strength ($\delta B/B \sim 100\%$). The waves are most monochromatic near the foreshock boundary and become broadband in the form of steepened "shocklets" and evolved with the depth behind the foreshock boundary /10, 15/. The waves are strongly compressional deep in the foreshock region. Their existence in front of the bow shock is particularly important to the Earth's magnetosphere since they modify both the solar wind and the turbulence spectrum convected downstream to the magnetopause. The compressional waves cause significant density fluctuations, and thus dynamic pressure fluctuations in the unshocked solar wind. The density and dynamic pressure fluctuations can be ~ 20% of the background solar wind value /16/. These waves have long been regarded as one of major sources of ULF waves in the magnetosphere. However, power spectra of these waves have limited bandwidth /17/. The enhanced ULF wave power has a clear low-frequency cutoff near 5 mHz, below which the power spectra are similar in the undisturbed solar wind and in the foreshock. Thus, large-amplitude waves in the foreshock can be directly responsible for only a fraction of the waves in the magnetosphere.

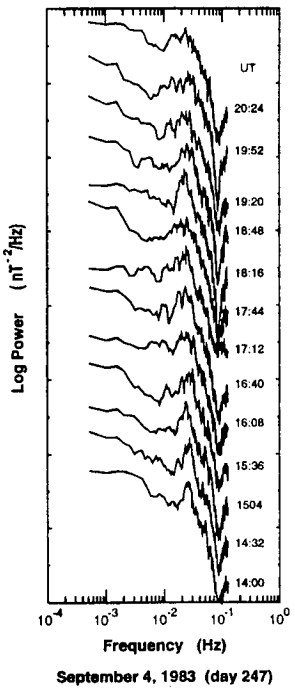

Fig. 4. Evolution of power spectra in the foreshock. The power spectra of 32-minutes magnetic field data with starting times indicated in the figure on September 4, 1983 /15/.

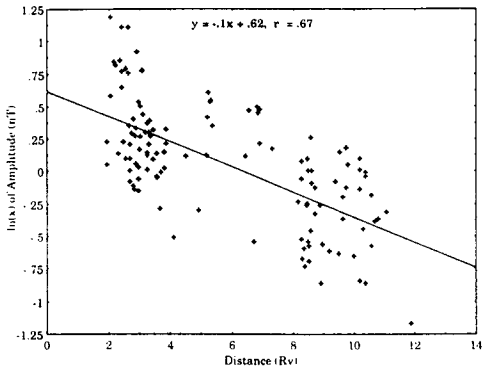

Fig. 5. Variation in amplitude of upstream propagating whistlers (one-Hz waves) with distance from the shock measured along the magnetic field line /27/.

Compressional 30-s waves exhibit both left-handed and right-handed polarization in the spacecraft frame, while the nearly sinusoidal waves are always left-handed in the spacecraft frame. The left-handed and right-handed compressional waves are similar in form, frequency and wavelength /10/. Several mechanisms related to the electromagnetic ion/ion instabilities have been proposed for the generation of these waves (see /18/ for a review). It is in general agreement that the nearly sinusoidal waves are generated by the Doppler-shifted ion/ion resonant instability, in which the right-handed polarized waves resonate with the backstreaming ion beams /19, 20/. This instability generates right-handed waves propagating upstream

in the solar wind frame, and thus observed as left-handed waves in the spacecraft frame when they are convected downstream. This instability is not so successful for the compressional waves, since it can only explain left-handed compressional waves. For the right-handed compressional waves two mechanisms have been proposed, the non-resonant firehose instability /21/ produced by fast and dense backstreaming ion beams and the left-handed Alfvén/ion resonant instability produced by extremely hot backstreaming ions /22/. The first instability generates right-handed magnetosonic waves propagating downstream in the solar wind frame; the second generates left-handed Alfvén waves propagating upstream in the solar wind frame. In both cases, the waves will be right-handed in the spacecraft frame. However, this is still conjecture. No effort has been made to identify the intrinsic wave mode of these waves and to examine the backstreaming ions associated with them. No one has examined the correlation between the wave handedness and the density, velocity, and temperature of the backstreaming ions. Despite the many theoretical treatments of these waves there is much we do not know. For example, polarization of these waves has been found to be a function of their amplitude /23, 16/. Although we still do not understand this observation, it may be an important clue to the underlying instabilities.

Upstream Propagating Whistlers (1-Hz Waves)

The waves which we now call "upstream propagating whistlers" were discovered in the Earth's foreshock by Russell et al. /8/ and characterized in detail by Fairfield /9/. Fairfield correctly identified them as whistler mode waves propagating upstream against the solar wind flow with a phase speed generally less than that of the solar wind, but with a group velocity greater than that of the solar wind so that the wave energy could propagate upstream. Hoppe et al. /10/ also noted the waves in ISEE 1 and 2 data but preferred to interpret the waves in terms of a local instability. By a detailed investigation of the magnetic fields associated with upstream field aligned beams, Hoppe et al. /11/ found that the beam presence was not a sufficient condition for the observation of these waves, although these waves are often observed in association with the ion beams. At the same time they determined the intrinsic properties of the waves by using simultaneous magnetometer data from ISEE 1 and 2. Their results showed that these waves were obliquely propagating whistler modes, with frequencies ~ 20–100 Ω_p, where Ω_p is the proton gyrofrequency, and wavelength ~ 100 km in the plasma rest frame.

The source of these waves has been controversial. Fairfield /9/ first suggested that these waves originate at the shock and propagate upstream. Later, locally generation in the foreshock by electron beams was also proposed /24, 25/. Feldman et al. /24/ showed a correlation between 1 Hz waves and backstreaming intermediate energy electrons at times when magnetic field lines connect to the bow shock. These backstreaming electrons make a positive slope in the observed electron distribution function. Sentman et al. /25/ found that this kind of distribution is unstable to an oblique whistler mode.

Recent studies of waves in other planetary foreshocks strongly favor the shock generation mechanism /26, 27/. Upstream propagating whistler waves are also seen in planetary foreshocks. They were first reported at Mercury /28/, and more recently they have been observed in the Venus foreshock /26/. These waves have similar amplitudes at all three planets and an interesting variation in polarization. The waves are observed to be always left-handed at the Mercury, mostly left-handed at Venus and about half the time left-handed at Earth. We can explain this in term of the varying spiral angle of the IMF. At Venus, the wave amplitude decreases with distance from the shock with about a 10 R_v scale length /27/ as shown in Figure 5. Another very important aspect of these waves has been deduced from the planetary data. The largest wave length of these waves is approximately the thickness of the bow shock /29/. This is more evidence for the shock generation of these waves.

Three-Second Waves

A new class of ULF waves upstream from the Earth's bow shock has been recently discovered in the ISEE magnetometer data /14/. There waves are observed in the upstream region only when the interplanetary magnetic field intersects the bow shock, in both quasi-parallel (Q||) and quasi-perpendicular (Q⊥)shock geometries. These waves are observed when solar wind plasma β is high. They are always right-handed and nearly circular polarized in the spacecraft frame. The direction of the waves vectors are in the general direction of the background magnetic field, and the waves are convected downstream. To identify the wave

mode and intrinsic polarization in the plasma rest frame, observed waves properties have been compared with the two-fluid warm plasma dispersion relation /30, 14/. It is found that two out of the three modes in a warm plasma match observed wave properties from the two-fluid theory, but the intrinsic wave mode can not be determined unambiguously. For all of the cases, the wave properties match the prediction of left-handed ion cyclotron waves under the assumption that the waves are propagating upstream in the solar wind frame. If these waves are indeed the ion cyclotron waves, the plasma rest frame frequency are estimated around 1/3 of the ion cyclotron frequency. However, recent work /31/ shows that the wave dispersion relation from linear kinetic theory is significantly different from the two-fluid theory for a high-β plasma, or for frequencies approaching the ion gyro-frequency. The two-fluid theory is therefore not a good approximation for the study of the 3-second waves, but a kinetic approach to mode identification has yet to be performed.

The free energy source of 3-second waves is presently a complete mystery. The backstreaming ions seem not to be the cause of these waves because the waves can occur when the backstreaming ions are completely absent. If these waves are ion cyclotron waves propagating upstream, the backstreaming ions can not satisfy resonance condition with left-handed waves propagating in the same direction. Only backstreaming electrons can resonate with these waves. However, the resonant condition requires streaming energies of tens of keV to a few hundred keV for the backstreaming electrons. It is unknown if such high energy backstreaming electrons exist deep into the foreshock. We also do not know if temperature anisotropies can be a possible source of the waves.

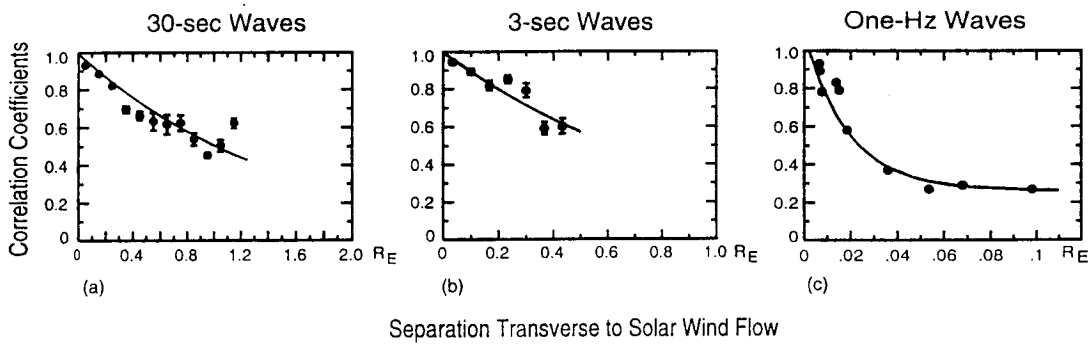

Fig. 6. Correlation coefficients of upstream ULF waves simultaneously observed by ISEE 1 and 2 as a function of spacecraft separation perpendicular to the solar wind flow. (a) Large-amplitude 30-sec waves; (b) Nearly monochromatic 30-sec waves; (c) Upstream propagating whistlers near one-Hz /32/.

COHERENCE LENGTHS OF ULF WAVES

Recently /32/, the simultaneous magnetic field data from the dual ISEE spacecraft were used to study the coherence lengths of upstream ULF waves. The cross-correlation between ISEE 1 and 2 observations were examined for different spacecraft separations and it was found that the coherence length varies with different types of ULF waves. The coherence length is related to the bandwidth of the power spectra and the wavelength as expected from the theory. For the large-amplitude ULF waves with periods near 30 seconds and wavelength close to 1 R_e, the coherence length is of the order of 1 R_e transverse to the solar wind flow, as shown in Figure 6a. For nearly monochromatic ULF waves with periods near 3 seconds, the coherence length is found to be equal to several wavelengths, again equaling about 1 R_e (Figure 6b). However for the much shorter wavelength upstream propagating whistler waves, the coherence length is ~ 100 km (Figure 6c). While all these coherence lengths are consistent with that estimated from the bandwidth, we see that the coherence length in kilometers varies markedly for different wave phenomena. Thus, a variety of different separations are needed to study the various wave phenomena in the upstream

region. In order to determine the properties of a wave phenomenon one needs to see the same wave with high coherence at all spacecraft. Large-amplitude waves near 30 s and 3-second waves can be studied with moderately large separations (> 1000 km), but studies of upstream propagating whistlers near 1-Hz require spacecraft to be spaced rather closely, at < 100 km.

KINETIC THEORY VERSUS HALL-MHD

In recent years it has become increasingly obvious that the dispersion relation of ULF waves is not adequately described by either single-fluid or two-fluid MHD /33/. This statement not only applies to the wave dispersion, but also the associated wave field properties, such as compressibility, polarization etc. Two-fluid (or Hall) MHD treats both the ions and electrons as fluids /34/, whereas single-fluid MHD combines both electrons and ions into one fluid. While two-fluid may be more descriptive, the dispersion relation is more often referred to as Hall-MHD, and we will also use that name. Hall-MHD was extended to moderate β /35/, and the theory was thought to be appropriate for ULF waves. However, as noted above, this does not appear to be the case, and a fully kinetic dispersion relation is required to adequately describe the wave dispersion and mode properties.

Krauss-Varban et al. /31/ have recently presented an extensive discussion of the differences between Hall-MHD and kinetic dispersion relations. As a result of their analysis, they have proposed a new naming convention for the wave modes. This is shown in Figure 7, where both Hall-MHD and kinetic dispersion curves are shown. The curves are plotted for propagation at 30° with respect to the ambient magnetic field. The panel at top left of Figure 7 shows dispersion curves for low β, using Hall-MHD, and we see the classical dispersion properties. The wave modes are named after their respective phase speeds: Fast (F), Intermediate (I), and Slow (S).

The panel at top right shows the dispersion curves for the same β, using kinetic (or Vlasov) theory. At low frequencies the dispersion curves look very similar, but as the wave frequency approaches the ion gyro-frequency the Intermediate and Slow mode dispersion curves cross. Thus at higher wave number the Slow mode is faster than the Intermediate mode! Hence Krauss-Varban et al. propose the modified naming convention: Fast/Magnetosonic (F/MS), Alfvén/Ion Cyclotron (A/IC), and Slow/Sound (S/SO). This naming convention retains some connection with the Hall-MHD naming convention, applicable for low β and low frequency, but also describes more completely the dispersive properties of the wave. In particular it is the Alfvén/Ion Cyclotron wave that encounters the ion gyro-resonance, not the Slow/Sound wave. The differences between Hall-MHD and kinetic theory are even more marked for higher β, as shown in the bottom two panels of Figure 7. In these panels there is no commonality in the dispersion curves, even at low frequency.

In addition to the dispersive properties of the waves, the polarization, compressibility, etc., are markedly different in Hall-MHD and kinetic theory /31/. This was further demonstrated through direct comparison with magnetic field data acquired by the Pioneer Venus Orbiter /36/. The comparison in /36/ was made using small amplitude ULF waves with frequency ~ 0.1 Hz. These waves were chosen since terrestrial studies (see, e.g., /30/) show that the waves are intrinsically right-hand polarized in the plasma frame, propagating upstream. However, the waves are observed to be left-hand polarized in the spacecraft because of Doppler-shift by the solar wind. Although comparison with theory requires the assumption that the waves are right-handed and propagating upstream, minimum variance analysis yields the direction of the wave vector (the 180° ambiguity is removed through the assumption of upstream propagation). Since the propagation direction is known, as well as the ambient plasma conditions, and the frequency in the observer's frame, it is possible to carry out direct comparison between data and theory. Two specific parameters were compared in /36/, the magnetic polarization, and the magnetic compression ratio. The results of this comparison are summarized in Figure 8.

The top row of Figure 8 shows, from left to right, the magnetic polarization for Fast/Magnetosonic mode from kinetic theory, the Fast mode from Hall-MHD, and the Intermediate mode from Hall-MHD. In each case the abscissa shows the observed polarization (assumed to be right-handed, hence restricted to the range 0 to 1), while the ordinate shows the theoretical prediction. If the theory and data match the points will lie along a line of unit slope. The dashed lines are least squares fits to the points. The bottom row

compares the magnetic compression ratio. Again a unit slope indicates a good match. While some points show agreement in the comparison with Hall-MHD, the figure indicates that kinetic theory better represents the data. The remarkable consistency with kinetic theory found in /36/, where the data are also compared as a function of β and propagation angle strongly supports the use of kinetic theory, rather than Hall-MHD, in analyzing ULF foreshock waves.

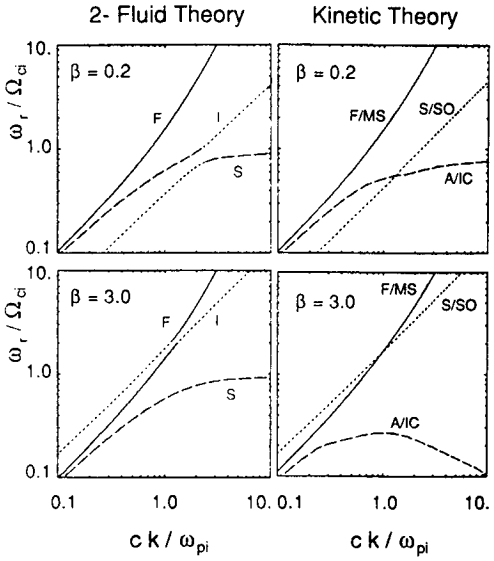

Fig. 7. Comparison of the wave dispersion relations derived from Hall-MHD (left) and kinetic (right) theory (after /31/).

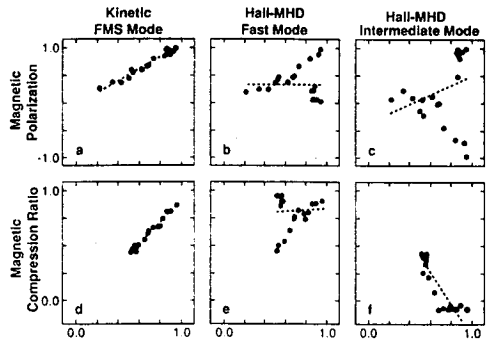

Fig. 8. Comparison of theoretical and observed magnetic polarization and compression ratio (after /36/).

THE MACROSCOPIC PERSPECTIVE

Observations

The extended regions marked electron foreshock and ion/ULF foreshock in Figure 1 are, with few exceptions, enlightened extrapolations informed by measurements at or inside the ISEE 1,2 circle. There are, however, two completely certifiable entities at great distance from the Earth. These are, first, the straight line representing the electron foreshock boundary and, second, known streams of energetic protons traveling upstream within the ion/ULF region. The electron line, actually a surface in real three dimensional space, has been observed by energetic-electron detectors of ISEE 3 /37/ and inferred from plasma wave VLF measurements of electron plasma frequency (f_{pe}) signals at ISEE 3 /38/ at distances of 100 to 240 Re. A cool beam of electrons reflected and accelerated by the quasiperpendicular (Q⊥) shock streams against or across the solar wind along the IMF line tangent to the shock, generating electrostatic plasma waves at frequency f_{pe}. The region behind the line is also the scene of plasma wave activity with $f < f_{pe}$, detected by Galileo at Venus /39/ and by ISEE 3 at Earth /38/. Near the shock a less energized, but much hotter, population of counterstreaming electrons reflected from the shock and/or emitted by the heated plasma of the magnetosheath, has been directly observed by ISEE 1,2 /40, 41/. In fact, counterstreaming electrons have been used, without reference to the magnetic field orientation, as an indicator of recognized connection from an observation point to the shock: absence of electrons means the observer is outside any foreshock. From the distant plasma wave activity and the close-in electron observations we infer the presence of the generalized distant electron foreshock noted in the figure, but, as remarked earlier in this report, we don't know how deeply these electrons occur.

Another line or surface between the two shown in Figure 1, not necessarily bounding a broad region, and not illustrated here, is formed by protons energized by multiple reflections along the Q⊥ section of the shock. These protons are released at or slightly downwind from the IMF tangent point to stream against or across the solar wind, depending on the instantaneous orientation of the field relative to V_{SW}, for distances up to 240 R_e /37/.

The next region, designated the ion/ULF foreshock in Figure 1, is where ULF waves prevail, largely by inference, in an analogous setting to electrons and plasma waves. Like VLF plasma wave activity, ULF activity accompanies particular particle populations, in this case, protons counterstreaming from the bow shock. Near Earth's bow shock, the sunward boundary of all ULF waves coincides with the line of departure of protons outward along $\mathbf{B}_{SW}$ behind the contact point of the line of the IMF. Cold beams of accelerated protons or singly reflected protons, with speed $V_p \approx 2V_{SW}$ in the solar wind frame leave the shock from where $\theta_{Bn} \approx 60^\circ$ to 45°. Reflected beams of protons streaming along $\mathbf{B}_{SW}$ at the appropriate speed are indeed observed, as are beams with a variety of hotter ("diffuse") energy spectra, departing the Q|| shock where $\theta_{Bn} < \approx 45^\circ$. The hot, diffuse distributions include a high energy tail of protons of energies comparable to those accelerated by the Q⊥ shock and released at the tangent IMF line. The forward boundary of the ion/ULF foreshock is, like its electron counterpart, a surface, represented as a line in the two dimensional conceptualization. Thus depicted ion/ULF boundary in Figure 1 marks the beginning of a region of protons either reflected from the shock around the transition between Q⊥ and Q|| structures or scattered and accelerated further along the Q|| structure to form a hot population with a high energy tail. Whether all distant observations of energetic ions were of Q⊥-accelerated beams or of tail members of heated distributions from deeper in the distant ion foreshock, some were accompanied by weak ULF waves /42/, so we know that waves can extend as far upstream from the shock as do counterstreaming protons /12/, and that by themselves they define a ULF boundary from which some downwind convection should be expected. From the combination of these data, from a study of the ULF foreshock boundaries at Venus and Earth, and from extensive investigations of ULF waves within the inner circle of Figure 1, we deduce that the region behind the ion foreshock boundary in the figure is inhabited by, if not filled with, ULF oscillations.

The waves corresponding to $\theta_{Bn} < \approx 45^\circ$ become increasingly complex and enlarged in amplitude close to the shock, i.e., deeper in the ion/ULF foreshock along the solar wind direction, as described in detail earlier. These elements of wave complexity do not appear, however, at the far flank of the shock, outside and very deeply downwind from the region of detailed observation /38/ or along the Q|| terminator flank when $B_x = 0$. When the IMF is nearly perpendicular to the solar wind flow, the foreshock is confined in two relatively small regions near the flanks. Upstream waves and particles have not been investigated in this geometry, but we know of no examples of well defined shocklets when the IMF is nearly at right angles to the solar wind flow.

Theory

An initially uniform, counterstreaming beam of cold protons in an infinite, homogeneous solar wind supports an instability that generates transverse ULF waves which scatter some of the beam protons into a warmer, less focused ("intermediate") distribution. Further development in time results in compressional waves of larger amplitudes and eventually an accompanying hot, diffuse distribution. The hot distribution includes a skewed tail of protons energized by Fermi scattering between upstream wave gradients, and between wave gradients and the shock. The highest energy protons, unaffected by the most distant, small waves far upstream from the shock, escape the foreshock into the distant upstream solar wind to become low energy cosmic rays /43/. The ultimate development of a diffuse population and large compressional waves is unsupported, although not necessarily contradicted, by observation because its growth time is longer than the distance the solar wind is seen to travel between its first encounter with the cold proton beam and the appearance of compressional ULF waves. Theory has, however, independently provided wave growth by interaction of a diffuse population with the solar wind /21/. Analysis has also provided, conveniently, for the escape of hot particles from the Q|| magnetosheath to provide just such a distribution /44/ or to augment the intermediate one already present. The original initial value scenario has been replaced by a boundary value calculation that includes the shock and comes closer to approximating the natural foreshock of observation /45/.

Numerical simulations

Computer modeling of the Q|| shock has offered a scenario in which convected upstream waves encountering protons reflected from the outermost steep field gradient are amplified until one wave crest grows to become a "reformed" shock consisting of a new steep, Q⊥-like gradient followed downstream by trains of amplified waves /46, 47/. The real upstream region then presumably consists of a bath of reflected ions

plus whatever populations of waves and particles, including hot, backstreaming ions /48/ and electrons from the magnetosheath, have been supplied by the already existing foreshock originating in more sunward portions of the curved bow shock.

Summary

We know, from plasma waves indicating the presence of small populations of reflected protons and the absence of steepened waves and wave packets along the far flank, where $X \approx -50$ to -100 R_e and $Y \approx -60$ to -100 R_e, that conditions in this part of the deep Q|| foreshock do not support the steepening of ULF waves leading to Q|| shock reformation. Either the local low Mach shock therefore does not generate enough reflected protons to instigate its own reformation or the foreshock in that part of the downstream solar wind does not carry the waves or particles necessary to initiate the reformation process. Both explanations seem likely. Hence there is a region of the downstream foreshock for $Y < \approx -50$ R_e where we should expect to find only particle populations below instability thresholds and convected transverse waves of small to moderate amplitudes, if any.

Closer to the ion/ULF foreshock boundary, we may infer from our knowledge of the existence of energetic protons returned from the Q|| shock, that transverse ULF waves must surely be present at some amplitude, either generated locally or convected downwind from the boundary beam itself. Still closer to both the shock and the boundary, but outside the inner circle of Figure 1, we expect to find returning populations of both hot electrons with beam velocities more or less parallel to the electron foreshock boundary and diffuse or escaping energetic protons with beam velocities more or less parallel to the ion foreshock boundary, plus transverse and, possibly, compressional waves of appreciable amplitudes but seldom large enough to become steepened shocklets. We may thus speculate that there is a region in the foreshock of considerable interest containing an inhomogeneous mixture of cross streaming electrons, protons, and ULF waves neither documented by observation nor modeled by theory or simulation.

CONCLUSIONS AND RECOMMENDATIONS

Our present understanding of the foreshock's morphology is still incomplete, even within the inner circle of extensive measurements (Figure 1), and we must never lose sight of the assumed distinction between the physics of curved, inhomogeneous bow shocks of planetary scales and the inherent physics of large scale interplanetary or interstellar shocks where cross communication may play a negligible role. Foreshock morphology as we know it is largely controlled by the IMF cone angle and the peculiarities of Earth's hyberboloidal shock. Most of previous observations are made at small and moderate IMF cone angle and near the subsolar region, so the subsolar foreshock is well documented by high resolution magnetometers under this condition, and by particle detectors of moderate sampling rates. In essence, observations and theory have already reached, but not mastered, a scale below fluid physics, in the realm of kinetic plasma processes. One compelling requirement of future investigation of the close-in foreshock therefore is deployment of high time resolution ion analyzers and plasma wave VLF-detectors capable of recording transient anisotropic distributions of reflected and magnetosheath-emitted ions, and electrostatic bursts, involved in the process of ion scattering where and when the ULF waves are generated.

As we demonstrated in previous sections, a second major task in future upstream wave study is to identify the intrinsic wave modes in the solar wind frame, with attention to departure from classical model of infinite plane waves. In the strongly Doppler shifting environment of the solar wind, multiple spacecraft observations are needed to determine unambiguously those frame-dependent wave properties such as frequency and phase velocity. The waves have finite coherence lengths, and the multiple spacecraft must be located within a coherence length of each other to ensure that they are observing the same wave. It is still important to define coherence lengths of different types of waves using existing datasets. The knowledge of coherence lengths can help us to develop a separation strategy for future multiple spacecraft missions.

The foreshock region beyond the orbit of previous spacecraft is largely unknown, but is important because the phenomenology of this region, including escaping energetic particles and distant waves of scattering capability, has the greatest prospect of application to the solar wind at large and the interaction physics of remote obstacles with stellar plasmas not so easily sampled directly. The distant foreshock begs for ULF

mapping, with or without accompanying instrumentation capable of detecting counterstreaming particles. Some particle properties can be reasoned from wave properties where interaction products have stabilized. Existing databases collected from this region need to be exploited to guide future missions to truly undocumented areas, and future missions need to include itineraries designed to answer remaining open questions.

ACKNOWLEDGMENTS

This work was supported at UCLA by NASA grants NAGW–3477 and NAG2–485.

REFERENCES

1. Greenstadt, E. W., I. M. Green, G. T. Inouye, A. J. Hundhausen, S. J. Bame, and I. B. Strong, Correlated magnetic field and plasma observations of the Earth's bow shock, *J. Geophys. Res.* 73, 51 (1968).

2. Fairfield, D. H., Bow shock associated waves observed in the far upstream interplanetary medium, *J. Geophys. Res.* 74, 3541 (1969).

3. Sonnerup, B. U. O., Acceleration of particles accelerated in a shock, *J. Geophys. Res.* 74, 1301 (1969).

4. Paschmann, G., N. Sckopke, J. R. Asbridge, S. J. Bame, and J. T. Gosling, Energization of solar wind ions by reflection from the Earth bow shock, *J. Geophys. Res.* 85, 4598 (1980).

5. Armstrong, T. P., M. E. Pesses, and R. B. Decker, Shock drift acceleration, in *Collisionless Shocks in the Heliosphere: Review of Current Research*, eds. B. T. Tsurutani and R. G. Stone, AGU Geophysical Monograph 35, 271 (1985).

6. Scholer, M., Diffusive acceleration, in *Collisionless Shocks in the Heliosphere: Review of Current Research*, eds. B. T. Tsurutani and R. G. Stone, AGU Geophysical Monograph 35, 287 (1985).

7. Gosling, J. T., and A. E. Robson, Ion reflection, gyration and dissipation at supercritical shocks, in *Collisionless Shocks in the Heliosphere: Review of Current Research*, eds. B. T. Tsurutani and R. G. Stone, AGU Geophysical Monograph 35, 207 (1985).

8. Russell, C. T., D. D. Childers, and P. J. Coleman, OGO-5 observations of upstream waves in the interplanetary medium: discrete wave packets, *J. Geophys. Res.* 76, 845 (1971).

9. Fairfield, D. H., Whistler waves observed upstream of collisionless shocks, *J. Geophys. Res.* 79, 1368 (1974).

10. Hoppe, M. M., C. T. Russell, L. A. Frank, T. E. Eastman, and E. W. Greenstadt, Upstream hydromagnetic waves and their association with backstreaming ion population: ISEE 1 and 2 observations, *J. Geophys. Res.* 86, 4471 (1981).

11. Hoppe, M. M., C. T. Russell, L. A. Frank, and T. E. Eastman, Characteristics of ULF waves associated with upstream ion beams, *J. Geophys. Res.* 87, 643 (1982).

12. Greenstadt, E. W., and L. W. Baum, Earth's compressional foreshock boundary revisited: Observations by ISEE 1 magnetometer, *J. Geophys. Res.* 91, 9001 (1986).

13. Le, G., and C. T. Russell, A study of ULF wave foreshock morphology, I. ULF foreshock boundary, *Planet. Space Sci.* 40, 1203 (1992).

14. Le, G., C. T. Russell, M. F. Thomsen, and J. T. Gosling, Observations of a new class of upstream waves with periods near 3 seconds, *J. Geophys. Res.* 97, 2917 (1992).

15. Le, G., and C. T. Russell, A study of ULF wave foreshock morphology, II. Spatial variation of ULF waves, *Planet. Space Sci.* 40, 1215 (1992).

16. Le, G., and C. T. Russell, The morphology of ULF waves in the Earth's foreshock, in *Solar Wind Source of Magnetospheric Ultra-Low-Frequency Waves*, eds M. Engebretson, K. Takahashi and M. Scholer, Geophysical Monograph 81, p.81, AGU, Washington DC (1994).

17. Le, G., and C. T. Russell, Observations of the magnetic fluctuation enhancement in the Earth's fore-shock region, *Geophys. Res. Lett.* 17, 905 (1990).

18. Gary, S. P., Electromagnetic ion/ion instabilities and their consequences in space plasma: A review, *Space Sci. Rev.* 56, 373 (1991).

19. Barnes, A., A theory of generation of bow-shock-associated hydromagnetic waves in the upstream interplanetary medium, *Cosmic. Electrodyn.* 1, 90 (1970).

20. Gary, S. P., Electromagnetic ion beam instability and energy loss of fast alpha particles, *Nucl. Fusion* 18, 327 (1978).

21. Sentman, D. D., J. P. Edmiston, and L. Frank, Instabilities of low frequency, parallel propagating electromagnetic waves in the Earth's foreshock region, *J. Geophys. Res.* 86, 7487 (1981).

22. Gary, S. P., C. W. Smith, M. A. Lee, M. L. Goldstein, and D. W. Forslund, Electromagnetic ion beam instabilities, *Phys. Fluids* 27, 1852 (1984). Correction, *Phys. Fluids* 28, 438 (1985).

23. Russell, C. T., J. G. Luhmann, R. C. Elphic, D. J. Southwood, M. F. Smith and A. D. Johnstone, Upstream waves simultaneously observed by ISEE and UKS, *J. Geophys. Res.* 92, 7354 (1987).

24. Feldman W. C., R. C. Anderson, S. J. Bame, S. P. Gary, J. T. Gosling, D. J. McComas, M. F. Thomsen, G. Paschmann, and M. M. Hoppe, Electron velocity distribution near the Earth's bow shock, *J. Geophys. Res.* 88, 96 (1983).

25. Sentman, D. D., M. F. Thomsen, S. P. Gary, W. C. Feldman, and M. M. Hoppe, The oblique whistler instability in the Earth's foreshock, *J. Geophys. Res.* 88, 2048 (1983).

26. Orlowski, D. S., G. K. Crawford, and C. T. Russell, Upstream waves at Mercury, Venus and Earth: Comparison of the properties of one Hertz waves, *Geophys. Res. Lett.* 17, 2293 (1990).

27. Orlowski, D. S., and C. T. Russell, ULF waves upstream of the Venus bow shock: Properties of the one Hertz waves, *J. Geophys. Res.* 96, 11,271 (1991).

28. Fairfield, D. H., and K. W. Behannon, Bow shock and magnetosheath at Mercury, *J. Geophys. Res.* 81, 3891 (1976).

29. Orlowski, D. S., and C. T. Russell, On the source of one Hertz waves at Venus, *J. Geophys. Res.*, submitted, 1994.

30. Le, G., *Generation of upstream waves in the Earth's foreshock*, Ph.D. Dissertation, University of California, Los Angeles, 1991.

31. Krauss-Varban, D., N. Omidi, and K. B. Quest, Mode properties of low frequency waves: Kinetic theory versus Hall-MHD, *J. Geophys. Res.* 99, 5987 (1994).

32. Le, G., C. T. Russell, and D. S. Orlowski, Coherence lengths of upstream ULF waves: Dual ISEE observations, *Geophys. Res. Lett.* 20, 1755 (1993).

33. Lacombe, C., F. G. E. Panatelli, D. Hubert, C. C. Harvey, A. Mangeney, G. Belmont, and C. T. Russell, Mirror and Alfvénic waves observed by ISEE 1-2 during crossings of the Earth's bow shock, *Ann. Geophys.* 10, 772 (1992).

34. Stringer, T. E., Low-frequency waves in an unbounded plasma, *J. Nucl. energy, Part C* 5, 89 (1963).

35. Formisano, V., and C. F. Kennel, Small amplitude waves in high β plasma, *J. Plasma Phys.* 3, 55 (1969).

36. Orlowski, D. S., C. T. Russell, D. Krauss-Varban, and N. Omidi, A test of the Hall-MHD model: Application to low-frequency upstream waves at Venus, *J. Geophys. Res.* 99, 169 (1994).

37. Anderson, K. A., Measurements of bow shock particles far upstream from the Earth, *J. Geophys. Res.* 86, 4445, (1981).

38. Greenstadt, E. W., G. K. Crawford, R. J. Strangeway, S. L. Moses, and F. V. Coroniti, Spatial distribution of electron plasma oscillations in the Earth's foreshock at ISEE-3, in preparation, 1994.

39. Hospodarsky, G. B., D. A. Gurnett, W. S. Kurth, M. G. Kivelson, R. J. Strangeway, and S. J. Bolton, Fine structure of Langmuir waves observed upstream of the bow shock at Venus, *J. Geophys. Res.* 99, 13,363–13,371 (1994).

40. Feldman, W. C., Electron velocity distributions near collisionless shocks, in *Collisionless Shocks in the Heliosphere: Review of Current Research*, eds. B. T. Tsurutani and R. G. Stone, AGU Geophysical Monograph 35, 195, (1985).

41. Klimas, A. J., The electron foreshock, in *Collisionless Shocks in the Heliosphere: Review of Current Research*, eds. B. T. Tsurutani and R. G. Stone, AGU Geophysical Monograph 35, 237, (1985).

42. Sanderson, T. R., K.-P. Wenzel, R. Reinhard, E. C., Roelof, and E. J. Smith, Observations of upstream protons and low frequency waves on ISEE 3, *J. Geophys. Res.* 88, 85, 1983.

43. Lee, M. A., Coupled hydromagnetic wave excitation and ion acceleration upstream of the earth's bow shock, *J. Geophys. Res.* 87, 5063, 1982.

44. Edmiston, J. P., C. F. Kennel, D. Eichler, Escape of heated ions upstream of a quasi-parallel shock, *Geophys. Res. Lett. 9*, 531, 1982.

45. Skadron, G., R. D. Holdaway, and M. A. Lee, Formation of the wave compressional boundary in the Earth's foreshock, *J. Geophys. Res.* 93, 11,354 (1988).

46. Burgess, D, Cyclic behavior at quasi-parallel collisionless shocks, *Geophys. Res. Lett.* 16, 345 (1989)

47. Onsager, T. G., D. Winske, and M. F. Thomsen, Ion injection simulations of quasi-parallel shock reformation, *J. Geophys. Res.* 96, 21,183 (1991).

48. Kucharek, H., and M. Scholer, Origin of diffuse superthermal ions at quasi-parallel supercritical collisionless shocks, *J. Geophys. Res.* 96, 21,195 (1991).

Pergamon

Adv. Space Res. Vol. 15, No. 8/9, pp. (8/9)29–(8/9)42, 1995

0273–1177/95 $9.50 + 0.00

0273-1177(94)00082-4

VLF WAVES IN THE FORESHOCK

R. J. Strangeway* and G. K. Crawford**,[1]

** Institute of Geophysics and Planetary Physics, University of California at Los Angeles, Los Angeles, CA 90024, U.S.A.*
*** Radio Atmospheric Science Center, Kyoto University, Uji, Kyoto 611, Japan*

ABSTRACT

Plasma waves observed in the VLF range upstream of planetary bow shocks not only modify the particle distributions, but also provide important information about the acceleration processes that occur at the bow shock. Electron plasma oscillations observed near the tangent field line in the electron foreshock are generated by electrons reflected at the bow shock through a process that has been referred to as Fast Fermi acceleration. Fast Fermi acceleration is the same as shock-drift acceleration, which is one of the mechanisms by which ions are energized at the shock. We have generated maps of the VLF emissions upstream of the Venus bow shock, using these maps to infer properties of the shock energization processes. We find that the plasma oscillations extend along the field line up to a distance that appears to be controlled by the shock scale size, implying that shock curvature restricts the flux and energy of reflected electrons. We also find that the ion acoustic waves are observed in the ion foreshock, but at Venus these emissions are not detected near the ULF foreshock boundary. Through analogy with terrestrial ion observations, this implies that the ion acoustic waves are not generated by ion beams, but are instead generated by diffuse ion distributions found deep within the ion foreshock. However, since the shock is much smaller at Venus, and there is no magnetosphere, we might expect ion distributions within the ion foreshock to be different than at the Earth. Mapping studies of the terrestrial foreshock similar to those carried out at Venus appear to be necessary to determine if the inferences drawn from Venus data are applicable to other foreshocks.

INTRODUCTION

Collisionless shocks provide a myriad of phenomena that occur on many different scales, from ion inertial lengths, through ion Larmor radii, to scales of many planetary radii. At the same time, the physics involved may be expressed by simple magnetohydrodynamics, or particle trajectory analysis, or fully kinetic plasma theory. The tools employed include analytic theory, simulations, and data analysis. In this paper we will discuss just one aspect of collisionless shocks, that is the VLF waves that are observed upstream of a planetary bow shock in the region known as the foreshock. Although primarily based on data analysis, we will also discuss some wave instability theory, and the mechanisms by which particles gain energy at a shock.

VLF wave generation is a microscale phenomenon, but the morphology of the waves allows us to make inferences concerning the energization processes that occur at a shock. Moreover, we will show that while the energization occurs on mesoscales, the macroscale of the shock itself appears to be a limiting factor on this process. This will be most clear through analysis of the waves observed in the electron foreshock, and we will devote much of this paper to the electron foreshock, although we will also discuss ion foreshock waves. Our understanding of the electron dynamics within the shock and foreshock appears to be much firmer /1, 2, 3/. While there has been significant progress in our understanding of the

[1]Now at SRI International, Menlo Park, California 94025, U.S.A.

ion dynamics /4, 5, 6, 7/, how the ion distributions within the foreshock interact, how they evolve, and nature of their relationship with both ULF and VLF waves is still a topic of some debate /8, 9, 10/.

Before discussing the VLF observations we will briefly review some of the basic theory on electron reflection and energization at a shock. This will not be a comprehensive review of particle dynamics and energization. In particular we will not discuss in detail why electron dynamics are best investigated in the de Hoffman-Teller (HT) frame /11/, while ion dynamics are more readily understood in the normal incidence frame (NIF). Instead we refer the reader to the excellent articles that discuss why the presence of a non-coplanar magnetic field allows the magnetized electrons to be only affected by the HT frame cross-shock potential, while the unmagnetized ions respond to the full potential in the NIF /12, 13, 14/. Having reviewed the electron reflection process at the shock, we will present some examples of VLF wave data, obtained by the Pioneer Venus Orbiter (PVO). We will then present images of the VLF emissions in the ion and electron foreshock generated from statistical studies of the foreshock at Venus. The most significant result of the imaging is the observation of a finite extent to the electron foreshock emissions, which we attribute to the scale size of the shock acting to restrict the availability of energetic electrons far from the shock. We will then discuss why the limitations of the PVO wave instrument do not allow us to observe down-shifted plasma oscillations in the foreshock. Lastly, we will summarize the results presented in the paper, including some comments on the apparent disparity between the ULF and VLF waves within the ion foreshock.

ELECTRON ACCELERATION

The energetic electrons responsible for the generation of VLF waves in the electron foreshock are mainly of solar wind origin. While energetic electrons could possibly be of magnetospheric origin at the Earth, the presence of electron foreshock VLF waves upstream of the bow shock of Venus, for example, implies that the electrons are indeed accelerated at the shock. Leroy and Mangeney /15/, amongst others, discussed the acceleration of electrons at a bow shock, using the de Hoffman-Teller (HT) transformation /11/ to facilitate their discussion of acceleration, transmission and reflection. The HT transformation is carried out by moving along the shock surface with the velocity that aligns the upstream flow velocity and magnetic field in the transformed frame. In this frame the motional electric field has been transformed away. Thus there can be no energization of reflected electrons in the HT frame, assuming a time stationary shock structure.

The HT frame is a particularly useful frame for discussing the processes involved in electron transmission and reflection at the shock, as can be seen in Figure 1. The left of this figure, after /15/, shows phase space contours of the incident and reflected solar wind electrons. The solar wind has been transformed into the HT frame, and the incident flow is field-aligned, with positive velocities corresponding to flow into the shock from upstream. The dashed hyperbola in the figure gives the boundary between transmitted and reflected electrons. In the HT frame only the jump in the magnetic field causes electron reflection at the shock. In the absence of a field-aligned electric field within the shock, the boundary between transmitted and reflected electrons is a cone. The shock electric field, which retards the ions, accelerates the electrons through the shock, widening the transmission cone into the hyperbolic shape sketched in panel a) of Figure 1. The portion of the incident solar wind that lies outside of this boundary is reflected at the shock and travels back upstream. It is this reflected population that is believed to generate electron plasma oscillations in the electron foreshock.

The de Hoffman-Teller velocity in the observer's frame (which is assumed to be at rest with respect to the shock surface) is given by

$$\mathbf{v}_{HT} = \frac{\mathbf{n} \times (\mathbf{v}_0 \times \mathbf{b})}{\mathbf{b} \cdot \mathbf{n}} = \mathbf{v}_0 - \mathbf{b} \frac{\cos \theta_{vn}}{\cos \theta_{bn}} v_0 \qquad (1)$$

where $\mathbf{n}$ is the shock normal, $\mathbf{v}_0$ is the solar wind velocity in the observer's frame, $\mathbf{b}$ is the unit vector along the magnetic field, θ_{vn} is the angle between the solar wind velocity vector and the shock normal, and θ_{bn} is the angle between the magnetic field and the shock normal. Taking primed vectors to be measured in the HT frame, the transformation from shock frame to HT frame is given by $\mathbf{v}' = \mathbf{v} - \mathbf{v}_{HT}$.

In the HT frame the solar wind moves towards the shock with a speed given by $v_0' = v_0 \cos \theta_{vn} / \cos \theta_{bn}$ along the magnetic field. Since the magnetic field increase at the shock acts as a mirror, the solar wind sees a magnetic mirror moving with the speed v_0', and particles reflected by this moving mirror gain twice this speed in the solar wind frame. Thus this process has been named Fast Fermi acceleration /16/.

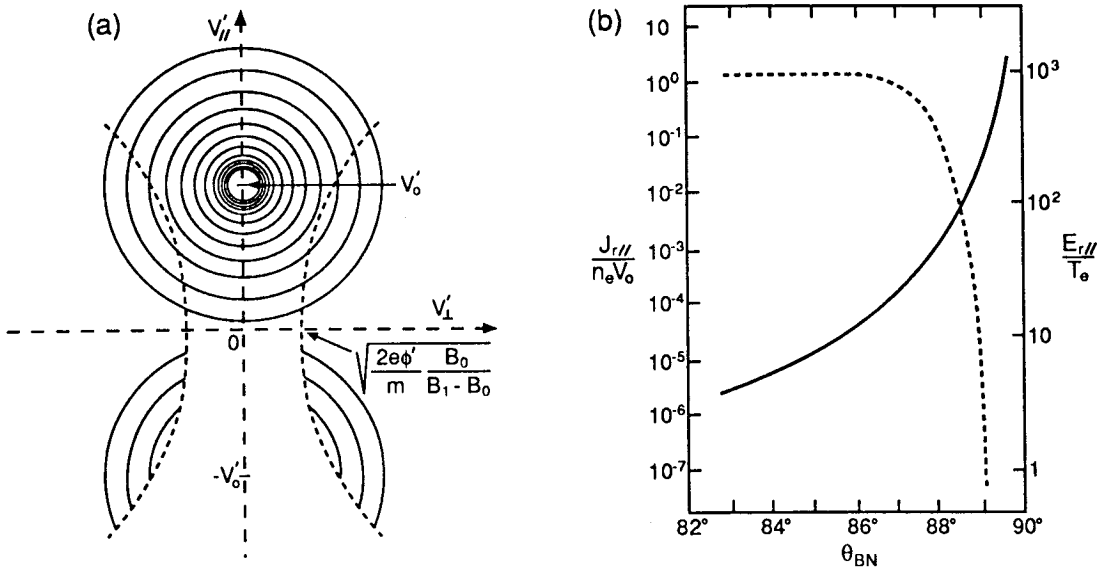

Fig. 1. a) Phase space contours of the incident and reflected solar wind electron population, in the de Hoffman-Teller frame (after /15/). b) Reflected electron flux and energy as a function of θ_{bn} (after /15/).

At first sight, it appears that electrons can gain an arbitrary amount of energy, depending on θ_{bn}. As $\theta_{bn} \rightarrow 90°$, $v_0' \rightarrow \infty$, ignoring relativistic effects. However, as pointed out in /15/, the mirror efficiency $\rightarrow 0$ as $\theta_{bn} \rightarrow 90°$. This can be seen on consideration of Figure 1. As v_0' increases, the whole solar wind population moves to higher parallel velocity, and more and more of the solar wind population lies within the transmission cone. This is further demonstrated in panel b) of Figure 1.

Another point alluded to in /15/ and /16/, but not discussed in detail, concerns the effect of shock curvature. In carrying out the HT frame transformation we assume an infinite planar shock. In reality, planetary bow shocks are curved. This affects the reflection process in two ways. First the area of the curved bow shock over which reflection occurs becomes vanishingly small as $\theta_{bn} \rightarrow 90°$, and so the net flux of reflected particles must $\rightarrow 0$. Second, the amount of energy gain will be restricted by the curvature of the shock. In the HT frame the reflected particles gain no energy, but in the shock frame the particles have gained energy, corresponding to the moving mirror speed. This energy gain can only come from the motional electric field $-\mathbf{v}_0 \times \mathbf{B}$. Furthermore, the electrons gain this energy by drifting along the shock, i.e., shock-drift acceleration /4, 5/. Although shock-drift acceleration is usually discussed in the context of ion acceleration at the shock, the same principles apply to electron acceleration. Taking a solar wind flow velocity of 400 kms^{-1}, and an upstream magnetic field strength of 10 nT, the motional electric field is ≈ 4 mV/m. The tangential electric field is continuous across the shock, and so a particle gains an energy of the order 25 keV/R_e in drifting along the shock surface. For a shock, such as the terrestrial bow shock, whose radius of curvature is of the order 20 R_e, electrons can gain moderately high energies before shock curvature effects become significant. However, for smaller shocks, such as the Venus bow shock, whose radius of curvature $\approx 2\ R_v$ (1 R_v = 6052 km, 1 R_e = 6371 km), curvature effects are likely to limit the energy gain of the electrons. At Mars, with an even smaller radius of curvature, and weaker magnetic field, we would expect the effect of shock curvature to be even more significant.

Since shock curvature changes θ_{bn} along the bow shock, we expect electrons which encounter the shock further downstream to in general gain less energy than those electrons that encounter the bow shock near the point of where the IMF is a tangent to the shock surface. This tangent field line also marks the limit of accessibility for reflected particles, since they are convected downstream by the solar wind motional electric field. The lower energy particles take longer to travel any given distance along the field, and so they are convected further downstream by the solar wind electric field. This time-of-flight effect was first used by Filbert and Kellogg /17/ to explain the presence of electron plasma oscillations in the electron foreshock. In Figure 1 all the particles outside of the transmission cone are reflected. However, at any particular location in the foreshock, there exists a critical parallel velocity, below which the particles are convected downstream before they can propagate from the shock to the point of observation. The resultant low energy cut-off in the reflected population introduces a positive slope in the reduced distribution function (i.e., the distribution function integrated over $v_\perp$), which can generate plasma oscillations through the bump-on-tail instability.

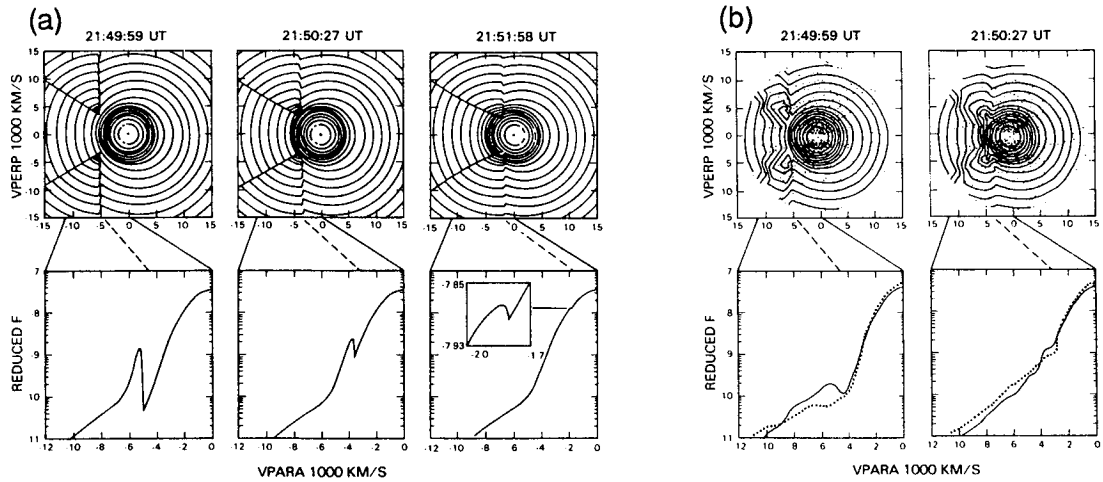

Fig. 2. Foreshock electron distributions (after /18/). The left panels (a) show theoretical phase space density contours, together with the reduced distribution function. The right panels (b) show the same phase distributions, but sampled in a manner similar to a particle instrument. In this case the reduced distribution functions (solid curves) are compared with actual observations (dotted curves).

Fitzenreiter et al. /18/ developed a model for electron distributions in the foreshock. In their work they took into account the curvature of the shock through changes in the HT speed as a function of θ_{bn}, and through kinematic restrictions on the allowed trajectories. Figure 2 shows some results of their modeling. Two effects are clear from the figure. The first is that the reflected distribution lies at oblique angles with respect to the magnetic field. The boundaries of the "earlike" structure are given by the transmission cone at high energy, and the time-of-flight cut-off velocity at low energy. As discussed in /18/, the distribution is built up from reflected electrons from different portions of the shock. The net effect of this is to steepen the time-of-flight gradient in the distribution. The second effect in Figure 2 is that the instrument sampling smears any gradients in the phase space distribution. Thus, because of instrument sampling, and also the smoothing that occurs in response to the wave generation, the typical signature of the reflected electrons tends to be a high energy tail. The break in the distribution marks the cut-off velocity.

The basic concepts of "Fast Fermi" acceleration at the bow shock and time-of-flight cut-offs appear to be sufficient to explain many of the features of VLF waves in the electron foreshock, as we shall see below. However, there are still some effects not yet incorporated into theory, primarily the restriction on electron energization imposed by shock curvature, as briefly discussed above. This can best be seen through studies of the electron foreshock at Venus.

VLF EMISSIONS AT VENUS: EXAMPLES

In order to understand VLF wave phenomena in the Venus foreshock it useful to make use of a coordinate system first derived for terrestrial observations /17, 19/, shown in Figure 3 for the Venus bow shock /20, 21/. This figure shows the IMF, solar wind, bow shock, and the observing spacecraft (PVO) in the aberrated Venus Solar Orbital (VSO) coordinate system. (VSO coordinates are analogous to Geocentric Solar Ecliptic Coordinates.) In Figure 3 we have assumed that the plane containing the solar wind and IMF, the B-v plane, also contains the center of the planet. For convenience we refer to this as the equatorial plane. In general, the observing spacecraft need not lie in the equatorial plane, but the geometry is similarly defined, except that the B-v plane containing the spacecraft intersects the bow shock in a plane parallel to the equatorial plane. The tangent field line then intersects the shock further downstream from the point of tangency in the equatorial plane.

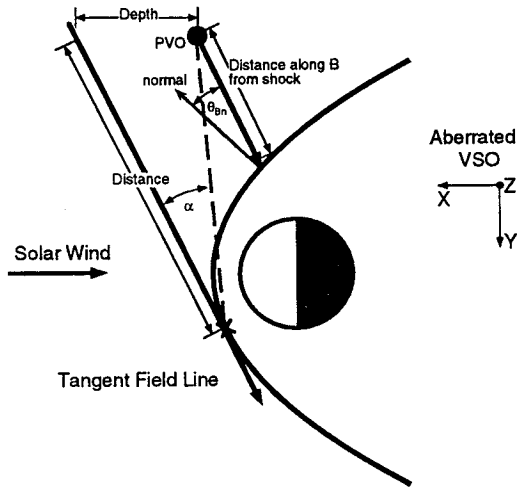

Fig. 3. Foreshock coordinate system at Venus (after /20, 21/).

Depending on the phenomenon of interest, various coordinates systems can be chosen. However, given the discussion in the previous section, we use the distance along the tangent field line and the depth downstream from the tangent field line to the point of observation as the foreshock coordinate system. For a reflected particle the distance depends primarily on the parallel reflection velocity, while the depth is governed by the solar wind flow. An alternative coordinate system could use the time-of-flight angle (α), and the distance traveled along the time-of-flight velocity vector, indicated by the dashed line. Other parameters of interest include the shock normal direction (θ_{bn}) as measured at the point of intersection on the bow shock of the field line passing through the spacecraft, and the distance along the field line from the bow shock to the spacecraft. Note that as drawn in Figure 3 the shock normal lies in the B-v plane, but this is not the case when the B-v plane containing the spacecraft lies above or below the equatorial plane.

An example of the VLF emissions observed in the foreshock of Venus is shown in Figure 4 /20, 21/. This figure shows 1 hr 45 min of data acquired by PVO when it was in the solar wind, some 5 R_v behind and the terminator and about 7 R_v from the Venus-Sun line. The top four panels show wave electric field intensity, measured at 30 kHz, 5.4 kHz, 730 Hz, and 100 Hz, which are the four frequency channels of the Orbiter Electric Field Detector (OEFD). The OEFD was restricted to these four frequencies because of the power, weight, and telemetry restrictions of the Pioneer Venus Orbiter /22, 23, 24/. Because the OEFD antenna is so short, 0.76 m, the wave instrument suffers from high levels of interference when the spacecraft is in sunlight and the plasma Debye length is large, as occurs when the spacecraft is in the solar wind. The 100 Hz channel is most susceptible to this interference. However, in Figure 4 we have applied a noise removal scheme based on Bayesian statistical methods /25/ to the data, and much of the

noise has been removed. The middle four panels in Figure 4 show the magnetic field components in VSO coordinates and total field strength. The bottom two panels show depth behind the tangent field line, and θ_{bn} at the bow shock intersection point of the field line passing through the spacecraft. When the depth is negative the spacecraft is upstream of the tangent field line, and θ_{bn} is not defined. On the other hand, depth is not defined if the magnetic field becomes sufficiently close to radial that there is no field line that is tangent to the bow shock, although θ_{bn} is defined. The changes in depth and θ_{bn} are mainly due to changes in the IMF orientation, rather than spacecraft motion.

In Figure 4 waves are observed at 30 kHz for the first 20 min of data shown. At this time depth is small and positive, while θ_{bn} is > 45°, indicating that the spacecraft is in the electron foreshock. Around 0605 UT there is a rotation in the IMF, and from 0605 UT to 0627 UT most of the wave activity occurs in the 5.4 kHz and 730 Hz channels. Depth is generally larger than before this time, and the waves are most intense when θ_{bn} drops below 45°. This suggests that at this time the spacecraft is in the ion foreshock. Also some ULF waves are present when the VLF waves are most intense, again indicative of the ion foreshock. After 0630 UT depth is mainly negative until 0645 UT, at which time the rotation in the IMF causes the electron foreshock to rapidly sweep over the spacecraft, and we observe a brief burst of 30 kHz noise. From 0650 UT until the end of the data the spacecraft is deep in the ion foreshock, and intense 5.4 kHz, 730 Hz, and ULF waves are observed. Throughout most of the interval after 0650 UT the spacecraft is upstream of a quasi-parallel bow shock.

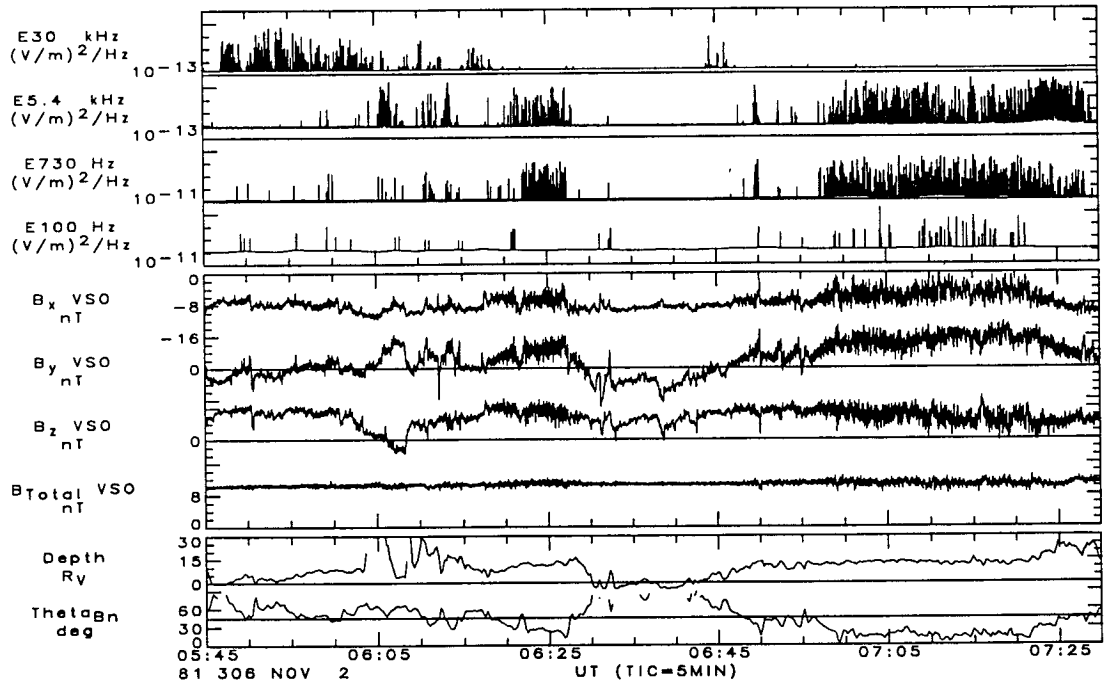

Fig. 4. Example of VLF emissions observed in the foreshock at Venus (after /20, 21/).

Figure 4 provides a succinct overview of the types of wave phenomena observed by PVO in the foreshock at Venus. The VLF waves observed in the foreshock of Venus have been analyzed in terms of polarization, intensity as a function of location within the foreshock, and dependence on solar wind plasma density /20, 21, 26/. The 30 kHz wave intensity peaks at the tangent field line, with a peak amplitude around 10 mV/m /26/, comparable to plasma oscillations detected at the Earth /17/. Using the variation in plasma density to scan in frequency, the 30 kHz wave intensity is centered on the local plasma frequency /26/, and the waves are polarized parallel to the magnetic field /21, 26/. It is hence clear that the waves generated at the tangent field line are indeed plasma oscillations. The 5.4 kHz and lower frequency waves, on the other hand, tend to be observed further downstream from the tangent field line

/21/. Comparisons with terrestrial observations shows a similar spectral shape, with the wave power extending up to 10 times the ion plasma frequency, with intensities comparable to those observed by the ISEE-2 spacecraft /21/. Through comparison of wave power as observed on both the ISEE-1 and -2 spacecraft it was concluded that the wavelength of the VLF waves in the terrestrial foreshock was > 30 m (the length of the ISEE-2 antenna), but less than 215 m (ISEE-1) /27/. The PVO antenna is even shorter than the ISEE-2 antenna, but since the wavelength is greater than the antenna length in both cases, the observed wave power is independent of wavelength. At Venus the 5.4 kHz waves were found to be parallel polarized /21/, which contradicts a terrestrial study /28/ that used wave interference patterns to show that the wave vector direction was typically 40° away from the magnetic field. This apparent contradiction has yet to be resolved, but may be a consequence of the spin averaging used for determining wave polarization in the PVO studies.

VLF EMISSIONS AT VENUS: MAPPINGS

Although the PVO plasma wave instrument suffers from a lack of frequency resolution, there are advantages to studying VLF data at Venus. First of all, the PVO orbit had apoapsis around 12 R_v, much larger than the size of the Venus obstacle, and so the spacecraft spent a significant amount of time on each orbit in the unshocked solar wind. Furthermore, the spacecraft was in the solar wind both in the sub-solar region, and also well past the planetary terminator, thus allowing a much larger area of the foreshock to be mapped. Last the spacecraft was in orbit around Venus for 14 years, and we can carry out large statistical studies. A preliminary study /29/ using data from nearly one Venus year (200 orbits) showed the usefulness of imaging the Venus foreshock using VLF data. Subsequently /20/, this study was extended using a separate set of 650 orbits. The results of this study are presented in Figures 5 and 6.

In Figure 5 the data have been restricted to those intervals for which the IMF was within ± 10° of the nominal Parker spiral in the B-v plane. As discussed in /20/ and /29/, the technique employed in generating the maps is to calculate for each observation the distance along the tangent field line and depth behind the tangent line using the instantaneous IMF, and a model bow shock that has been scaled to the observed bow shock location for each orbit. In scaling the bow shock, we have only changed the semi-latus rectum (L) of the conic of revolution that specifies the shock. This conic of revolution is given by

$$R = \frac{L}{1 + \varepsilon \cos \theta_{sz}} \tag{2}$$

where R is radial distance from the focus, ε is the eccentricity, and θ_{sz} is the solar zenith angle with respect to the focus. In generating the maps we used a bow shock model with $\varepsilon = 1.03$, and focus at 0.45 R_v sunward of the planet /20, 21, 30/. When matching bow shock models to actual observations, it is preferable to keep the shock shape (specified by ε) and focus fixed, and allow the size (specified by L) to change /31/.

Having calculated depth and distance, these are then converted to a Cartesian coordinate location with respect to the point of tangency in the B-v plane by assuming the IMF is at the nominal Parker spiral angle (35° at Venus), even though the instantaneous IMF may be at some other angle. This is done to prevent "smearing" of the tangent field line, which would occur if the instantaneous IMF orientation was used to specify the location. Finally, all the parallel B-v planes are mapped to the equatorial plane, using the point of tangency in each plane as the common reference point. Although we have mixed flank bow shock intersections with sub-solar intersections, this does not appear to drastically alter the statistical results /20/. Once the data have been mapped to a common foreshock geometry, the data are accumulated in bins with 1 × 1 R_v resolution.

At the top left of Figure 5 we show the 9th decile of the 30 kHz wave intensity. Although the data have been accumulated in 1 × 1 R_v bins we have interpolated the data in generating the maps. The color scale shows the $\log_{10}$ of the wave intensity. The small black dot is the point of tangency. At the bottom left of the figure we show the $\log_{10}$ of the number of samples per 1 × 1 R_v bin. Throughout most of the distribution we have over 100 samples per bin, and thus we have high statistical confidence in the results. In

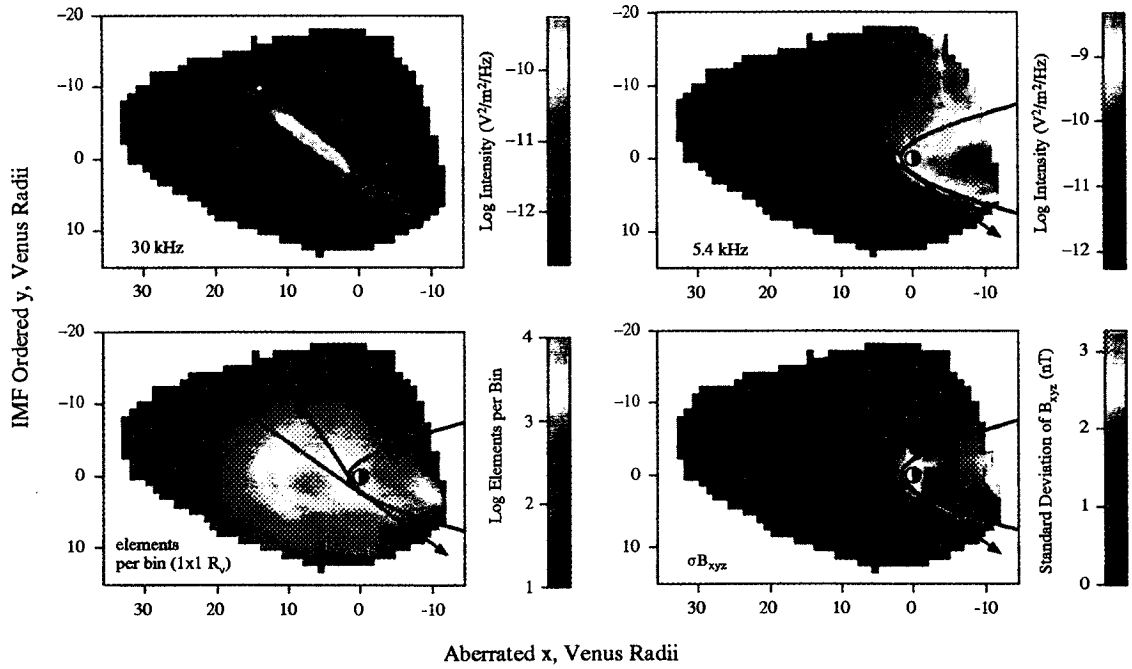

Fig. 5. VLF map of the Venus foreshock for nominal Parker spiral (after /20/).

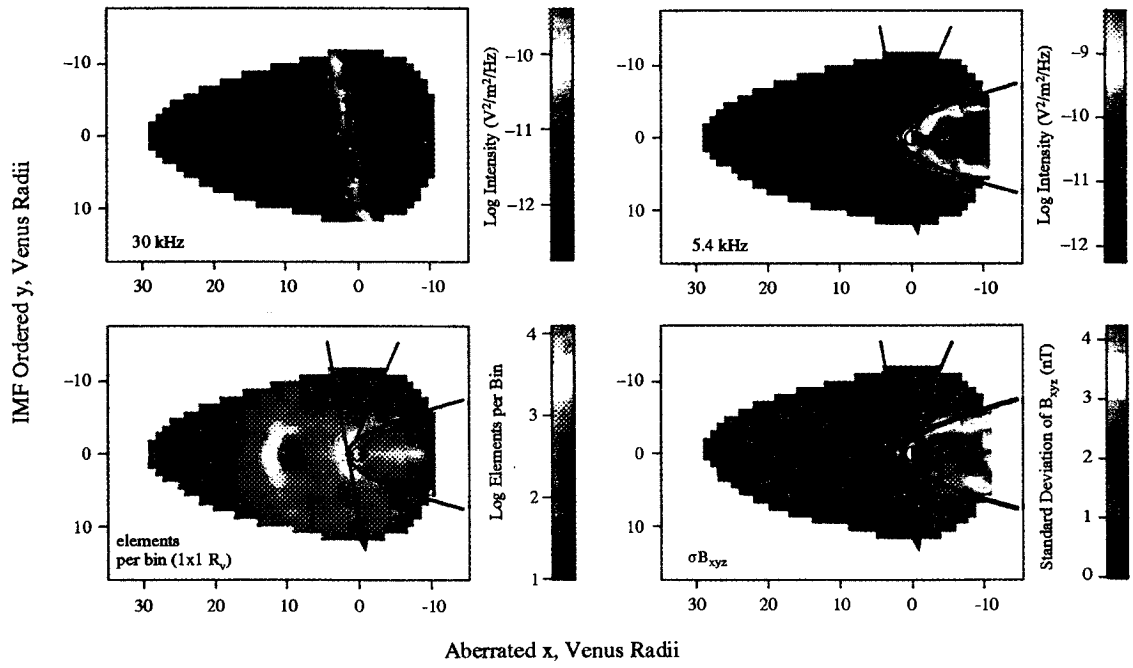

Fig. 6. VLF map of the Venus foreshock for perpendicular IMF (after /20/).

the bottom panel we have superimposed the reference bow shock model used in generating the maps, given by $L = 1.69\ R_v$ /21, 26/.

It is clear that the 30 kHz emissions occur mainly along the tangent field line. In addition, the wave intensity only reaches a maximum a few R_v away from the point of tangency. Moreover, the wave intensity shows a marked decrease some 15 R_v upstream of the point of tangency. Similar mapping studies using ISEE–3 data show wave emissions extending up to ~ 100 R_v along the tangent field-line /32/. Thus the electron foreshock emissions seem in part to be controlled by the scale size of the shock, consistent with limits being imposed on the Fast Fermi process through shock curvature, as noted earlier. If the drop-off was due to some inherent properties of the plasma instability and subsequent saturation processes, we would expect the drop-off scale to be independent of shock-size, instead being controlled by some scale dependent on the ambient plasma parameters. Since the solar wind is very similar at the Earth and Venus, such a scale factor would be the same at both planets.

We also note that in Figure 5 the electron foreshock emissions that are upstream of the tangent point appear to be stronger than the emissions in the downstream region. This could be attributed to two possible causes /20/. The first is that the solar wind electron distribution is asymmetric, there is a heat flux from the sun, and electrons energized at the bow shock will be flowing in the same direction as this heat flux in the downstream foreshock, thus reducing the slope in the distribution function, and hence the growth rate for instability. The second possibility can be seen on inspection of (1). While the electrons are coming from regions with roughly the same θ_{bn}, the shock normal is almost parallel to the solar wind flow in the sub-solar region, while the shock normal is more nearly perpendicular along the flanks. The θ_{vn} dependence of the de Hoffman-Teller velocity implies that the electron acceleration will be weaker for the downstream foreshock. However, the interplay between changes in θ_{vn} and changes in θ_{bn} requires further analysis, similar to /18/, but taking into account both upstream and downstream foreshocks.

In this paper we have concentrated on the electron foreshock emissions, but one or two remarks are in order concerning the ion foreshock emissions at Venus, as revealed in the Figure 5. At the right of Figure 5 we include maps of the 9th decile of wave intensity measured at 5.4 kHz, and the standard deviation of the trace of the magnetic field. The 5.4 kHz channel is used to monitor the ion acoustic emissions in the foreshock, while the magnetic field deviation is a proxy for the presence of ULF waves. The line intersecting the model bow shock behind the tangent field line is the ULF boundary obtained from terrestrial studies /33/, but modified for the nominal Parker spiral orientation at Venus /21/. The ULF waves are most intense near the bow shock, and tend to be confined to locations behind the ULF boundary. The 5.4 kHz emissions, on the other hand, appear to be confined to locations even further downstream of the model ULF boundary. It is normally assumed, and Figure 4 appears to bear this out, that the ULF waves and VLF ion acoustic waves are both seen together. However, Figure 5 implies that this is only the case for observations deep in the ion foreshock. This suggests that different plasma populations are responsible for the different waves. Unfortunately, no similar mapping studies of the terrestrial ion foreshock have been carried out to determine if this result is unique to Venus. The smaller shock scale size at Venus will probably result in weaker Fermi and shock-drift acceleration, This, together with the lack of magnetosphere to act as a reservoir of energetic leakage particles, leads us to expect that the ion foreshock at Venus will be populated by lower energies and fluxes than at the Earth.

In Figure 6 we repeat the foreshock analysis, but now for IMF orientations nearly perpendicular to the solar wind flow. We find that the electron foreshock emissions are still present, but with intensities that lie between those observed in the upstream and downstream foreshock as shown in Figure 5. That the 30 kHz emissions are weaker than in the upstream foreshock of Figure 5 is consistent with our arguments concerning the θ_{vn} dependence of the electron reflection process. The ion foreshock VLF emissions are almost completely absent. There is perhaps a hint of ULF emissions close to the shock behind the model ULF boundary.

DOWN-SHIFTED PLASMA OSCILLATIONS

In addition to the emissions at the plasma frequency that occur close to the tangent field, VLF waves are also observed at frequencies below the plasma frequency in the terrestrial foreshock /34, 35/. These waves are referred to as down-shifted plasma oscillations. It should be noted that "down-shift" does not mean that the waves are shifted in frequency due to a frame transformation, as opposed to ion acoustic waves, for example, which are "up-shifted" to several kHz in the ion foreshock because of their short wavelength. The down-shift is too large to be accounted for simply by Doppler-shift /35/. An example of down-shifted plasma oscillations is shown in Figure 7. The top panel shows wideband electric field data from the ISEE-1 spacecraft. The bottom panel shows the distance behind the tangent field line ("Diff"). The sign convention for Diff is the opposite of the convention we have used in discussing the PVO observations, with negative Diff corresponding to locations behind the tangent field line. A narrow-band intense wave emission is observed when the spacecraft is close to the tangent line. Just behind the tangent line this emission tends to increase in frequency, but at much greater depths the emission moves to lower frequencies. Typically the plasma frequency wave amplitude is a few mV/m, while the down-shifted emission is much weaker, only a few 100 mV/m /34/. In terms of wave power, the plasma frequency emission can be as intense as 10^{-10} $V^2/m^2/Hz$, and the down-shifted emission is typically less than 10^{-12} $V^2/m^2/Hz$ /34/.

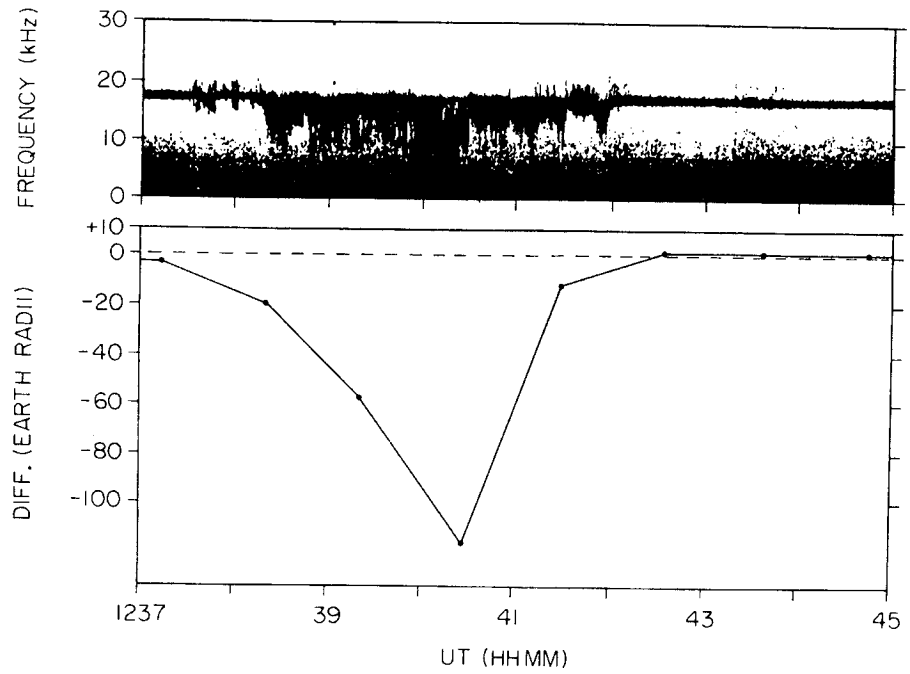

Fig. 7. Example of down-shifted plasma oscillations observed in the terrestrial electron foreshock (after /35/).

The most energetic reflected electrons are found close to the tangent field line. At greater depths the energy decreases. This decrease in the electron beam energy appears to explain the down-shift, as shown in Figure 8 (after /35/). This figure shows the results of a linear stability analysis where the ambient electrons are represented by a Maxwellian distribution, and the beam electrons are modeled by a Lorentzian distribution. The left panel of the figure shows that the maximum growth rate decreases as the beam velocity decreases with respect to the ambient electron thermal velocity. In addition, the frequency at which the maximum growth occurs shifts to progressively lower frequencies with respect to the plasma frequency. This conclusion is reinforced in the right panel which shows the frequency of maximum growth as a function of beam velocity for different beam temperatures.

Given many of the similarities of the terrestrial and Venusian bow shock and electron foreshock, it appears reasonable to expect that down-shifted plasma oscillations should also be present at Venus, but Figures 5 and 6 show no evidence of these waves. The lack of down-shifted oscillations appear to be mainly due to the limitations of the PVO wave instrument /26, 32/. First, the large frequency spacing between channels (5.4 kHz and 30 kHz), coupled with the relatively narrow bandwidth of the frequency filters (30%) implies that down-shifted waves will not be well sampled by the instrument. Second, and perhaps more importantly, the short antenna length reduces the sensitivity of the PVO instrument. The background level of the color plots in Figures 5 and 6 is the instrument background. At 30 kHz this level is $\approx 5 \times 10^{-13}$ $V^2/m^2/Hz$. The peak intensities at the tangent field line are $\approx 5 \times 10^{-10}$ $V^2/m^2/Hz$, which is comparable to the terrestrial observations, while the instrument threshold is comparable to the down-shifted wave intensities /34/. Thus the PVO instrument is not likely to observe the down-shifted waves. However, such waves are present at Venus. The much more sensitive Galileo wave instrument detected down-shifted plasma oscillations during the flyby of Venus. These emissions depended on depth in a manner similar to the terrestrial observations /36/.

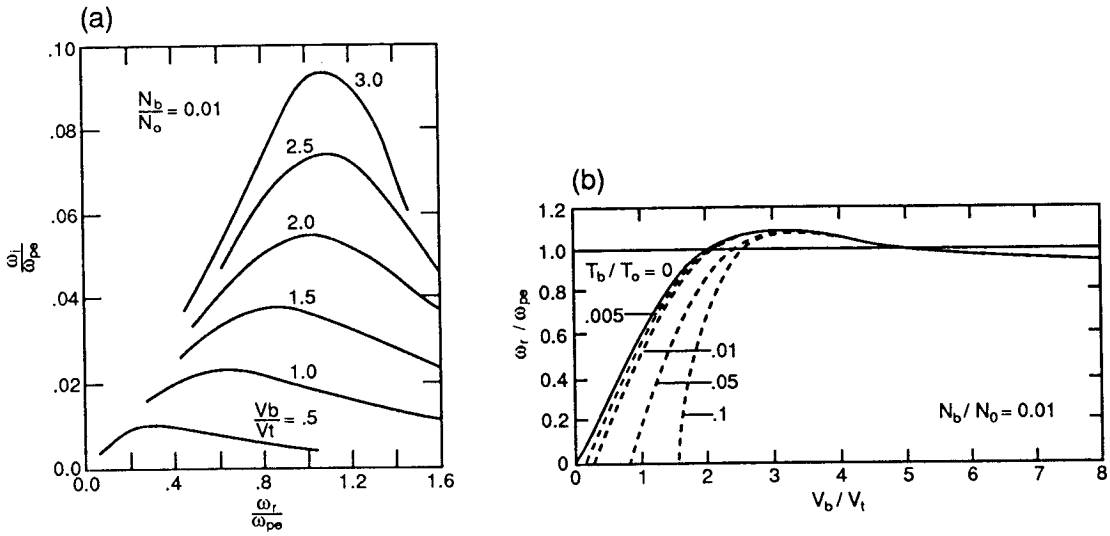

Fig. 8. Solutions of the beam-plasma dispersion relation. The left panel shows growth rate versus frequency for different beam velocities. The right panel shows the frequency at which maximum growth occurs as a function of beam velocity for different beam temperatures (after /35/).

SUMMARY AND CONCLUSIONS

VLF waves observed in the electron foreshock that is present upstream of planetary bow shocks appear to be a useful diagnostic of the energization processed that occur at the bow shock. First, the waves themselves provide a very clear marker of the tangent field line. As such they can be used for remote sensing of the bow shock /37/, although some care must be exercised in inferring the bow shock location /31/. Some of the more extreme shock shapes in /37/ arise from allowing the focus of the shock to change, rather than the semi-latus rectum. Varying the latter parameter is more physically realistic since it determines the size of the forward part of the shock near the obstacle, which will vary as a function of Mach number, while the focus is mainly fixed by the obstacle.

Second, the evolution of the waves as a function of both depth and distance provide information on the energization process. The changes that are a function of depth are clearly related to the decrease in reflection energy, and provide confirmation of both the time-of-flight models, and also the validity of Fast Fermi (or alternatively, electron shock-drift) acceleration. The dependence on distance observed within the Venus foreshock may also have important lessons concerning the effects of curved shocks on

the electron energization. It appears that the shock radius of curvature is an important controlling factor in limiting the availability of energetic electrons in the foreshock. As such we might expect the plasma emissions to be observed at progressively larger distances as the shock radius of curvature decreases. Studies of the terrestrial foreshock appear to confirm this /32/.

A comparison with foreshock data from the outer planets and also from interplanetary shocks would be useful. Unfortunately, it is only statistical studies, such as shown in Figures 5 and 6, that allow us to determine the spatial extent of the foreshock emissions. Most wave observations at the outer planets are from flybys, or from relatively close orbiters such as the Phobos spacecraft at Mars /38, 39/.

The ion foreshock appears to be much more complicated than the electron foreshock. As other papers in this issue indicate /8, 9, 10/, our understanding of the ion foreshock is far from complete. This is not only the case for the VLF waves, but also for the source of the ions in the foreshock, and the role that ULF waves have to play in modifying the ion distributions. From our studies of the ion foreshock at Venus we are drawn to the conclusion that the ULF and ion acoustic waves are not necessarily observed at the same time, especially further away from the shock. Figure 5 indicates that the VLF waves in the ion foreshock are generated well downstream of where ion beams are expected to be present, rather they are observed where we might expect diffuse ions to be present. Unfortunately, the solar wind instrument on PVO was not able to provide detailed distributions within the foreshock. Also, since similar studies have not been carried out at the Earth, we do not know if this separation of ULF and VLF signatures is specific to the Venus foreshock, or if such features are also present at the Earth.

In conclusion, VLF waves observed in planetary foreshocks can provide information about the underlying plasma that generates the waves. The waves of course indicate the presence of free energy within the plasma. However, through maps of the wave emissions we may be able to infer more about the mechanisms that are responsible for the free energy. This appears to be the case for the electron foreshock, where maps of the VLF emissions suggest that shock curvature limits the energization of the electrons. For the ion foreshock, on the other hand, it may be necessary to reconsider the source of the VLF waves. Rather than being generated by ion beams /40/, the waves may be generated by the more diffuse distributions, implying that the waves are generated through pitch angle anisotropy within the ion distribution. Maps of the ion foreshock emissions at planets other than Venus would probably help in determining the validity of this speculation.

ACKNOWLEDGMENTS

This work was supported by NASA grants NAG2–485 and NAGW–3497.

REFERENCES

1. Klimas, A. J., The electron foreshock, in *Collisionless Shocks in the Heliosphere: Reviews of Current Research* (eds. B. T. Tsurutani, and R. G. Stone), pp. 237–252, Geophysical Monograph 35, American Geophysical Union, Washington, 1985.

2. Fitzenreiter, R. J., The electron foreshock, *Adv. Space Res.*, this issue.

3. Scudder, J. D., A review of the cause of electron temperature increase in collisionless shocks, *Adv. Space Res.*, this issue.

4. Forman, M. A., and G. M. Webb, Acceleration of energetic particles, in *Collisionless Shocks in the Heliosphere: A Tutorial Review* (eds. R. G. Stone, and B. T. Tsurutani), pp. 91–114, Geophysical Monograph 34, American Geophysical Union, Washington, 1985.

5. Armstrong, T. P., M. A. Pesses, and R. B. Decker, Shock drift acceleration, in *Collisionless Shocks in the Heliosphere: Reviews of Current Research* (eds. B. T. Tsurutani, and R. G. Stone), pp. 271–285, Geophysical Monograph 35, American Geophysical Union, Washington, 1985.

6. Gosling, J. T., and A. E. Robson, Ion reflection, gyration, and dissipation at supercritical shocks, in *Collisionless Shocks in the Heliosphere: Reviews of Current Research* (eds. B. T. Tsurutani, and R. G. Stone), pp. 141–151, Geophysical Monograph 35, American Geophysical Union, Washington, 1985.

7. Thomsen, M. F., Upstream suprathermal ions, in *Collisionless Shocks in the Heliosphere: Reviews of Current Research* (eds. B. T. Tsurutani, and R. G. Stone), pp. 253–270, Geophysical Monograph 35, American Geophysical Union, Washington, 1985.

8. Greenstadt, E. W., G. Le, and R. J. Strangeway, ULF waves in the foreshock, *Adv. Space Res.*, this issue.

9. Fuselier, S. A., Ion distributions in the Earth's foreshock upstream from the bow shock, *Adv. Space Res.*, this issue.

10. Scholer, M., Interaction of upstream diffuse ions with the solar wind, *Adv. Space Res.*, this issue.

11. de Hoffman, F., and E. Teller, Magneto-hydrodynamic shock, *Phys. Rev.*, 80, 692 (1950).

12. Goodrich, C. C., and J. D. Scudder, The adiabatic energy change of plasma electrons and the frame dependence of the cross-shock potential at collisionless magnetosonic shock waves, *J. Geophys. Res.*, 89, 6654–6662 (1984).

13. Scudder, J. D., A. Mangeney, C. Lacombe, C. C. Harvey, and T. L. Aggson, The resolved layer of a collisionless, high b, supercritical, quasi-perpendicular shock wave 2. Dissipative fluid electrodynamics, *J. Geophys. Res.*, 91, 11,053–11,073 (1986).

14. Ellison, D. C., and Jones, E. C., Non-coplanarity magnetic fields in shock transition layers, *Adv. Space Res.*, this issue.

15. Leroy, M. M. and A. Mangeney, A theory of energization of solar wind electrons by the Earth's bow shock, *Annales Geophysicae.*, 2, 449–456 (1984).

16. Wu, C. S., A fast Fermi process: Energetic electrons accelerated by a nearly perpendicular bow shock, *J. Geophys. Res.*, 89, 8857–8862 (1984).

17. Filbert, P. C., and P. J. Kellogg, Electrostatic noise at the plasma frequency beyond the Earth's bow shock, *J. Geophys. Res.*, 84, 1369 (1979).

18. Fitzenreiter, R. J., J. D. Scudder, and A. J. Klimas, Three-dimensional analytical model for the spatial variation of the foreshock electron distribution function: Systematics and comparisons with ISEE observations, *J. Geophys. Res.*, 95, 4155–4173 (1990).

19. Greenstadt, E. W., and L. W. Baum, Earth's compressional foreshock boundary revisited: Observations by the ISEE 1 magnetometer, *J. Geophys. Res.*, 91, 9001–9006 (1986).

20. Crawford, G. K., *A Study of Plasma Waves Arising from the Solar Wind Interaction with Venus*, Ph. D. Thesis, University of California at Los Angeles, 1993.

21. Crawford, G. K., R. J. Strangeway, and C. T. Russell, VLF emissions in the Venus foreshock: Comparisons with terrestrial observations, *J. Geophys. Res.*, 98, 15,305–15,317 (1993).

22. Scarf, F. L., W. W. L. Taylor, and P. V. Virobik, The Pioneer Venus Orbiter plasma wave investigation, *IEEE Trans. Geosci. Remote Sens.*, GE-18, 36–38 (1980).

23. Scarf, F. L., W. W. L. Taylor, C. T. Russell, and R. C. Elphic, Pioneer Venus plasma wave observations: The solar wind–Venus interaction, *J. Geophys. Res.*, 85, 7599–7612 (1980).

24. Strangeway, R. J., Plasma waves at Venus, *Space Sci. Rev.*, 55, 275–316 (1991).

25. Higuchi, T., G. K. Crawford, R. J. Strangeway, and C. T. Russell, Separation of spin synchronous signals, *Annals of the Institute of Statistical Mathematics* 46, 405–428, 1994.

26. Crawford, G. K., R. J. Strangeway, and C. T. Russell, Electron plasma oscillations in the Venus foreshock, *Geophys. Res. Lett.*, 17, 1805–1808 (1990).

27. Anderson, R. R., G. K. Parks, T. E. Eastman, D. A. Gurnett, and L. A. Frank, Plasma waves associated with energetic particles streaming upstream into the solar wind from the Earth's bow shock, *J. Geophys. Res.*, 86, 4493–4510 (1981).

28. Fuselier, S,. A., and D. A. Gurnett, Short wavelength ion waves upstream of the Earth's bow shock, *J. Geophys. Res.*, 89, 91–103 (1984).

29. Crawford, G. K., R. J. Strangeway, and C. T. Russell, VLF imaging of the Venus foreshock, *Geophys. Res. Lett.*, 20, 2801–2804 (1993).

30. Slavin, J. A., R. E. Holzer, J. R. Spreiter, and S. S. Stahara, Planetary Mach cones: Theory and observation, *J. Geophys. Res.*, 89, 2708–2714 (1984).

31. Farris, M. H., and C. T. Russell, Determining the standoff distance of the bow shock: Mach number dependence and use of models, *J. Geophys. Res.*, 99, 17,681–17,689 (1994).

32. Greenstadt, E. W., G. K. Crawford, R. J. Strangeway, S. L. Moses, and F. V. Coroniti, Spatial distribution of electron plasma oscillations in the Earth's foreshock at ISEE-3, in preparation, personal communication, 1994.

33. Le, G., and C. T. Russell, A study of ULF wave foreshock morphology–1: ULF foreshock boundary, *Planet. Space Sci.*, 40, 1203–1213 (1992).

34. Etcheto, J., and M. Faucheux, Detailed study of electron plasma waves upstream of the Earth's bow shock, *J. Geophys. Res.*, 89, 6631–6653 (1984).

35. Fuselier, S. A., D. A. Gurnett, and R. J. Fitzenreiter, The downshift of electron plasma oscillations in the electron foreshock region, *J. Geophys. Res.*, 90, 3935–3946 (1985).

36. Hospodarsky, G. B., D. A. Gurnett, W. S. Kurth, M. G. Kivelson, R. J. Strangeway, and S. J. Bolton, Fine structure of Langmuir waves observed upstream of the bow shock at Venus, *J. Geophys. Res.*, 99, 13,363–13,371 (1994).

37. Cairns, I. H., C. W. Smith, W. S. Kurth, D. A. Gurnett, and S. Moses, Remote sensing of Neptune's bow shock: Evidence for large scale shock motions, *J. Geophys. Res.*, 96, 19,153–19,169 (1991).

38. Skalsky, A., R. Grard, S. Klimov, C. M. C. Nairn, J. G. Trotignon, and K. Schwingenschuh, The Martian bow shock: Wave observations in the upstream region, *J. Geophys. Res.*, 97, 2927–2933 (1992).

39. Trotignon, J. G., A. Skalsky, R. Grard, C. Nairn, and S. Klimov, Electron density in the Martian foreshock as a by-product of the electron plasma oscillation observations, *J. Geophys. Res.*, 97, 10,831–10,840 (1992).

40. Fuselier, S. A., S. P. Gary, M. F. Thomsen, S. J. Bame, and D. A. Gurnett, Ion beams and the ion/ion acoustic instability upstream from the Earth's bow shock, *J. Geophys. Res.*, 92, 4740–4744 (1987).

JOURNAL OF GEOPHYSICAL RESEARCH, VOL. 100, NO. A8, PAGES 14,523–14,535, AUGUST 1, 1995

Intermediate transition in the Venus ionosheath

H. Perez-de-Tejada
Institute of Geophysics, National University of Mexico Ensenada, Baja California

D. S. Intriligator
Carmel Research Center, Santa Monica, California

R. J. Strangeway
Institute of Planetary Geophysics and Space Physics, University of California, Los Angeles

Abstract. We present the results of an analysis of Pioneer Venus Orbiter (PVO) plasma and electric and magnetic field data with evidence of a plasma transition along the flanks of the Venus ionosheath for 8 PVO passes near the terminator. This transition occurs between the bow shock and the ionopause and represents a stationary change in the properties of the shocked solar wind that streams around the Venus ionosphere. We find that the intermediate transition is characterized by three concurrent features: (1) A noticeable electric field burst measured with the 30 kHz channel of the electric field detector of the PVO; (2) a severe drop of the magnetic field intensity accompanied by a strong rotation of the magnetic field orientation to a direction closer to the Sun-Venus axis in the inner ionosheath; and (3) substantially enhanced plasma fluxes detected at the time when these changes in the electric and magnetic fields are measured. The peak particle flux and the peak magnetic field intensity measured at this transition in the data of the 17 PVO orbits are also presented. It is found that large values of the enhanced particle fluxes occur mostly when the peak magnetic field intensity is large.

Introduction

Concepts regarding the structure of the shocked solar wind flow around Venus have been extensively analyzed from the available experimental data. Over the last few years much has been done to examine the presence of a plasma boundary located between the bow shock and the ionopause. This feature was first identified in the Mariner 5 plasma measurement reported by *Bridge et al.* [1967] and *Sheffer et al.* [1979] and has been reported in studies based in other observations [*Vaisberg et al.* 1976; *Romanov et al.* 1979; *Perez-de-Tejada et al.* 1984, 1991, 1993]. In the Mariner 5 measurements it was pointed out that the density and flow speed of the shocked solar wind begin a strong decrease as the spacecraft approached the Venus wake. These variations are initiated across a sudden transition that extends downstream along the flanks of the ionosheath and that separates two different flow regimes between the inner and outer ionosheath. Those early observations showed that at this transition the speed and the density of the flow in the inner ionosheath begin a steady decrease together with a substantial drop of the magnetic field intensity and an apparent increase in the temperature of the local plasma.

Measurements conducted with the Venera 9 and 10 spacecraft show plasma variations in the Venus ionosheath which are consistent with those reported from the Mariner 5 experiment [*Vaisberg et al.* 1976; *Romanov et al.* 1979]. In this case there is also evidence of a significant decrease of the flow speed and a strong increase in the plasma temperature beginning at a transition that is encountered between the bow shock and the ionopause. Changes in the local density or in the magnetic field intensity across that transition were not included in those Venera reports.

Information which further supports the presence of a plasma transition in the Venus ionosheath was obtained from the early analysis of the Pioneer Venus Orbiter (PVO) measurements. This was first inferred from measurements conducted with the electric field detector onboard that spacecraft [*Perez-de-Tejada et al.* 1984]. Measurements carried out in a set of selected orbits suggested that electric field signals detected in the 30-kHz channel of the electric field instrument may

Paper number 95JA00329.
0148-0227/95/95JA-00329$05.00

reflect sudden changes in the plasma properties of the Venus inner ionosheath flow. This view was obtained from measurements made with the PVO plasma analyzer in that region of space [*Intriligator*, 1982]. From observations conducted with both instruments it was argued that across a plasma transition located in the Venus inner ionosheath the shocked solar wind is significantly weaker than that in the outer ionosheath.

More recent studies [*Perez-de-Tejada et al.* 1991] have shown that these changes represent a characteristic feature of the flow conditions in the shocked solar wind. As in the Mariner 5 measurements there are indications in the PVO data that the variations in the flow properties seen in the inner ionosheath are also accompanied by a significant local decrease of the magnetic field intensity [*Perez-de-Tejada et al.* 1993]. In this case we find that the magnetic field between the intermediate transition and the ionopause is oriented along directions near the Sun-Venus axis (the magnetic field acquires a strong draping configuration at the intermediate transition in a configuration similar to that reported by *Fedorov et al.* [1991] from studies of the magnetic field data in the Venus far wake). Despite the different character of the measurements made in the Mariner 5, the Venera 9 and 10 and the PVO experiments it is significant that in all of them the plasma parameters at the intermediate transition exhibit comparable and equivalent changes.

The work conducted on plasma wave activity and electric field structure in the Venus plasma environment was recently reviewed by *Strangeway* [1991]. A summary of observations of the electric and magnetic fields across the intermediate transition and across ionospheric plasma clouds was also presented in that study. Although in some instances the change in both fields at the intermediate transition is similar to that seen across plasma clouds the intermediate transition is usually located farther away from Venus than plasma clouds. While this issue will be discussed in a separate study we wish to note that the drop of the magnetic field intensity across the intermediate transition is different from that observed around plasma clouds. In the latter case the magnetic field intensity is low only in the vicinity of plasma clouds. By contrast when an intermediate transition is located the magnetic field remains low throughout most of the region between that boundary and the ionopause.

In addition to the electric and magnetic field variations seen across the intermediate transition there is new evidence suggesting that simultaneous changes in the plasma flux intensity also occur across that feature. Below we will examine this issue for the first time and show that the electric and magnetic fields variations indicated above are consistently accompanied by a distinct enhancement in the plasma flux. Our results show that the intermediate transition has now been identified from the simultaneous observation of persistent changes in the plasma properties measured in various PVO orbits. The discussion is initiated with the preliminary analysis of two PVO passes (corresponding to orbits 39 and 51) in which strong changes in the plasma flux and in the electric and magnetic fields are detected as a distinguishable intermediate transition. These cases are further substantiated by the presentation of the same plasma data in a comparative figure that better exhibits their time association with the observed electric and magnetic field variations. A similar analysis has also been made for other PVO orbits including a set of six additional passes (corresponding to orbits 52, 70, 72, 87, 120 and 530) which are also described in the text for a better discussion of the intermediate transition measurements.

Electric and Magnetic Field PVO Measurements

In the results reported earlier on the PVO plasma properties of the Venus inner ionosheath [*Perez de-Tejada et al.* 1991] it was noted that there is clear evidence of electric field signals detected as a brief but strong burst in the 30 kHz channel of the electric field instrument. At the present time we have collected about 80 PVO passes in which that event appears as a separate burst at positions located between the bow shock and the ionopause. In most cases the 30- kHz burst occurs on an otherwise flat 30-kHz electric field signature that extends across the entire ionosheath and is associated with noise detected in other (5.4-kHz and 100 Hz) channels of the electric field detector. From the examination of the magnetic field data associated with the PVO passes where the 30-kHz electric field signals are detected in the ionosheath it is found that in many of them there is a local response that nearly coincides in time with the electric field burst. When the 30-kHz burst is observed there is evidence that the magnetic field intensity drops severely and that its orientation rotates to a direction nearly along the Sun-Venus axis. A summary of 26 PVO passes in which these variations are observed is presented in Table 1. In each case we have indicated the time when the ionopause and the bow shock are crossed and when the decrease of the magnetic field intensity is observed at the intermediate transition (the last two columns indicate the altitude and solar zenith angle of the PVO at this latter crossing). While there are examples corresponding to both the inbound and the outbound passes, we find that the later are dominant in the data set (note that in most of the cases included the time difference between the ionopause and the intermediate transition is larger than ~3 min).

Table 1. Plasma boundaries in the Venus plasma environment (the PVO altitude and solar zenith angle are at the intermediate transition)

Orbit		Ionopause	Intermediate Transition	Bow Shock	Altitude	SZA
		UT	UT	UT	km	deg
23	outbound	1730	1737	1804	2531	107.5
35	outbound	1856	1902	1928	3686	114.9
39	outbound *	1913	1920	1940	3453	118.0
45	outbound	1944	1948	2014	4241	116.5
46	outbound *	1941	1950	2013	3833	118.9
51	outbound *	2003	2008	2029	3989	118.9
52	outbound *	2002	2009	2033	3605	121.6
60	inbound	1954	1950	1937	2516	92.4
70	outbound *	2022	2028	2049	3763	118.0
72	inbound *	1957	1953	1939	2121	102.3
79	inbound	1947	1941	1929	2472	100.8
83	inbound *	1936	1925	< 1921	3973	88.6
85	outbound *	1942	1959	2016	3242	113.9
87	outbound *	1944	1953	2008	3405	111.2
92	inbound	1913	1903	1849	2099	108.4
94	inbound	1900	1852	1839	3062	99.8
103	outbound *	1921	1928	1946	3180	100.5
120	inbound *	2013	2011	1938	2341	104.8
470	inbound *	1020	1017	1002	1380	82.2
494	outbound *	1115	1120	1142	3988	116.1
508	outbound *	1057	1103	1123	4282	114.4
509	outbound *	1049	1058	1122	3662	118.9
530	outbound *	0948	0952	1009	3706	110.1
538	outbound *	1025	1027	1046	3632	105.8
552	inbound	1120	1115	1056	2980	104.2
562	outbound	1242	1246	1306	2186	95.3

* These are cases in which the plasma probe measurements made across the intermediate transition show enhanced particle flux intensities.

Two of the examples that best represent the observed changes in the electric and magnetic field are the outbound pass of orbits 39 and 51. The data of the latter orbit was briefly discussed in a previous study [*Perez de-Tejada et al.* 1995] and is further examined here to more extensively analyze the behavior of the plasma fluxes throughout the ionosheath. The electric field noise seen in the 5.4 and 30-kHz channels and the magnetic field components measured in orbit 39 are reproduced in Figure 1. The vertical lines at ~ 1833 and at ~1858 UT in the inbound pass and at ~1940 and ~1913 UT in the outbound pass mark the position of the bow shock and the ionopause as recorded along the PVO trajectory. The electric field burst detected outbound at ~1920 UT occurs at a time when the magnetic field components exhibit strong changes (the transverse components B_y and B_z decrease strongly to low values in the inner ionosheath and the B_x component changes sign but remains strong). As a result the magnetic field intensity B_T drops substantially at that time and remains low throughout most of the inner ionosheath. The label "intermediate transition" at the top of Figure 1 marks the changes in the electric and magnetic field seen at ~1920 UT.

The position of the ionopause and intermediate transition detected outbound in orbit 39 are also illustrated in Figure 2. The upper panel shows the electron density profile obtained from the orbit electron temperature plasma (OETP) measurements (L. Brace, personal communication, 1992). The vertical arrow at ~1920 UT represents the intermediate transition which occurs about 7 min after the ionopause. The distance between both boundaries along the PVO trajectory is approximately ~2000 km and implies that they may not be directly connected in space. The lower panel of Figure 2 shows a general view of the position of the bow shock, the ionopause and the intermediate transition in a plane in which the vertical coordinate is the distance to the Sun–Venus axis. The position of the intermediate transition between the bow shock and the ionopause is comparable to that indicated earlier from observations conducted in other orbits [*Perez-de-Tejada et al.* 1991, 1993] and is consistent with the fact that it may appear far from the ionopause.

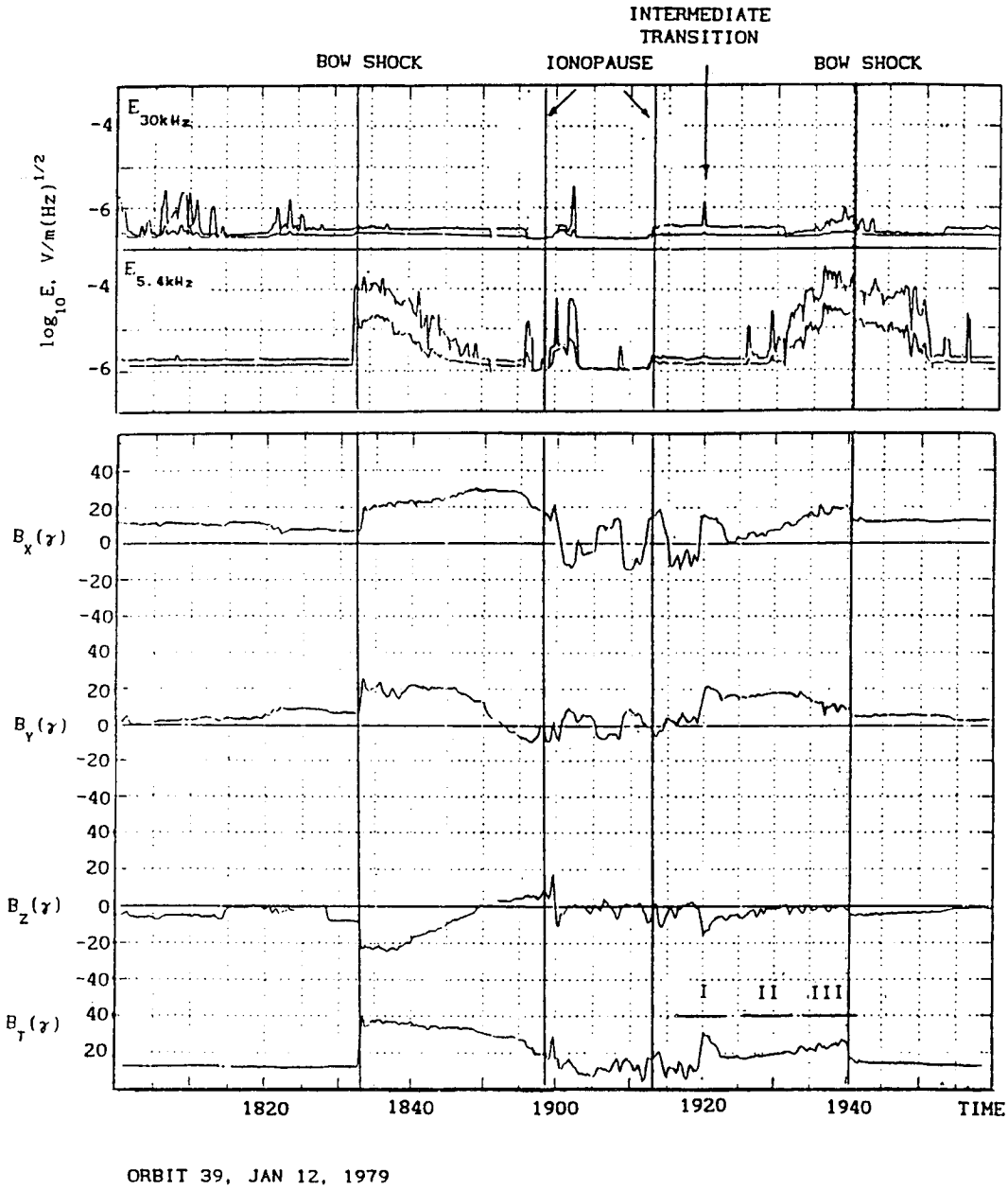

Figure 1. (upper) Electric field signals measured with the 30-kHz and 5.4-kHz channels of the electric field detector of the PVO in the inbound and outbound pass of orbit 39. (lower) Magnetic field components B_x, B_y, and B_z and magnetic field intensity B_T measured during the inbound and outbound pass of orbit 39. The inbound and outbound crossings of the bow shock and ionopause are indicated by the vertical lines (the bow shock crossings are obtained from the electric and magnetic field data and the ionopause crossings from the electron density data).

The electric and magnetic field data measured during the inbound and outbound crossings of the Venus ionosheath in orbit 51 are presented in Figure 3. The behavior of the 30 and 5.4-kHz electric field signals and the magnetic field components seen in the outbound pass of this orbit is similar to that of the outbound pass of orbit 39. We note first of all that in addition to the vertical lines at ~ 2004 and at ~2029 UT, which mark the outbound crossings of the ionopause and bow shock, there are distinct signals at ~2008 UT consistent with the presence of the intermediate transition in the outbound pass. The intense 30-kHz noise detected upstream from the bow shock in both the inbound and outbound passes (at < 1919 UT and at > 2030 UT) is far stronger than that seen in orbit 39. Also notable is the correlation between the enhancements seen at ~ 2008 UT in the 30 and 5.4-kHz electric field noise and sharp changes in the magnetic field components (we note a sharp drop in the B_y component, while the B_x component rotates and remains dominant in the vicinity

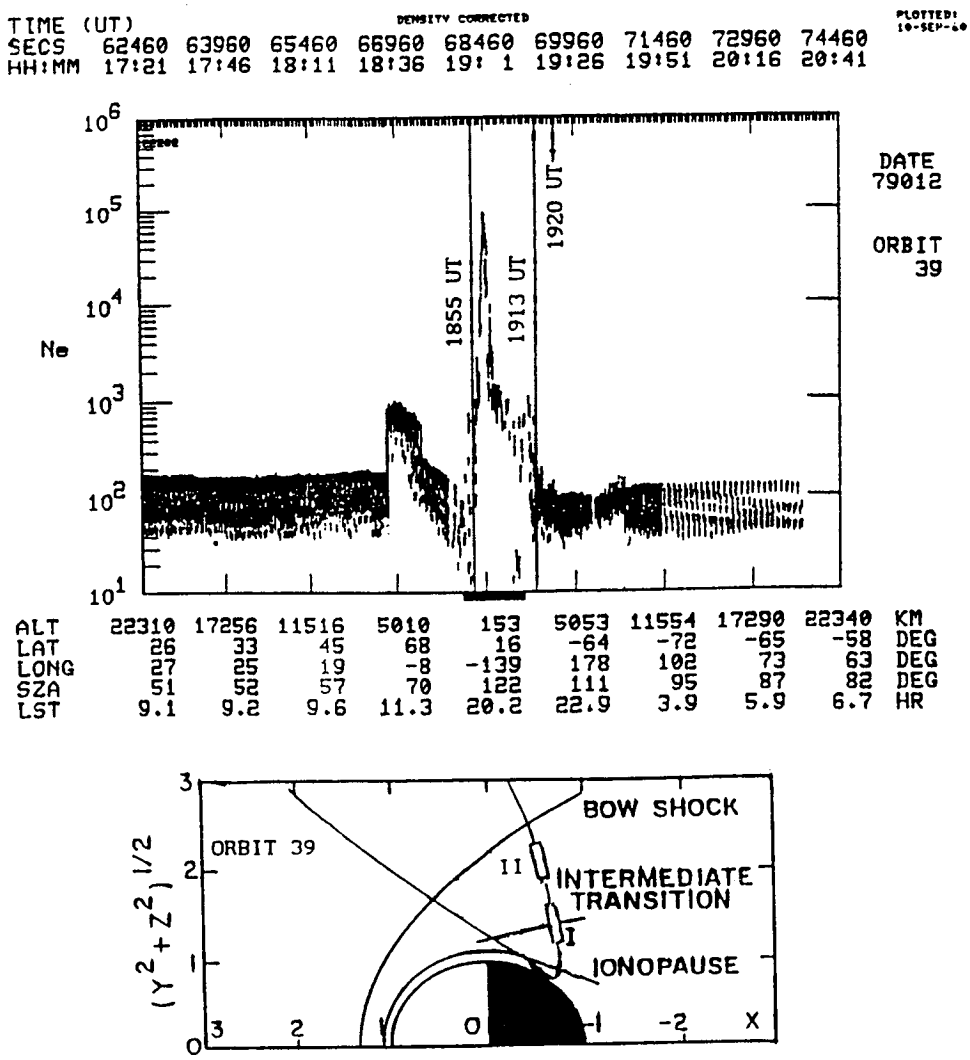

Figure 2. (upper) Electron density profile obtained from the OETP instrument of the PVO across the Venus ionosphere during orbit 39. The position of the ionopause at ~1855 UT (inbound) and at ~1913 UT (outbound) is indicated by the vertical lines (the intermediate transition detected at ~1920 UT is described by the vertical arrow). (lower) Trajectory of the PVO in orbit 39 projected on one quadrant of a plane in which the vertical coordinate is the distance to the Sun–Venus axis. The approximate position of the bow shock, the intermediate transition, and the ionopause detected along the PVO trajectory are also indicated.

of the intermediate transition). As in orbit 39, the magnetic field intensity decreases substantially at the intermediate transition and keeps low values between this boundary and the ionopause.

The time and space position of the intermediate transition and the ionopause in orbit 51 are presented in Figure 4. The upper panel shows the electron density profile and the relative position of the ionopause and the intermediate transition detected in that pass. As in the data of orbit 39, the intermediate transition occurs a few minutes after the ionopause so that the distance between both boundaries along the PVO trajectory in this orbit is also similar. The lower panel of Figure 4 describes the geometry of the bow shock, the ionopause, and the intermediate transition as detected in the outbound pass of orbit 51.

PVO Plasma Measurements

Independent of the electric and magnetic field measurements conducted during orbits 39 and 51 there is a substantial amount of PVO plasma data that is connected with the observations shown in Figures 1–4. A composite of three ion energy spectra recorded in each pass is presented in Figures 5 and 6. The starting time of the measured spectra is indicated in each curve and their time extent is described by horizontal lines above the magnetic field intensity profile shown in Figures 1 and 3. In each spectrum of Figures 5 and 6 there are ~12 s (1 spacecraft revolution) between measurements made at successive energy per unit charge (E/q) steps. The first spectrum in both orbits applies to the inner ionosheath and the second and third spectra to the outer

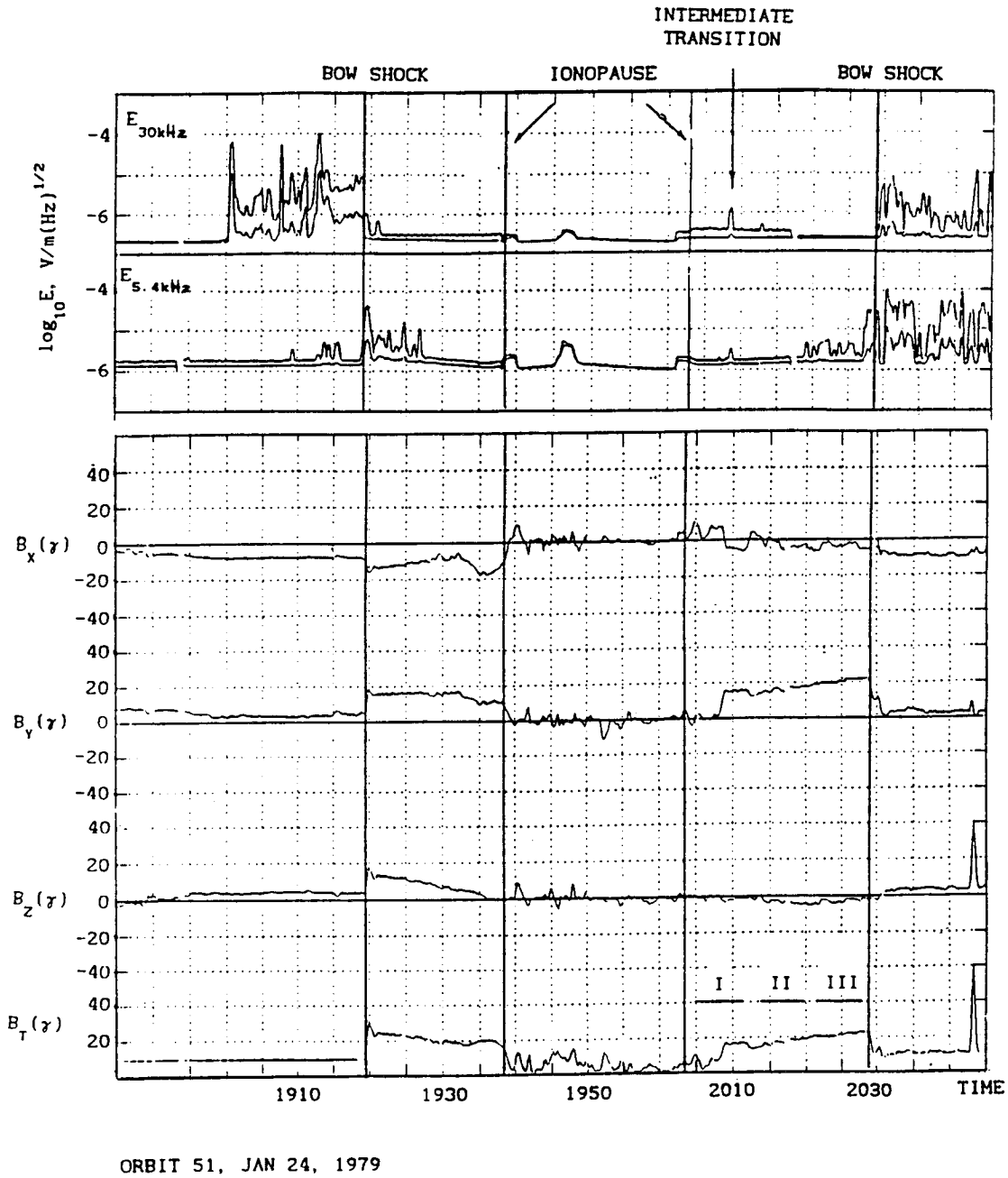

Figure 3. (upper) Electric field signals measured with the 30-kHz and 5.4-kHz channels of the electric field detector of the PVO in the inbound and outbound pass of orbit 51. (lower) Magnetic field components B_x, B_y, and B_z and magnetic field intensity B_T measured during the inbound and outbound pass of orbit 51. The inbound and outbound crossings of the bow shock and ionopause are indicated by the vertical lines (the bow shock crossings are obtained from the electric and magnetic field data and the ionopause crossings from the electron density data).

ionosheath (the PVO position at the time when the spectra I and II were calculated is indicated by the boxes added to its trajectory in the lower panel of Figures 2 and 4). Spectra II and III in Figures 5 and 6 show a general similarity in the energy of their peak values even though their local flux intensity can be different. On the other hand, the first spectrum in both passes has an overall different shape, and its peak flux is shifted to higher energies. Note in particular that in orbit 51 the dominant fluxes of spectrum I involve energies much higher and peak intensities substantially lower than those of spectra II and III.

The most notable property of spectrum I shown in Figures 5 and 6 is the fact that its peak flux occurs very nearly at the time when the intermediate transition is identified from the electric and magnetic field data. Useful times along that spectrum are indicated by the letters A, B, and C in Figures 5 and 6 with position B

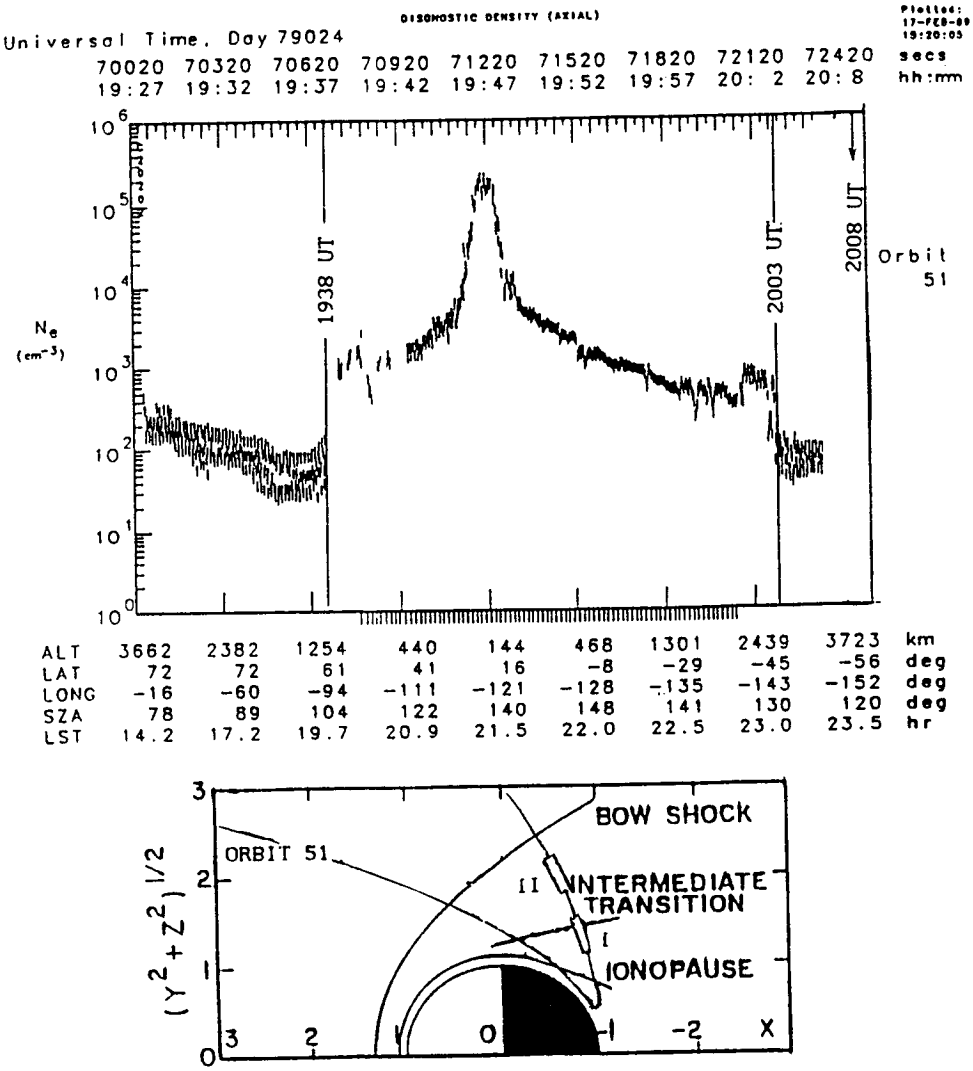

Figure 4. (upper) Electron density profile obtained from the OETP instrument of the PVO across the Venus ionosphere during orbit 51. The position of the ionopause at ~1938 UT (inbound) and at ~2003 UT (outbound) is indicated by the vertical lines (the intermediate transition detected at ~2008 UT is indicated by the vertical arrow). Note that the timescale in this profile is different from that in the upper panel of Fig. 2. (lower) Trajectory of the PVO in orbit 51 projected on one quadrant of a plane in which the vertical coordinate is the distance to the Sun–Venus axis. The approximate position of the bow shock, the intermediate transition, and the ionopause detected along the PVO trajectory are also indicated.

indicating that of the peak flux. For example, in the outbound pass of orbit 39 (Figure 5) the peak flux of spectrum I was detected at 1920:16 UT within a ~90 s–long time interval in which enhanced fluxes were recorded (between 1919:30 and 1921:00 UT). The time position of the peak flux measured in this spectrum coincides with that shown in the upper panel of Figure 1 where a strong 30–kHz electric field burst was detected outbound in the ionosheath. The same agreement is found for the sudden drop of the magnetic field intensity and the strong rotation of the magnetic field orientation that is seen at the intermediate transition. From the comparison of the data shown in Figures 1 and 5 it is apparent that evidence for the intermediate transition is available not only from the electric and magnetic field measurements but also from the plasma flux data analysis.

A similar agreement in the results of all three PVO experiments is also present in Figure 6 for the outbound pass of orbit 51. In this case the peak flux of spectrum I is detected at 2008:15 UT within a nearly 1 min–long time interval of enhanced plasma fluxes (between 2008:00 and 2009:00 UT). As shown in the top panel of Figure 3, the peak fluxes of spectrum I occur at the time when a strong 30–kHz electric field burst was detected within the ionosheath. The same is true for the sudden drop in the magnetic field intensity and the rotation of the magnetic field orientation. All these variations occur nearly simultaneously and thus suggest that the feature

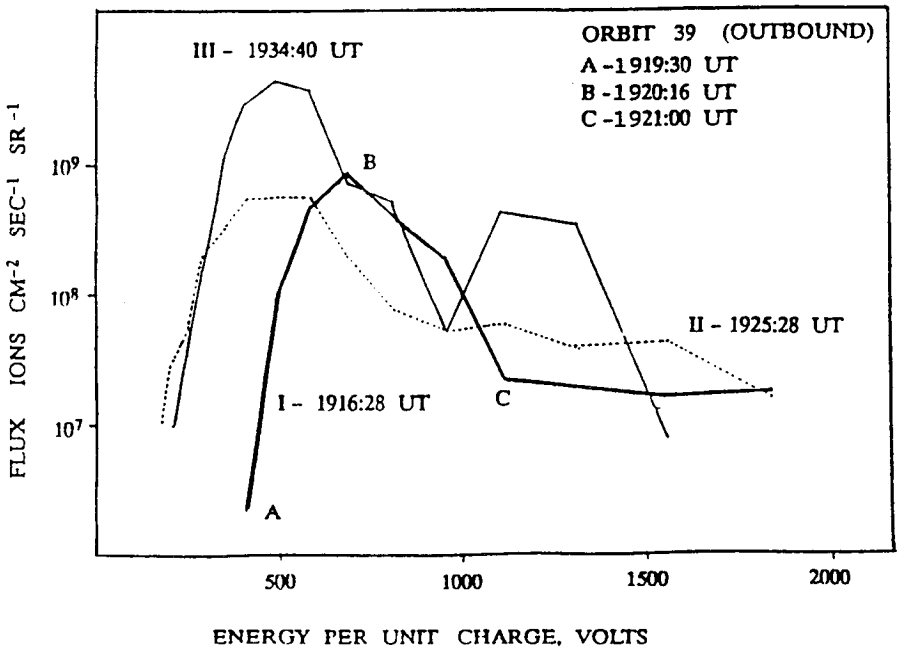

Figure 5. Ion energy spectra measured with the PVO plasma instrument throughout the Venus ionosheath during the outbound pass of orbit 39. Each spectrum shows the starting time of the energy measurements and the entire timing is indicated by the horizontal lines above the magnetic field intensity profile shown in the lower panel of Figure 1 (positions A, B, and C in spectrum I mark the time interval across the intermediate transition reported from the electric and magnetic field measurements).

identified as the intermediate transition in the outbound pass of orbits 39 and 51 is also evident in the plasma data.

Time Distribution of the PVO Plasma Data

An analysis of plasma properties similar to that presented in Figures 5 and 6 has been conducted on other PVO orbits. From those orbits included in Table 1 we have collected 17 cases in which the plasma probe measurements made across the intermediate transition show particle flux intensities with variations comparable to those described above (these are labeled with the asterisk * in Table 1). In this sense the relation between

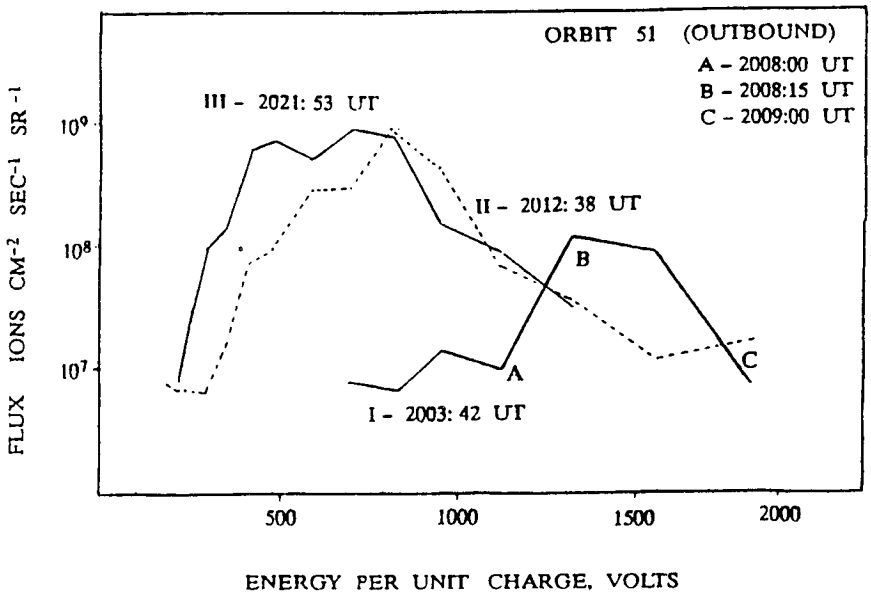

Figure 6. Ion energy spectra measured with the PVO plasma instrument throughout the Venus ionosheath during the outbound pass of orbit 51. Each spectrum shows the starting time of the energy measurements and the entire timing is indicated by the horizontal lines above the magnetic field intensity profile shown in the lower panel of Figure 3 (positions A, B, and C in spectrum I mark the time interval across the intermediate transition reported from the electric and magnetic field measurements).

the changes observed in the electric and magnetic fields and those in the particle flux intensity inferred from the study of the orbit 39 and 51 plasma data are representative of a behavior well documented in other PVO passes. The 9 cases not selected in the 26 listed in Table 1 are those in which the PVO plasma probe did not conduct measurements in the energy range where plasma fluxes are observed at the intermediate transition.

In order to better substantiate the identification of the intermediate transition in terms of concurrent variations in the electric and magnetic fields together with those observed in the plasma fluxes we have displayed the energy spectra in plots in which the particle flux intensity is given as a function of time. This enabled us to show plasma profiles on the same time scale as that of the electric and magnetic field data thus allowing for an accurate time comparison among all three measurements. Below we present these results for eight selected PVO orbits including the outbound pass of orbits 39 and 51. These two latter cases are reexamined in Figure 7 where the curve in the upper panel replaces the flux intensity measured in spectrum I of Figures 5 and 6. The time interval is in the vicinity of the intermediate transition identified from the 30-kHz electric field burst (bottom panel) and the magnetic field intensity profile (middle panel) of Figures 1 and 3. As noted earlier both cases show a notable agreement between the time location of that feature and the time interval where enhanced plasma fluxes are recorded. The most notable result is the fact that strong plasma fluxes are measured at the time when the main decrease in the magnetic field intensity is observed.

Comparable conditions are also obtained from the analysis of the plasma data of orbits 52 and 70 which are presented in Figure 8. In these cases the intermediate transition is also detected as a well-defined feature observed in the electric and magnetic fields and in the plasma fluxes. This is observed at ~2009 UT in orbit 52 and at ~2028 UT in orbit 70 when the magnetic field intensity (middle panel) exhibits a large decrease within the ionosheath. An agreement is also noticeable in the time position of the intense plasma fluxes and the electric field burst seen in the 30-kHz channel shown in the lower panel. Despite the fact that in both cases the latter signals are also detected up to 2 min away from the enhanced plasma fluxes no comparable fluctuations in the electric field are found in other regions of the ionosheath.

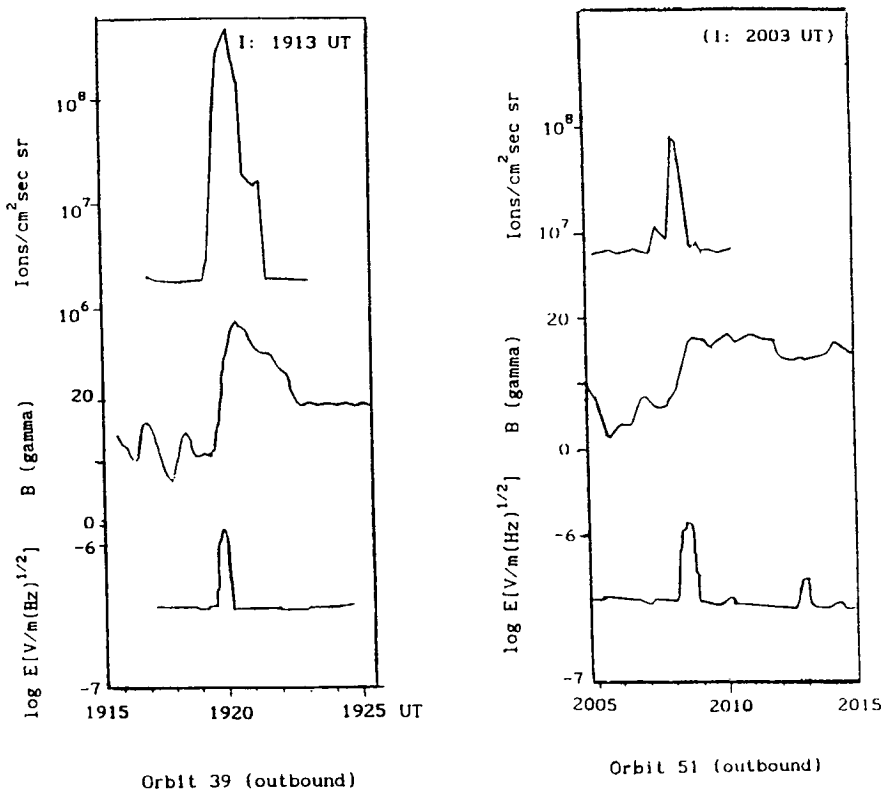

Figure 7. (left) Time distribution of the (upper) particle flux intensity, (middle) magnetic field intensity profile, and (lower) electric field burst in the 30-kHz channel measured across the intermediate transition during the outbound pass of orbit 39. (right) Time distribution of the (upper) particle flux intensity, (middle) magnetic field intensity profile, and (lower) electric field burst in the 30-kHz channel measured across the intermediate transition during the outbound pass of orbit 51. The time when the ionopause is detected in each case is indicated by the label I at the top of each figure.

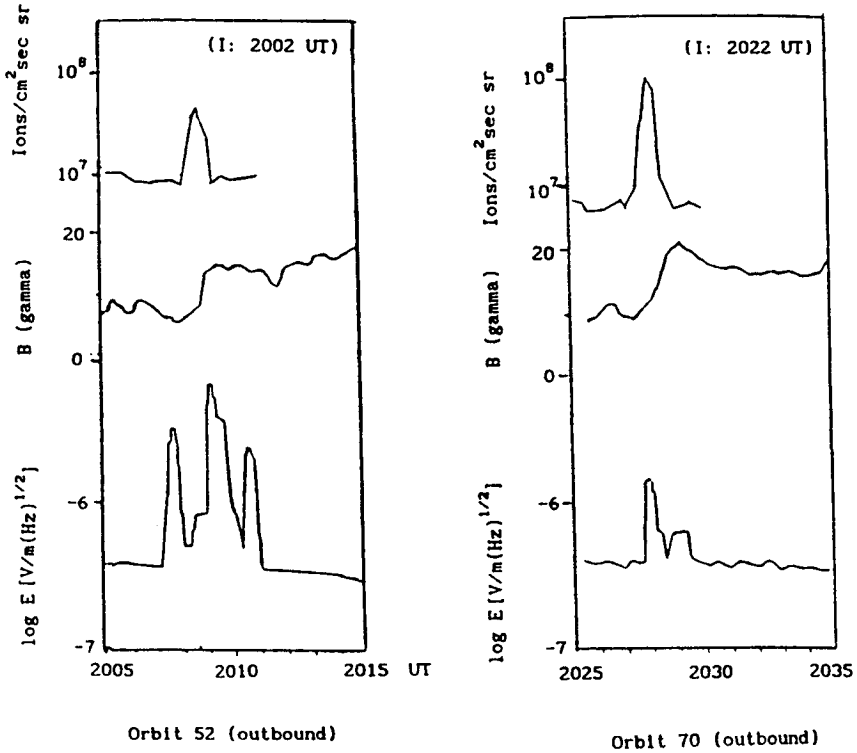

Figure 8. Same as Figure 7 for the (left) outbound pass of orbit 52 and for the (right) outbound pass of orbit 70.

A third pair of orbits with a similar arrangement is presented in Figure 9. In the inbound pass of orbit 72 the crossing of the intermediate transition (at ~ 1953 UT) is evidenced by the agreement in the observation of enhanced plasma fluxes and the strong decrease of the magnetic field intensity that begins nearly at that time. The same is true in the outbound pass of orbit 87 where intense plasma fluxes (at ~ 1952:30 UT) occur within the magnetic field gradient. A discussion of the variations seen in this latter case was presented in a previous report [*Perez-de-Tejada et al.* 1993]. However, the data in Figure 9 expresses more clearly the simultaneous observation of enhanced plasma fluxes (upper panel), the strong drop of the magnetic field intensity (middle panel), and the enhanced noise detected in the 30-kHz electric field channel (lower panel).

Two useful additional examples in which the plasma and the electric and magnetic field data exhibit concurrent variations across the intermediate transition are described in Figure 10. Once again, we can identify that the large enhancement in the plasma flux intensity measured in the inbound pass of orbit 120 (at ~2011 UT) and in the outbound pass of orbit 530 (at ~0952 UT) occurs nearly at the time when the magnetic field intensity shows a strong decrease from values seen in the outer ionosheath. A similar agreement between the enhanced plasma fluxes and an appreciable increase in the 30-kHz electric field noise is also evident in both cases. We should also emphasize here that as in the previous examples no concurrent changes in the electric and magnetic fields and in the plasma data are observed anywhere else within the ionosheath.

Discussion

Much of what has been presented here is also applicable to other PVO orbits. So far we have completed a similar plasma data analysis on those orbits of Table 1 marked with the asterisk. In all of them we find that the most severe changes seen across the ionosheath in the magnetic field measurements and in the 30-kHz electric field noise occur at the time when enhanced plasma fluxes are recorded. The cases that were not studied in Table 1 correspond to situations in which the plasma probe did not measure the peak flux of the energy spectrum at the time when the intermediate transition was detected. Using the set of PVO orbits of Table 1 with evidence of this transition in the plasma and magnetic field data we have compared the peak particle flux and the peak magnetic field intensity measured across that feature. The results of this comparison are shown in Figure 11. The data points indicate that the particle flux shows a general increase with the peak magnetic field intensity but no preferred value range for any of these two quantities is evident in that figure. With the plasma

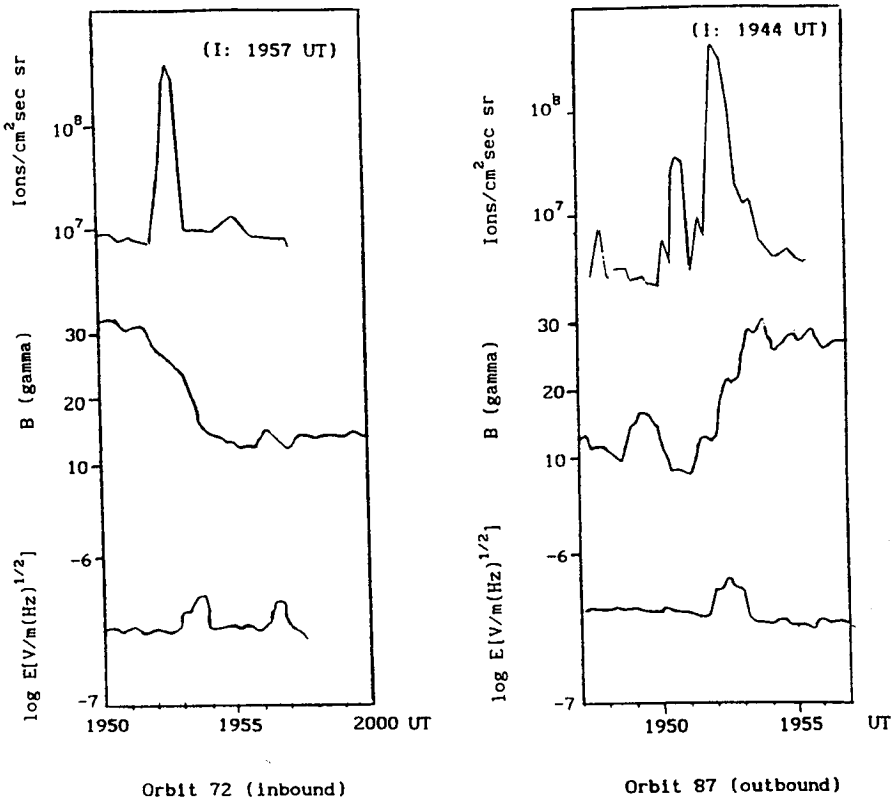

Figure 9. Same as Figure 7 for the (left) inbound pass of orbit 72 and for the (right) outbound pass of orbit 87.

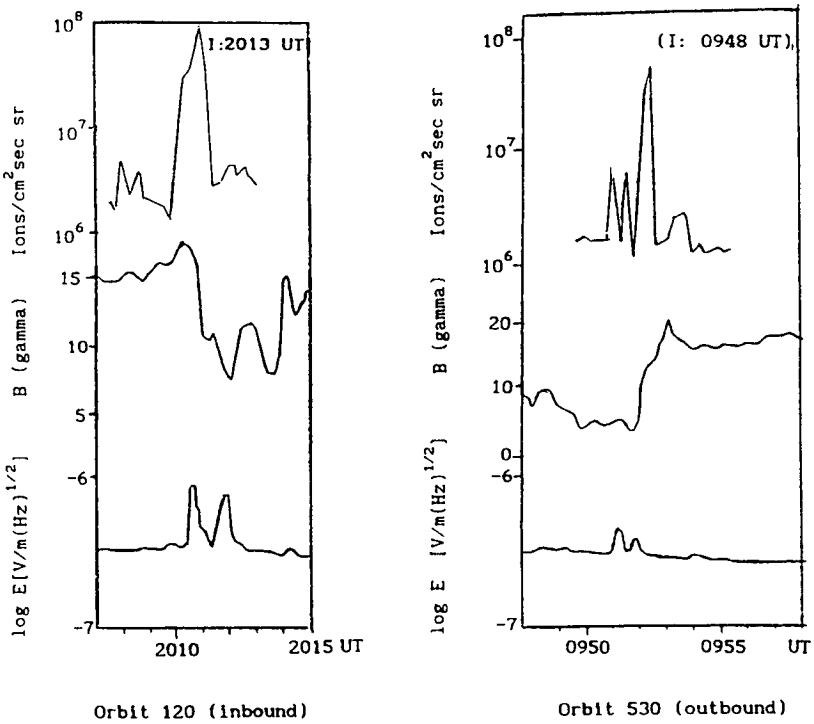

Figure 10. Same as Figure 7 for the (left) inbound pass of orbit 120 and for the (right) outbound pass of orbit 530.

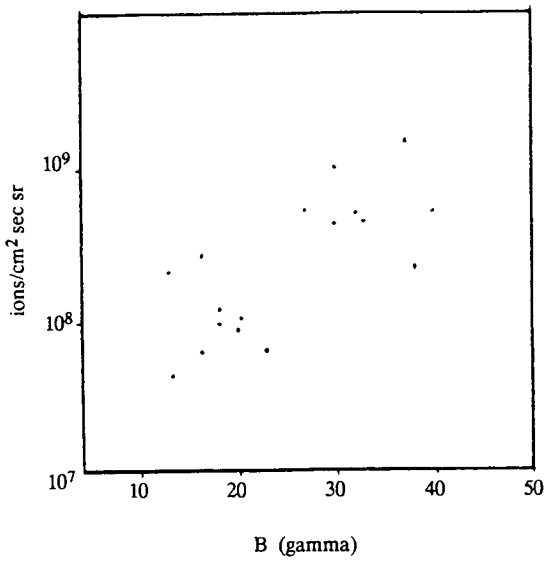

Figure 11. Peak particle flux intensity and peak magnetic field intensity measured at the intermediate transition in 17 PVO passes of Table I.

flux and the electric and magnetic field profiles shown in Figures 7–10 we conclude that there is now a wide range of experimental information supporting the existence of the intermediate transition.

Arguments related to the presence of this transition in the Venus ionosheath have been advanced in connection with the dynamics of gasdynamic flows streaming around obstacles. In that view the intermediate transition may represent the outer boundary of a friction layer that is produced through the anomalous transfer of solar wind momentum to the Venus ionospheric plasma [*Perez de-Tejada,* 1995]. While studies are required to examine the origin of this process it is necessary to resolve whether the properties of the intermediate transition are adequate to that interpretation. For example, an alternative view of that transition may be related to the observation of plasma clouds near the magnetic polar regions of the Venus plasma environment [Russell et al. 1982, Scarf et al. 1985]. In this case the B_x component would be required to reverse polarity as in the outbound pass of orbit 39 (Figure 1). We should note, however, that in many PVO passes the B_x component does not reverse polarity at the intermediate transition. A further examination of this issue will be addressed in a separate study.

The presence of the intermediate transition in the inner ionosheath may also be relevant to examine a similar feature in the Mars plasma environment. Measurements conducted with instruments onboard the Phobos spacecraft [*Lundin et al.*, 1990a,b, 1991] indicate the presence of a feature in the Mars magnetosheath with properties similar to those of the intermediate transition in the Venus ionosheath. A strong velocity shear is observed beginning at that transition with a change in the plasma composition from mostly solar wind particles outside to a population dominated by particles of planetary origin below. At that feature the magnetic field also exhibits changes that are similar to those detected across the intermediate transition in the Venus inner ionosheath [*Sauer et al.*, 1992]. Further studies are required in order to compare the properties of this transition in the Venus and Mars plasma environments. At Venus this should involve the analysis of the data of more PVO orbits including the distribution of thermal and suprathermal ions between the ionopause and the intermediate transition.

Acknowledgements. We wish to thank C. T. Russell and L. Brace for providing magnetic field and ionospheric electron density PVO data used in this study. The work at Carmel Research Center and at the University of California was supported, respectively, by the Pioneer Venus Project Office under contracts NAS2-12912, and NAG2-485. Services provided by the Space Environmental Lab. of NOAA in Boulder, Colo. are appreciated.
The editor thanks two referees for their assistance in evaluating this paper.

References

Bridge, H. S., A. J. Lazarus, C. W. Snyder, E. J. Smith, I. Davies, P. L. Coleman, and D. E. Jones, Plasma and magnetic fields observed near Venus, *Science, 158,* 1669, 1967.

Fedorov, A., O. Vaisberg, D. Intriligator, R. Sagdev, and A. Galeev, A large amplitude rotational wave in the Venus ionosheath, *J. Geophys. Res., 96,* 87, 1991.

Intriligator, D. S., Observations of mass addition to the shocked solar wind in the Venus ionosheath, *Geophys. Res. Lett., 9,* 727, 1982.

Lundin, R., A. Zakharov, R. Pellinen, S. Barabashm, H. Borg, E. Dubinin, B. Hultvquist, H. Koskinen, I. Liede and N. Pissarenko, ASPERA/PHOBOS measurements of the ion outflow from the Martian ionosphere, *Geophys. Res. Lett., 17,* 873, 1990a.

Lundin, R., A. Zakharov, R. Pellinen, H. Borg, B. Hultvquist, N. Pissarenko, E. Dubinin, S. Barabash, I. Liede and H. Koskinen, Plasma composition measurements of the Martian magnetosphere morphology, *Geophys. Res. Lett., 17,* 877, 1990b.

Lundin, R., et al., On the momentum transfer of the solar wind to the martian topside ionosphere, *Geophys. Res. Lett., 18,* 1059, 1991.

Perez-de-Tejada, H., Plasma boundary within planetary ionosheaths, *Space Science Rev.* in press, 1995.

Perez-de-Tejada, H., D. Intriligator and F. Scarf, Plasma and electric field PVO measurements in the Venus ionosheath, *Geophys. Res. Lett., 11,* 31, 1984.

Perez-de-Tejada, D. S. Intriligator, and R. J. Strangeway, Steady state plasma transition in the Venus ionosheath, *Geophys. Res. Lett., 18,* 131, 1991

Perez-de-Tejada, H., D. S. Intriligator and R. J. Strangeway, Magnetic field properties of the intermediate transition of the Venus ionosheath, *Geophys. Res. Lett., 20,* 991, 1993.

Perez-de-Tejada, H., D. S. Intriligator and R. J. Strangeway, Plasma expansion layer in the Venus inner ionosheath, *Adv. Space Res.*, in press, 1995.

Romanov, S., V. Smirnov, and O. Vaisberg, On the nature of the solar wind–Venus interaction, *Cosmic Res., 16,* 603, 1979.

Russell, C. T. J. Luhmann, R. Elphic, F. Scarf, and L. Brace, Magnetic field and plasma wave observations in a plasma cloud at Venus, *Geophys. Res. Lett., 9,* 45, 1982.

Sauer, K., T. Roasch, U. Motschmann, K. Schwingenschuh, R. Lundin, H. Rosenbauer and S. Livi, Observations of boundaries and phenomena around Mars with Phobos 2, J. *Geophys. Res., 97,* 6227, 1992.

Scarf, F., S. Neumann, L. Brace, C. T. Russell, J. Luhmann, and A. Stewart, Current-driven plasma instabilities and auroral types particle acceleration at Venus, *Adv. Space Res., 5(9),* 185, 1985.

Sheffer, R., A. Lazarus, and H. Bridge, A re-examination of plasma measurements from the Mariner 5 Venus encounter, *J. Geophys. Res., 84,* 2109, 1979.

Strangeway, R. J., Plasma waves at Venus, *Space Sci. Rev. 55,* 275, 1991.

Vaisberg, O. L., S. A. Romanov, V. N. Smirnov, I. P. Karpinsky, B. I. Khazanov, B. V. Polenov, A. V. Bogdanov, and N. M. Antonov, Ion flux parameters in the solar wind Venus interaction region according to Venera 9 and Venera 10 data, in *Physics of Solar Planetary Environments,* vol. 2, edited by D. J. Williams, p. 904, AGU, Washington, D. C., 1976.

D. S. Intriligator, Carmel Research Center, Santa Monica, CA 90406.

H. Perez-de-Tejada, Institute of Geophysics, National University of Mexico, P.O. Box 189003, Coronado, CA 92178.

R. J. Strangeway, Institute of Planetary Geophysics and Space Research, University of California, Los Angeles, CA 90264.

(Received May 17, 1994; revised January 20, 1995; accepted January 24, 1995.)

JOURNAL OF GEOPHYSICAL RESEARCH, VOL. 100, NO. A10, PAGES 19,933–19,939, OCTOBER 1, 1995

Spatial distribution of electron plasma oscillations in the Earth's foreshock at ISEE 3

E. W. Greenstadt,[1] G. K. Crawford,[2,3] R. J. Strangeway,[4] S. L. Moses,[1] and F. V. Coroniti[1]

Abstract. Electric field oscillations recorded by the 10–56 kHz channels of TRW's plasma wave detector during parts of two of the ISEE 3 circumterrestrial orbits in 1983 have been used to make the first mapping of Earth's electron plasma wave foreshock. By combining data from the two trajectory segments, each of which provided relatively meager spatial sampling outside the bow shock, but high variation of interplanetary magnetic field (IMF) direction, a first-order pattern of occurrence of electron plasma waves, hence also backstreaming electrons, has been determined. We depict the pattern with an adaptation of the mapping program previously used for the Venus electron foreshock. As at Venus, plasma wave activity was concentrated most densely along the IMF line tangent to the bow shock where energized electrons stream against the solar wind from the quasi-perpendicular part of the shock. The size of the Earth's electron plasma wave foreshock, however, is vastly greater than that of Venus, implying that a foreshock's dimension scales with the size of its diamagnetic obstacle and associated bow shock. Our mappings with three additional ISEE 3 channels surrounding the local electron plasma frequency indicate a richer distribution of waves in the foreshock than the single electron frequency channel of Pioneer Venus Orbiter could detect around Venus.

Introduction

Electron plasma oscillations in the solar wind outside the Earth's bow shock were discovered and related to the shock system more than two decades ago [*Scarf et al.*, 1971; *Fredricks et al.*, 1971]. Yet these waves were not mapped in any systematic way in any foreshock until the extensive recent study of waves at the electron plasma frequency f_{pe} in Venus' foreshock [*Crawford et al.*, 1993a, b; *Strangeway and Crawford*, 1995a, b]. In this report we present the first attempt to map the Earth's electron plasma wave (pw) foreshock.

During some of its lengthy Earth-orbiting passes in 1983, ISEE 3 sampled the foreshock over distances that encourage investigation of the spatial distribution of plasma waves. We adapted the methods of *Crawford et al.* [1993] to the ISEE 3 data set in order to map the distribution of electron plasma oscillations in the Earth's foreshock and compare the results with those obtained at Venus. Figure 1 shows the trajectories of the two passes of ISEE 3 used in this study.

Processing

Compressed plasma wave spectrograms were created from ISEE 3 TRW records by selecting peak readings every 360 s and defining a common color scale for all frequencies covering the full range of voltages. The spectrograms showed a clear separation between ion acoustic range (IAR) activity at frequencies less than 10 kHz and signals near the electron plasma frequency, which were almost always confined to the 17- and 31-kHz channels.

Simultaneous values of the interplanetary magnetic field (IMF) $\mathbf{B}_{sw}$ in the solar wind were taken from either high-resolution measurements made available at TRW by Jet Propulsion Laboratory (JPL) or averaged values from the data pool tapes at University of California at Los Angeles (UCLA), all derived from the ISEE 3 JPL magnetometer. Electron densities N_e were obtained from Los Alamos National Laboratory (LANL) measurements in the common pool data at UCLA. Because source data from these three instruments were not recorded with a common sampling interval, merged data sets of pw, magnetic field, and electron density data were created by finding the peak pw amplitude in the channel in which f_{pe} fell during each 360-s interval. The time of the peak was then redefined as the center time of the interval, and the corresponding 360-s-average values of $B = |\mathbf{B}_{sw}|$ and N_e were computed using a triangular filter with vertex at the center time. The 360-s sampling period was chosen as the highest time resolution obtainable while still smoothing out shorter-period waves and perturbations of the IMF that do not contribute to global movements of the foreshock.

Data and Their Intervals

ISEE 3 plasma wave data derive from the TRW/University of Iowa instrument described by *Scarf et al.* [1978]; electron densities were obtained from measurements by the Los Alamos instrument on ISEE 3 [*Bame et al.*, 1978] provided in the ISEE 3 data pool tapes; magnetic field data are from the ISEE 3 JPL magnetometer [*Frandsen et al.*, 1978]. Plates 1 and 2 display the magnetic field, plasma density, and pw spectrograms of the 17- and 31-kHz channels for the September and December passes, respectively. During most of the September

[1]Space and Technology Division, TRW, Redondo Beach, California.
[2]Radio Atmospheric Science Center, Kyoto University, Kyoto, Japan.
[3]Now at SRI International, Menlo Park, California.
[4]Institute of Geophysics and Planetary Physics, University of California, Los Angeles.

Paper number 95JA01400.
0148-0227/95/95JA-01400$05.00

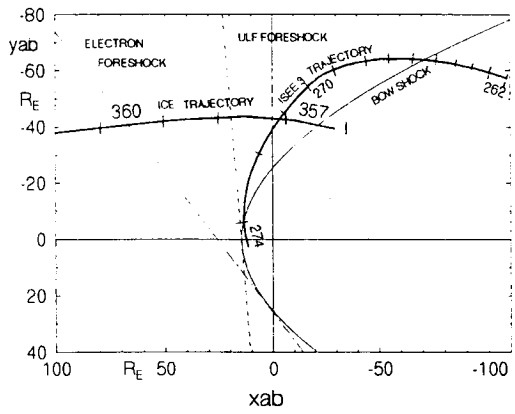

Figure 1. The late September and December trajectory segments show the locations of the spacecraft relative to the nominal bow shock and foreshock boundaries corresponding to the most common IMF stream angle. The ISEE-C spacecraft was referred to as ISEE 3 after launch and renamed Interplanetary Comet Explorer (ICE) after its final gravity assist toward comet Giacobini-Zinner, which occurred before day 357. All plotted curves are in a solar ecliptic coordinate system adjusted for nominal 4° solar wind aberration, indicated by notation xab,yab.

interval, which began with an interplanetary storm interval and ended just after ISEE 3 entered the bow shock (Plate 1, *B* plot), the ambient density in the foreshock tended to place f_{pe} in the 17-kHz channel. We indicate this by the dashed horizontal lines in the density panel of Plate 1. The density during the December pass (Plate 2) placed f_{pe} between the 17- and 31-kHz center frequencies of the two plotted channels (dashed lines again), but the 31-kHz channel was the most active, as we verify below.

The spatial coverage of the ISEE 3 trajectories illustrated in Figure 1 was admittedly quite limited. However, despite the relatively small track of the absolute space sampled by the orbit segments, the orientation of the IMF underwent sufficient variations to have shifted the foreshock's tangent surface and orientation to the shock appreciably in response to the IMF's changes. The spacecraft therefore typically occupied different regions of the foreshock even during short segments of its trajectory. Thus large variations in IMF direction enabled ISEE 3 to sample a vast volume of the foreshock in normalized coordinates [*Greenstadt and Baum*, 1986] making the mapping study meaningful as we shall illustrate. The most common direction of the IMF, at least in the September pass, was about 0° latitude and −45° longitude, corresponding to the nominal direction of the IMF and location of the foreshock in the sketch of Figure 1.

Combined Data Set

The program developed for the Pioneer Venus Orbiter's (PVO) mapping of Venus' foreshock used the 30-kHz channel of its pw instrument when investigating f_{pe} emissions, since none of the other three channels included a likely electron plasma frequency. To employ this code at the Earth, we had to account for f_{pe} occurring principally in either of two of several channels of the ISEE 3 instrument, as depicted in our Plates 1 and 2. We sought to combine the ISEE 3 September and December sets in order to obtain uniform coverage over a larger volume of the foreshock than either set provided by itself. We therefore merged data sets with attention to the appropriate filter channel applicable at every sampling interval in either set. We sought to determine the appropriate channels by using independent measurements of electron density to decide which channel should have contained each peak amplitude sample.

For each interval in either pass, we determined the channel whose center frequency f_{ch} was closest on a log scale to f_{pe}, determined independently from N_e. We then defined a virtual "f_{pe} channel" and assigned it to the wave amplitudes measured in the closest channel to f_{pe}. During the September pass, the great majority, and the largest, of the f_{pe} signals fell in the 17-kHz channel, in accord with the indication of f_{pe} = 17 kHz most of the time in the N_e panel of Plate 1. The bulk of the measured amplitudes in adjacent channels were at least an order of magnitude smaller, and most of those signals can be attributed to attenuated readings due to overlapping channel bandwidths. Similarly, during the December pass, the bulk of the f_{pe} signals and the highest amplitudes were recorded in the 31-kHz channel, consistent with the density plot of Plate 2, with amplitudes again exceeding those in the adjacent channels by more than an order of magnitude. Since the ranges of peak amplitudes in the most common corresponding channels of the September and December data were approximately the same, no disparity was introduced by intermingling readings from either set that occurred at the same mapped location in the normalized foreshock coordinate frame described in the next section. We therefore merged measurements from the two sets into a single database without regard for which pass they came from.

Mapping

The instantaneous position of ISEE 3 and orientation of the IMF produce a unique foreshock geometry and idealized one-point map corresponding to each datum. A comprehensible map of all the observations must therefore be constructed on an idealized common foreshock diagram. Our normalized conceptualization was obtained using depth from the instantaneous tangent field line to the spacecraft, and distance from the tangent point to the aberrated (−4°) X line through the spacecraft in solar foreshock coordinates (SFC), using the bow shock model of *Greenstadt and Baum* [1986] [*Crawford et al.*, 1993]. Idealized positions so derived were then plotted on a single diagram with the nominal shock and tangent IMF line appropriate to the Earth. Our mappings of the Earth's f_{pe} foreshock, using normalized foreshock coordinates on a common diagram of the nominal IMF at 45° stream angle and nominal shock, appear in Plate 3.

Because of the relatively small population of points provided by ISEE 3, we divided the normalized plane into 20 × 20 R_E squares overlapping one another on a 10 × 10 grid. Our data set for each square was the set of all points that fell in that square from the combined database. We represent the activity in each 20 × 20 square by the ninth decile of peak wave amplitudes of the points that fell in the square. The representation consists of a color corresponding to a value from the actual range of amplitudes in the database. Thus the color of each square corresponds to the amplitude below which 90% of the measurements in that square fell, according to the accompanying color scale. The overlapping squares are intended to

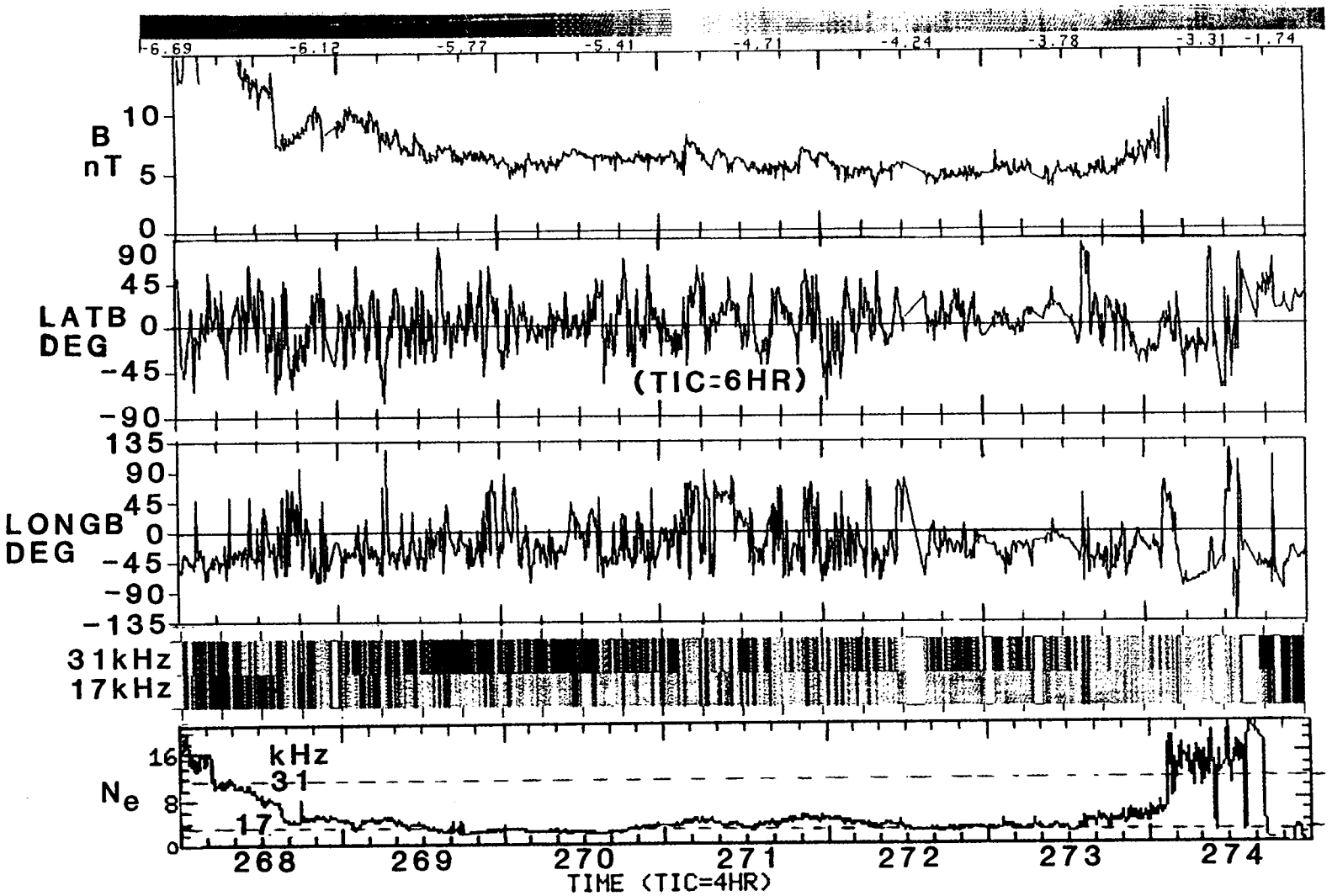

Plate 1. Magnetic field, pw, and density data for the September 25 to October 1, 1983, pass of ISEE 3, days 268–274 on the bottom time axis. First panel from the top, below the color strip showing the log amplitude scale of pw signals: the magnitude of the IMF; second, SEC latitude of the IMF; third, SEC longitude of the IMF; fourth (color panel), amplitudes of pw signals in two channels enclosing the electron plasma frequency; bottom, solar wind electron density. IMF data are 6-min averages; pw data are 6-min peaks of wave amplitude in units of log(V/m), not normalized for channel bandwidth. An interplanetary storm, in progress when the depicted interval began, ended about midway through day 269; the spacecraft entered the bow shock where the plot of magnitude ended, top panel, about 0300, day 274.

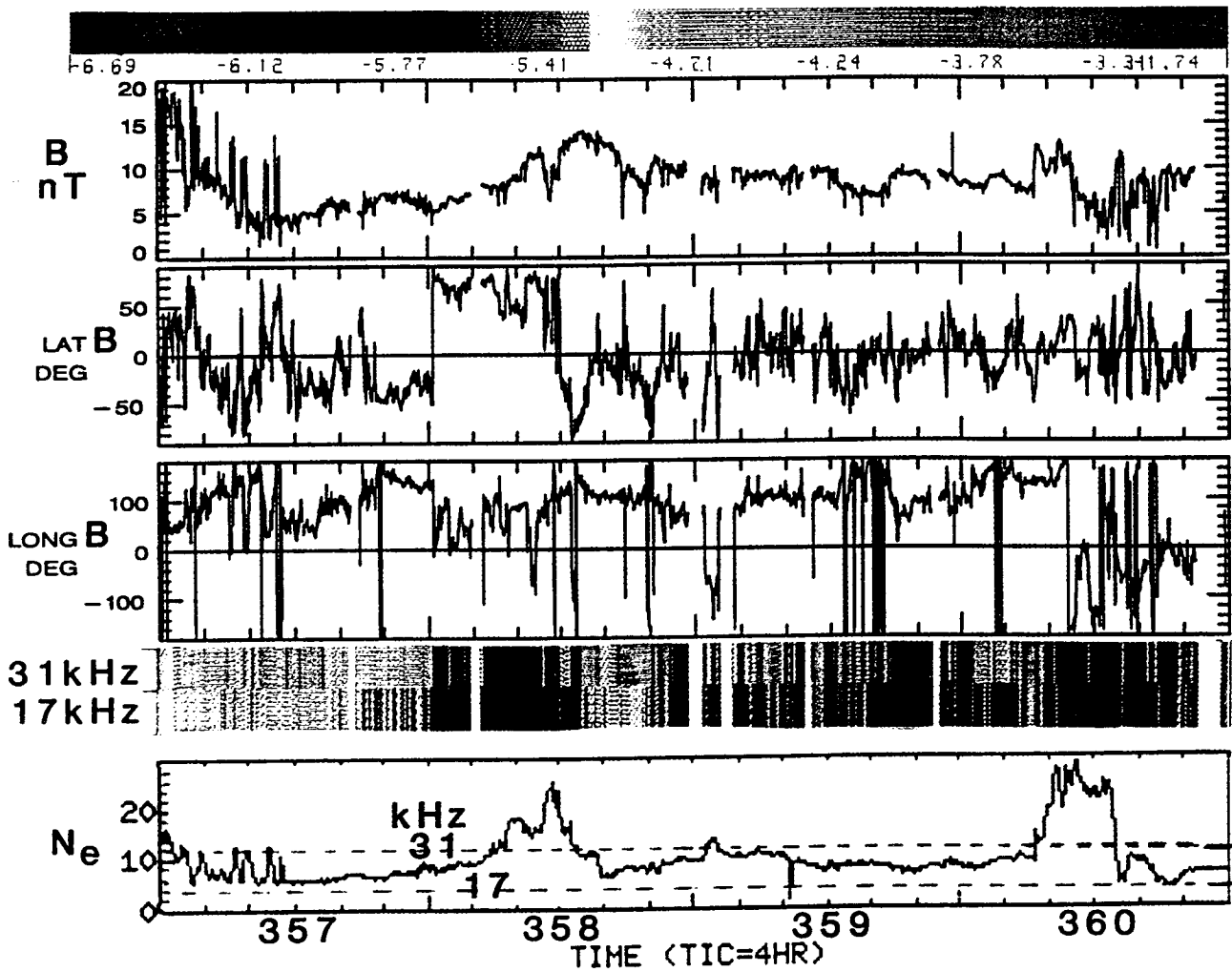

Plate 2. IMF, pw, and density data for the December 22–27, 1983, pass of ISEE 3, days 356–361 on the bottom time axis. Panels in the same order as in Plate 1.

smooth the color transitions from square to square of the graph.

The combined coverage from the two passes in Plate 3a illustrates, via the corresponding color bar, the relative scarcity of normalized spatial samples and the concentration of the densest sampling east and west of, and just upstream from, the shock's vertex. In striking contrast, the locations of maximal pw amplitude in the f_{pe} map of Plate 3b provides a persuasive demonstration that maximal excitation of electron plasma waves occured along or behind the tangent field line for each contributing element of the map, within the accuracy of the collection boxes and the uncertainties imposed on the mapping procedure by the limited data sample. Clearly, there is an unexpected and improbable excursion of the highest wave amplitudes into the solar wind ahead of the model tangent field line. Other high-resolution individual observations of backstreaming electrons and electron oscillations have found a relatively sharp boundary at that line. Since neither the nominal bow shock model nor its location was corrected for solar wind variations, some scatter may have been introduced into the map by the September storm of days 267 and 268, which could have raised f_{pe} by one or two channels. The storm could also have introduced some interplanetary plasma oscillations and changed the Mach number from its assumed average, moving the bow shock from its nominal position.

A short list of other plausible causes of geometrical degradation would include routine variations of $\mathbf{B}_{sw}$ and $\mathbf{V}_{sw}$ directions under normal, nonstorm solar wind conditions. The same inspection of Plates 1 and 2 that reveals the variations of field angles that enabled us to generate any map at all from the restricted trajectory locations also shows how much short-term variation there was in the representations of these quantities as 360-s averages. Each variation changes the **B-X** plane and the tangent line direction in which the electrons stimulating the corresponding pw peak-value travel. Moreover, the instantaneous direction of $\mathbf{B}_{sw}$ at the time of the peak pw signal within each 360-s interval need not equal the average direction of $\mathbf{B}_{sw}$ for the interval. Small variations in $\mathbf{B}_{sw}$ and $\mathbf{V}_{sw}$ orientations can swing the instantaneous tangent lines appreciably away from the model used to overlay the measurements. Ideally, we would have isolated subsets of measurements for restricted geometric combinations, but the meager data base could not have supported meaningful results unless we also enlarged the mapping boxes and thus vitiated the effort. We believe these almost certain contributions of uncertainty make the inferred

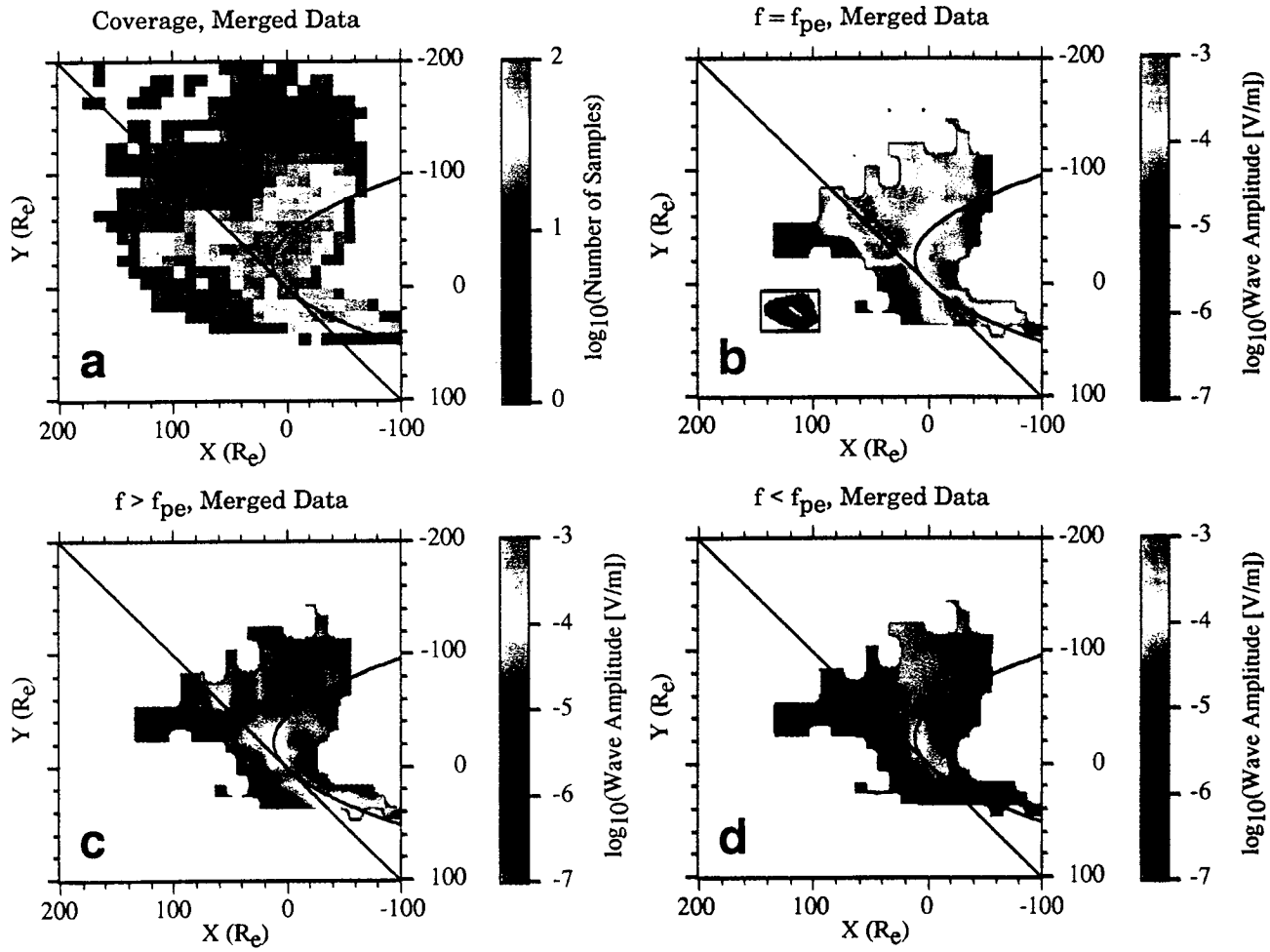

Plate 3. The ISEE 3 mappings of Earth's electron pw foreshock: (a) spatial coverage; (b) composite of the ninth deciles of 17- and 31-kHz wave amplitude distributions from September and December passes, respectively; (c) similar composite of 31- and 56-kHz wave amplitude distributions from September and December passes; (d) similar composite of 10- and 17-kHz wave amplitude distributions from September and December passes. The small rectangular insert in the lower left of Plate 3b is a miniature reproduction of the entire map of the Venus 30-kHz pw foreshock on the same scale as our representation of Earth's foreshock. Shock diagrams are aberrated by $-4°$.

concentration of f_{pe} occurrence near the tangent line in Plate 3b all the more credible.

Plates 3c and 3d are mappings of the foreshock similarly constructed, respectively, from combined data sets of pw amplitudes in the channels above and below the f_{pe} channels; i.e., primarily from the 31 (>17) kHz and 56 (>31) kHz data channels of the September and December intervals, respectively, in Plate 3c; and primarily from the 10 (<17) kHz and 17 (<31) kHz data channels of the September and December intervals, respectively, in Plate 3d. We see that the amplitudes of off-f_{pe} signals in both Plates 3c and 3d were well below those in the f_{pe}-channel map in Plate 3b and formed somewhat different patterns with highest amplitudes around the conjunction of the bow shock and IMF tangent line, thus filling in a section of the line unemphasized by red in the map of Plate 3b. There was also a concentration of signals in the downstream foreshock in Plate 3d.

The result compares well with the earlier mapping of the Venus f_{pe}-foreshock [*Crawford et al.*, 1993a], if we allow for the striking difference in the huge scale of the foreshock at Earth relative to Venus. The small rectangle at lower left of Plate 3b defines the size of the entire depicted box in the earlier Venus figure [*Crawford et al.*, 1993a], of which the actual mapped area occupied only a portion, just as it does in the ISEE 3 panel. The region of most intense electron plasma oscillations, at PVO's only available f_{pe} channel of 30 kHz, occurred in the Venus foreshock close to the tangent IMF line, as mapped in a foreshock normalized to the typical IMF orientation at Venus in the SFC frame. The most common strong electron plasma wave activity in the Earth's foreshock also occurred at or close to the tangent IMF line, in the SFC frame normalized for the Earth. However, despite their vastly greater scale, the ISEE 3 passes covered insufficient distance to reveal the upstream limit of the waves. In contrast, the PVO orbits allowed the data to show that the strong activity ran out about 16 R_V upstream along the line from the tangent point, and Venus' region of concentration was sharply confined in both distance along, and depth from, the tangent line.

The number of ISEE 3 samples at Earth was more than an order of magnitude smaller than the number of PVO samples at Venus, and the satellite's passes provided insufficient coverage to continue our statistical mapping at all distances. Our

map of the ninth decile of amplitudes simply cannot occupy the part of the area of coverage where there were, say, five or fewer samples according to color scale of the spatial distribution of samples (Plate 3a). We see only that the region of Earth's intense pw activity extended to at least 100 R_E. Since $R_V \approx R_E$, Earth's electron foreshock boundary extends 6 or more times farther from its corresponding tangent point in absolute distance than does that of Venus.

The region behind Earth's electron foreshock boundary also contrasts with that of Venus, in that an appreciable amount of pw activity down to an order of magnitude less than peak amplitude continued well downstream from the boundary, as in Plates 3c and 3d. At Venus, the downstream foreshock appeared essentially invisible at the electron plasma frequency. However, the ISEE 3 instrument was far more sensitive than that of PVO, so amplitudes at Earth of 10^{-4} V/m, which translate to intensities of $\sim 10^{-12}$ $(V/m)^2/Hz$ (with 15% channel bandwidth) at Venus, would have produced the apparent minimal activity close to background at the latter planet. *Crawford et al.* [1993b] speculated that sub-f_{pe} (so-called "downshifted") activity in the foreshock, similar to that identified at Earth by *Fuselier et al.* [1985], may have occurred at frequencies for which the PVO detector had no channel. We can attempt to understand the downstream effect in the present mappings with help from the more recent Galileo flyby of Venus [*Hospodarsky et al.*, 1994], as we shall discuss.

Discussion

The data suggest that Earth's region of high amplitude extends at least to about 100 R_E, perhaps beyond the ISEE 3 sampling region. Thus the 14-to-1 magnification of the Earth's shock size over that of Venus seems to influence the scale of the Earth's electron foreshock. On a microscopic level the solar wind conditions at Venus and Earth do not differ significantly. Hence the parameters important to the microphysics of the plasma oscillation instability (e.g., electron temperature, electron beam density, and velocity) should be roughly comparable for nominal solar wind states. The large difference in the extent of the wave activity between the two planets shows that the macroscale properties of the foreshock are controlled by macroscopic and not microscopic phenomena. Thus the extent to which plasma oscillations are detected away from the shock, where the beam originates, is dependent on the size of the shock/solar wind interaction region more than on the parameters of the instability. We may speculate that if the scaling were by simple linear size multiplication, the Earth's zone of intense signals could reach 200 R_E ($\sim 14 \times 16$) along the tangent IMF, on an absolute scale of subsolar shock distances D, where $D_{\text{Earth}} \approx 14 D_{\text{Venus}}$. If the scaling were by radius of curvature, r, Earth's zone could reach 168 R_E (10.5×16), since $r_{\text{Earth}} \approx 10\ r_{\text{Venus}}$ and R_E 1.05 R_V [*Strangeway and Crawford*, 1995b].

Since the macroscopic solar wind at Earth does not differ appreciably from that passing Venus, and Earth's bow shock is only moderately stronger than Venus', a possible reason for the enlarged f_{pe}- (i.e., electron) foreshock at Earth is that drift acceleration along the quasi-perpendiclar section of Earth's much larger bow shock results in greater energies [*Strangeway and Crawford*, 1995b], densities, and quantities of electrons escaping upstream from the tangent field point. Some of the comparative flood of Earth's counterstreaming electrons may penetrate farther into the solar wind before the plasma wave excitation by their interaction with the solar wind reduces to background. We know that energetic electrons themselves reach as far as 240 R_E upstream close to the tangent field line [*Anderson*, 1981].

The data further suggest that Earth's pw, hence counterstreaming electron, foreshock extends, at some reduced level, throughout a large region behind the boundary, not revealed in the Venus map. One implication is that the ISEE 3 instrument may have recorded the same sub-f_{pe} electron plasma oscillations dropping in amplitude and frequency with distance behind the boundary as in the earlier study of "downshifting" by *Fuselier et al.* [1985] and in the recent report by *Hospodarsky et al.* [1994]. We have not resolved the open questions within the scope of this study, partly because limitations of the ISEE 3 pw instrument prevent detailed observations analogous to those from Galileo at Venus. The difficulty can be readily appreciated by a glance at Figures 3 and 4 of the Hospodarsky et al. report with the discrete frequency spacing of the ISEE 3 channels in mind. If this explanation holds, however, then the orange shaded part of the mapping at ($X > 10$, $Y < -60$) R_E in Plate 3b, which came from the September pass at 17 kHz, would imply the existence of extensive pw activity, with $f < f_{pe}$ downstream from the tangent line.

The new results on upstream Langmuir waves at Venus [*Hospodarsky et al.*, 1994] offer a more detailed comparison between the foreshocks of the two planets than previously available. Using high-resolution, high-sensitivity measurements from Galileo's pw experiment as it passed Venus, Hospodarsky et al. have demonstrated that Langmuir waves both at f_{pe} and at higher and lower frequencies persist downstream from the foreshock boundary for similar values of depth used in constructing the PVO maps, where no apparent activity was registered by PVO's more limited detector. The report by Hospodarsky et al. therefore presents a more complicated electron foreshock at Venus than that disclosed by PVO, which measured only the more intense pw activity, and proposes, without resolution, a number of explanations for the pw behavior there, including multispecies contributions, as we have mentioned above.

The multispecies proposal is compatible with our maps. While Earth's quasi-parallel magnetosheath may supply a much more intense stream of escaping hot electrons in the deep foreshock than does that of Venus, and these could produce overlapping beams of accelerated and heated electrons, the quasi-parallel shock certainly returns ion streams to the foreshock, causing a corresponding region of IAR pw activity along with the well-known ULF wave signals. The 5.4-kHz map at Venus [*Crawford et al.*, 1993a; Strangeway and Crawford, 1995b] and the depth of the forward boundary of the large bright region in our $f < f_{pe}$ map (Plate 3d), support a counterstreaming ion as well as electron influence in the deep foreshock. Combined effects are plausible.

Our results here encourage some useful first-order conclusions:

1. The respective foreshock pw activity, hence solar wind–electron interaction regions, scale according to the size of the respective planetary obstacles.

2. ISEE 3–Galileo similarities imply comparable results can be obtained from study of either foreshock.

3. Frequency-dependent maps such as those obtained from PVO and ISEE 3 pw records supply a valuable global context in which to interpret the physics of foreshock particle population interactions and instabilities.

Expansion of the database is necessary to improve the resolution of the mapping and determine whether the electron foreshocks truly differ at the two planets. Augmentation with electron data will be necessary to resolve the reason(s) for differing wave characteristics, if any, at Earth and Venus. The Galileo results suggest that more complicated and comprehensive maps than those derived from PVO or ISEE 3 so far should compare differences in patterns produced by a wide range of frequencies, including those observed simultaneously in wide-band, high-resolution spectrograms, and taking into account the differences in IMF angle at the two planets. Spectral pw details and maps of reverse-streaming electrons and ions need to be combined. The imprecision of our maps and the uncertainties of their construction noted in the second paragraph of our mapping section above make it clear that a definitive mapping of the Earth's foreshock remains to be accomplished.

Acknowledgments. The magnetic field data are from the JPL instrument of ISEE 3, courtesy of Ed Smith. Support for the UCLA contribution was by NASA grant NAGW-3497. Work at Kyoto was supported by a Japan Society for the Promotion of Science Fellowship.

The Editor thanks R. J. Grard and another referee for their assistance in evaluating this paper.

References

Anderson, K. A., Measurements of bow shock particles far upstream from the Earth, *J. Geophys. Res.*, *86*, 4445, 1981.

Bame, S. J., J. R. Asbridge, H. E. Felthauser, J. P. Glore, H. L. Hawk, and J. Chavez, ISEE-C solar wind plasma instrument, *IEEE Trans. Geosci. Electron.*, *GE-16*, 160, 1978.

Crawford, G. K., A study of plasma waves arising from the solar wind interaction with Venus, Ph.D. thesis, 321 pp, Univ. of Calif. at Los Angeles, 1993.

Crawford, G. K., R. J. Strangeway, and C. T. Russell, VLF imaging of the Venus foreshock, *Geophys. Res. Lett.*, *20*, 2801, 1993a.

Crawford, G. K., R. J. Strangeway, and C. T. Russell, VLF emissions in the Venus foreshock: Comparison with terrestrial observations, *J. Geophys. Res.*, *98*, 15,305, 1993b.

Frandsen, A. M. A., B. V. Conner, J. van Amersfoort, and E. J. Smith, The ISEE-C vector helium magnetometer, *IEEE Trans. Geosci. Electron.*, *GE-16*, 195, 1978.

Fredricks, R. W., F. L. Scarf, and L. A. Frank, Nonthermal electrons and high-frequency waves in the upstream solar wind, 2, Analysis and interpretation, *J. Geophys. Res.*, *76*, 669, 1971.

Fuselier, S. A., D. A. Gurnett, and R. J. Fitzenreiter, The downshift of electron plasma oscillations in the electron foreshock region, *J. Geophys. Res.*, *90*, 3935, 1985.

Greenstadt, E. W., and L. W. Baum, Earth's compressional foreshock boundary revisited: Observations by the ISEE 1 magnetometer, *J. Geophys. Res.*, *91*, 9001, 1986.

Hospodarsky, G. B., D. A. Gurnett, W. S. Kurth, M. G. Kivelson, R. J. Strangeway, and S. J. Bolton, The fine structuree of Langmuir waves observed upstream of the bow shock at Venus, *J. Geophys. Res.*, *99*, 13,363, 1994.

Scarf, F. L., R. W. Fredricks, L. A. Frank, and M. Neugebauer, Nonthermal electrons and high-frequency waves in the upstream solar wind, 1, Observations, *J. Geophys. Res.*, *76*, 5162, 1971.

Scarf, F. L., R. W. Fredricks, D. A. Gurnett, and E. F. Smith, The ISEE-C plasma wave instrument, *IEEE Trans. Geosci. Electron.*, *GE-16*, 191, 1978.

Strangeway, R. J., and G. K. Crawford, VLF waves in the foreshock, *Adv. Space Res.*, *15*(8/9), 29, 1995a.

Strangeway, R. J., and G. K. Crawford, Comparison of upstream phenomena at Venus and Earth, *Adv. Space Res.*, *16*(4), 125, 1995b.

G. K. Crawford, SRI International, MS 40217, 333 Ravenswood, Menlo Park, CA 94025.

F. V. Coroniti, E. W. Greenstadt, and S. L. Moses, TRW Inc., Space and Technology Division, One Space Park, R1-2144, Redondo Beach, CA 90278.

R. J. Strangeway, Institute of Geophysics and Planetary Physics, University of California, Los Angeles, CA 90024.

(Received November 8, 1994; revised April 17, 1995; accepted May 1, 1995.)

LARGE SOLAR WIND DISTURBANCES DURING LATE MAY AND EARLY JUNE 1991

J. D. MIHALOV
Planetary Systems Branch, NASA-Ames Research Center, Moffett Field, CA, U.S.A.
and
R. J. STRANGEWAY
Institute of Geophysics and Planetary Physics, UCLA, Los Angeles, CA, U.S.A.

(Received 27 March, 1995; in revised form 1 May, 1995)

Abstract. Solar wind data from the Ames experiment aboard the Pioneer Venus Orbiter, coincident with a period of unprecedented solar activity that began at the end of May, 1991, within the highly active earlier portion of 1991, are summarized and discussed. Some comparison is made with corresponding data from Earth. Some particularly large, strong shocks and solar ejecta were observed at Venus. The solar longitude of Venus, relative to associated flares, varied over a wide range, for a series of flares that produced X-rays that saturated the GOES X-ray counters. Some of the disturbances at Venus must be due to CMEs with longitudinal extents up to ~40–50 deg.

1. Introduction

Unprecedented solar activity was observed during the early part of June 1991, considering at least the flare X-ray class, which has been reported in *Solar Geophysical Data* (*SGD*), Part II. Analyses of detailed white-light images for four of the large flares have been presented by Schmieder *et al.* (1994). The peak activity for solar cycle 22 was maintained well into 1991 by large solar events which included those of early June, 1991. Also, a substantial portion of the largest interplanetary shock events observed during the 14-year Pioneer Venus Orbiter mission occurred during the first seven months of 1991. Some of these shock events must have been due to coronal mass ejections (CMEs, see Hundhausen (1988, 1993) and Howard *et al.* (1985)). Relationships between interplanetary shocks and CMEs have been discussed by Sheeley *et al.* (1985) and Bravo and Nikiforova (1994). The unusually intense solar activity discussed here was associated with the lowest galactic cosmic-ray flux ever measured over almost the past forty years of operation, at the Mount Washington neutron monitor (Webber and Lockwood, 1993; Van Allen, 1993). The cosmic-ray intensity >70 MeV decreased by about 20% over a wide span of the heliosphere (Van Allen, 1993); details of the cosmic-ray modulation and a presentation of plasma disturbances in the outer heliosphere may be found in McDonald *et al.* (1994) (see also Burlaga and Ness (1994) and the results from a 3-D MHD model, reported by Usmanov (1993)) An earlier study (Cliver *et al.*, 1987) sought to associate sizable, heliospheric Forbush-type cosmic ray decreases during June–July, 1982, with specific solar and interplanetary events. The flare

Solar Physics **160:** 363–370, 1995.

activity observed at that time, however, was neither as intense nor as frequent as during early June, 1991. In particular, there were no events exceeding an X-ray class of X10.

It may also be noted that an analysis of the 59 largest cosmic-ray decreases during 1978 to 1982 at 1 AU heliocentric distance identified four classes of events, based upon the principal causes of the decreases: an interplanetary shock, the associated driver, both of these, or corotating streams and ejecta (Cane, Richardson, and von Rosenvinge, 1993). A similar study was carried out, for solar minimum data from 1987, by Lopate and Simpson (1991).

The five largest flares during June 1991 actually saturated the GOES X-ray counters for varying lengths of time (X-ray class exceeded X12.0); this has occurred previously at times of unusually high-intensity solar flare activity, as, for example, also once in each of the months March, August, and October 1989, during the current solar cycle 22. Owing to the saturation, only lower limits to the peak X-ray energy flux are available from the GOES X-ray detectors for the five large June 1991 events. With regard to the saturation of the detectors, other information is available on the energetics of these flares: in addition to the Hα optical information in *SGD*, Part II, there are also radio emission data, and lists of ionospheric disturbances due to ionizing radiation from the flares (in Part I of *SGD*). In general, the decimetric (synchrotron) radio emission data are somewhat difficult to interpret, although they do track the (hard) X-ray fluxes (Zirin, 1988), as observed by the Compton telescope, for example. The hard X-ray fluxes, in turn, seem similar to the time derivative of the soft X-ray fluxes (Zirin, 1988; Li, Emslie, and Mariska, 1993), as measured, for example, by the GOES detectors. There is a long-standing relation between X-ray duration overall, and CME occurrence (Sheeley *et al.*, 1983). Here estimates of the peak X-ray energy flux are not made; rather, the associated solar wind disturbances as observed with the Ames experiment on the Pioneer Venus Orbiter are presented and discussed. Some comparisons are made with data from near Earth. The lack of coronagraph CME data during this time interval handicaps analyses, because CME masses and energies are not available.

The Pioneer Venus Orbiter (PVO) spacecraft (Colin, 1980) was launched on May 20, 1978, and injected into orbit around Venus later in the year, on December 4. The experiment payload included a plasma analyzer (Intriligator, Wolfe, and Mihalov, 1980) for solar wind studies, and a plasma wave experiment (Scarf, Taylor, and Virobik, 1980).

2. Gross Aspects of Solar Activity and Interplanetary Disturbances

In Figure 1 the solar activity is summarized, in terms of the flare X-ray class and solar longitude, as reported in *SGD*, Part II, for the May 28 through June 12 period. There was an additional X12.0 class flare on June 15 (AR 6659). From the figure one sees that the X-ray flares principally arose from just two active regions. During

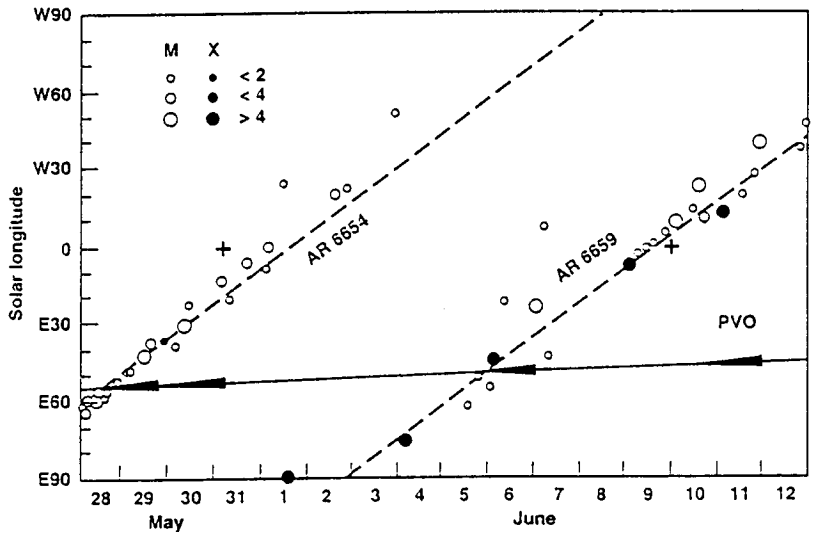

Fig. 1. Solar activity during late May and early June 1991, expressed as flare X-ray class, plotted on a time vs solar longitude (relative to Earth) grid. A diagonal line across the bottom of the plot gives the longitude of the Pioneer Venus Orbiter spacecraft. Symbols on the lower diagonal line indicate times when shock signatures were observed in the Orbiter plasma data, and times of hypothetical source events, as explained in the text. The times of two large-storm sudden commencements are also given, as '+' symbols, at the longitude of Earth (0 deg).

this period, the Pioneer Venus spacecraft was located at the longitude indicated by the line near the bottom of the figure. Four triangles indicate times of large solar wind disturbances, and of estimated origins; these are discussed subsequently. The left-hand apices of the triangles indicate the earliest times for launching plasma drivers whose preceding forward shocks are taken to be observed at the times that correspond with the right-hand edges of the triangles. These estimates for earliest launch times are based on the observed post-shock signature solar wind speeds, and assume no deceleration in transit from the Sun to the point of observation. During the period of Figure 1, the spacecraft is carried northward toward the heliographic equator, with Venus, from 3.5 deg S to 2.4 deg S; AR 6654 was, however, at 7 ± 3 deg N, and AR 6659 at 32 ± 5 deg N.

Also in Figure 1, the times of the two largest geomagnetic-storm sudden commencements (ssc, from *SGD*, Part I) during the period displayed, are given, at the longitude of Earth (0 deg; heliographic latitude, increasing from 1.2 deg S to 0.7 deg N). The largest ssc, on May 31, is presumably associated with the X1.0 flare of May 29. If so, effects of the CME were observed over a ~50 deg span of solar longitude. A shock was also observed at the IMP-8 spacecraft, somewhat later than the large ssc, at ~10:40 UT on May 31 (personal communication, MIT Plasma Group, 1994). Storm sscs have been found to be usually the result of interplanetary shocks (Smith *et al.*, 1986), and large geomagnetic storms are generally associated

with CMEs and/or shocks (Gosling *et al.*, 1991), and in particular, in addition, with large-amplitude, southward, interplanetary magnetic field components of several hours duration (Gonzalez and Tsurutani, 1987). An association of geomagnetic storm activity with the orientation of the magnetic field outside the magnetosphere was first found by Fairfield and Cahill (1966) (see the review article by Russell, 1980). Also, an earlier result about the connection between interplanetary shocks and geomagnetic activity was the observation of sc storms for 63% of shocks during 1971–1978, and more chance of geomagnetic activity for greater post-shock helium abundance (Borrini *et al.*, 1982). The corresponding result from Smith *et al.* (1986) was that 79% of the shocks during 1978–1979 were associated with sscs, while Gosling *et al.* (1991) found, for 1978–1982, that the larger geomagnetic disturbances were more likely to be associated with shocks (and/or CMEs). Kahler (1992) gives a historical discussion of the relationship between solar and geomagnetic activity, and also discusses associations of CMEs with several other indications of solar activity.

3. Interplanetary Plasma Data

In Figure 2 are given half-hour averages of solar wind proton speed (spacecraft frame), number density and isotropic temperature for May 28 through June 17, 1991, from the Pioneer Venus Orbiter. These parameters are obtained from least-squares fits of the experiment responses to simulated convecting, isotropic Maxwellian velocity distributions, to the measured plasma currents. A number of interplanetary forward shock signatures can be identified; four of the larger of these that are probably associated with large solar flares are listed in Table I, and are also indicated in the figure. The uncertain information for three of the four entries of the table is due to data gaps before (May 31) or after (June 6, 12) the shock transitions, that complicate the interpretations. The large event on June 1 may be a current sheet crossing that possibly terminates a period of low temperature shock driver gas associated with the May 29 flare; its detailed signature does not particularly resemble that of a strong shock. Most of the speed increase during this June 1 period occurs an hour or more after the increase of the proton temperature, and after a brief initial increase of the speed and the 30 kHz, 5.4 kHz, and 100 Hz electric field noise observed by the PVO plasma wave experiment; the proton density increase occurs even later.

The shock signatures generally seem to be followed by decreasing densities, and some of them are followed by decreasing wind speeds; the classic blast wave signature sometimes seen, has increasing post-shock densities and speeds, except for the case of instantaneous energy release, which has decreasing, post-shock densities and speeds (Parker, 1963; Hundhausen, 1972). It has been suggested that blast wave shocks do not accelerate ions (see Bai and Sturrock, 1989). Magnetic field measurements are not available for any of these shocks because the spacecraft

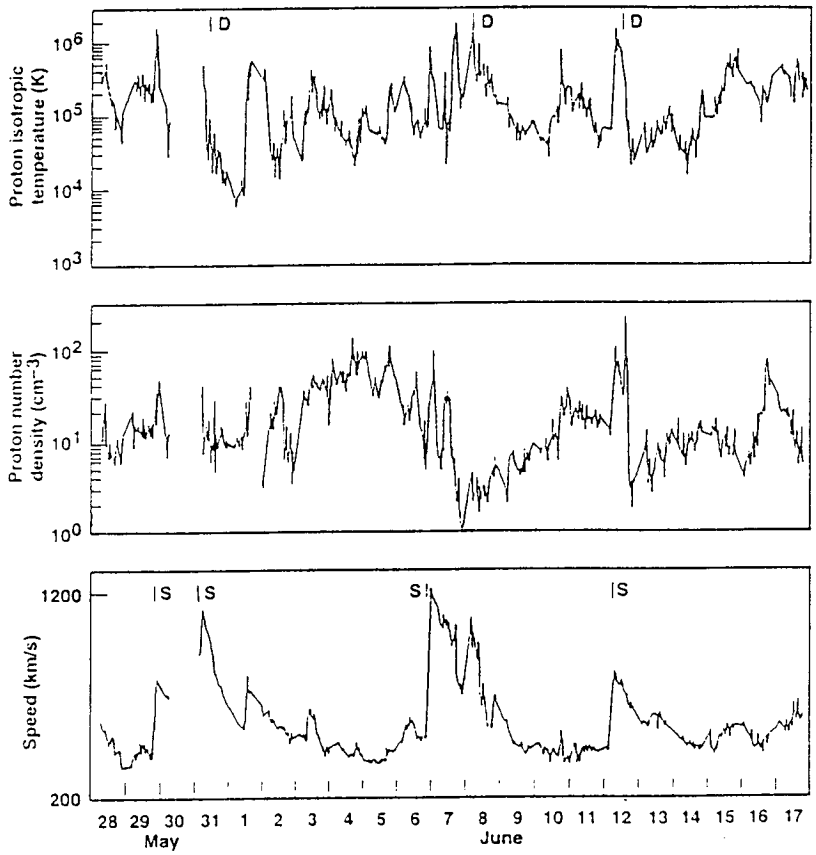

Fig. 2. Half-hour averages of solar wind proton speed, number density, and temperature, from the Ames experiment on the Pioneer Venus Orbiter, for May 28 through June 17, 1991. Times of four large shock signatures (S), and three candidates for the onset of driver gas (D), ejected by the Sun, are indicated.

magnetometer experienced a partial failure around October 15, 1988 (Russell *et al.*, 1993), and was generally operated only in the vicinity of periapsis, during late May and early June 1991.

We have attempted to locate driver gas (e.g., Richardson and Cane, 1993) in the solar wind data, for some of the shocks that have been discussed. The indication expected would be low temperature and enhanced helium, following a shock. Lower temperatures should be expected in a region of fast, unshocked material, with the shock forming ahead. The helium data available are largely unanalyzed. The principal feature of the proton temperature data following the shocks seems to be a more or less monotonic decrease, over a period of many hours. In some cases, abrupt decreases are observed within the monotonic declines; these could represent the leading edges of driver gas in the flows. The clearest instances seem to be on May 31, and on June 8 and 12, and are indicated in Figure 2, although

TABLE I

Four large forward shock signatures

Date, 1991, and time, UT	ΔV, km s^{-1}	$V_{dwnst.}$, km s^{-1}	Proton density ratio
May 29 1756:30 ± 5 s	210	580	2.4 ± 0.7
May 31 0000?	–	900?	–
June 6 1944 ± 1 min	670	1200?	>3
June 12 0455 ± 5 min	340?	~780	–

these abrupt decreases are barely resolvable on the figure as plotted. For June 8, the relative helium abundance is particularly high, following the abrupt decrease in temperature. The density is always high just after the shocks, and sometimes similarly jumps up at the beginning of the 'driver gas'.

Shock normals have been estimated, using velocity coplanarity, for the May 29 and June 6 signatures. The result for the May 29 case (0.92, −0.33, 0.20) has the principal nonradial component to the east (z component positive northward), opposite to what might be expected if the large M5.3 flare were close to the origin of the ejecta, as that flare is to the east of the spacecraft. For the June 6 signature the normal is (0.97, 0.19, 0.12), not suggestive of an origin near the preceding large X12.0 flare, which was ~30 deg to the north.

It may be noted that one suggestion resulting from the study by McDonald *et al.* (1994) of the outer heliospheric disturbances during the earlier part of 1991, was that of hypothetical major solar events on the Sun's back side, during late May and late June. Also, Cane and Richardson (1995) analyzed data near Earth's orbit, in October 1989, during the earlier solar activity peak of cycle 22, and concluded that four CMEs during the period studied extended up to 50 deg, but not more than 75 deg, from the sources.

4. Conclusions

The intense solar activity of early June 1991 resulted in a number of sizeable interplanetary disturbances that were observed in the solar wind at the Pioneer Venus spacecraft, located to the east of the Earth. Correlation of these disturbances with events in the solar flare lists suggests that the interplanetary disturbances first were associated with AR 6654, in late May, and then with AR 6659 as it rotated around the Sun's east limb. Other solar regions than these two have not been

associated with the largest interplanetary disturbances during this period. Detailed characteristics of some of the larger disturbances, interpreted as interplanetary shocks, include peak solar wind speeds up to 1230 km s^{-1}, and possible mean transit speeds from the Sun of up to ~1450 km s^{-1} (June 6 event; possibly up to ~1530 km s^{-1} to Earth for a ssc on June 10). Some of the disturbances are probably due to CMEs with longitudinal extents up to ~40–50 deg, but that angular size corresponds well with the mean extent in polar angle of CMEs (Hundhausen, 1993). This was also approximately the mean angular span for all CMEs observed during 1979–1981 (Howard *et al.*, 1985), but the angular span of small, faint CMEs alone was reported by those authors to be only about 25 deg.

Shock normal estimates (two cases) are not clearly consistent with the locations of flares that plausibly might be assumed as sources. It should be noted that CME locations are not distributed the same as those of small-scale solar magnetic features such as flares and active regions (Hundhausen, 1993), nor are flares found to lie in specific locations, relative to associated CMEs (Kahler, Sheeley, and Liggett, 1989; Harrison, 1986; Kahler, 1992).

References

Bai, T. and Sturrock, P. A.: 1989, *Ann. Rev. Astron. Astrophys.* **27**, 421.
Borrini, G., Gosling, J. T., Bame, S. J., and Feldman, W. C.: 1982, *J. Geophys. Res.* **87**, 4365.
Bravo, S. and Nikiforova, E.: 1994, *Solar Phys.* **151**, 333.
Burlaga, L. F. and Ness, N. F.: 1994, *J. Geophys. Res.* **99**, 19 341.
Cane, H. V. and Richardson, I. G.: 1995, *J. Geophys Res.* **100**, 1755.
Cane, H. V., Richardson, I. G., and von Rosenvinge, T. T.: 1993, *J. Geophys Res.* **98**, 13 295.
Cliver, E. W., Mihalov, J. D., Sheeley, N. R., Jr., Howard, R. A., Koomen, M. J., and Schwenn, R.: 1987, *J. Geophys Res.* **92**, 8487.
Colin, L.: 1980, *J. Geophys. Res.* **85**, 7575.
Fairfield, D. H. and Cahill, L. J., Jr.: 1966, *J. Geophys Res.* **71**, 155.
Gonzalez, W. D. and Tsurutani, B. T.: 1987, *Planetary Space Sci.* **35**, 1101.
Gosling, J. T., McComas, D. J., Phillips, J. L., and Bame, S. J.: 1991, *J. Geophys. Res.* **96**, 7831.
Harrison, R. A.: 1986, *Astron Astrophys.* **162**, 283.
Howard, R. A., Sheeley, N. R., Jr., Koomen, M. J., and Michels, D. J.: 1985, *J. Geophys. Res.* **90**, 8173.
Hundhausen, A. J.: 1972, *Coronal Expansion and Solar Wind*, Springer-Verlag, New York.
Hundhausen, A. J.: 1988, in V. J. Pizzo, T. E. Holzer, and D. G. Sime (eds.), *Proc. Sixth Int. Solar Wind Conf., NCAR/TN 306+Proc.* Vol. 1, National Center for Atmospheric Research, Boulder, Colorado, p. 181.
Hundhausen, A. J.: 1993, *J. Geophys. Res.* **98**, 13 177.
Intriligator, D. S., Wolfe, J. H., and Mihalov, J. D.: 1980, *IEEE Trans. Geosci. Remote Sens.* **GE-18**, 39.
Kahler, S. W.: 1992, *Ann. Rev. Astron. Astrophys.* **30**, 113.
Kahler, S. W., Sheeley, N. R., Jr., and Liggett, M.: 1989, *Astrophys. J.* **344**, 1026.
Li, P., Emslie, A. G., and Mariska, J. T.: 1993, *Astrophys. J.* **417**, 313.
Lopate, C. and Simpson, J. A.: 1991, *J. Geophys. Res.* **96**, 15 877.
McDonald, F. B., Barnes, A., Burlaga, L. F., Gazis, P., Mihalov, J., and Selesnick, R. S.: 1994, *J. Geophys. Res.* **99**, 14 705.
Parker, E. N.: 1963, *Interplanetary Dynamical Processes*, Interscience Publ., New York.
Richardson, I. G. and Cane, H. V.: 1993, *J. Geophys. Res.* **98**, 15 295.

Russell, C. T.: 1980, in S.-I. Akasofu (ed.), *Dynamics of the Magnetosphere*, D. Reidel Publ Co., Dordrecht, Holland, p. 3.
Russell, C. T., Strangeway, R. J., Luhmann, J. G., and Brace, L. H.: 1993, *Geophys Res. Letters* **20**, 2723.
Scarf, F. L., Taylor, W. W. L., and Virobik, P. F.: 1980, *IEEE Trans Geosci. Remote Sens.* **GE-18**, 36.
Schmieder, B., Hagyard, M. J., Guoxiang, A., Hongqi, Z., Kalmán, B., Györi, L., Rompolt, B., Démoulin, P., and Machado, M. E.: 1994, *Solar Phys.* **150**, 199.
Sheeley, N. R., Jr., Howard, R. A., Koomen, M. J., and Michels, D. J.: 1983, *Astrophys. J.* **272**, 349.
Sheeley, N. R., Jr., Howard, R. A., Koomen, M. J., Michels, D. J., Schwenn, R., Mühlhäuser, K. H., and Rosenbauer, H.: 1985, *J. Geophys. Res.* **90**, 163.
Smith, E. J., Slavin, J. A., Zwickl, R. D., and Bame, S. J.: 1986, in Y. Kamide and J. A. Slavin (eds.), *Solar Wind-Magnetosphere Coupling*, Terra Scientific Publ. Co., Tokyo, p. 345.
Usmanov, A. V.: 1993, *Solar Phys.* **148**, 371.
Van Allen, J. A.: 1993, *Geophys. Res. Letters* **20**, 2797.
Webber, W. R. and Lockwood, J. A.: 1993, *J. Geophys. Res.* **98**, 7821.
Zirin, H.: 1988, *Astrophysics of the Sun*, Cambridge University Press, Cambridge.

Pergamon

Journal of Atmospheric and Terrestrial Physics, Vol. 57, No. 5, pp. 537–556, 1995

0021-9169/95 $9.50+0.00

0021-9169(94)00080-8

Plasma wave evidence for lightning on Venus

Robert J. Strangeway

Institute of Geophysics and Planetary Physics, University of California at Los Angeles, U.S.A.

(*Received in final form* 19 *May* 1994; *accepted* 27 *June* 1994)

Abstract—Plasma wave data from the Pioneer Venus Orbiter provide the largest body of data cited as evidence for lightning on Venus. These data are also the most controversial, mainly because of the ambiguity in mode identification due to limited spectral information. We review some of the more recent studies of the plasma wave data at Venus, and we demonstrate that the characteristics of the 100 Hz waves are consistent with whistler-mode waves propagating vertically from below the ionosphere. We further show that *in situ* instabilities are too weak to generate whistler-mode waves, mainly because the thermal pressure is comparable with the magnetic field pressure in the ionosphere of Venus. The lower hybrid drift instability has also been suggested as an alternative source for the 100 Hz waves. However, the wave properties are more consistent with whistler-mode propagation; the lower hybrid drift instability requires very short gradient scale lengths to overcome damping due to collisions. We also note that an apparent association between Langmuir probe anomalies and 100 Hz waves is much lower than previously reported, once we apply a consistent intensity threshold for identifying wave bursts. The lightning hypothesis remains the most probable explanation of the plasma waves detected at low altitudes in the nightside ionosphere of Venus.

1. INTRODUCTION

Whether or not lightning occurs on Venus has been an issue of considerable debate over many years. Much of that debate has centered on the observation of plasma wave bursts in the ELF/VLF range, as measured by the Pioneer Venus Orbiter Electric Field Detector (OEFD) in the nightside ionosphere of Venus. Russell (1991) recently reviewed the evidence for lightning on Venus, and he describes the results of many of the earlier studies of the OEFD data. In particular, he notes that the plasma wave data are more consistent with a lightning source within the Venus cloud layer, rather than active volcanism as originally suggested by Scarf and Russell (1983). Thus, the interpretation of the plasma wave data has more to say about the atmosphere of Venus, rather than issues concerning active volcanism.

Lightning within the cloud deck of Venus has important implications for the dynamics and chemistry of the Venus atmosphere. In their search for an optical signature for lightning Borucki *et al.* (1991) pointed out that, based on our knowledge of terrestrial lightning, the meteorological conditions in the atmosphere of Venus may not be appropriate for the generation of lightning. Sulfuric acid, which is the main constituent in the clouds at Venus, has nearly the same dielectric constant as water, but it is not clear that sufficiently large particles are formed to allow charge separation. Thus, if lightning does occur on Venus, we may need to re-evaluate the mechanisms responsible for charge separation within its clouds. With regard to the importance of atmospheric lightning, Borucki *et al.* (1991) noted that lightning of sufficiently high rate can cause the formation of prebiological molecules. Russell (1991) also noted that a high lightning rate may be an issue for the safety of space probes, in addition to possible modifications of the atmospheric chemistry. The plasma wave data obtained by the Pioneer Venus Orbiter are the most extensive, and these data are hence suitable in determining lightning rates at Venus. It is therefore important to determine the likelihood that the wave bursts do correspond to lightning.

In support of the lightning interpretation of the VLF/ELF bursts, Russell (1991) pointed out that there is other evidence for lightning on Venus. Optical measurements from the Venera 9 spacecraft (Krasnopol'sky, 1983), and the observation of impulsive electromagnetic signals by the Venera landers (Ksanfomality *et al.*, 1983) both provide evidence for lightning within the Venus atmosphere. More recently, radio observations during the flyby of Venus by the Galileo spacecraft have also been interpreted as evidence for lightning (Gurnett *et al.*, 1991). The Galileo observations are probably the least controversial,

since the data were acquired several planetary radii from Venus, in the solar wind. It is highly unlikely that plasma instabilities can generate impulsive signals around 1 MHz in the solar wind.

On the other hand, there have also been negative results in the search for lightning at Venus, most notably in searches for optical signatures. Data from the VEGA balloons did not show any evidence for lightning. Borucki *et al.* (1991), using data from the star sensor on board the Pioneer Venus spacecraft, did not find any optical flashes whose rate exceeded the false alarm rate. However, both these searches tended to concentrate over the dawn local time sector, while it appears that lightning is mainly a dusk related phenomenon.

Irrespective of the other evidence for lightning, there is still the issue of whether or not the plasma waves observed in the nightside ionosphere are due to lightning. In testing the lightning hypothesis, we are investigating the plasma wave properties of a weakly magnetized and weakly collisional plasma which is quite different from the terrestrial ionosphere. In particular, as we will emphasize throughout this review, the energy density of the thermal plasma can be comparable with the magnetic field energy density. This has important implications for both wave propagation and also possible plasma instabilities.

Our approach in this review is to compare and contrast the expected plasma wave signatures from the lightning hypothesis with the various plasma instabilities proposed as alternatives. We hope to demonstrate the strengths and weaknesses of the different hypotheses. It is not our intention to prove, nor do we expect to find, that all plasma waves observed in the nightside ionosphere of Venus are due to atmospheric lightning. Rather, our purpose is to assemble sufficient evidence to determine the most probable source for the majority of the plasma waves observed at Venus. Given the nature of the plasma wave data, this assessment must be based on statistics, rather than case studies. The question then becomes, given the various statistical properties of the waves, which hypothesis best explains the bulk (but not necessarily all) of the data?

The structure of this review is as follows. In the next section we discuss the morphology of the wave bursts. We demonstrate why the ELF (100 Hz) waves are probably whistler-mode waves, and further that they entered the ionosphere from below, consistent with a lightning source. In the third section we discuss the likelihood that plasma instabilities can generate whistler-mode waves at low altitudes. Because of the relatively high electron thermal pressure, we show that whistler-mode waves tend to be damped, rather than driven unstable. In the fourth and fifth sections we discuss the most recent alternative explanation for the 100 Hz waves, that they are associated with density fluctuations corresponding with short wavelength lower hybrid resonance waves driven unstable through a gradient drift instability. However, this instability requires very steep density gradients to produce a large enough drift to overcome the damping due to collisions. In the final section we summarize the discussion presented in this review.

2. THE MORPHOLOGY OF THE VLF/ELF BURSTS

The ionosphere of Venus is highly variable in structure. Unlike the Earth, there is no planetary magnetic field to define the basic geometry of the magnetic field within the ionosphere. Instead, the magnetic field within the ionosphere is generated through the diffusion and transport of the Interplanetary Magnetic Field (IMF). The IMF is brought into contact with the ionosphere of Venus through the solar wind flow within the magnetosheath. Both the solar wind and the IMF are highly variable and, consequently, the ionosphere has some of that variability imposed on it. Indeed, the ionosphere can change considerably from day to day (Brace and Kliore, 1991). As such, then, any attempt to give an average view of the ionosphere of Venus is suspect. Instead, we resort to sketches such as Fig. 1 (after Crawford *et al.*, 1993), which are meant to represent some of the many different features observed within the highly variable ionosphere of Venus. It should be remembered that Fig. 1 is not a snapshot of the ionosphere; many of the structures shown in the figure are not always present on any particular pass through the ionosphere.

The most striking of the structures observed within the nightside ionosphere of Venus are "ionospheric holes". These are regions of reduced ionospheric plasma density and enhanced magnetic field. The field within holes is often close to radial and, as we shall discuss later, these regions of near-radial field act as ducts for whistler-mode waves. One other interesting feature of holes is that they are mainly a solar maximum phenomenon. Holes do not appear to have been detected during the entry phase of the Pioneer Venus Orbiter, which occurred during solar intermediate conditions (Theis and Brace, 1993). This implies that holes are generated through day to night transport of plasma and magnetic field, since this transport is reduced for lower levels of solar activity.

At low altitudes within the nightside ionosphere of Venus, two basic types of VLF/ELF signal are detected. Figure 2 shows an example of the first type

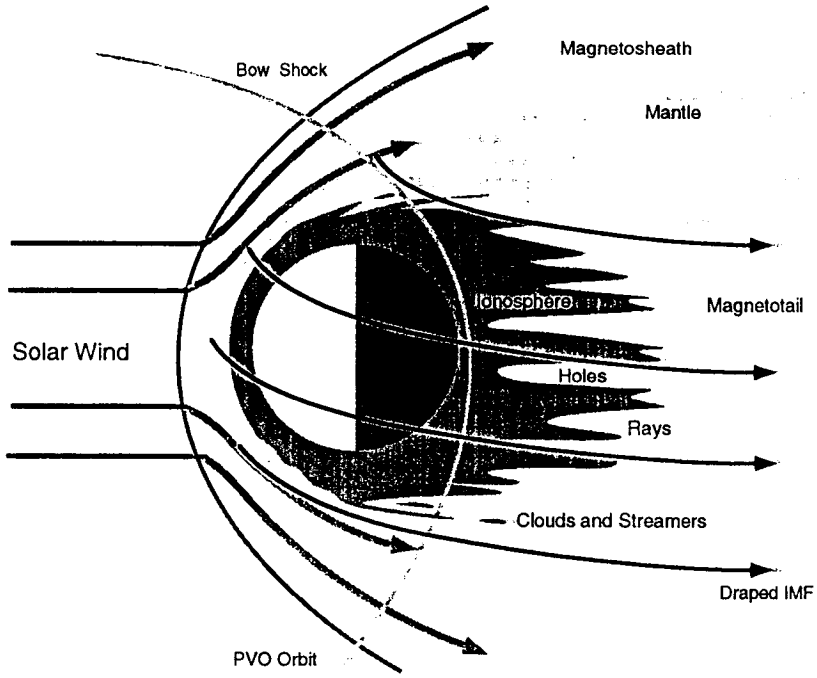

Fig. 1. Sketch of the solar wind interaction with the ionosphere of Venus (after Crawford *et al.*, 1993). The nightside ionosphere of Venus has considerable structure. Regions known as "holes", containing enhanced radial magnetic field and reduced plasma density, are often observed. These holes appear to act as ducts for upgoing whistler-mode waves.

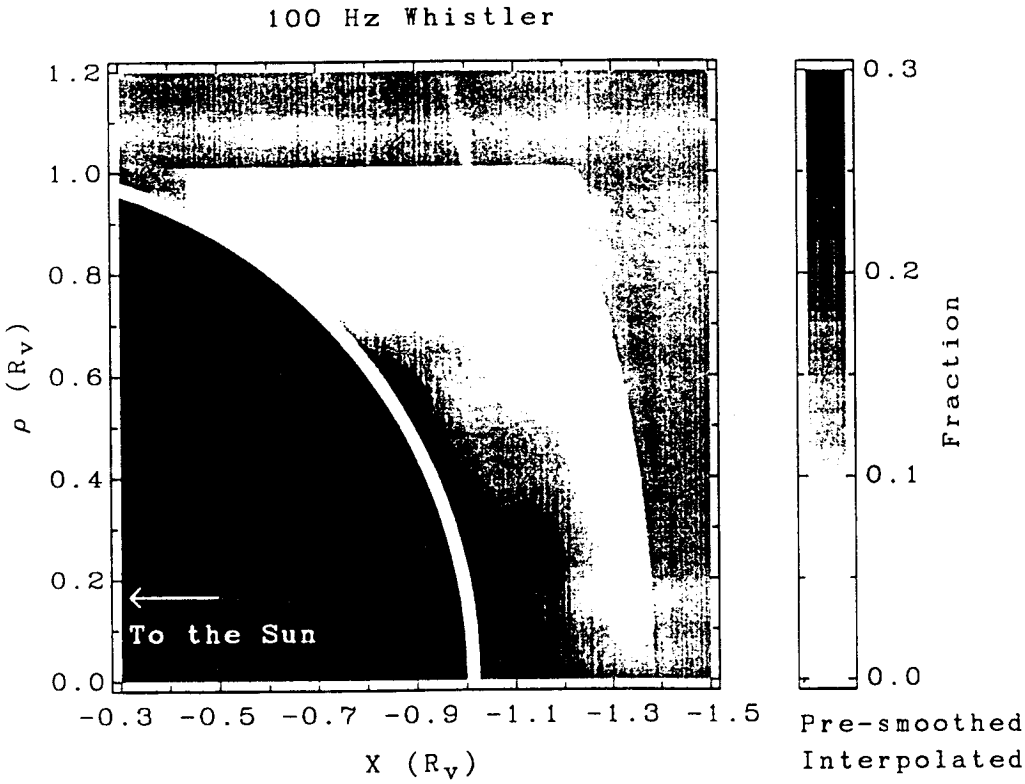

Fig. 4. Fractional occurrence for 100 Hz only bursts. Data from the first 22 seasons of nightside periapsis passes have been binned as a function of radial distance and solar zenith angle. The x-axis is along the Venus–Sun line, and the Sun lies to the left of the figure. The vertical axis gives the distance perpendicular to the Venus–Sun line, $\rho = \sqrt{(y^2 + z^2)}$. The data have been binned using 0.05 R_V by 3° bins, and then smoothed and interpolated to generate the plot.

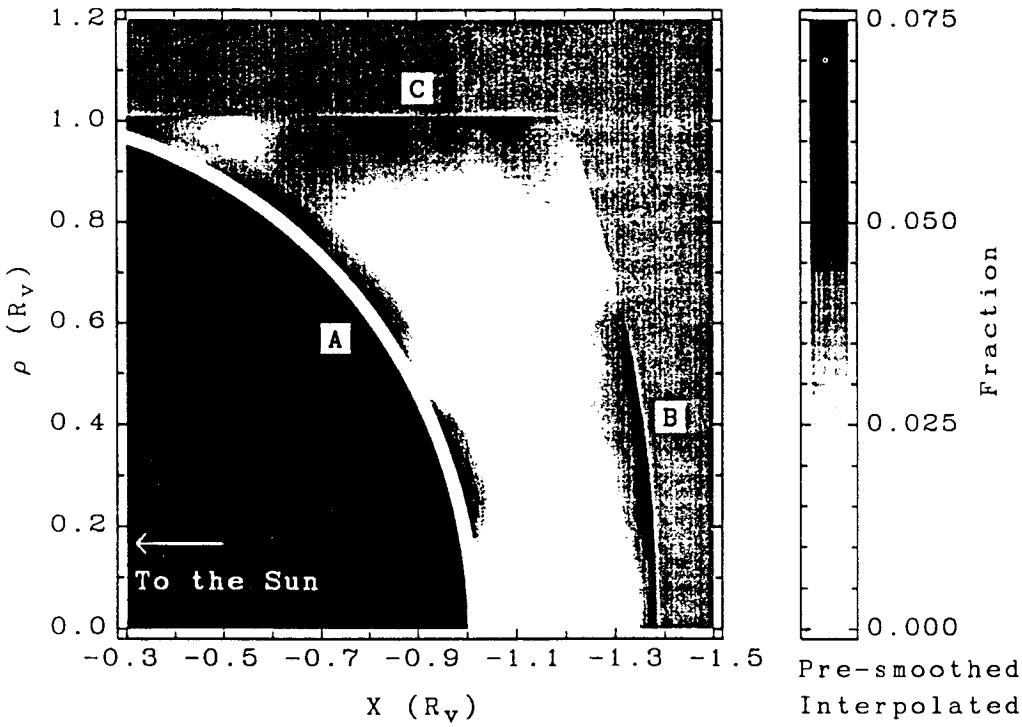

Fig. 5. Fractional occurrence rate for 5.4 kHz bursts. Similar in format to Fig. 4. Three different 5.4 kHz signals are observed, as indicated by the labels "A", "B" and "C".

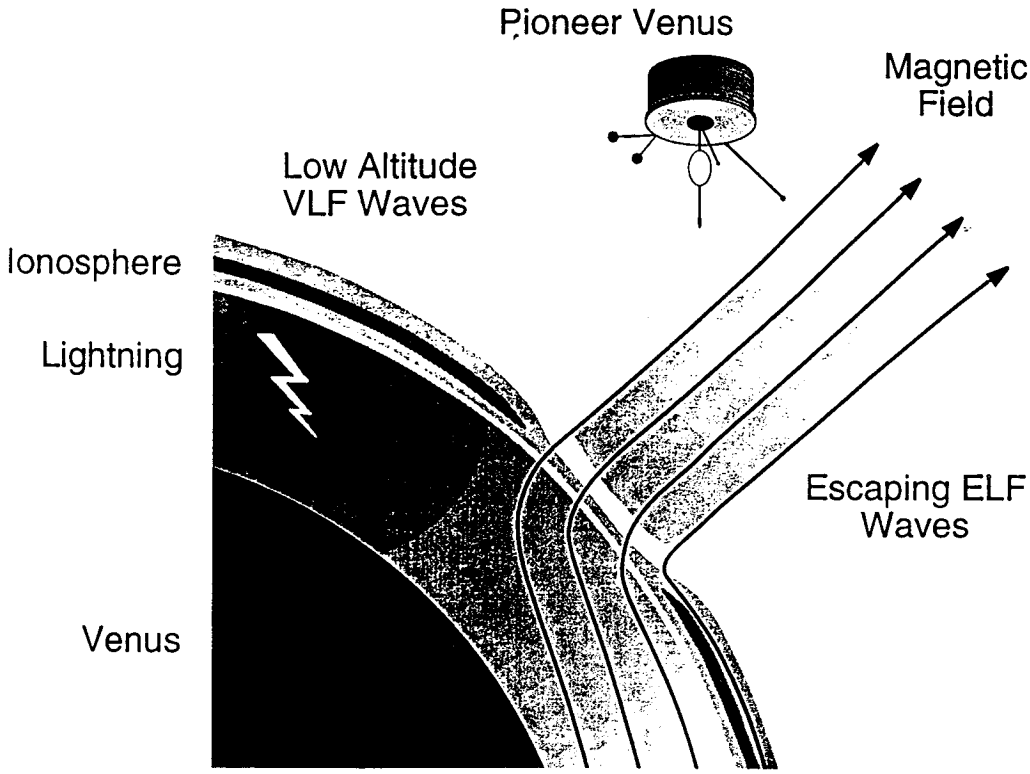

Fig. 12. Diagram illustrating the hypothesis that lightning is a source for plasma waves in the nightside ionosphere of Venus.

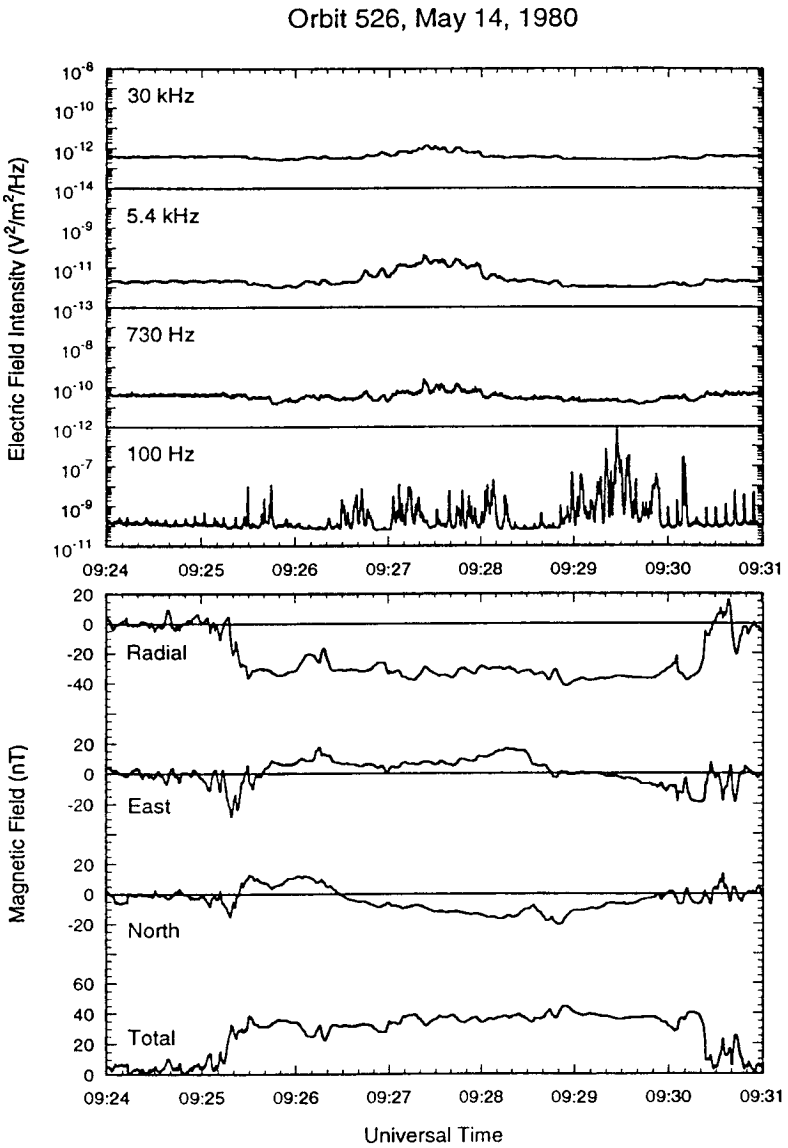

Fig. 2. Example of plasma wave and magnetic field data for orbit 526. These data are typical of the 100 Hz waves that have been attributed to lightning generated whistler-mode waves. The upper panels show the wave intensity in the four channels measured by the OEFD. The bottom four panels show the magnetic field data cast into radial–east–north coordinates.

of signal, which occurs only in the 100 Hz channel of the OEFD. Because of weight, power, and telemetry constraints, the OEFD has only four channels at 100 Hz, 730 Hz, 5.4 kHz and 30 kHz, with each channel having a bandwidth of $\pm 15\%$ of the center frequency (Scarf *et al.*, 1980b). The top four panels of Fig. 2 show the wave intensity, while the bottom four show the magnetic field data cast into radial–east–north coordinates. In this coordinate system, the radial component is vertically out, and the east component is horizontal and parallel to the Venus orbital plane. East is defined as positive in the direction opposite to the planetary rotation, since Venus rotates in a retrograde sense. North completes the triad. It can be seen that throughout most of the interval shown, the radial component of magnetic field dominates, and 100 Hz bursts are detected throughout this interval of strong radial field. Since these bursts only

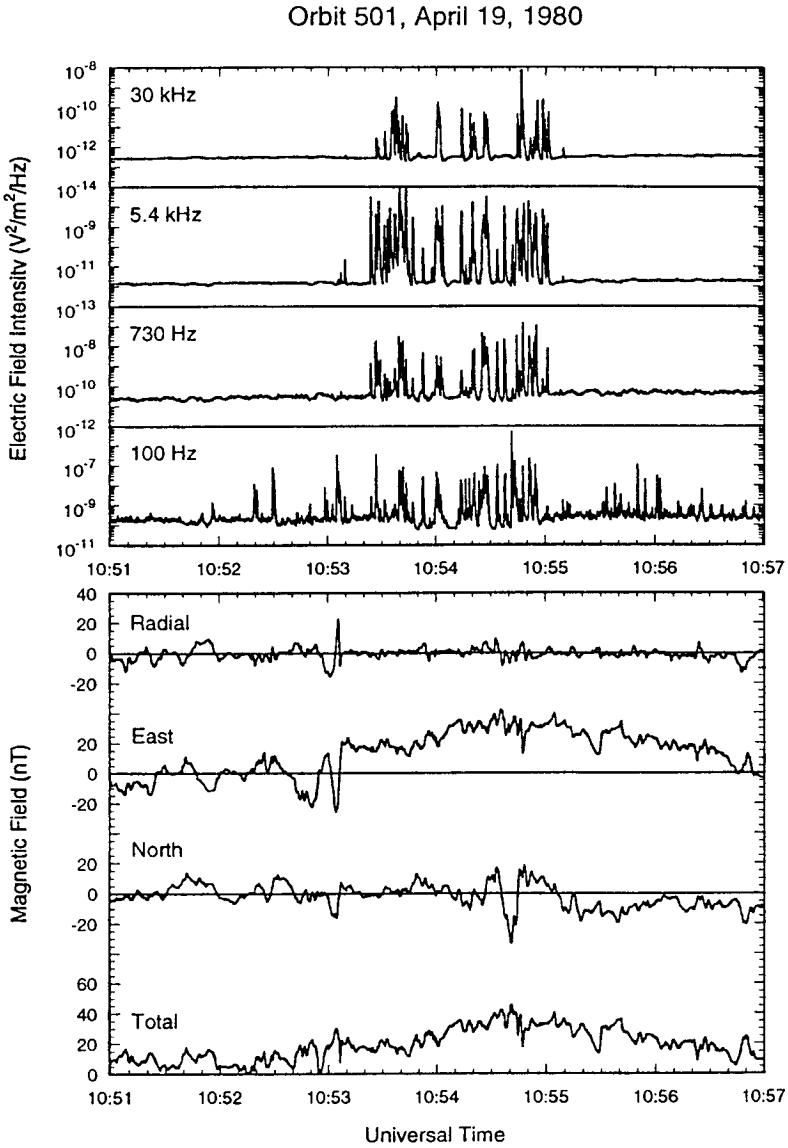

Fig. 3. Example of wideband bursts observed on orbit 501. Similar in format to Fig. 2.

occur at 100 Hz, they would have been counted as possible lightning generated whistlers in studies such as Scarf and Russell (1983).

The second type of signal often observed at low altitudes is shown in Fig. 3. These "wide-band" bursts have also been cited as possibly due to lightning (Singh and Russell, 1986; Russell, 1991). However these bursts are clearly not whistler-mode waves and, because of this, Scarf *et al.* (1980a) cautioned against using signals at higher frequencies as being possible lightning signals. Unlike the 100 Hz only bursts, Fig. 3 shows that the wide-band bursts are detected in regions of mainly horizontal field (Ho *et al.*, 1992). In discussing the wide-band signals, it should be noted that, while the earlier study of Singh and Russell (1986) suffered from contamination due to the inclusion of spikes caused by telemetry errors (Taylor and Cloutier, 1988; Russell and Singh, 1989), subsequent studies (e.g. Ho *et al.*, 1991, 1992) specifically excluded possible telemetry errors.

Sonwalkar and Carpenter (1995) have argued that the wide-band bursts are non-propagating modes and

therefore generated locally within the plasma. Hence, they do not consider wide-band bursts as being lightning generated. While this is almost certainly true for many of the higher altitude bursts (altitudes greater than ~ 1000 km), this need not be the case for the lower altitude bursts. At the Earth, for example, anomalous VLF bursts which arrived prior to the whistler-mode wave packet have been detected in the ionosphere above lightning (Kelley *et al.*, 1985). Boeck *et al.* (1992) have reported observations of lightning induced brightening of the airglow, while Burke *et al.* (1992) have reported the detection of keV electrons and large electric field transients above a hurricane. These various observations all suggest that, at the Earth, at least, lightning may couple to the ionosphere. The coupling mechanisms are not well understood, but it seems probable that "capacitive coupling" through the displacement current may drive conduction currents within the ionosphere (Hale and Baginski, 1987). In light of these observations, it is possible that the "wide-band" bursts detected at low altitudes in the Venus ionosphere could be due to direct coupling between lightning and the ionosphere.

To further emphasize the altitudinal dependence of the bursts detected at Venus, we present maps of the fractional occurrence of bursts in the 100 Hz channel only (Fig. 4) and in the 5.4 kHz channel (Fig. 5). In these two figures, we have binned the data for the first 22 seasons of nightside periapsis passes of the Pioneer Venus Orbiter. We have employed a technique similar to that described by Russell *et al.* (1988) and Russell (1991), where the data are separated into 30 s intervals, and each interval is classified as being active or quiet at each frequency. The fractional occurrence rate of 100 Hz burst activity is plotted as a function of position in Fig. 4, where position is expressed in units of Venus radii (R_v, and 1 $R_v = 6052$ km). The 100 Hz only signals tend to occur most frequently at low altitudes, and extend to highest altitudes near the anti-subsolar point. In generating Fig. 4, we have excluded all intervals for which additional signals occur at higher frequencies. For this reason, we have classified the events as 100 Hz whistler events.

Figure 5, on the other hand, shows the presence of several distinct plasma wave populations as measured at 5.4 kHz. First, at lowest altitude, we see several peaks in the occurrence rate, labeled "A". These correspond with the "wide-band" bursts discussed above. Second, at high altitudes and high solar zenith angles (i.e. $\rho < 0.7\ R_v$ and $x < -1.2\ R_v$), there is a peak in the occurrence rate, labeled "B". Unlike the low altitude wide-band bursts, there are no additional signals at higher or lower frequencies when these waves occur at 5.4 kHz, and they are plasma oscillations in very low density regions of the Venus tail (Ho *et al.*, 1993). Lastly, additional wave bursts occur near the edge of the optical shadow (i.e. $\rho > 0.7\ R_v$), labeled "C". These waves are often correlated with waves at lower frequencies (730 Hz and 100 Hz), and may correspond to ion acoustic waves generated in the low density wake region of the planet. It is clear from Fig. 5 that the properties of the VLF bursts at high altitudes cannot be used to infer the source of VLF bursts at low altitude.

There have been several studies on the morphology of the low altitude bursts (see Russell, 1991), and we will describe only the more recent results. In their recent studies Ho *et al.* (1991, 1992) developed a method for determining the burst rate of the VLF waves observed at low altitudes, as opposed to the occurrence rate as shown in Figs 4 and 5. The burst rate studies are useful for comparison with the lightning rate at the Earth, for example, but suffer from possible over- or under-sampling, depending on the data rate. The occurrence rates cannot be easily compared with other rates, but do not suffer from dependence on the telemetry rate. With these points in mind, Fig. 6 shows the burst rate as a function of local time for all four channels of the OEFD. As with other studies, the higher frequency bursts tend to peak in the dusk local time sector, while the 100 Hz bursts occur throughout the nightside.

Strangeway (1991a) and Sonwalkar *et al.* (1991) point out that, if the 100 Hz waves are lightning generated whistler-mode waves, then they will be refracted vertically on entering the ionosphere from below. This is because the refractive index in the ionosphere is typically around 1000. Whistler-mode waves can only propagate within a cone about the ambient field, known as the resonance cone. The resonance cone angle is given by $\cos\theta_r = f/f_{ce}$, where f is the wave frequency (100 Hz), and f_{ce} is the electron gyro-frequency ($= 28B$ Hz, where B is the magnetic field strength in nT). If the magnetic field makes an angle θ_{br} with respect to the vertical, then the resonance cone test requires $\theta_{br} < \theta_r$. Alternatively, the resonance cone test requires that the vertical component of the magnetic field $B_r > f/28 = 3.6$ nT for 100 Hz.

As an example of the importance of the resonance cone test, Fig. 7, from Ho *et al.* (1992), shows the burst rate as a function of altitude. For the 100 Hz waves, each sample has been tested to determine if vertical whistler-mode propagation is allowed, and the rate for the 100 Hz waves inside the resonance cone is plotted separately from the 100 Hz waves outside the resonance cone. It is clear from the figure that the waves observed at low altitudes separate into two types of signal. The rate for 100 Hz waves inside the

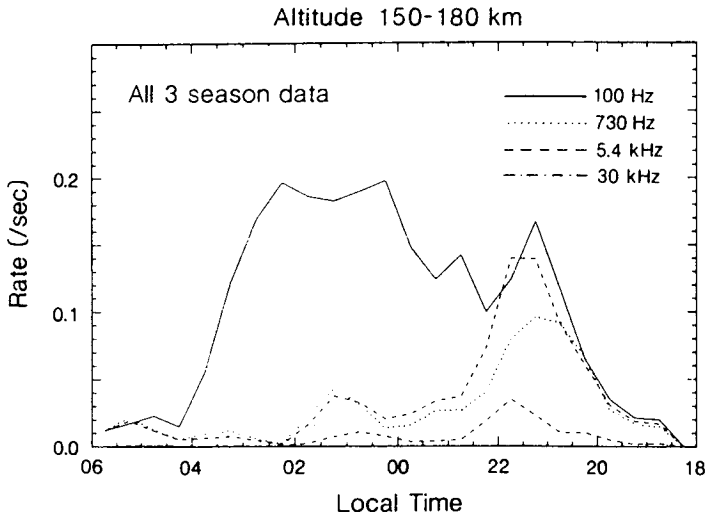

Fig. 6. VLF ELF burst rate as a function of local time for the low altitude bursts detected in the first three seasons of nightside periapsis passes (after Ho *et al.*, 1991).

resonance cone decreases slowly with increasing altitude. The higher frequency waves and the 100 Hz waves outside the resonance cone all decrease rapidly with increasing altitude, and further all decrease at roughly the same rate with a scale height of about 20 km.

Figure 7 implies a common source for the 100 Hz waves outside the resonance cone and the high frequency bursts. The rate is generally highest at low altitude, while Fig. 6 shows that the wide-band bursts are observed mainly in the post-dusk local time sector. We do not expect the ionosphere to display a strong asymmetry as a function of local time. However, the neutral atmosphere does, because of super-rotation. Thus, an atmospheric source for the non-whistler-mode signals is probable, and lightning coupling directly to the ionosphere is a reasonable explanation for the wide-band signals. As will become clear in discussing the 100 Hz whistler-mode signals in subsequent sections, the dominant controlling factor for the whistler-mode waves is the degree of accessibility for these signals. The whistler-mode waves are observed wherever a propagation window is present, while the non-whistler signals are more closely related

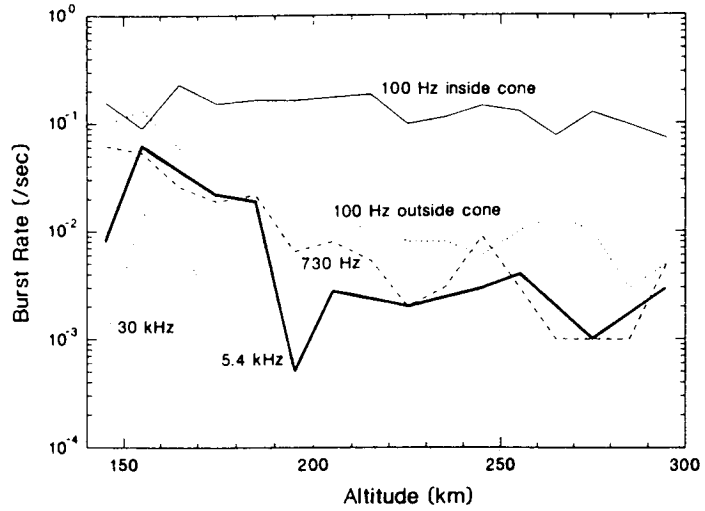

Fig. 7. VLF/ELF burst rate as a function of altitude (after Ho *et al.*, 1992).

to the underlying source. Thus, the wideband data are used to determine lightning rates and Ho *et al.* (1991) found planet-wide rates comparable to those for terrestrial lightning.

The resonance cone test is very powerful. It only applies for waves that are assumed to have propagated from below the ionosphere. That the 100 Hz waves separate into two distinct classes by applying this test is strongly supportive of the lightning hypothesis, since any *in situ* instability does not require vertical propagation. Strangeway (1991b) also used the resonance cone test to investigate the polarization of the 100 Hz waves. He found that the waves which satisfied the resonance cone test were polarized perpendicular to the ambient field, as expected for whistler-mode waves. Sonwalkar *et al.* (1991) applied the resonance cone test to several burst intervals, and they found that 6 7 of the intervals which contained wave activity at 100 Hz only were consistent with whistler-mode propagation from below the ionosphere.

3. LIGHTNING OR WHISTLER-MODE INSTABILITY

Several authors have suggested that the VLF bursts detected at low altitudes in the Venus nightside ionosphere are generated locally, rather than through lightning in the Venus atmosphere. In addition to comments on the association of 100 Hz waves with holes, Taylor *et al.* (1987) noted that the waves detected at 100 Hz were observed primarily when the spacecraft velocity vector was perpendicular to the ambient magnetic field. They argued that the waves were in fact short wavelength waves propagating parallel to the ambient field which could be Doppler-shifted to higher frequencies and the selection criterion used by Scarf and Russell (1983) requiring bursts at 100 Hz only artificially excluded those waves that had been Doppler-shifted through spacecraft motion. Figure 8, from Ho *et al.* (1992), shows that the burst rate for 100 Hz waves was largest when the magnetic field was vertical. The data are plotted as a function of the angle between the magnetic field and the radial direction (θ_{br}), and the angle between the magnetic field and the spacecraft velocity vector (θ_{bv}). Since the spacecraft motion is nearly horizontal around periapsis, a vertically oriented magnetic field will be perpendicular to the spacecraft velocity vector. In determining the dependence on magnetic field orientation, no selection criteria, other than an intensity threshold, were applied to the data. Thus, that the waves are observed for a vertical field is an intrinsic property of the signals, and is not due to some selection criteria artificially rejecting those events for which

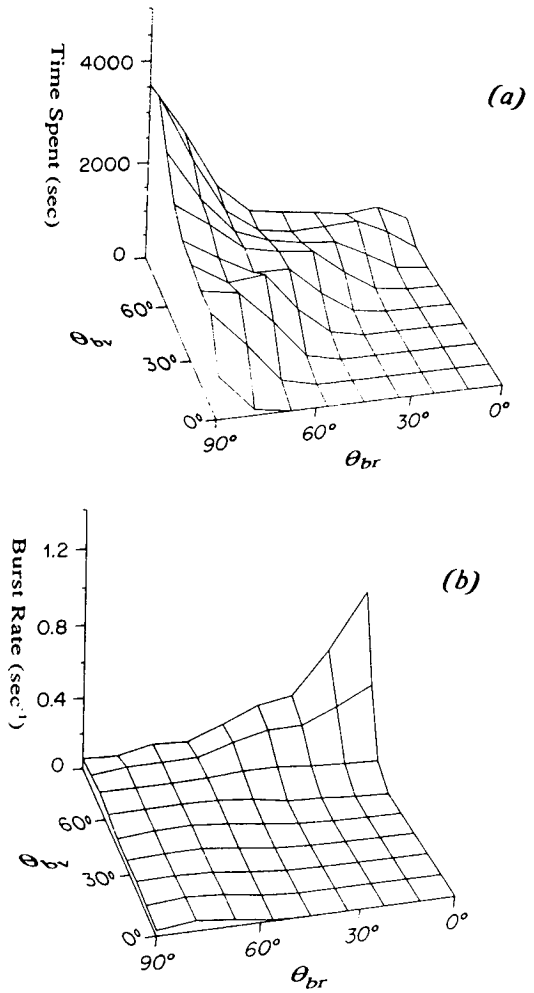

Fig. 8. 100 Hz burst rate dependence on the magnetic field orientation (after Ho *et al.*, 1992). The upper plot shows the time spent as a function of θ_{br} (the angle between the magnetic field and the radius vector) and θ_{bv} (the angle between the magnetic field and the spacecraft velocity vector). Note that, for $\theta_{br} \approx 0$, $\theta_{bv} \approx 90$. The lower plot shows the burst rate, which peaks at $\theta_{br} \approx 0$. At higher θ_{br}, there is no dependence on θ_{bv}.

the spacecraft velocity vector is perpendicular to the field. It is hence unlikely that the 100 Hz bursts are parallel propagating ion acoustic waves. Alternative wave instabilities that have been suggested are cyclotron resonant whistler-mode instabilities (Maeda and Grebowsky, 1989) and short wavelength lower hybrid waves (Huba, 1992). Both these instabilities generate waves that would be detected in the 100 Hz channel of the OEFD.

In this section we concentrate on whistler-mode instabilities. Maeda and Grebowsky (1989) argued

that the signature of VLF saucers, which occur at low altitudes in the Earth's auroral zone ionosphere, would be similar to the bursts detected at Venus by the OEFD, if the same instrument were to be flown at the Earth. However, this argument neglects a fundamental difference between the terrestrial and Venusian ionosphere. At the Earth, there is a strong internal magnetic field that ensures that the plasma β is low ($\beta = 2\mu_0 n k_B T/B^2$, the ratio of thermal to magnetic energy density, where μ_0 is the permeability of free space, n is the plasma number density, k_B is the Boltzmann constant, T is the plasma temperature, and B is the ambient magnetic field strength). At Venus, on the other hand, the magnetic field is relatively weak and the plasma can have a high β, as noted by Strangeway (1990).

This point was discussed further by Strangeway (1992). For the sake of discussion, we assume that the electron density in an ionospheric hole $\approx 3 \times 10^3$ cm^{-3}, and the magnetic field ≈ 30 nT. For these values, the electron plasma frequency to gyro-frequency ratio (ω_{pe}/Ω_e) ≈ 500. This ratio will be higher outside the holes since the magnetic field is weaker and the density is higher. Whistler-mode dispersion curves for this ratio are shown in Fig. 9. The figure shows that the highest parallel phase speed is ≈ 300 km s^{-1}, corresponding to an electron energy of 0.26 eV. Thus, we expect whistler-mode waves to be damped by thermal electrons in the nightside ionosphere of Venus, and this damping will suppress any whistler-mode instability.

To demonstrate this point more clearly, in Fig. 10 we plot the damping rate of 100 Hz waves as a function of the normalized electron thermal velocity $(v_T/c)(\omega_{pe}/\Omega_e)$, where v_T is the thermal velocity of the electrons. We have used the convention that $1/2 m_e v_T^2 = k_B T$. The normalized thermal velocity $= \sqrt{\beta_e}$, where β_e is the electron beta. In calculating β_e, we have used 2-s averages of the electron density and temperature measured by the Langmuir probe onboard the Pioneer Venus Orbiter, and the magnetic field. The data were acquired from orbits 484–560, and we have restricted the altitude range to < 300 km. The convective damping rate has been calculated for parallel propagating waves at 100 Hz. We find that for $\sqrt{\beta_e} = 1$, the damping decrement is ≈ 5 dB/km. Thus, the wave intensity will have decreased by ten orders of magnitude after propagating some 20 km in the nightside ionosphere. Clearly, whistler-mode waves cannot propagate any great distance in the high β_e regions of the nightside ionosphere. Thus, ionospheric holes, which are low β_e, are where whistler-mode waves are more likely to be found. The magnetic fields within holes also have a large vertical component, allowing vertical propagation of whistler-mode waves from below the ionosphere. That 100 Hz wave bursts are found within ionospheric holes is entirely consistent with the lightning hypothesis. Strangeway (1992) further showed that the 100 Hz wave intensity was largest in regions where the thermal electron damping was lowest.

As a last comment on the work of Maeda and Grebowsky (1989), Strangeway (1992) also investigated a beam driven instability. He assumed a beam density of 5 cm^{-3}, parallel drift speed = parallel thermal velocity = $0.007c$ (12.5 eV), and a temperature anisotropy $T\perp/T = 2$. This beam represented precipitating solar wind electrons that had gained access to the nightside ionosphere of Venus. He found growth rates less than 0.1 dB/km, requiring growth paths of at least 1000 km for a gain of 100 dB. It is hence very difficult for whistler-mode waves to grow to appreciable intensities within the nightside ionosphere, especially at low altitudes.

4. LIGHTNING OR DENSITY FLUCTUATIONS

Grebowsky *et al.* (1991) recently reported observations of density irregularities by the Langmuir probe onboard the Pioneer Venus Orbiter. (The Langmuir Probe is also known as the Orbiter Electron Temperature Probe, or OETP.) Grebowsky *et al.* also noticed a correlation between the Langmuir probe anomalies and changes in the wave intensity measured at 100 Hz by the OEFD. They found that between 56% and 73% (depending on the event selection criteria) of the Langmuir probe anomalies had 100 Hz bursts associated with them. Unfortunately, the study of Grebowsky *et al.* suffered from several factors that made comparison with other studies of the burst rate difficult. First, each Langmuir probe sweep lasted 0.5 s, but only one sweep was transmitted to the Earth every 8 s. The other sweeps were reduced onboard before transmission. Thus, while anomalies could be tested for associated 100-Hz bursts, the reverse was not the case.

Grebowsky *et al.* (1991) did compare their rate of coincidence with that expected from the burst rate studies of Ho *et al.* (1991). However, the burst rate studies used a fixed threshold of 2×10^{-9} V^2/m^2/Hz, while Grebowsky *et al.* counted signals as low as a factor of 2 above background as being bursts. For reference, the background of the 100 Hz channel is variable, but is typically around 10^{-10} V^2/m^2/Hz. Thus it is difficult to compare the coincidence rate as reported by Grebowsky *et al.* (1991) with that expected for random coincidence. Furthermore,

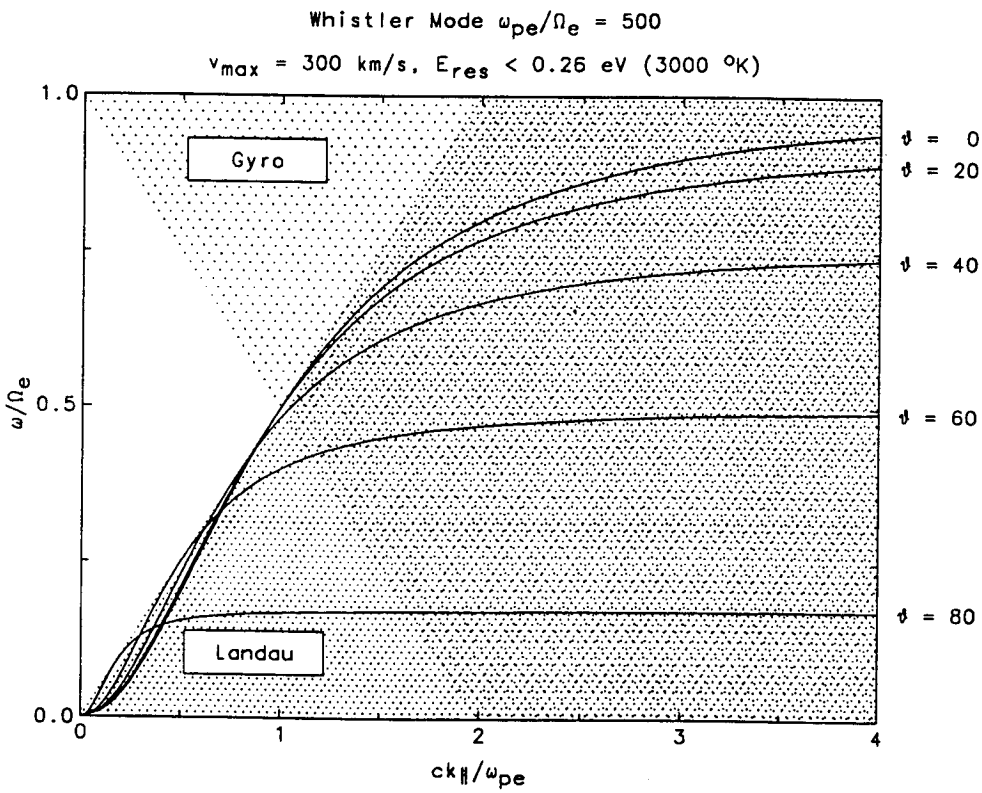

Fig. 9. Whistler-mode dispersion curves for different propagation angles (after Strangeway, 1992). Wave frequencies are normalized to the electron gyro-frequency, while the parallel wave vector is normalized to the inverse of the plasma skin depth. The shaded regions show where thermal electron Landau and gyro-damping are expected to occur.

Grebowsky *et al.* did not compare the coincidence rate for anomalous scans with the rate found for normal scans, again making a comparison with random coincidence difficult.

Here, we take a statistical approach to determine if the apparent association of Langmuir probe anomalies is more than simply random coincidence. We have used the Langmuir probe anomaly data (J. M. Grebowsky, personal communication, 1992) for the first three nightside periapsis seasons as a basis for this determination. As a first step, we use the burst counting method of Ho *et al.* (1991) to calculate the probability that one or more bursts exceeding the 2×10^{-9} $V^2 m^{-2} Hz$ threshold will occur in any 2-s interval. We have chosen this length of interval since the Langmuir probe anomaly timing is given to the nearest second. Using that probability, we can then compare the coincidence rate for bursts and Langmuir probe anomalies with that expected through random coincidence.

The first row of Table 1 shows the results of this calculation for all the data acquired within 0.9 R_v of the Venus–Sun line, and altitudes < 300 km in the nightside ionosphere. The table shows that 20% of the Langmuir probe anomalies have one or more 100 Hz bursts occurring within a 2-s interval including the Langmuir probe sweep. Since the probability that one or more bursts will occur in any 2-s interval is $\approx 7\%$, the observed degree of coincidence lies in the upper 0.1% of the tail of the binomial distribution for 150 samples with a 7% event probability, under the assumption of independent events. Another way of assessing the significance of the observed degree of coincidence is to note that for a binomial distribution with event probability of 7%, the mean number of events is 10 for 150 samples, while the variance is also 10. The standard deviation is therefore ≈ 3, and the observed number of coincident events is at least 6 standard deviations away from the mean. Thus, the 20% coincidence is statistically significant, but it is

Table 1. Comparison of burst probability and the coincidence rate for Langmuir probe (OETP) anomalies. The binomial probability gives the probability that the number of coincident events $>m$, for N Langmuir probe anomalies (corresponding to a one-tail test)

	Burst probability	OETP anomalies (N)	Coincident anomalies (m)	Coincidence rate	Binomial probability
All intervals	6.61%	150	30	20.00%	<0.10%
Whistler	9.19%	90	16	17.78%	0.77%
Non-whistler	4.20%	60	14	23.33%	<0.10%

Table 2. Comparison of burst probability and the coincidence rate for Langmuir probe (OETP) anomalies, using those intervals for which Langmuir probe UADS data are available

	Burst probability	OETP anomalies (N)	Coincident anomalies (m)	Coincidence rate	Binomial probability
All intervals	6.45%	63	11	17.46%	0.22%
$\beta_e < 1$	12.98%	52	10	19.23%	12.98%

much less than that reported by Grebowsky *et al.* (1991).

In previous sections, we have emphasized that the 100 Hz waves correspond with vertically propagating whistler-mode waves. In computing the burst probability, however, we have assumed that the bursts occur independently of the underlying ionospheric conditions. In the lower two rows of Table 1, we have tested each interval for whether or not vertical whistler-mode propagation is allowed. The table shows that the probability of a burst occurring in an interval in which vertical propagation is allowed is $\approx 9\%$, somewhat higher than for all intervals, while the degree of coincidence has dropped slightly, $\approx 18\%$. Thus, the coincidence rate lies in the upper 1% of the binomial distribution for 90 samples with 9% event probability. This again suggests that the coincidence is not random, but is much less than one would expect for a direct causal relation between Langmuir probe anomalies and 100 Hz bursts. For completeness, Table 1 also includes the "non-whistler" intervals.

One interesting feature in the table is that, regardless of the selection criteria, the coincidence rate is roughly constant. This suggests that the coincidence occurs because of some underlying property of the ionosphere that is common to both signatures. In the previous section, we have shown that low β_e is required for whistler-mode propagation. Huba (1992) suggested that the Langmuir probe anomalies may be signatures of the lower hybrid drift instability, and he has shown that low β_e also applies to the lower hybrid drift instability. However, in Table 1, we have included all intervals, irrespective of β_e. This will reduce the predicted probability for 100 Hz bursts. In Table 2, we show the burst probability for those intervals for which $\beta_e < 1$. In order to determine β_e, we need to know the electron density and temperature. We have used Langmuir probe data from the Unified Abstract Data System (UADS) for this purpose. We have interpolated the data to the 2-s resolution used earlier. UADS data are not available for all the intervals, and we have included the probabilities for all intervals for which we have UADS data, and those intervals for which $\beta_e < 1$.

Table 2 shows that the coincidence rate is similar to the values given in Table 1 for all the intervals, although the probability of random coincidence is higher, because of the smaller sample. The bottom row of Table 2 shows that the burst probability is quite high, $\approx 13\%$, for $\beta_e < 1$, while the coincidence rate is $\approx 19\%$. For the number of samples, this rate lies in the upper 13% of the Binomial distribution. This is a "one-tailed" test, while it is usual to use a "two-tailed" test when testing against random coincidence. For this purpose, one can roughly double the percentage, and there is a less than 75% probability that the observed coincidence is not random. When testing for a non-random association of events it is usual to require at least a 95% probability before the null hypothesis of random coincidence is rejected (e.g. Pollard, 1977).

Given the relatively low likelihood of non-random coincidence, and the generally low degree of correlation (<20%), we conclude that the Langmuir probe anomalies do not explain the 100 Hz bursts.

Rather, both 100 Hz bursts and Langmuir probe anomalies tend to occur in regions of low β_e.

5. LIGHTNING OR LOWER HYBRID INSTABILITY

While the Langmuir probe anomalies are not strongly associated with the 100 Hz wave bursts, here we address the likelihood that the lower hybrid drift instability discussed by Huba (1992) and Huba and Grebowsky (1993) could be responsible for the 100 Hz bursts. Huba (1992) pointed out that, although the lower hybrid resonance frequency is only a few Hz in the nightside ionosphere, sufficiently short wavelength waves can be Doppler-shifted up to 100 Hz by the spacecraft motion. The spacecraft velocity ≈ 10 kms $^{-1}$, and a wave with wavelength 100 m will be Doppler-shifted to 100 Hz. For an electron temperature of 0.1 eV, and a magnetic field strength of 30 nT, the electron Larmor radius (ρ_e) is ≈ 35 m. Thus, $k\rho_e \approx 2$, where k is the wave vector. Huba (1992) found that this wavelength range is typically unstable to the lower hybrid drift instability.

The lower hybrid drift instability is generated by the relative drift between electrons and ions caused by a density gradient. The magnitude of the particle drift is determined by the gradient perpendicular to the ambient magnetic field; a parallel gradient does not cause a drift. The drift is perpendicular to both the magnetic field and the gradient, and the waves propagate in the direction of the drift. For a particular species, the density gradient drift is given by

$$v_n = v_T^2/2L_n\Omega, \tag{1}$$

where v_T is the thermal velocity of the species, L_n is the scale length of the density gradient and Ω is the species gyro-frequency. For a magnetic field gradient, the drift is given by

$$v_b = v_T^2/2L_b\Omega, \tag{2}$$

where L_b is the scale length for the change in magnetic field magnitude.

If the plasma is in pressure balance, then it can be shown that

$$L_b(\beta_e + \beta_i) = -2L_n, \tag{3}$$

where the subscripts e and i denote electrons and ions, respectively. If the ion and electron temperatures are equal, then $L_b\beta_e = -L_n$. Thus, as β_e increases, the magnetic field gradient drift becomes comparable with the pressure gradient drift, but it is in the opposite direction, and the instability is quenched for $\beta_e > 1$. Low β_e is therefore a necessary condition for both the lower hybrid drift instability and whistler-mode propagation in the nightside ionosphere of Venus.

However, unlike the whistler-mode, low β_e is not the only requirement for the lower hybrid instability. As noted above, the lower hybrid resonance frequency is only a few Hz, and the electron collision frequency can be large enough to damp the instability, especially for high densities and weak magnetic fields. The electron collision frequency $\nu = 2.91 \times 10^{-6} n T_e^{-3/2} \lambda\ \mathrm{s}^{-1}$, where λ is the Coulomb logarithm ≈ 15, the density is expressed in cm $^{-3}$ and the temperature is in eV (Huba and Grebowsky, 1993). For a density of 10^4 cm $^{-3}$ and a temperature of 0.1 eV, $\nu = 15\ \mathrm{s}^{-1}$, while the lower hybrid resonance frequency (ω_{lh}) ≈ 30 rads $^{-1}$ when $B = 30$ nT. Thus, the collision frequency can be comparable with the wave frequency.

Another condition that applies to the 100 Hz waves, but not to the density fluctuations, is the requirement that the wavelength be ≈ 100 m, so that the wave can be Doppler-shifted to 100 Hz through spacecraft motion. Huba and Grebowsky (1993) found maximum growth occurred for $k\rho_e \approx 2$, although the actual value depended on the choice of the plasma parameters, and the gradient scale length. As noted above, this implies an electron Larmor radius ≈ 35 m, which for $T_e = 0.1$ eV, requires a magnetic field strength of 30 nT. If the field strength is smaller than this, then the $k\rho_e$ required for Doppler-shift to 100 Hz becomes too large, and the waves tend to be damped.

Thus, the lower hybrid drift instability requires low β_e, low collision frequencies, and small electron Larmor radii to generate short wavelength waves that can be Doppler-shifted to 100 Hz. In Fig. 11, we show where the burst intervals used in determining the burst rates discussed above occur as functions of electron density and magnetic field strength. In order to explore whether or not these bursts correspond with lower hybrid drift waves, we have plotted several reference curves. Above, we discussed the various parameters relevant to the lower hybrid instability assuming an electron temperature of 0.1 eV. However, the temperature is not constant, and we find that $T_e = 0.188\ (n/2.45 \times 10^3)^{-0.445}$ for the burst intervals, using a least squares regression, where T_e is in eV, and n is in cm $^{-3}$. The correlation coefficient is 0.686, with 1234 points. This regression line allows us to specify the temperature for a given density, and so determine the following reference curves as a function of density and magnetic field strength: $\beta_e = 1$, $\nu/\omega_{lh} = 0.25$, and $k\rho_e = 3$. As an approximate rule of thumb, we expect the lower hybrid drift instability to generate Doppler-shifted 100 Hz waves in regions for smaller values of these parameters.

Figure 11 indicates that there are large regions of the B–n parameter space where bursts occur, but the

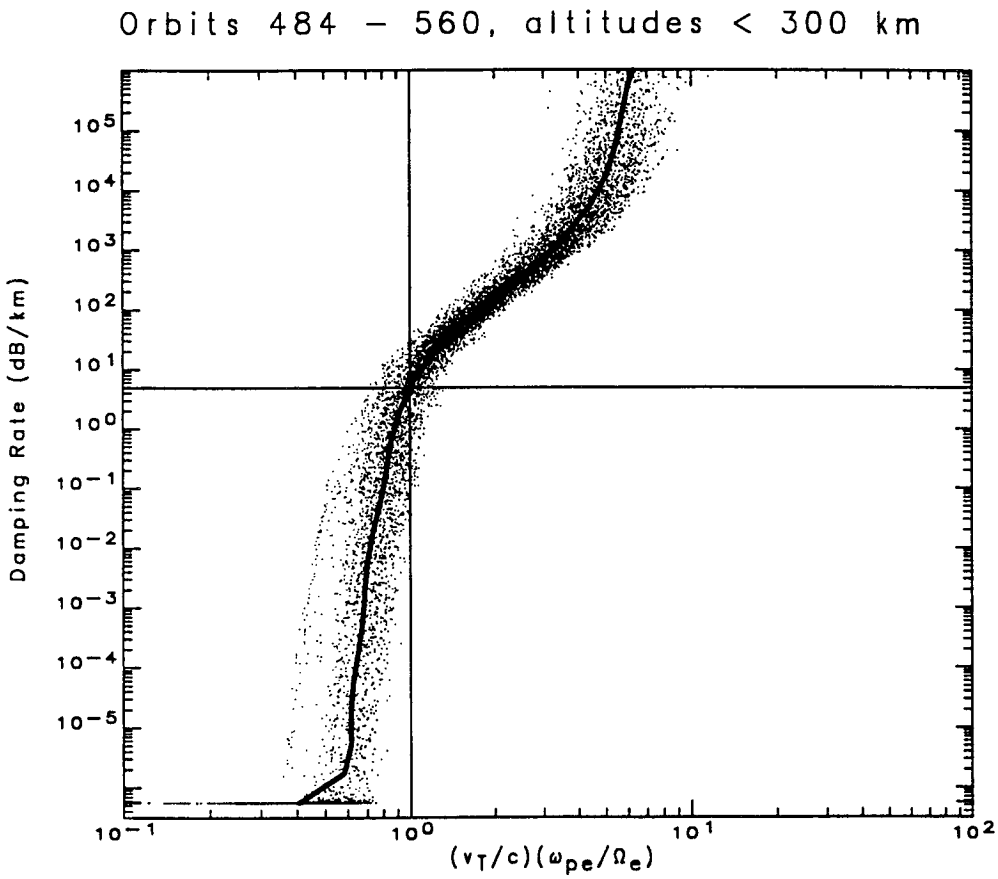

Fig. 10. The convective damping rate of 100 Hz whistler-mode waves as a function of the normalized electron thermal velocity ($= \sqrt{\beta_e}$). The observed magnetic field strength, electron density and temperature are used to calculate the damping rate for parallel propagating whistler-mode waves at 100 Hz, assuming an isotropic plasma. The thick line passing through the data gives the median $\sqrt{\beta_e}$ as a function of the damping rate, binned every half decade. A damping rate of 8.686 dB/km corresponds with 1 e-folding of the wave amplitude/km.

approximate conditions for lower hybrid instability are not satisfied. However, most of the bursts occur in the region where $\beta_e < 1$, as we expect for the whistler-mode. A word of caution is in order when interpreting Fig. 11. The various limiting curves are indicative of the likely region of lower hybrid drift instability, but we have not performed an instability analysis. Huba and Grebowsky (1993) present instability limits in a similar format. They find that for sufficiently high drift speeds, corresponding to short gradient scales, the collision frequency and β_e constraint can be relaxed for high densities, while the Larmor radius restriction is less important for low densities. The maximum drift speed used is twice the ion thermal velocity, i.e. $v_n \approx 2$ km s^{-1}. From equation (1) $v_n/v_{Ti} = \rho_i/2L_n$, implying that $L_n \approx 0.25\rho_i$. The ion Larmor radius is ≈ 10 km for $B \approx 30$ nT, and the high drifts invoked by Huba and Grebowsky (1993) correspond to gradient scale lengths ≈ 2.5 km. This is an extremely short scale length; with this scale length, the density changes by two orders of magnitude in ≈ 12 km which, for a spacecraft velocity of 10 kms^{-1}, would correspond to a two-order of magnitude change in density in just over 1 s. Another possible restriction of the applicability of the lower hybrid drift instability at Venus is the extremely narrow propagation angle because the plasma composition is mainly O^+. Huba and Grebowsky (1993) note that electron Landau damping will become important for angles $\sim 0.33^\circ$ away from perpendicular propagation.

In summary, it is possible that the lower hybrid drift instability can operate in the Venus nightside

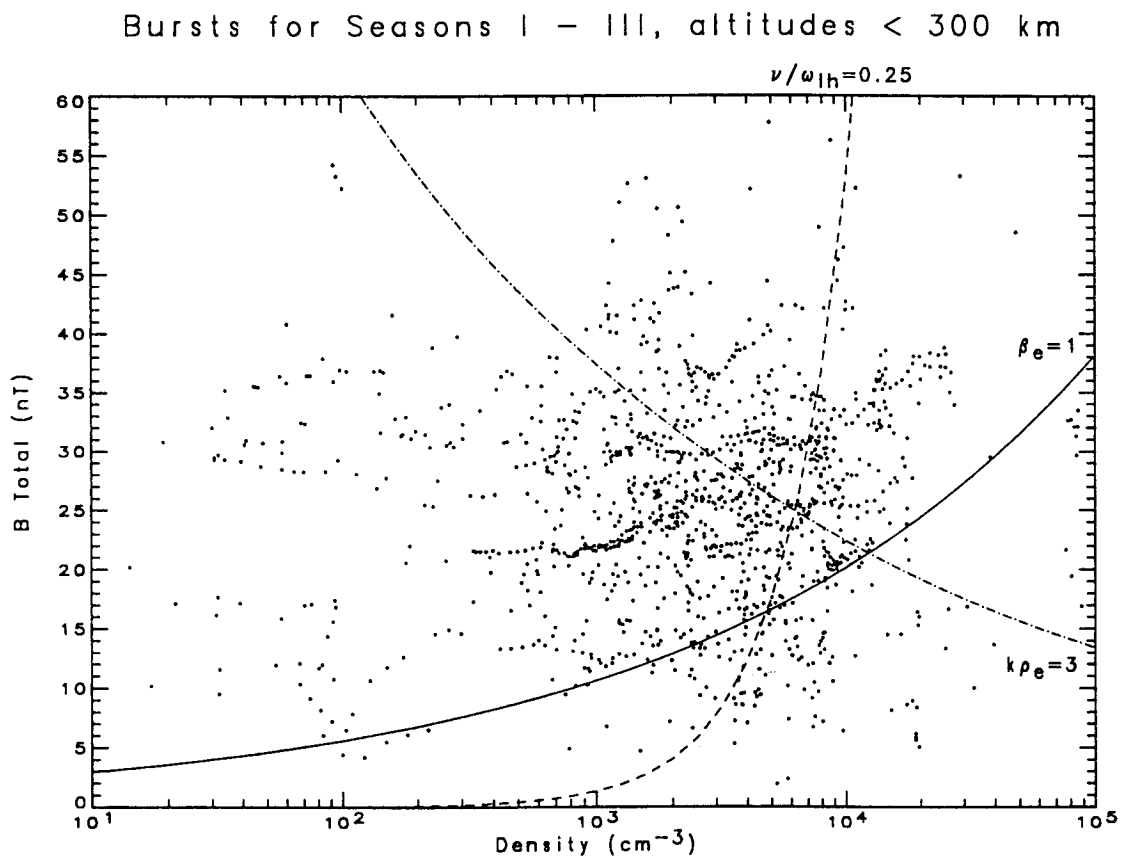

Fig. 11. Scatter plot of burst occurrence as a function of electron density and magnetic field strength. Various limiting curves are also shown. The lower hybrid drift instability is most likely to occur for low β_e, low ν/ω_{lh}, and low $k\rho_e$. The whistler-mode requires low β_e only. At any particular density, lower values of β_e, ν/ω_{lh}, and $k\rho_e$ lie above the limiting curves shown.

ionosphere. However, the gradients required are extremely steep, and electron Landau damping is likely to be important. In addition, we noted earlier that the association between Langmuir probe anomalies and 100 Hz bursts is low, about 20%. Thus, the lower hybrid drift instability may explain the anomalies reported by Grebowsky (1991), but it only explains a small fraction of the 100 Hz bursts observed at Venus. The 100 Hz waves are more likely to be whistler-mode waves.

6. CONCLUSIONS

There is now a large body of evidence that supports the hypothesis that atmospheric lightning is a source of plasma waves in the nightside ionosphere of Venus. Figure 12 gives a sketch of how signals generated by lightning are detected by the Pioneer Venus Orbiter. The sketch shows a portion of the nightside ionosphere containing an ionospheric hole. The magnetic field within a hole is thought to be generated by IMF field lines that are transported to the nightside ionosphere. Therefore, the field lines within a hole must ultimately be connected to the IMF, and holes are thought to come in pairs (Brace *et al.*, 1982). The field lines that exit the bottom of the figure are assumed to be connected to another hole, where they pass back out of the ionosphere into the solar wind. Given the high magnetic field strength within an ionospheric hole, it is likely that some of the field passes through the ionosphere and enters the atmosphere below. At low frequencies, electromagnetic waves generated by lightning may propagate some distance in the surface ionosphere waveguide. A hole will provide a region where whistler-mode radiation can escape because of the enhanced magnetic field and reduced density. Thus, we expect the 100 Hz bursts to be detected at large distances from the source. At higher frequencies,

it is possible that the spacecraft detects "near-field" effects, perhaps due to direct coupling to the ionosphere, and we expect the high frequency bursts to occur close to the lightning source.

On escaping from the atmosphere, whistler-mode waves will be refracted vertically, assuming a horizontally stratified medium, and we can determine if the waves are within the whistler-mode resonance cone solely from the orientation of the magnetic field with respect to the vertical. The resonance cone test, which applies only for a wave source below the ionosphere of Venus, clearly shows that many of the 100 Hz wave bursts are whistler-mode waves propagating from below the ionosphere. Vertical refraction explains why the burst rate of 100 Hz waves is a maximum for vertical magnetic fields. The burst rate for 100 Hz waves inside the resonance cone decreases much more slowly with increasing altitude, in contrast with the non-whistler-mode high frequency bursts and the 100 Hz bursts outside the resonance cone. The waves within the resonance cone are polarized perpendicular to the ambient field.

One alternative explanation for the 100 Hz waves is that they are whistler-mode waves generated *in situ* by a plasma wave instability. However, because of the weak magnetic field in the nightside ionosphere of Venus, the electron beta (β_e) can be large. Thus, we expect 100 Hz waves to be detected in "ionospheric holes", where the plasma density is low, and the ambient field is large, with a large vertical component. The damping due to thermal electrons will be lowest in such a region. However, even in holes, there is sufficient damping to quench any instability due to precipitating electrons that may have come from the solar wind.

More recently, the lower hybrid drift instability has been postulated as an alternative explanation of the 100 Hz waves. As with the whistler-mode, the lower hybrid waves are expected to occur in regions of low β_e. However, the lower hybrid drift instability requires small electron Larmor radii, and hence large fields, since the wavelength of the waves must be ≈ 100 m to be Doppler-shifted to 100 Hz through spacecraft motion. Additionally, the required gradient scale length must be very short, ≈ 2.5 km, so that the resultant gradient drift velocity is large enough to overcome the damping due to collisions in high density regions. The ion Larmor radius is typically ≈ 5 km.

The lower hybrid instability may better explain the Langmuir probe anomalies investigated by Grebowsky *et al.* (1991). Grebowsky *et al.* reported a high degree of coincidence between 100 Hz wave bursts and Langmuir probe anomalies, but they did not use a consistent identification criterion for the wave bursts. We find a much lower degree of coincidence ($\approx 20\%$). This level of coincidence appears to be because both the wave bursts and Langmuir probe anomalies are mainly detected in regions of low β_e, rather than being due to a common source.

The major question remaining for the 100 Hz waves concerns how much of the energy generated by lightning gains access to the ionosphere. Huba and Rowland (1993) have determined the attenuation due to collisions as the waves enter the atmosphere. They found that, for peak densities of 10^4 cm^{-3}, approximately 0.1% of the incident wave energy could be transmitted through the ionospheric density peak, provided that the vertical magnetic field was ≈ 30 nT. The attenuation scale depends quite strongly on the ambient magnetic field strength and plasma density. Strangeway *et al.* (1993) compared the observations at very low altitudes (≈ 130 km) obtained during the Pioneer Venus Orbiter entry phase with predictions for the attenuation scale. The observed attenuation scale lengths were ≈ 1 km, consistent with lightning generated whistler-mode waves propagating through a moderately dense plasma with a vertical field < 10 nT. However, possible spacecraft interactions with the neutral atmosphere cannot be completely discounted as a source for the waves at very low altitudes.

The wide-band bursts detected at low altitudes may also be due to lightning, and may be evidence for direct coupling of lightning into the ionosphere of Venus. However, this interpretation is somewhat speculative, and an additional study of coupling mechanisms and alternative sources is warranted. Some insight into the nature of the broadband waves may be obtained through comparison with the recent GEOTAIL results (Matsumoto *et al.*, 1994). The GEOTAIL data indicate that broadband signals observed in the geomagnetic tail consist of short wave packets, which have a broad frequency signature when sampled as a function of frequency. Doppler-shift may cause additional broadening of the signal. By analogy with these signals, the broadband bursts detected at Venus may correspond to short duration wave packets, as expected from an impulsive source such as lightning.

In conclusion, the preponderance of the evidence points towards atmospheric lightning as the dominant source of plasma waves at low altitudes within the nightside Venus ionosphere. Some may reject this explanation, citing an as yet unknown plasma instability as an alternative. However, in the absence of any viable alternative, and given the consistency of the observations with the lightning hypothesis, the plasma wave data acquired by the Pioneer Venus

Orbiter provide strong evidence for the existence of lightning in the atmosphere of Venus.

Acknowledgements—I wish to thank C. T. Russell and C. M. Ho for many useful discussions on lightning and the plasma wave observations at Venus. I also wish to thank J. M. Grebowsky and J. D. Huba for many fruitful exchanges. The late F. L. Scarf was the original Principal Investigator for the Orbiter Electric Field Detector. His efforts were the motivation behind much of the work presented in this paper. This work was supported by NASA grant NAG2-485.

REFERENCES

Boeck W. L., Vaughan O. H. Jr, Blakeslee R., Vonnegut B. and Brook M.	1992	Lightning induced brightening in the airglow layer. *Geophys. Res. Lett.* **19,** 99–102.
Borucki W. J., Dyer J. W., Phillips J. R. and Pham P.	1991	Pioneer Venus Orbiter search for Venusian lightning. *J. geophys. Res.* **96,** 11,033–11,043.
Brace L. H. and Kliore A. J.	1991	The structure of the Venus ionosphere. *Space Sci. Rev.* **55,** 81–163.
Brace L. H., Theis R. F., Mayr H. G., Curtis S. A. and Luhmann J. G.	1982	Holes in the nightside ionosphere of Venus. *J. geophys. Res.* **87,** 199–211.
Burke W. J., Aggson T. L., Maynard N. C., Hoegy W. R., Hoffman R. A., Candy R. M., Liebrecht C. and Rodgers E.	1992	Effects of a lighting discharge detected by the DE 2 satellite over hurricane Debbie. *J. geophys. Res.* **97,** 6359–6367.
Crawford G. K., Strangeway R. J. and Russell C. T.	1993	VLF emissions at the Venus dayside ionopause. In *Plasma Environments of Non-Magnetic Planets*, T. I. Gombosi (ed.), pp. 253–258. Pergamon Press, Oxford.
Grebowsky J. M., Curtis S. A. and Brace L. H.	1991	Small-scale plasma irregularities in the nightside Venus ionosphere. *J. geophys. Res.* **96,** 21,347–21,359.
Gurnett D. A., Kurth W. S., Roux A., Gendrin R., Kennel C. F. and Bolton S. J.	1991	Lightning and plasma wave observations from the Galileo flyby of Venus. *Science* **253,** 1522–1525.
Hale L. C. and Baginski M. E.	1987	Current to the ionosphere following a lightning stroke. *Nature* **329,** 814–816.
Ho C.-M., Strangeway R. J. and Russell C. T.	1991	Occurrence characteristics of VLF bursts in the nightside ionosphere of Venus. *J. geophys. Res.* **96,** 21,361–21,369.
Ho C.-M., Strangeway R. J. and Russell C. T.	1992	Control of VLF burst activity in the nightside ionosphere of Venus by the magnetic field orientation. *J. geophys. Res.* **97,** 11,673–11,680.
Ho C.-M., Strangeway R. J. and Russell C. T.	1993	Evidence for Langmuir oscillations and a low density cavity in the Venus magnetotail. *Geophys. Res. Lett.* **20,** 2775–2778.
Huba J. D.	1992	Theory of small scale density and electric field fluctuations in the nightside Venus ionosphere. *J. geophys. Res.* **97,** 43–50.
Huba J. D. and Grebowsky J. M.	1993	Small-scale density irregularities in the nightside Venus ionosphere: Comparison of theory and observations. *J. geophys. Res.* **98,** 3079–3086.
Huba J. D. and Rowland H. L.	1993	Propagation of electromagnetic waves parallel to the magnetic field in the nightside Venus ionosphere. *J. geophys. Res.* **98,** 5291–5300.
Kelley M. C., Siefring C. L., Pfaff R. F., Kintner P. M., Larsen M., Green R., Holzworth R. H., Hale L. C., Mitchell J. D. and Le Vine D.	1985	Electrical measurements in the atmosphere and the ionosphere over an active thunderstorm. I. Campaign overview and initial ionospheric results. *J. geophys. Res.* **90,** 9815–9823.
Krasnopol'sky V. A.	1983	Venus spectroscopy in the 3000–8000 Å region by Veneras 9 and 10. In *Venus*, D. M. Hunten, L. Colin, T. M. Donahue and V. I. Moroz (eds), pp. 459–483. University of Arizona Press, Tucson.
Ksanfomality L. V., Scarf F. L. and Taylor W. W. L.	1983	The electrical activity of the atmosphere of Venus. In *Venus* D. M. Hunten, L. Colin, T. M. Donahue and V. I. Moroz (eds), pp. 565–603. University of Arizona Press, Tucson.
Maeda K. and Grebowsky J. M.	1989	VLF emission bursts in the terrestrial and Venusian nightside troughs. *Nature* **341,** 219–221.

Matsumoto H., Nagano I., Anderson R. R., Kojima H., Hashimoto K., Tsutsui M., Okada T., Kimura I., Omura Y. and Okada M.	1994	Plasma wave observations with GEOTAIL spacecraft. *J. geomagn. Geoelect.* **46,** 59–95.
Pollard J. H.	1977	*A Handbook of Numerical and Statistical Techniques.* Cambridge University Press, New York.
Russell C. T.	1991	Venus lightning. *Space Sci. Rev.* **55,** 317–356.
Russell C. T. and Singh R. N.	1989	A re-examination of impulsive VLF signals in the night ionosphere of Venus. *Geophys. Res. Lett.* **16,** 1481–1484.
Russell C. T., von Dornum M. and Scarf F. L.	1988	The altitude distribution of impulsive signals in the night ionosphere of Venus. *J. geophys. Res.* **93,** 5915–5921.
Scarf F. L. and Russell C. T.	1983	Lightning measurements from the Pioneer Venus Orbiter. *Geophys. Res. Lett.* **10,** 1192–1195.
Scarf F. L., Taylor W. W. L., Russell C. T. and Brace L. H.	1980a	Lightning on Venus: Orbiter detection of whistler signals. *J. geophys. Res.* **85,** 8158–8166.
Scarf F. L., Taylor W. W. L. and Virobik P. F.	1980b	The Pioneer Venus Orbiter plasma wave investigation. *IEEE Trans. Geosci. Remote Sens.* **GE-18,** 36–38.
Singh R. N. and Russell C. T.	1986	Further evidence for lightning on Venus. *Geophys. Res. Lett.* **13,** 1051–1054.
Sonwalkar V. S. and Carpenter D. L.	1995	Notes on the diversity in the properties of radio bursts observed on the nightside of Venus. *J. atmos. terr. Phys.* **57,** 557–573.
Sonwalkar V. S., Carpenter D. L. and Strangeway R. J.	1991	Testing radio bursts observed on the nightside of Venus for evidence of whistler mode propagation from lightning. *J. geophys. Res.* **96,** 17,763–17,778.
Strangeway R. J.	1990	Radioemission source disputed. *Nature* **345,** 213–214.
Strangeway R. J.	1991a	Plasma waves at Venus. *Space Sci. Rev.* **55,** 275–316.
Strangeway R. J.	1991b	Polarization of the impulsive signals observed in the nightside ionosphere of Venus. *J. geophys. Res.* **96,** 22,741–22,752.
Strangeway R. J.	1992	An assessment of lightning or *in situ* instabilities as a source for whistler-mode waves in the night ionosphere of Venus. *J. geophys. Res.* **97,** 12,203–12,215.
Strangeway R. J., Russell C. T. and Ho C. M.	1993	Observation of intense wave bursts at very low altitudes within the Venus nightside ionosphere. *Geophys. Res. Lett.* **20,** 2771–2774.
Taylor H. A. Jr and Cloutier P. A.	1988	Telemetry interference incorrectly interpreted as evidence for lightning and present-day volcanism at Venus. *Geophys. Res. Lett.* **15,** 729–732.
Taylor H. A. Jr, Cloutier P. A. and Zheng Z.	1987	Venus "lightning" signals reinterpreted as *in situ* plasma noise. *J. geophys. Res.* **92,** 9907–9919.
Theis R. F. and Brace L. H.	1993	Solar cycle variations of the electron density and temperature in the Venusian nightside ionosphere. *Geophys. Res. Lett.* **20,** 2719–2722.

Pergamon

Planet. Space Sci., Vol. 42, No. 10, pp. 813–823, 1994

0032–0633/94 $7.00+0.00

0032-0633(94)E0056-V

Spatial distribution of plasma wave activity in the nightside ionosphere of Venus

C.-M. Ho,* R. J. Strangeway and C. T. Russell

Institute of Geophysics and Planetary Physics, University of California, Los Angeles, CA 90024, U.S.A.

Received 2 August 1993; revised 21 February 1994; accepted 21 February 1994

Abstract. In this study we use 14 years of Pioneer Venus Orbiter Electric Field Detector (OEFD) data to define the characteristics of VLF burst activity in the nightside ionosphere of Venus. Our statistical results show that there are essentially four types of VLF signals. The first type of signal is only observed in the 100 Hz channel and not in any of the higher frequency channels (730 Hz, 5.4 kHz or 30 kHz). Occurrence of these waves is controlled by the magnetic field with a weaker dependence on electron density. The occurrence rate decreases with increasing altitude to a height of 600 km. For higher altitudes beyond 600 km the occurrence rate remains roughly constant. The statistics of these signals are what one would expect for whistler mode waves from a subionospheric source. The second type of signal is broadband wave activity appearing below 300 km in the low altitude ionosphere. These signals often occur in all four channels of the OEFD. These signals are also thought to come from a subionospheric source. The third type of signal is strong mid-frequency broadband burst signals appearing near the edge of the planetary optical shadow. They are probably ion acoustic waves generated by a current driven instability associated with plasma clouds in the wake. The fourth type of signal is a narrow band wave. It occurs in either of the two high frequency channels in the high altitude tail region, and is attributed to locally generated Langmuir waves. In addition, we also observe spacecraft interference noise in both the 100 and 730 Hz channels. These signals mainly occur near the edge of the planetary optical shadow and have an inbound and outbound asymmetry in activity.

1. Introduction

Nearly 14 years of plasma wave data were acquired by the Pioneer Venus Orbiter (PVO) in orbit around Venus, since PVO was inserted into the orbit of Venus in December of 1978 and before it descended in October of 1992. PVO had an elliptical orbit with apoapsis of 72,000 km and a variable periapsis from 150 to 2200 km. When the spacecraft was in sunlight spacecraft associated noise often dominated the plasma wave measurements, but when the spacecraft entered eclipse these noise sources ceased and the measurements more clearly represented ambient signals, although there were still some more intermittent sources of interference. Through the 14 year period, orbits with periapsis in the nightside ionosphere have covered the entire nightside region at altitudes ranging from 150 to 3000 km. In the low altitude ionosphere many intense VLF wave bursts have been detected, which have been attributed to lightning (Scarf *et al.*, 1980; Russell, 1991; Strangeway, 1991a). Until recently, work has concentrated on these low altitude signals because of their possible implications for the occurrence of lightning. Hence, how VLF signals are distributed at higher altitudes and whether or not there are other wave sources in the upper ionosphere remained unknown. The purpose of this paper is to look at the full range of observations of the Pioneer Venus plasma wave instrument to determine what types of plasma wave emissions are seen at high and low altitude, and to determine how the low altitude signals relate to the signals at high altitudes.

The solar wind interaction with Venus forms a wake region immediately behind Venus (Brace *et al.*, 1987). The central part of this region lies inside the optical shadow of Venus. Here the spacecraft is out of the direct influence of the solar wind and solar extreme ultraviolet radiation. However, the plasma density and the magnetic field distributions in the nightside ionosphere are quite non-uniform (Brace *et al.*, 1982). There are tail ray structures in the upper ionosphere, and density troughs with radial magnetic fields in the lower ionosphere. These features may affect both the propagation and the possible generation of plasma waves.

Previous studies of VLF burst signals focused on the data of the first few PVO eclipse seasons with low periapsis altitude and high telemetry rate. Scarf *et al.* (1980) ana-

*Present address: Jet Propulsion Laboratory, Pasadena, CA 91109, U.S.A.
Correspondence to: C.-M. Ho

lyzed the VLF data in terms of the instantaneous direction of the magnetic field and showed that lightning-like impulses were detected when projection of the local magnetic field intersected the planetary atmosphere. Scarf *et al.* (1987) studied burst activity as a function of altitude and position for the first 10 eclipse seasons (up to orbit 2124). However, the occurrence rate was not normalized by time spent at each altitude. Using data from orbit 1 to orbit 1895, Taylor *et al.* (1987) suggested that burst event rates decreased at lowest altitude. They thought that the source which generates these signals was in the low altitude ionosphere instead of the lower atmosphere. But recent studies show that at low altitudes it is unlikely that any ionospheric source in the Venus nightside can produce those signals which have been identified to be in the whistler mode (Strangeway, 1991b; Ho *et al.*, 1991).

Russell *et al.* (1988) undertook normalized studies of the altitude distribution of impulsive signals for the first four seasons. They checked whether or not burst activity occurred within each 30 s interval of the electric field data for each channel of the four available frequencies (100 Hz, 730 Hz, 5.4 kHz and 30 kHz). If the signal exceeded a threshold chosen to be well above the instrument background, a burst was defined to have occurred in a 30 s interval. The percent occurrence rate was calculated by dividing the number of intervals containing bursts by the total number of observed intervals. Recently, Ho *et al.* (1991) used a new definition for burst signals and performed statistics for the first three seasons of high resolution data. However, these results were obtained at low altitude, and the local time variation and the magnetic field dependence should be further tested using high altitude data.

The present study uses an experimental technique similar to that of Russell *et al.* (1988) to examine all nightside data between 20 December 1978 and 1 March 1992 (orbits 16–4834) to calculate fractional burst occurrence rate. We investigate the spatial distribution of all burst signal activity in the nightside to find the spatial positions of the sources. We calculate the altitude distribution and the seasonal variation using all data. This altitude distribution will assist us in finding local sources of these waves. However, the apparent altitude variation may also be affected by secular variations of the ionosphere. We will attempt to distinguish these variations (seasonal and altitude) to find the most probable source for the burst signals. To facilitate this, we will investigate their correlation with the magnetic field and plasma density.

2. Measurements

When the Pioneer Venus Orbiter electric field detector (OEFD) enters the Venus optical shadow, plasma wave noise levels decrease in all frequency channels due to the weakening of photo-emission. We consequently select data starting from the inbound shadow edge and ending at the outbound edge. The data period acquired for each orbit is variable and depends on periapsis altitude and local time. We have included all orbits from season 1 to season 22 (1978–1992) as long as the periapsis of the orbit is in the nightside shadow region. But for the magnetic field and electron data, only the first 16 seasons were available for use in the present study.

In this study we define bursts using the technique described by Russell *et al.* (1988) and Scarf *et al.* (1987). The data are divided into 30 s intervals for each channel. If the signal exceeds a previously defined threshold amplitude in any particular interval, then a burst is said to have occurred, whether it is a single short burst or many longer signals. Threshold levels for the four channels are 2×10^{-5}, 1.5×10^{-5}, 3×10^{-6} and 9×10^{-7} $Vm^{-1}Hz^{-1/2}$ at 100 Hz, 730 Hz, 5.4 kHz and 30 kHz, respectively. After surveying all 22 seasons of nightside data, we find that generally there are four types of natural signal and one type of artificial interference signal observed by the OEFD. Four examples of these typical signals are shown in Figs. 1a, 1b, 2a and 2b for four different orbits. While orbit 531 is at a low altitude (periapsis altitude: 153 km), orbits 1163, 1175 and 1662 are at a higher altitude (periapsis altitudes are 1062 km, 1103 km and 1728 km, respectively). We see that there are some narrowband signals which only appear in the 100 Hz channel on the left side of Fig. 1a. They are below the gyrofrequency f_{ce} (average 560 Hz in this region) and have all the features expected of a whistler mode signal. We define these signals as 100 Hz narrowband (NB) signals. If there is any signal occurring simultaneously in one or more of the three high frequency channels, even though their amplitudes are below the threshold level in that channel, these 100 Hz bursts are not considered to be possible 100 Hz NB signals. However, these signals may be classified as other types of signal. The second type of signal which is shown on the right side of Fig. 1a is a stronger impulsive broadband signal. These signals have relatively larger amplitude well above the threshold levels (indicated by dashed lines) in the 5.4 and 30 kHz channels. We will investigate these high frequency (HF) broadband signals through their activity in the two high frequency channels in the low ionosphere. The interference signals with a 6 s interval (half spin period of spacecraft) at the right of Fig. 1a in the 100 Hz channel has been excluded from our statistical study, as well as any telemetry noise.

In Fig. 1b, we see a signal which is relatively weaker and mainly appears in both 100 and 730 Hz channels. However, in the 730 Hz channel, the signal is at or below the threshold level. These 100 and 730 Hz signals are strongly correlated and both seem to extend from outside the shadow into the inner shadow region. We define this type of signal as low frequency (LF) wideband signal in this study. These signals may be interference due to an interaction between the spacecraft and the background plasma. We will identify these signals through their spatial distribution and properties later.

The other two types of signal are shown in Fig. 2a and b, respectively. The third type of signal (Fig. 2a) is a strong mid-frequency (MF) burst signal. These MF bursts often appear in 100 Hz, 730 Hz and 5.4 kHz channels. Occasionally they may extend into 30 kHz channel. They usually appear near the optical shadow edge and have 1 or 2 min duration. These signals are different from the weak LF interference noises appearing in the left side of Figs. 2a and 1b. As shown in Fig. 2b, the fourth type of signal is a high frequency narrowband signal, which has

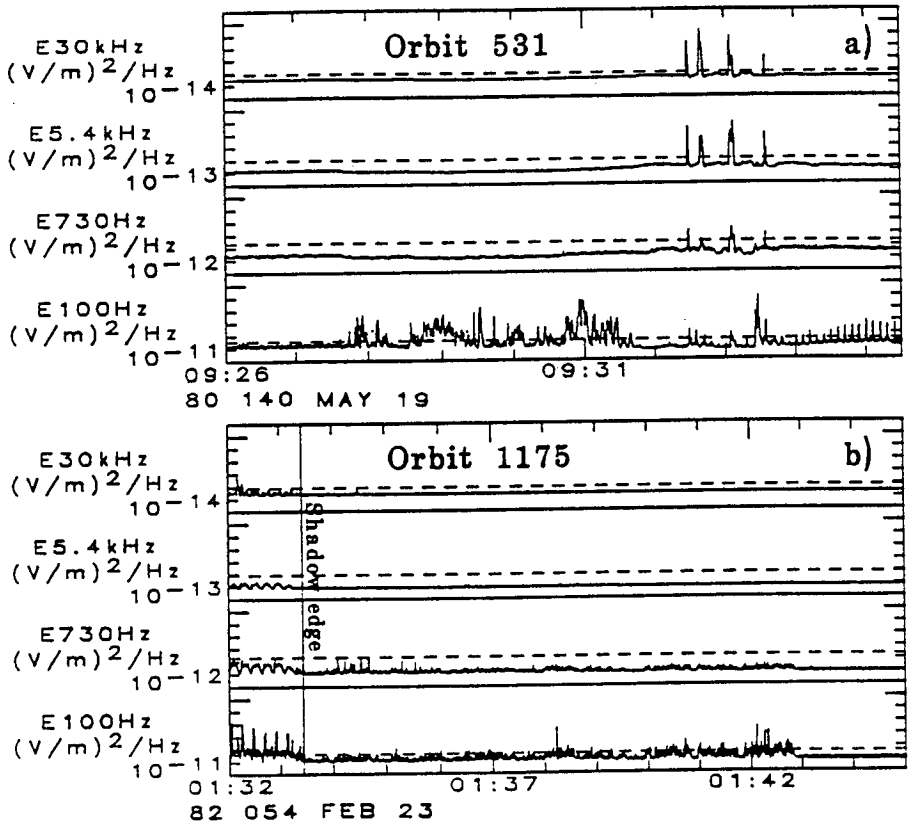

Fig. 1. Two orbits which show two types of signal and one type of noise observed in the nightside ionosphere. Dashed lines in each channel show the threshold levels used in the present study. (a) For orbit 531 there are two types of signal, the 100 Hz NB signal (at left), as opposed to wideband signals (at right). Also we can see some interference spikes in the 100 Hz channel in the right of the plot. (b) For orbit 1175 some interference noise in both the 100 and 730 Hz channels are weak and correlated. The optical shadow edge is also shown. At left, outside the shadow, the background noise caused by photoelectrons and the interference due to spacecraft spin are very strong

completely different features from the HF wideband signals at low altitudes. These signals often appear in the 30 kHz channel in the upper ionosphere near the tail region, but sometimes appear only in the 5.4 kHz channel. They do not simultaneously appear in both channels.

3. Spatial distribution

First, we need to choose a coordinate system in which to analyze the data. Because Venus has no significant intrinsic magnetic field, we expect the interplanetary magnetic field (IMF) would exert some control on the magnetic structure of the nightside ionosphere (Phillips *et al.*, 1986). However, we do not know to what extent IMF orientation would also affect the distribution of plasma wave activity. We have examined the occurrence patterns in a coordinate system ordered by the upstream IMF direction. Our statistical study shows that most types of signals are not significantly ordered in the upstream IMF coordinate system and the IMF does not control the wave activity in any obvious manner. Thus, for statistical purposes, we have assumed that all burst activity is axially symmetric. Figure 3a–f shows these distributions in a cylindrical coordinate system (ρ,X), with X in the direction of the Venus–Sun line and ρ is the distance from X.

We are concerned with both the available spatial coverage and the spatial distribution of the burst activity. Figure 3a shows the observational coverage by the spacecraft. Note that we have used a logarithmic scale to show the spatial variation of the number of 30 s time intervals. The coverage region is restricted to ρ from 0 to 1.05 R_v, and X from -0.3 to -1.5 R_v (1 $R_v = 6052$ km). The optical shadow edge is somewhat greater than 1 R_v because the ultraviolet radiation from the sun is absorbed in the upper atmosphere. The blank region at left shows the planet while the blank area to the right shows the region with no coverage. In the regions beyond $\rho = 1$ and around midnight ($\rho < 0.1$), the time coverage is very low (less than five intervals of 30 s). Thus, the normalized signal occurrence rates will be less accurate in these regions.

The signal distribution for 100 Hz NB signals is shown in Fig. 3b. Here, we have interpolated the data to make the contour map. There is some spreading of the contours beyond the actual data which is due to the interpolation scheme used to plot the data. Gradients near the edge of the map should be ignored. Because the 100 Hz NB signals have been identified as not being associated with any signals above the electron gyrofrequency, we have excluded the possibility that they are wideband ion acoustic waves. We can see that the most intense burst activity

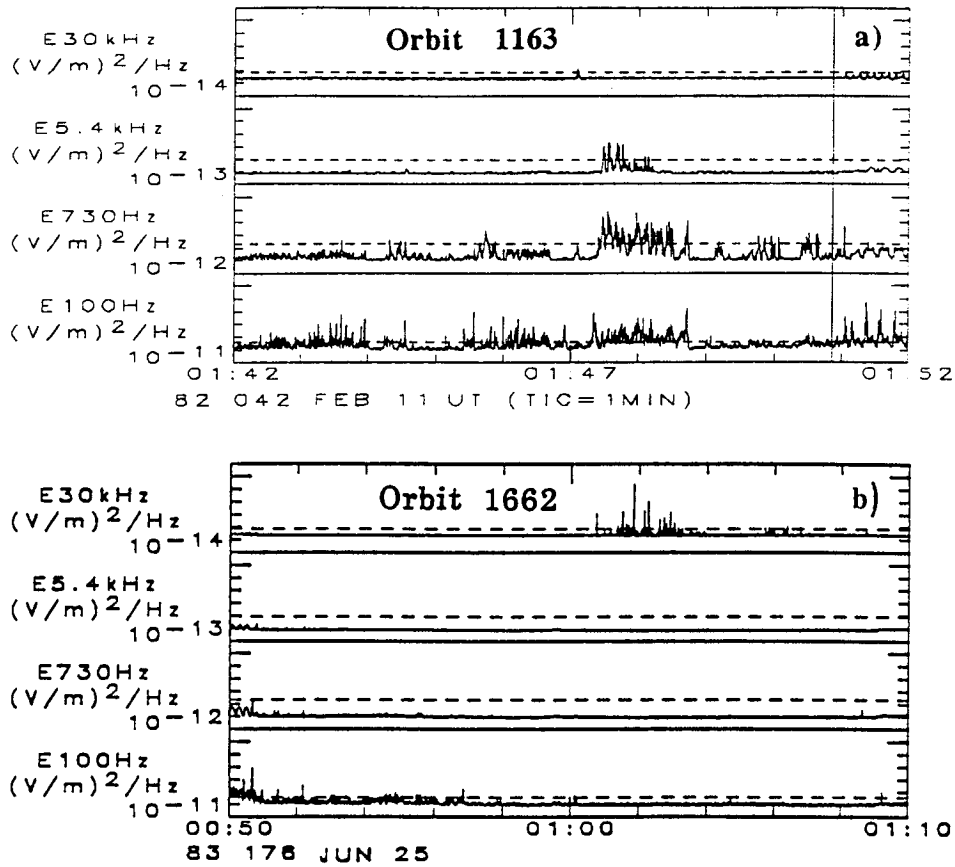

Fig. 2. Two types of signal observed on two high altitude orbits. (a) For orbit 1163 some strong mid-frequency broadband burst signals occur near the shadow edge. They extend from 100 Hz into 730 Hz and 5.4 kHz channels. These signals are different from the weak LF wideband noises appearing on the left-hand side in the two lower frequency channels. (b) For orbit 1662 some signals appear in the 30 kHz channel only in the upper ionosphere and tail

occurs at lowest altitudes and spreads toward higher altitudes. This low altitude activity has been studied extensively in the past and attributed to a subionospheric source (Scarf *et al.*, 1980, 1987; Russell, 1991; Strangeway, 1991a, b). Around midnight, the 100 Hz NB occurrence rate is higher and extends into higher altitudes. This may be attributed to a higher occurrence of density holes with radial magnetic field around this region as reported previously (Brace *et al.*, 1987). At very low ρ (<0.1) there is some variability in the occurrence rate, but this is mainly due to the low counting statistics. The general trend is similar to that seen at lower solar zenith angles.

Strangeway (1991b) has shown that at low altitudes 100 Hz burst signals, which are within the whistler resonance cone ($\theta_{res} = \cos^{-1}(100\text{Hz}/f_{ce})$) have polarization consistent with whistler mode waves. If we assume that the 100 Hz NB signals shown in Fig. 2b are propagating vertically, we find that 80% of them are propagating inside the whistler resonance cone. The fact that we have used 30 s average values for the total magnetic field, and that the instantaneous field may be different from the average value may at least in part explain the 20% apparently outside the resonance cone.

The signals in the 730 Hz channel are below f_{ce} only when the magnetic field strength is greater than 26 nT. Because they are often associated with 100 Hz and 5.4 kHz wideband signals, they are probably not whistler mode signals. From the 730 Hz signal occurrence distributions (Fig. 3c), we can find that there are many burst signals which appear just inside the shadow edge, ρ between 0.8 and 1 R_v. These signals have a high degree of coincidence with signals in the 100 Hz channel, which we have defined as LF wideband signals. Figure 3d shows the occurrence rate of the LF wideband signals. In Fig. 3d we have counted all 100 Hz signals which are correlated with the burst activity in the 730 Hz channel, even though the 730 Hz signals may be below threshold. As a comparison, those signals only above the threshold are counted at 730 Hz in Fig. 3c. Thus, there is a much higher burst occurrence rate for the LF wideband signals than the rate for the 730 Hz signals. Their intensity is stronger around the shadow edge and becomes weaker as ρ decreases. As we will see later, we have identified these signals as being due to spacecraft interference. We can see a clear boundary between the LF signals along the shadow edge and the 730 Hz signals at low altitudes. The two signals come from different sources.

There are also some high frequency broadband signals appearing in the lower ionosphere close to the planet as shown in Fig. 3e. Usually their amplitude is stronger relative to background and they extend from the 100 Hz into the 5.4 kHz and 30 kHz channels. On comparing with the other frequencies, we see a large wideband burst peak occurring at low altitudes around $X = -0.6$ and

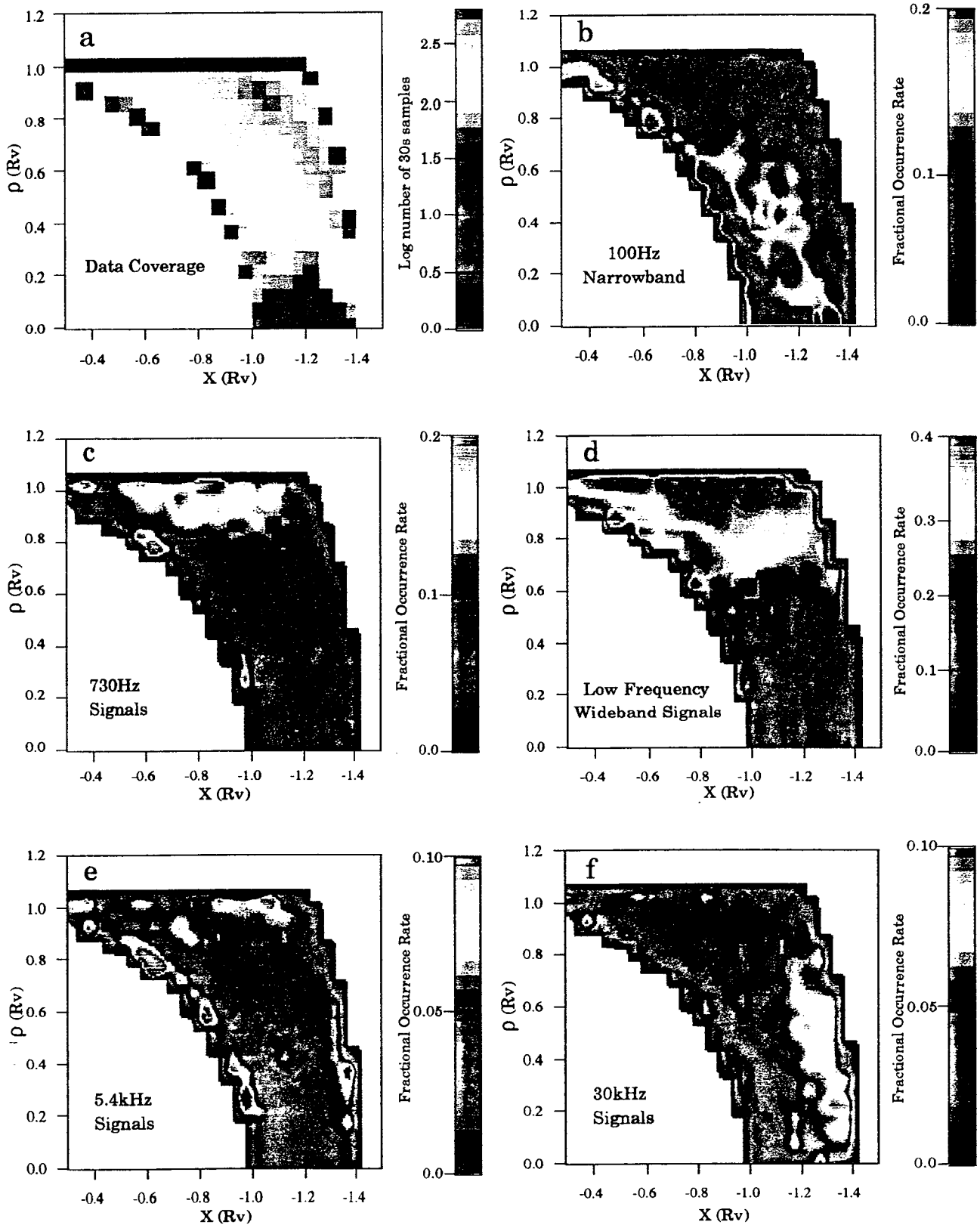

Fig. 3. Spatial distribution of normalized fractional occurrence rates of VLF signals in the nightside Venus ionosphere. A cylindrical coordinate system (X, Venus–Sun line, vs ρ, distance from X) has been used for displaying the data. The lower left side is the planet while there is no data coverage at the right. (a) Time coverage of 30 s intervals. (b) 100 Hz NB signal occurrence rate. (c) 730 Hz signal rate. (d) Low frequency wideband signal rate. (e) 5.4 kHz signal rate. (f) 30 kHz signal rate

$\rho = 0.8R_v$. These low altitude signals become less strong in the 30 kHz channel (Fig. 3f).

Along the shadow edge we also see some wave activity in the 5.4 kHz channel as shown in Fig. 3e. Detailed study shows that they are strong broadband mid-frequency signals. Though these signals also appear close the optical shadow edge, they are significantly different from the LF interference noise. They often extend from 100 Hz channel into 730 Hz, and 5.4 kHz channels. Occasionally, they may extend into the 30 kHz channel. While the interference noise has weaker amplitude around or below the threshold level, the MF broadband signals are much stronger and well above the thresholds in each channel. They have about 1 or 2 min duration and usually only occur once per orbit. In the 30 kHz channels the MF broadband signals become much fewer in number as shown in Fig. 3f.

At higher altitudes in the tail region (>1200 km), there is burst activity in the higher frequency channels, 5.4 and 30 kHz. However, these waves are narrow band waves, because they never appear simultaneously in both channels. The signals in the 30 kHz are relatively strong and extend into middle altitudes from the tail region. It is unlikely that these signals come from a low altitude source. They may be generated by a local instability in the tail region, and are probably Langmuir oscillations (Ho *et al.*, 1993). If so this implies that the density is about 10 cm^{-3} when the 30 kHz signals are seen and about 0.36 cm^{-3} when the 5.4 kHz signals are seen.

In short, through the entire nightside spatial distributions of the burst activity, we find that there are mainly four types of signal which come from different sources. The first one is the 100 Hz narrowband signals. The second one is a high frequency broadband wave. Both occur in the lower ionosphere. The third one is a mid-frequency broadband burst. It mainly appears near the shadow edge. The fourth one is a high frequency narrow band signal, which appears in the 30 kHz and 5.4 kHz channels in the upper ionosphere. Also we find some interference noise near the Venus nightside optical shadow. We will identify these waves and discuss their generation mechanism in the following sections.

4. Low altitude source

From the spatial distributions of all signal activities, we may generally determine two categories: low altitude source signals and high altitude source signals. First, we examine the properties of the signals from the low altitude source. They include the 100 Hz NB and HF broadband signals. We will see how these signals are damped with increasing altitude.

After the first three eclipse seasons, the PVO periapsis altitude began to rise as shown in Fig. 4. Maximum periapsis altitude of 2270 km was reached in season 13. Then the altitude gradually declined. Thus, PVO took a period of over 10 terrestrial years to complete the measurement of the entire upper ionosphere of Venus through changes in the orbit altitude. These observations included both spatial and temporal variations. Since the period of the

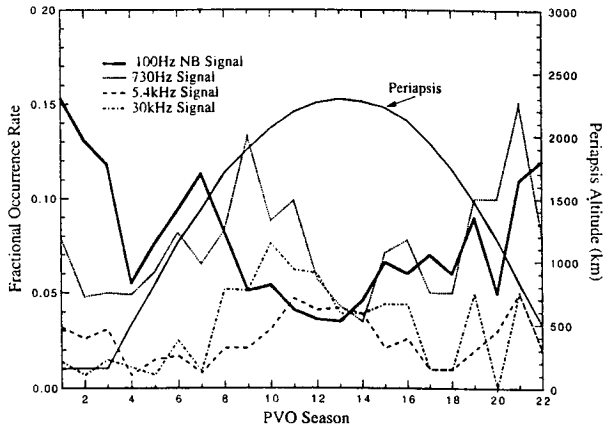

Fig. 4. Seasonal variation of burst activity in the four available frequency channels. The average PVO periapsis altitude of each season is also shown. Generally, the activity of signals from the low altitude source decreases with increasing spacecraft periapsis altitude

sunspot cycle is similar to that of the PVO altitude variation, and since solar activity affects the ionosphere, it is important to attempt to distinguish the altitude variation of burst activity from any seasonal variation.

Because no single season covers all altitudes in the nightside ionosphere, the apparent altitude distribution may be affected by the variations with season, planetary surface coverage or local time. Moreover, since each season has much different altitude coverage, it is almost impossible to obtain a seasonal or temporal variation in a fixed and relatively narrow altitude range over ten year period. In Fig. 4 we can see the variation of the burst signal activity for the four channels of the OEFD as a function of season from December 1978 to March 1992. The variation of the spacecraft average periapsis altitude for each season is also shown. The burst signal occurrence is closely related to the periapsis altitude of spacecraft. In the first three seasons the average periapsis altitude of PVO is as low as 150 km. The 100 Hz NB signal activity is relatively high. After season 3, the activity decreases as periapsis altitude gradually increases from 500 to 2200 km. However, the 100 Hz NB signal activity is enhanced in seasons 5–8, even though the periapsis altitude has increased to 1000 km altitude, but then it falls in later seasons. After season 20 when periapsis declines, the 100 Hz NB activity rises again.

In this 14 year period, the solar cycle varies from maximum to minimum activity, while the spacecraft periapsis rises and then falls. In order to separate the temporal variation from the altitude variation, when studying the altitude dependence of signal occurrence, we divide the data into three periods. The solar maximum period starts in 1979 and ends in 1981 (season 1–5). The solar intermediate year is from 1982 to 1984 (season 6–10), while the solar minimum corresponds to 1985–1987 (season 11–15). Figure 5 shows the altitude dependence of the fractional occurrence rates for the burst signals in the 100 Hz only (left panel), 5.4 kHz (middle panel) and 30 kHz (right panel). As we mentioned before, we have identified the narrowband signals which only appear in the 100 Hz channel. The high frequency signals in the low altitudes

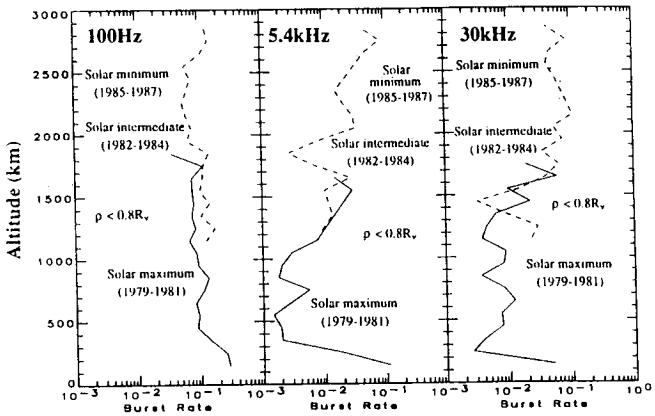

Fig. 5. Altitude distributions of burst signal activity during three different solar activity periods. Fractional occurrence rates for the 100 Hz NB (left panel), 5.4 kHz (middle panel) and 30 kHz (right panel) signals are shown. The solid line shows burst rates during solar maximum, while the dashed line is for solar intermediate and the dotted line for solar minimum. It seems that there is no obvious solar cycle effect on these altitude variations

are broadband signals down to the 100 Hz channel, but they are narrowband signals in the upper ionosphere. We do not show the 730 Hz and LF wideband signals, because they do not have an obvious altitude dependence, rather they have a ρ dependence.

We can see that this altitude variation is basically consistent with the spatial variation as shown in Fig. 3. The 100 Hz NB and HF broadband signals at the lowest altitudes (below 500 km) have the higher fractional activity rates, even though the HF broadband signal activity is relatively lower. The data are mainly from the first four low altitude seasons at solar maximum. The occurrence rates quickly decrease with increasing altitude and reach a minimum between 300 and 600 km. The HF broadband signal occurrence declines more quickly. For example, from 200 to 400 km altitude the 100 Hz NB rate decreases by a factor of 2–3, while the rates in the two higher frequency channels decrease more than one order of magnitude. This suggests that there also is a HF broadband source below the 140 km altitude.

For the 100 Hz NB signals, the altitude dependence displays different behavior in two different altitude ranges. The 100 Hz NB signals have a decline with increasing altitude below 600 km. However, between 600 and 1800 km, the 100 Hz NB activity roughly remains constant as altitude varies. We see that there is a slight increase for burst rate in solar intermediate period (dashed line). Scarf *et al.* (1988) have found that the 100 Hz NBs have different activity characteristics in the altitudes below 600 km and above 600 km. They suggested that the 100 Hz signals observed below 600 km are due to direct propagation, while those signals detected above 600 km come from duct propagation. The duct propagation has less attenuation than non-duct propagation. Our altitude distribution is generally consistent with Scarf *et al.* (1988). Also because later seasons provide data over a different region of the Venus surface, we have investigated the topographic correlation of these signals. We find that topographic dependence of the signal activity is not strong enough to explain the altitude variation as shown in Fig. 5a.

The 100 Hz NB signal activity strongly depends on magnetic field strength, especially in the lower altitudes (Ho *et al.*, 1992). The signal activity is also strongly controlled by the orientation of the magnetic field. We can see this clearly from Fig. 6a. The whistler mode occurrence rate is larger for radial field at both low altitude (<600 km) and high altitude (>600 km). The occurrence rate is higher at low altitudes than that at high altitude. The control of the burst activity by the magnetic field radial angle at low altitudes has been noted previously (Ho *et al.*, 1992).

The correlation of the 100 Hz NB signal activity with the plasma electron density is not obvious, as shown in Fig. 6b. The whistler burst observed below 600 km has a slight peak for densities less than 10^3 cm^{-3}. However, the relatively flat variation of burst rate with electron density suggests that the 100 Hz NB activity at low altitudes is only weakly dependent on the local plasma density. Above 600 km the whistler signals appear to be damped in the higher density regions.

Combining the magnetic field orientation dependence (Fig. 6a) and electron density dependence (Fig. 6b) of burst rates, we can see clear attenuation of 100 Hz narrowband signals at high altitudes. This attenuation is mainly due to Laudau damping of upward propagating of waves. Figure 6a shows that the waves are more strongly damped for more oblique propagation angles. Figure 6b shows that the waves are attenuated more in high density regions.

Strangeway (1992) investigated the relationships between the 100 Hz wave intensity and the magnetic field as well as the electron density for season three data. His results showed that the waves are most intense when the magnetic field is high, but there is little or no dependence on electron density. A strong magnetic field results in low electron plasma β and makes the plasma more transparent to whistler mode waves. Because we always see the higher burst activity in lower altitudes, we think that this is due to upward propagation of whistler waves from below. The resonance cone propagation argument only applies for upward propagation of whistler mode waves from below

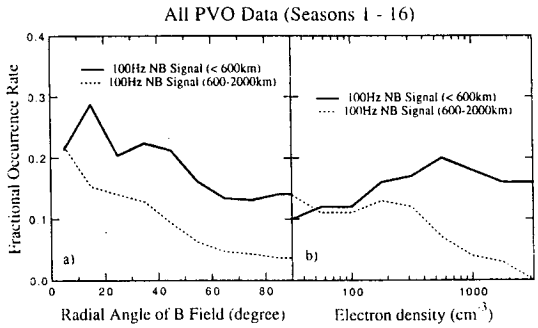

Fig. 6. Dependence of the 100 Hz burst activity in the low and high ionosphere on: (a) the magnetic field orientation and (b) electron density. The 100 Hz NB signal activity decreases with increasing radial angle of the magnetic field, while it is less dependent on plasma densities in the lower ionosphere. Following Brace *et al.* (1982), we have define the lower ionosphere as altitude below 600 km. Both dependencies show that the 100 Hz NB signals have large damping for oblique propagation and larger plasma densities

the ionosphere. Given the large refractive index of whistler mode waves in the ionosphere, Snell's law requires that waves entering the ionosphere from below propagate vertically in a horizontally stratified medium. At the bottom of the ionosphere, the refractive index quickly changes from 1 to 1000. The wave normal will be refracted into the vertical (radial) direction and fall within the resonance cone when the field is sufficiently close to vertical. At higher altitudes the refractive index will change slowly. This mechanism does not apply for downward propagation.

5. High altitude source

From the distributions of VLF waves shown in Figs 3 and 5, we also see that some waves occur more frequently at higher altitudes. We expect that these signals are locally generated in the upper ionosphere or the tail. They mainly include weak LF wideband noises, mid-frequency broadband signals along the shadow edge and high frequency narrowband signals in the tail. From Fig. 5 we see that above 600 km altitude, the signals in the two higher frequency channels gradually increase with increasing altitude and become more active above 2000 km. This variation would be difficult to reconcile with a subionospheric source.

We have examined the possibility that an ion acoustic wave is responsible for the MF waves near the optical shadow edge. Through analysis of the individual data we find that the 5.4 kHz signals associated with the MF waves are often observed in conjunction with reversals of the B_x component of the magnetic field. Furthermore the density can be enhanced by an order of magnitude. These features are the signatures of attached or detached plasma clouds. Because these waves are broadband waves and have parallel polarization in the 5.4 kHz channel, they are probably ion acoustic wave generated by a current driven instability. These signals are different from the weak LF interference noise (see Figs 1b and 2a).

The high frequency narrow band signals almost always correspond to lower density regions in the upper ionosphere (Fig. 3f). Ho *et al.* (1993) have shown that the signals in both channels have parallel polarization relative to the background magnetic field. We have performed a statistical study to identify these high frequency wave modes. Figure 7 shows the correlation between the average maximum intensity, and burst rate of the 30 kHz waves with the electron density. They both peak around $10\ cm^{-3}$ in electron density. We know that electron plasma oscillations with this density have a frequency around 30 kHz. Considering the $\pm 15\%$ bandwidth of this frequency channel, the plasma density may be between 8.0 and 14.7 cm^{-3}. Thus, they are presumably Langmuir waves. They always appear in the top of the ionosphere, where the solar wind electrons may excite some instabilities. When the electron density is extremely low ($\sim 0.36\ cm^{-3}$), the plasma frequency equals 5.4 kHz. It is possible that the density reaches such a low value and excites waves in the 5.4 kHz channel as shown in Fig. 2e. For a $\pm 15\%$ bandwidth with frequency centered on 5.4 kHz the corresponding electron density ranges from 0.26 to 0.48 cm^{-3}. However, the Langmuir probe is unable to resolve such a low density. The evidence for Langmuir oscillation is discussed more fully by Ho *et al.* (1993).

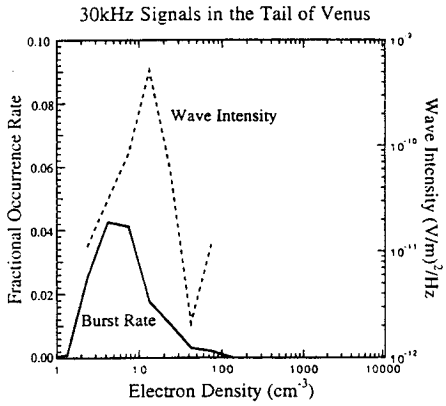

Fig. 7. The correlation of the 30 kHz signal intensity (dashed line) and burst rate (solid line) with local plasma density in the upper ionosphere. Most signals correspond to the density level of 10 cm^{-3}. The waves are probably Langmuir waves

In order to identify the wave mode of the weak LF wideband noises, we have performed polarization tests on these signals. We find that the polarization pattern of these signals is not clear. While some signals have maximum electric field intensity nearly parallel to the background magnetic field, others peak nearly perpendicular to the ambient magnetic field. We also do not find control of the signals by the magnetic field orientation and the spacecraft motion. This means that these signals are not a whistler mode and also are not Doppler-shifted. Because the LF wideband burst signals mainly appear around the shadow edge, their occurrence rate has a clear dependence on ρ, instead of an altitude dependence. Furthermore, we find that most LF wideband signals are observed mainly in the inbound leg of an orbit, rather than outbound. This asymmetry in the occurrence rate is clearly shown in Fig. 8.

In Fig. 8 we show the burst rates of all 22 seasons for altitudes above 600 km using a superposed epoch analysis. In the left panel of the figure, we have superposed the data from each orbit using the exit from sunlight as the reference time. We have not stretched the data, but kept the time spent for each orbit constant. For example, a pass of 10 min duration contributes to the first 10 min of the left panel. Similarly, we have used the exit from shadow to sunlight as the reference time for the right-hand panel, the same orbit with 10 min duration therefore contributes to the last 10 min of this panel. Thus, the data sampling is a minimum at the center of the figure. We see that burst rates are basically symmetric for 730 Hz and 5.4 kHz signals. However, for the LF (100 Hz) wideband signals there is an obvious asymmetry in the occurrence rate. From the inbound plot, we see that the rate suddenly decreases at about 400–600 s after the shadow edge. From the outbound plot, we see that the rate is a maximum near the center of the figure and then gradually decreases towards the outbound shadow edge. This slow decrease is due to the superposition of different orbits where time of shadow entry occurs at different times with respect to

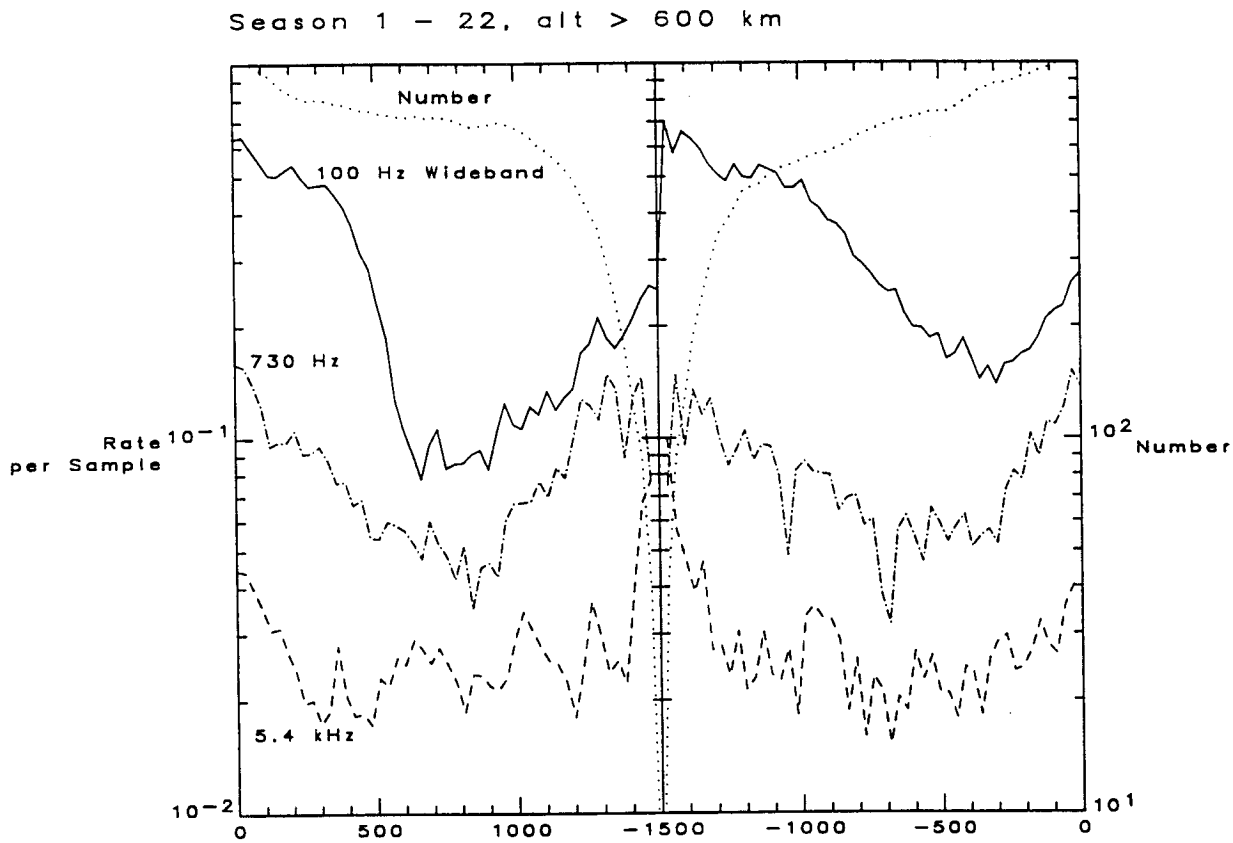

Fig. 8. Occurrence rate dependence on time with respect to the inbound and outbound shadow edge. In the left panel, orbits are superposed starting at the time of the inbound shadow crossing. The data in the right panel are plotted with respect to the outbound shadow crossing time. The 730 Hz and 5.4 kHz signal rates are symmetric, while the LF (100 Hz) wideband signals are clearly asymmetric. There is a sudden drop in the occurrence rate about 10 min from the inbound shadow edge

shadow exit. We also find that the wave amplitude and activity are higher near the shadow edge. This feature strongly implies that the signals are related to the spacecraft interaction with plasma. Even though we cannot completely exclude the possibility of some ambient sources, any naturally occurring waves propagating from outside the sheath should not display any inbound/outbound asymmetry. We note that the other signals are symmetric. Perhaps some residual charging due to photoelectron emission remains on the spacecraft on entering the optical shadow. This charge is then slowly reduced and hence we observe the noise mainly on the inbound legs, but we do not know how or why the spacecraft would retain the charge. Additionally, we note that no spacecraft operation commands are correlated with the inbound/outbound structures. Thus, it is still a mystery as to what kind of mechanism generates these interference signals.

6. Summary

This statistical study has presented the entire Venus nightside spatial distribution of VLF burst activity using data obtained over most of the PVO lifetime. The extension of our study to greater altitudes and over a longer interval has helped reveal the characteristics of the wave activity in the higher ionosphere. A general picture we can draw is that below 600 km, 100 Hz NB signals propagate upward with rapid attenuation with increasing altitude. Above 600 km, the 100 Hz NB signals may be ducted by irregularities in the magnetic field and plasma density in that altitude region. This propagation will produce smaller damping for the whistler mode signals so that they can extend to 3000 km altitude. However, when averaged over *all altitudes* only 23% of all 100 Hz burst events have properties consistent with whistler mode waves. The rest are wideband signals. Solar variations do not appear to affect the VLF signal activity. The variation of the subionospheric source appears to play the main role in whistler burst activity. This study also verifies the results of previous studies of the altitude, magnetic orientation and electron density dependence. Since we have used 30 s averages for this study, the dispersion effect of the waves is not distinguishable and the resonance cone test also is less accurate. The high frequency wideband signals seem also to have a low altitude source. They are quickly damped with increasing altitude in the lowest ionosphere.

Around the wake region, the strong mid-frequency broadband burst signals occasionally appear. Though they also appear along the optical shadow edge, they are significantly different from the weak LF wideband interference noise. These MF broadband signals are probably associated with plasma clouds. Because they always appear as wideband waves, they appear to be locally generated ion acoustic waves. In the tail above 1500 km we observed narrowband waves in the two high frequency

channels. These waves have different features from the low altitude high frequency waves, suggesting they are generated locally. They are closely correlated with low plasma density regions in the tail. The 30 kHz signals usually are associated with the electron density level of 10 cm^{-3}, while the 5.4 kHz signal corresponds to an undetectable density presumably below the Langmuir probe threshold. Assuming these waves are at the electron plasma frequency, we can map the location of plasma cavities within the tail (Ho *et al.*, 1993).

We also observed some weaker and low frequency wideband noise in both the 100 and 730 Hz channels. The noise is seen primarily near the edge of the planetary optical shadow and has an inbound to outbound asymmetry. It is still unclear what causes these signals. Spacecraft interference is a more likely source, in contrast to a local wave instability.

Through this survey of 22 PVO seasons in the Venus nightside ionosphere, we conclude that there are essentially three wave sources which are responsible for the following four types of VLF waves observed by PVO.

(1) The first type is only observed in the 100 Hz channel and not in any of the higher frequency channels. This 100 Hz signal occurrence is also controlled by the magnetic field strength and orientation, but with a weaker dependence on electron density. The occurrence rate decreases with increasing altitude to a height of 600 km. For higher altitudes beyond 600 km the occurrence rate remains roughly constant. We deduce that these signals are whistler-mode waves which come from a subionospheric source, presumably lightning.

(2) The second type is a broadband wave appearing in the lower ionosphere. The signal often extends from the 100 Hz into 730 Hz, 5.4 kHz and 30 kHz channels. These broadband signals are more impulsive and have stronger intensity relative to the background in the 5.4 kHz channel. They mainly appear below 500 km. These signals are also thought to come from a subionospheric source.

(3) The third type is mid-frequency broadband burst signals occur in the wake region. They usually last 1–2 min and are well above the threshold level in each channel. These signals are closely associated with a current layer (B_x reversal) around plasma clouds. They are probably ion acoustic wave generated by a current driven instability.

(4) Lastly, we observe some signals which appear in the higher frequency channels. They are narrow band waves and appear either in the 30 or the 5.4 kHz channel. They occur in the upper ionosphere, corresponding to the plasma cavity in the tail region, where the electron density is below 10 cm^{-3}. Thus, they are presumably Langmuir waves.

Acknowledgment. This work was supported by NASA under grants NAG2-485, NAG2-501, NAGW-3492 and NAGW-3497.

References

Brace, L. H., Theis, R. F. and Hoegy, W. R., Plasma clouds above the ionopause of Venus and their implications. *Planet Space Sci.* **30**, 29–27, 1982.

Brace, L. H., Kasprzak, W. T., Taylor, H. A., Theis, R. F., Russell, C. T., Barnes, A., Mihalov, J. D., and Hunten, D. M., The ionotail of Venus: Its configuration and evidence for ion escape. *J. geophys. Res.* **92**, 15–26, 1987.

Ho, C. M., Strangeway, R. J., and Russell, C. T., Occurrence characteristics of VLF bursts in the nightside ionosphere of Venus. *J. geophys. Res.* **96**, 21361–21369, 1991.

Ho, C. M., Strangeway, R. J., and Russell, C. T., Control of VLF burst activity in the nightside ionosphere of Venus by the magnetic field orientation. *J. geophys. Res.* **97**, 11673–11680, 1992.

Ho, C. M., Strangeway, R. J., and Russell, C. T., Evidence for Langmuir oscillations and a low density cavity in the Venus magnetotail. *Geophys. Res. Lett.* **20**, 2775–2778, 1993.

Phillips, J. L., Luhmann, J. G., and Russell, C. T., Magnetic configuration of the Venus magnetosheath. *J. geophys. Res.* **91**, 7931–7938, 1986.

Russell, C. T., Venus lightning. *Space Sci. Rev.* **55**, 317–356, 1991.

Russell, C. T., von Dornum, M. and Scarf, F. L., The altitude distribution of impulsive signals in the night ionosphere of Venus. *J. geophys. Res.* **93**, 5915–5921, 1988.

Scarf, F. L., Taylor, W. W. L., Russell C. T., and Brace. L. H., Lightning on Venus: Orbiter detection of whistler signals. *J. geophys. Res.* **85**, 8158–8166, 1980.

Scarf, F. L., Jordan K. F., and Russell, C. T., Distribution of whistler mode bursts at Venus. *J. geophys Res.* **92**, 12407–12411, 1987.

Strangeway, R. J., Plasma waves at Venus. *Space Sci. Rev.* **55**, 275–316, 1991a.

Strangeway, R. J., Polarization of the impulsive signals observed in the night ionosphere of Venus. *J. geophys. Res.*, **96**, 22741–22752, 1991b.

Strangeway, R. J., An assessment of lightning or in situ instabilities as a source for whistler-mode waves in the night ionosphere of Venus. *J. geophys. Res.* **97**, 12203–12215, 1992.

Taylor, H. A., Jr., Cloutier, P. A. and Zheng, Z., Venus "lightning" signals reinterpreted as in situ plasma noise. *J. geophys. Res.* **92**, 9907–9919, 1987.

JOURNAL OF GEOPHYSICAL RESEARCH, VOL. 99, NO. A9, PAGES 17,413–17,420, SEPTEMBER 1, 1994

Evidence for ion transport and molecular ion dominance in the Venus ionotail

D. S. Intriligator,[1] L. H. Brace,[2] P. A. Cloutier,[3] J. M. Grebowsky,[4] R. E. Hartle,[4] W. T. Kasprzak,[4] W. C. Knudsen,[5] and R. J. Strangeway[6]

Abstract. We present analyses from the five Pioneer Venus Orbiter plasma experiments and the plasma wave experiment when a patch of plasma with enhanced densities was encountered in the near-Venus ionotail during atmospheric entry at an altitude of ~1100 km in the nightside ionosphere. Our analyses of the thermal and superthermal ion measurements in this plasma feature provides the first evidence that at times molecular ions in the 28-32 amu mass range are dominant over atomic mass species thus yielding evidence for a transport mechanism that reaches into the lower ionosphere. Analysis of plasma analyzer (OPA) observations at this time indicates the presence of ions measured in the rest frame of the spacecraft at ~27 and 37 volt energy per unit charge steps. In the rest frame of the planet these superthermal ions are flowing from the dawn direction at speeds (assuming they are O_2^+) of ~8 km/s and with a flow component downward (perpendicular to the ecliptic plane) at speeds of ~2 km/s. OPA analyses also determine the ion number flux, energy, flow angles, and angular distributions. Plasma wave bursts appear to indicate that plasma density decreases within and on the equatorward edge of the patch of enhanced plasma densities are associated with ion acoustic waves and relative ion streaming.

Introduction

We present analyses of a plasma feature observed during atmospheric entry in the nightside Venus ionosphere. While we observe the feature for the first time, in fact it may be quite common, but the instrument configurations and orbiter location were rarely optimal for its detection. During our event all five of the Pioneer Venus Orbiter (PVO) plasma instruments were appropriately configured and 27 and 37 V ion flux enhancements were present in the orbiter plasma analyzer (OPA) data. We analyze these OPA measurements obtained in the low-energy (0 to +250 V) ion mode [*Intriligator et al.*, 1980]. We also analyze simultaneous orbiter electron temperature probe (OETP) Langmuir probe observations [*Brace et al.*, 1980]; orbiter ion mass spectrometer measurements (OIMS) [*Taylor et al.*, 1980]; orbiter retarding potential analyzer (ORPA) results [*Knudsen et al.*, 1980]; orbiter neutral mass spectrometer (ONMS) observations [*Niemann et al.*, 1980]; and OEFD orbiter electric field data [*Scarf et al.*, 1980] measurements.

This is the first publication of analyses of the OPA plasma measurements during atmospheric entry in the near (<1 R_V) Venus ionotail. Vaisberg et al. [1977] discussed Venera 9 and 10 measurements in this region. Brace et al. [1987] described the ionotail of Venus as the near-tail region where the ionosphere becomes increasingly filamentary with increasing altitude, apparently forming cometlike tail rays that extend several thousand kilometers behind the planet.

Analysis of Measurements

Figure 1a shows the OPA low-energy ion plasma flux as a function of time during the nightside periapsis passage on orbit 4574 on June 14, 1991. Except for the ionosheath fluxes at the end of this time interval (>4800 s), the highest OPA fluxes are observed from 3911 to 3963 s which we will refer to as the ~3900 s plasma feature in the nightside ionosphere. The trajectory information at the bottom of Figure 1 indicates that this superthermal ion feature was traversed at an altitude of ~1100 km, a latitude of +12°, a longitude of +103°, a solar zenith angle of 165°, and at a local time of 0.6 hour. The OETP electron densities are shown in Figure 1b. The dark vertical bars along the bottom represent the region where the spacecraft was in the optical umbra of Venus and serve to illustrate the scale size of the ionotail structures relative to the size of the planet.

[1]Space Plasma Laboratory, Carmel Research Center, Santa Monica, California.

[2]Space Research Laboratory, University of Michigan, Ann Arbor, Michigan.

[3]Space Physics Department, Rice University, Houston, Texas.

[4]NASA Goddard Space Flight Center, Greenbelt, Maryland.

[5]Knudsen Geophysical Research, Monte Sereno, California.

[6]Institute of Geophysics and Planetary Physics, University of California, Los Angeles.

Paper number 94JA01341.
0148-0227/94/94JA-01341$05.00

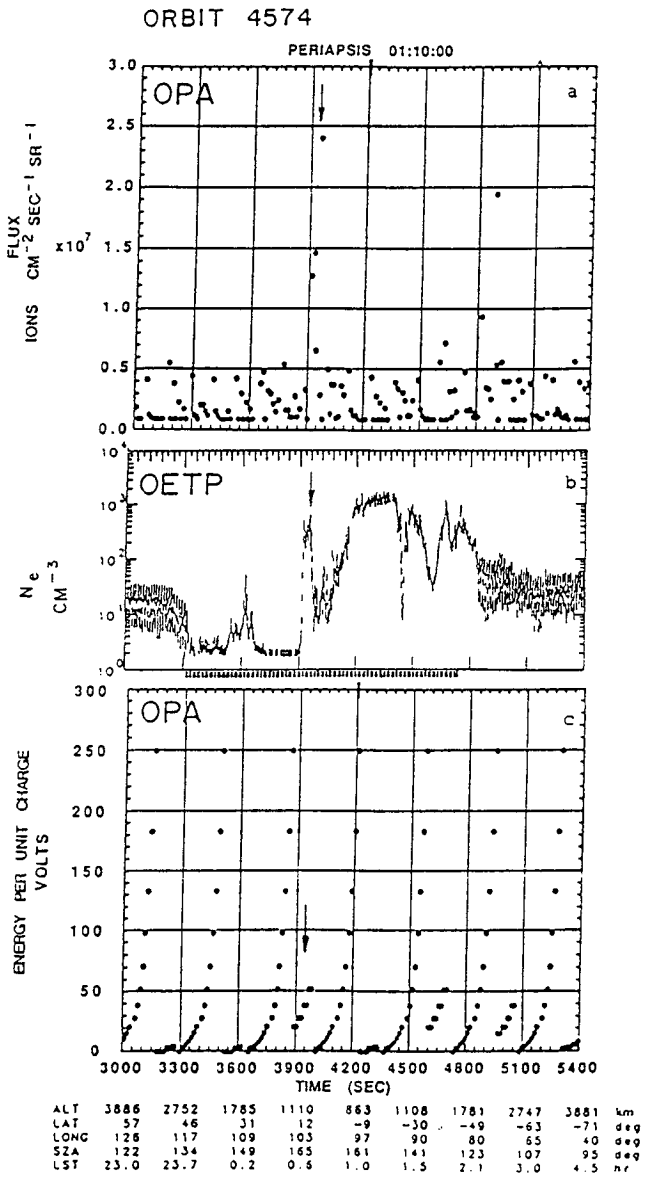

Figure 1. (a) Orbiter plasma analyzer (OPA) low energy ion plasma flux (using measurements obtained ~13 s apart) as a function of time during nightside periapsis on orbit 4574 on June 14, 1992. The highest fluxes are associated with a superthermal ion feature near 3900 s. (b) Orbiter electron temperature probe (OETP) electron densities as a function time on orbit 4574. The superthermal ion feature at ~3900 s is evident in these data. (c) OPA low-energy ion energy per unit charge (*E/Q*) steps (obtained ~13 s apart) in volts as a function of time. Each 16 *E/Q* step maximum flux scan is followed by a 4 *E/Q* step angular scan in the vicinity of the *E/Q* step where the peak flux was measured during the previous 16 *E/Q* step maximum flux scan [*Intriligator et al.*, 1980]. As Pioneer Venus Orbiter (PVO) traversed the ~3900 s plasma features the OPA coincidently was performing angular scans at 27 and 37 V.

In this panel the plasma feature at ~3900 s is evident, as is its limited spatial and/or temporal extent. Since the feature is so narrow, only a small portion of the OPAs energy and angular scans coincide with the spacecraft's traversal of the feature. Inspection of Figure 1c indicates that these 27 and 37 V measurements were made in the four *E/Q* step polar and azimuthal angular scans following the sixteen *E/Q* step maximum flux scan [*Intriligator et al.* 1980]. Comparison of Figures 1a, 1b, and 1c indicates that it was simply coincidental that the OPA energy cycle was at the 27 and 37 V *E/Q* steps in the vicinity of the plasma feature. Thus, from the OPA measurements alone it is only possible to conclude that 27 and 37 V ions in the rest frame of the spacecraft were present in association with the plasma feature, and it is not possible to conclude whether lower-energy or higher-energy ions also were present. Thus it is not possible to obtain agreement with the total density measurements from other instruments.

In Figure 2 we show a schematic of the location of the plasma feature and the southward motion of the spacecraft. The OPA orientation and the field of view also are shown and these will be discussed later.

Figure 3a shows the densities from the OIMS, OETP, OPA, and ORPA, and also the OPA flux as a function of time. The plasma feature ~3900 s that we are focusing on is evident in all these data sets between ~3900 and 3960 s. The OIMS densities show a small rise in the 0^+ density (the open circles) and very large increases in the 0_2^+ density (the crosses) and in the NO^+ density (the open squares). Mass 28 ions also were present with densities comparable to those of 0_2^+. It is clear from the OIMS observations that primarily thermal moleculars in the 28-32 amu mass range are dominant over thermal atomic ion species. It is likely that crosstalk [e.g., *Grebowsky et al.*, 1993] between signals for the 32 amu ions and the signals in nearby mass channels (e.g., those for 30 and 28 amu ions) produce current signals in the 28 and 30 amu settings that add to the current collection of ambient ions with the same masses. When we use the term crosstalk for the OIMS response, it must be emphasized that this does not mean that only a fraction of the source ion species current that should be collected at the proper amu setting is spilling into an anomalous mass setting. As discussed by *Grebowsky et al.*, [1993], superthermal ions or offsets in internal OIMS voltages from nominal operating conditions, can produce a detuning of the response of the instrument. In such a case the current collected at an anomalous mass setting can exceed the current measured at the correct setting for an incoming ion species. An analysis of the instrument response for example indicates this to be the case for 28 amu signatures that are produced by superthermal 30 or 32 amu ions. Hence one cannot use the OIMS deduced molecular ion concentrations in this obviously perturbed region of space to infer unambiguously the dominant molecular ion species, but it is certain that thermal moleculars in the 28-32 amu mass range are dominant and that 0^+ is a minor constituent. For example, it is evident in Figure 3a that the measured 0^+ densities (as well as H^+ which is not plotted) are far lower than the total electron density measured in the OETP. The computed molecular densities, on the other hand, are comparable to the electron densities (the dark circles).

To further examine the ion composition associated with

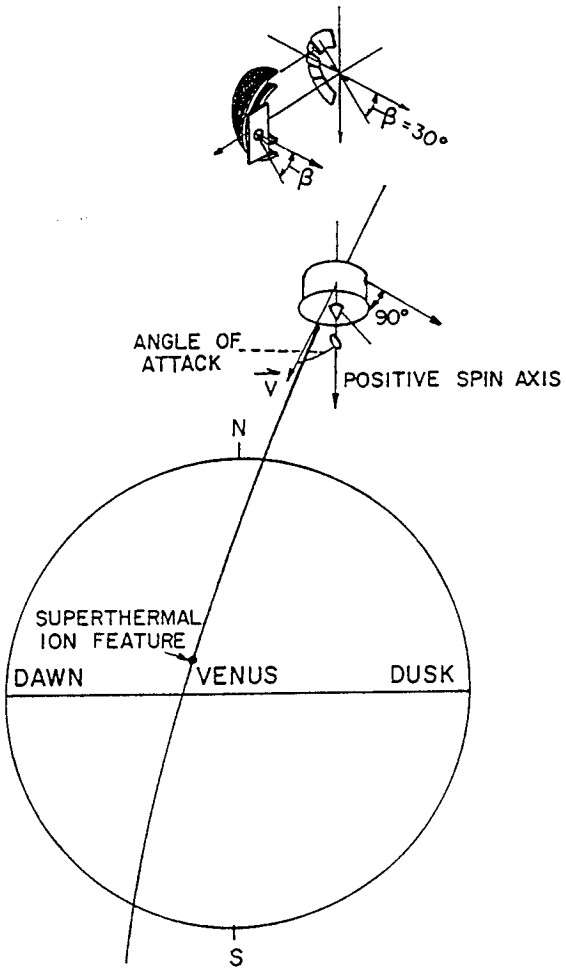

Figure 2. Schematic illustration of PVO angle of attack and orientation and the location of the plasma feature. The OPA field of view, circular entrance aperture, curved plates, and the array of five current collectors beyond the exit aperture are also shown. The OPA simulations show that in the spacecraft frame the β angle is 30° northward flow (with respect to the ecliptic plane) associated with the plasma feature. However, in the rest frame of the planet, since the spacecraft is mainly moving south at this time, the OPA measurements indicate a southward component of flow (see text). The superthermal ion feature ~3900 s is primarily associated with OPA azimuthal flow ~-90° which is flow from the dawn direction.

the region under consideration, O_2^+ (mass 32) and O^+ (mass 16) for energies >36 eV measurements of the ONMS fluxes are shown in Figure 3b as a function of time. These measurements clearly show that there is a substantial peak in the O_2^+ superthermal fluxes (the open squares) in association with the plasma feature at ~3900 s. The ONMS also sees enhanced superthermal 30 amu ions. Hence it is assumed that molecular superthermal ions are part of the bulk distribution. The ONMS measurements above 36 eV clearly provide more evidence that molecular ions (e.g., O_2^+) and not atomic ions (e.g., O^+) are dominant within the patch of enhanced plasma fluxes. Comparison of the magnitudes of the superthermal O_2^+ fluxes relative to the O^+ fluxes from the ONMS (Figure 3b) with the corresponding ratios of ion densities deduced by the OIMS (Figure 3a) for the same masses indicate that in both energy regimes the molecular ion abundances are more than an order of magnitude above those of the O^+ in the plasma feature.

At this time the ORPA also measures increased ion densities and the OPA measures increased ion fluxes, but these instruments by themselves cannot unambiguously determine the ion masses. On the basis of OIMS and ONMS determinations, we assume that O_2^+ is the most abundant species, and this is accepted for interpretation of the ORPA measurements and the OPA simulation. The ORPA results and the results of the OPA simulations (see below) are relatively insensitive to whether mass 28, 30, or 32 is assumed. We derive a thermal O_2^+ density of 373 cm^{-3}

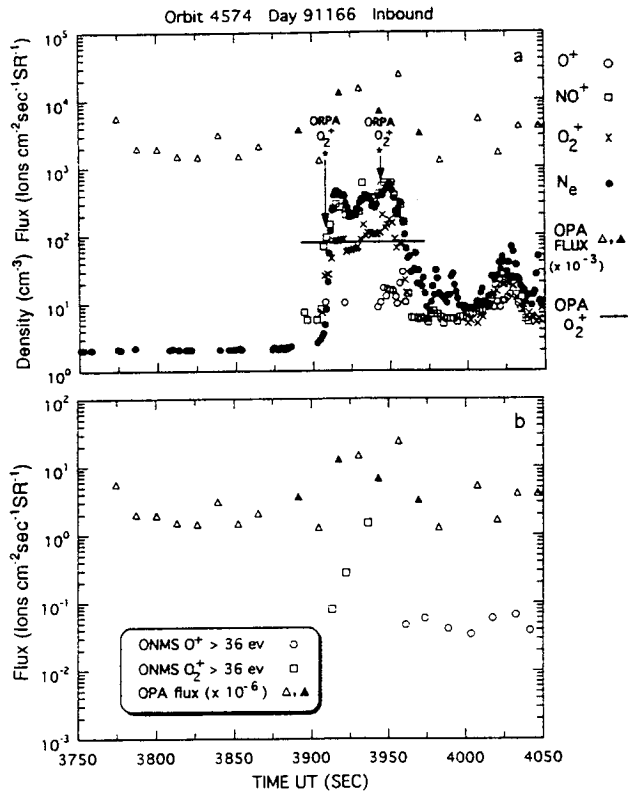

Figure 3. (a) Orbiter ion mass spectrometer (OIMS), OETP, orbiter retarding potential analyzer (ORPA), and OPA densities and OPA flux as a function of time in the vicinity of the plasma feature. The tip of the arrow indicates the actual location of the ORPA densities. The OIMS measurements show molecular ions are dominant (see text). The solid triangles indicate the OPA polar scan fluxes used as input in the simulation (see Figure 5). The straight line shows the OPA density estimated in the simulation. The narrow temporal/spatial extent of the plasma feature introduces uncertainties in the OPA density estimates. The OPA estimate could be lower than the ambient density but the magnitude of the uncertainties is difficult to assess (see text). (b) Orbiter neutral mass spectrometer (ONMS) and OPA fluxes as a function of time. Note that the ONMS identifies O_2^+ as the dominant ion in this plasma feature.

from the ORPA observations at 3942 s, a number that is consistent with the N_e measurements. This is derived based on the measurements in a 0.16 s I-V scan using the ORPA measured vehicle potential of -0.6 V and the knowledge of the exact orientation of the ORPA axis with respect to the spacecraft velocity vector at the time of measurement. Similarly, at 3909 s, on the polarward edge of the feature, the ORPA density is 124 cm^{-3} for thermal O_2^+. O_2^+ temperatures and velocities were also derived and these will be discussed in the relevant sections below. The ORPA densities are denoted by the end of the arrows from the asterisks in Figure 3a.

The O_2^+ density for the higher energy population estimated from the OPA simulations (see Figure 4) is ~80 cm^{-3} and is denoted by the horizontal line in Figure 3a. The input data (the solid triangles in Figure 3) used in the OPA instrument simulation were the ion fluxes obtained on collectors 5 and 4 in the polar scan on four *E/Q* steps in the vicinity of the peak [*Intriligator et al.*, 1980]. These observations were obtained between 3891.5 and 3969.5 s. We emphasize the narrow time/spatial extent of the plasma event. The OPA observations contain contributions from spatial and/or temporal variations whose magnitude cannot be easily assessed. This may result in our obtaining a lower density and a lower temperature than those characteristic of the ambient plasma since, for the purpose of this simulation we assumed a quasi-steady state during this 78 s time interval. As emphasized by the four solid triangles in Figure 3, this does not appear to be the case, but it allows us to fit the four solid triangles with one distribution function. A convecting Maxwell-Boltzmann plasma distribution function was assumed. The output of the simulation is the plasma parameters - density, temperature, speed, and north-south angles of flow associated with the distribution. The east-west (azimuthal) flow angle distributions in the ecliptic plane are determined independently in the azimuthal scans and are shown in Figure 5. Since the duration of the plasma feature only extended from ~3910 to 3950 s, only one set of polar scans was obtained near it (and these straddle the feature as shown in Figure 3), and, thus only one set of parameters could be obtained from the simulation. These simulations also indicated that in the spacecraft frame the polar flow is ~30° from the ecliptic plane to the north, i.e., flow from the south (see below). In the rest frame of the planet the flow has a component to the south. The O_2^+ temperature and speed estimates are discussed below.

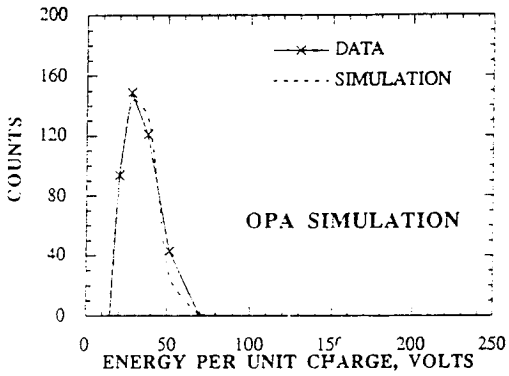

Figure 4. OPA low-energy ion flux (solid line) obtained on collector 5 in the polar scan as a function of volts for the four *E/Q* steps, that is, the solid triangles in Figure 3 in the vicinity of the plasma feature. Results of a preliminary instrument simulation of these 78 s of data are indicated by the dashed line. The assumptions and uncertainties associated with the simulation are discussed in the text.

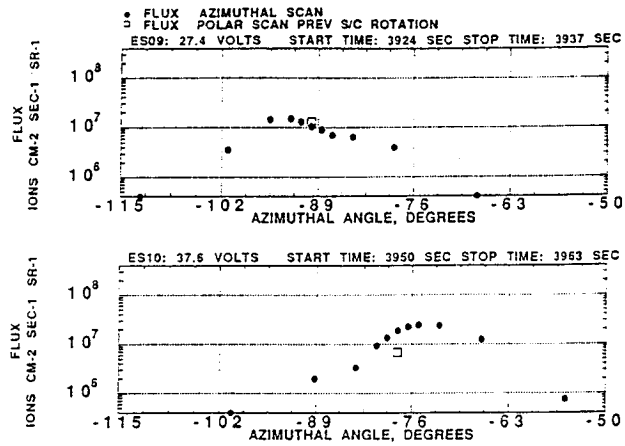

Figure 5. OPA azimuthal angle distributions showing the flux as a function of azimuthal angle for the 27 V (upper) and 37 V (lower) *E/Q* steps. The peak polar angle at each energy step is obtained ~13 s (i.e., one spacecraft revolution) before the peak azimuthal angle for that energy step. The duration of each of the data points is ~25 ms. The angular scans shown here were obtained in four sequential spacecraft rotations (polar 27 V, azimuthal 27 V, polar 37 V, azimuthal 37 V). The negative angles denote flow from the east. The 27 V scan peaks at ~-89° indicating that these ions are flowing from the east horizontally (parallel to the surface of Venus) which means that the flow in this poleward portion of the plasma feature is from the dawn direction. The 37 V azimuthal scan peaks at ~-77° indicating a slight component of the flow directed outward from the planet at the equatorward edge of the feature.

It should be noted that the OETP measures the electron (i.e., total ion) density. The ORPA, OIMS, ONMS measurements, and to some extent the OPA measurements, are dependent on the flow characteristics of the ions with respect to the instrument apertures.

With respect to plasma temperatures the OETP measurements yield an electron temperature of ~7000K, which is typical of the nightside ionosphere at this altitude. The ORPA derivation at 3942 s in the plasma feature yields an O_2^+ temperature of 10,237K and at 3904 s a temperature of 17,394K is obtained on the poleward edge of the feature. In the plasma feature the OPA simulation estimates a temperature of ~10,000 ± 250K which, as discussed above, may be lower than the ambient plasma temperature since measurements were only obtained on two energy steps in the plasma feature due to its limited spatial/temporal extent.

The component of the ORPA ion bulk velocity parallel to the instrument axis was calculated. It is positive when directed along the outward direction of the instrument axis. At 3942 s in the plasma feature the direction cosines of the ORPA instrument axis in solar ecliptic coordinates were 0.35, -0.2, and -0.94. At 3942 s the velocity component along the instrument axis derived from the 0.16 s sweep was +0.46 km/s. Similarly, at 3909 s on the poleward edge of the plasma feature, the comparable direction cosines of the ORPA axis were -0.48, 0.12, and -0.87 and the component of velocity along the ORPA instrument axis was +1.93 km/s. The OPA simulation shown in Figure 4 yields an O_2^+ bulk speed in the spacecraft frame of ~12.5 km/s after correcting for vehicle potential.

It is useful to convert the OPA velocity from the rest frame of the spacecraft to the planet's rest frame. The OPA measures (see Figures 2 and 5) the peak azimuthal flow direction as ~-90° (for the 27.4 V polar and azimuthal scans). If we assume that -90°, flow from dawn to dusk, is the azimuthal flow direction (ϕ) and as determined from the OPA simulation β = 30° (Figure 2) is the north-south flow direction then we obtain (0, -10.8, +6.3) for the relative ion velocity in solar ecliptic coordinates with respect to the spacecraft. Using the 3942 s values for the spacecraft velocity (+0.19, +2.51, -8.77), then we obtain (+0.19, -8.3, -2.5) for the ion velocity relative to the planet. This implies that the ions measured by the OPA are predominantly moving toward the negative Y component (i.e., to dusk from dawn) at 8.3 km/s and downward (toward the south with respect to the ecliptic plane) at 2.5 km/s. (If there had been no Z (north-south) component of flow then the OPA should have been 8.77 instead of 6.3 as the Z component.)

To compare the OPA velocity (derived by combining and then fitting samples obtained between 3911 and 3950 s) with the ORPA velocity component along the direction of the ORPA instrument axis (derived from a 0.16 s sample at 3942 s) we dot the OPA velocity vector into the direction of the ORPA instrument axis. This yields +4.1 km/s but the ORPA measures +0.46 km/s at 3942 s. This discrepancy may be due to changes in the flow parameters in the plasma feature since the OPA simulation assumes a steady state from the first polar scan peak flux to the fourth polar scan peak flux (~3892 s to 3970 s). However, the OPA azimuthal angle scans (Figure 5) indidcate a 12° change in azimuthal flow during this time and the density profiles (Figures 3a and 3b) also show changes during this time.

In order to clearly focus on the azimuthal flow angles, Figure 5 shows angular distributions. These azimuthal scans look very real with a well-defined direction. They indicate flow from dawn to dusk in agreement with the ONMS results which represent ions with energies exceeding 36 V (see Figure 6 and text below).

Figure 6 shows the azimuthal flow angles of the superthermal component of the ions measured by the ONMS. The O_2^+ flow angle in association with the plasma feature between ~3910 and 3960 s is ~-80° to -110°. In the ONMS convention this represents flow from the dawn direction. Thus the ONMS and the OPA azimuthal flow information agree.

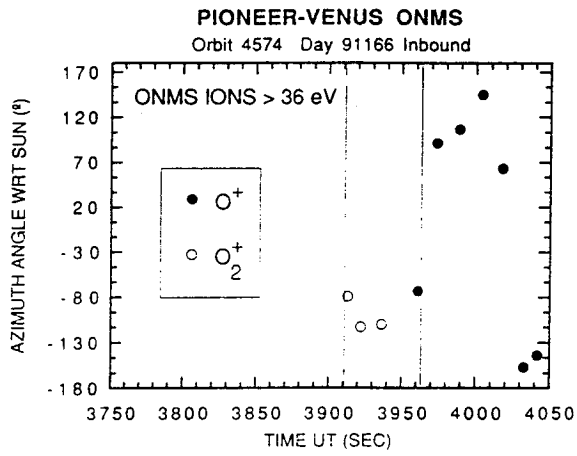

Figure 6. ONMS azimuthal flow angle as a function of time on the same time scale as in Figure 3. The O_2^+ flows between ~3910 and 3960 s are in the vicinity of ~80° to -110°. These O_2^+ flow angles indicate dawn to dusk flow and are consistent with the O_2^+ flow angles from the OPA (Figure 5).

In Figure 7 we present the high- resolution OEFD plasma wave observations for the 100-Hz, 730-Hz, 5.4-kHz, and 30-kHz channels for the same time interval as that shown in Figures 3a, 3b, and 6. There are enhancements in the plasma wave signals in the 730-Hz and 5.4-kHz channels associated with the plasma feature at ~3900 s. There is a step-like rise, particularly in the 5.4-kHz channel and to a lesser extent in the 730-Hz channel between ~3910 and 3960 s that clearly corresponds to the increase in plasma density associated with the ~3900 s plasma feature as seen in the OETP data and in the other plasma observations in Figure 3. Between ~3920 and 3930 s there is a large plasma wave burst which is particularly evident in the 730-Hz channel and to a lesser extent in the 5.4-kHz channel. Comparison of the plasma data in Figure 3 with this plasma wave burst indicates that the burst is coincident with the decrease in plasma density in the OETP and OIMS data. This 730-Hz and 5.4-kHz burst may be indicative of the presence of ion acoustic waves. These waves could be the result of flows in the plasma similar to the ion streaming near the magnetotail boundary in the extended Venus tail region where ion acoustic waves were present [*Intriligator and Scarf*, 1984]. For example, there could be relative streaming between two ion species (e.g., O_2^+ and O^+) or relative streaming between ions of the same species where the ions in one of the streams have been accelerated at some other location. There is another set of 730-Hz and 5.4-kHz bursts which occurs between 3950 and 3960 s. Again, comparing the timing of this set of bursts with the plasma data in Figure 3 indicates that these bursts are coincident with the first sharp density decrease at the equatorward edge of the plasma feature. Similarly, the smaller plasma wave spikes in the 730-Hz channel (and less discernably but still present in the 5.4-kHz channel)

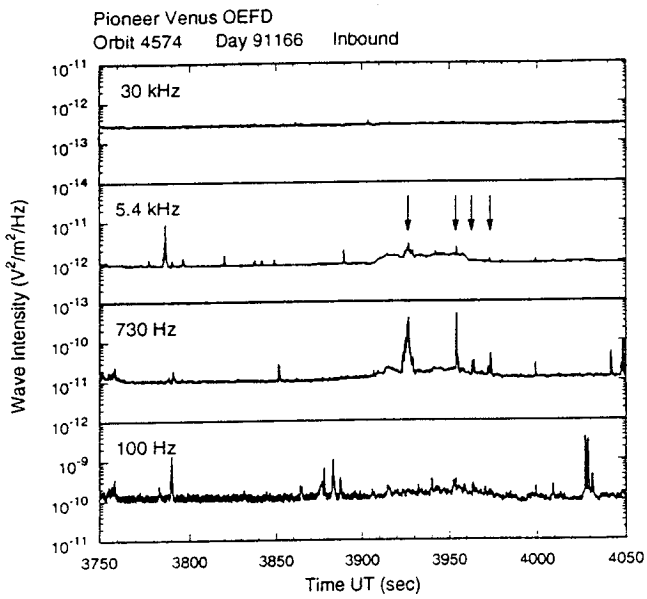

Figure 7. OEFD plasma wave signals in four channels as a function of time on the same time scale as in Figure 3. Enhanced signals are evident (e.g., between 3920 and 3930 s, between 3950 and 3960 s) in the 730-Hz and 5.4-kHz channels, in association with sharp density decreases within the superthermal ion feature and along its equatorward edge. The arrows denote regions associated with simultaneous plasma density decreases (see Figure 3).

between 3960 and 3970 s and again between 3970 and 3980 s also correspond to steplike decreases in the OETP plasma density (see Figure 3). All of the plasma wave enhancements are most likely associated with ion acoustic waves due to relative ion streaming in the plasma. The behavior of the magnetic field data at the time of the plasma feature (~3900 s) is difficult to resolve (since the only component available is perpendicular to the ecliptic plane and it exhibits an offset that may not be physical [C. T. Russell, private communication, 1993], but there does appear to be a small increase in B_z (the component perpendicular to the ecliptic plane) just before the plasma feature.

Discussion

We have chosen a specific plasma feature to study since modes of all five of the PVO plasma instruments were appropriately configured at this time and low-energy ion flux enhancements were present in the OPA data. These circumstances occur rarely or can only rarely be seen because of instrument cycling. All five of the PVO plasma measurements indicate a spikelike spatial and/or temporal gradient is associated with this plasma feature. The OIMS and the ONMS measurements indicate that it is primarily associated with moleculars (e.g., O_2^+) and not atomic ions (e.g., O^+). The OETP, OIMS, and ORPA measurements indicate that the total ion densities are of the order of 300-500 cm^{-3}. The OPA simulation estimates superthermal molecular densities on the order of ~80 cm^{-3}. This estimate may be lower than the ambient density due to the narrowness of the plasma feature as discussed above.

As a result of the present study, we are able to make an independent determination of the superthermal plasma fluxes, of their energies, and the angles of flow both in the ecliptic plane and perpendicular to it. We also are able to determine that primarily molecular ions (e.g., O_2^+) are present and that the instruments appear to be sampling different regimes of the same energy distribution function. We also conclude that ion transport is taking place and that the velocity changes in magnitude and direction across the feature. The plasma wave observations indicate that, within the feature and along the equatorward edge of the feature, ion acoustic waves are present that may be indicative of relative ion streaming. These waves appear to occur when there are sharp density decreases in the plasma. The dominance of molecular ions (e.g., in the ONMS measurements) suggests that the ions originate from altitudes below 200 km which is the only region where chemical processes exist which can produce molecular ions at concentrations exceeding those of the atomic ions.

Kar et al., [1994] have recently shown that day-to-night transport of ionospheric plasma was diminished considerably near solar minimum. Consequently, it is not too likely that the O_2^+ produced on the dayside was flowing to the nightside during the time when O_2^+ was observed in the ionotail. The dominance of O_2^+ in the ionotail is, however, consistent with the nightside ionospheric plasma being transported upward from the O_2^+ peak region. The recent reentry OIMS measurements of the nightside ionosphere near solar minimum revealed that O_2^+ was at least an order of magnitude more dense than O^+ at the ionization peak; furthermore, analysis of this ionization layer showed that it was produced primarily by electron impact ionization [*Kar et al.*, 1994]. Thus it is quite natural to expect ions to tend to fill a "void" and flow away from their source region and, at least occasionally, be accelerated to the high energies observed. Such a scenario leads to O_2^+ being the dominant ion in the ionotail, with O^+ flowing upward with a proportionately lower concentration level (too low to be observed by the OIMS and near background count rates by the ONMS). The horizontal component of the observed flow would seem to indicate that the acceleration could be occurring near the terminator.

The PVO observations are consistent with this scenario. The ONMS and OPA azimuthal flow angles (~-90°) indicate flow into the instruments from the dawn direction and at times (equatorward of the feature when the flow is -77°) with some component outward from the planet. The OPA polar (north-south) flow information indicates that the flow is directed northward at an angle of ~30° to the ecliptic plane (i.e., it originates in the south). This polar flow direction is consistent with the ram direction of the spacecraft at this time as the spacecraft is traveling from the north to the south (see Figure 2). The OPA simulation, after correcting for the spacecraft velocity and vehicle potential, provides a total O_2^+ drift speed of ~8.7 km/s which does not exceed the escape speed (~10 km/s). It is possible that the OPA speed is lower than the ambient O_2^+

speed if the limited extent of the event precluded obtaining accurate data within the plasma feature. The enhanced plasma wave activities associated with the plasma feature are consistent with the presence of relative ion streaming. Perhaps the plasma wave bursts are indicative of the upward flow or the acceleration of moleculars. The OETP electron temperature of 7000K and the ORPA (at 3942 s) and OPA (based on 3891.5 to 3969.5 s data) temperatures of ~10,000K are consistent with an ionospheric source for the plasma feature assuming that all instruments are sampling parts of the same O_2^+ energy distribution function. However, due to the narrowness of the plasma feature the OPA temperature estimate may be low since measurements only were made on two energy steps in the plasma feature.

Brace et al. [1987] discussed the uncertainty in determining the magnitude of the superthermal ion energy based solely on the OIMS measurements. The OPA measurements presented here provide evidence for ions with energy per unit charge of 27 and 37 V in the rest frame of the spacecraft. On the basis of comparisons with the ONMS and OIMS we conclude these are primarily O_2^+ ions.

We have presented the first analysis of OPA low-energy ion measurements during atmospheric entry in the nightside Venus ionosphere. We provided the first plasma density, speed, components of flow, and temperature analysis for the low energy ion OPA measurements. We obtain OPA measurements at 27 and 37 V, the plasma number flux, and angles of flow. We present (Figure 5) the first azimuthal angular distributions of OPA measurements. These parameters are generally consistent with those from the other plasma instruments. This is also the case for the plasma parameters derived from the ORPA observations obtained in two different 0.16 s sweeps. However, the OPA velocity dotted into the ORPA instrument axis yields a different (larger) velocity component than that measured by the ORPA. Since the OPA determination assumes steady state and we know that between 3911 and 3950 s conditions are changing this could be why the ORPA value at 3942 s is different.

There is general agreement between the superthermal fluxes as measured by the ONMS and the OPA. *Kasprzak et al.* [1991] report that the average O^+ flux for O^+ ions >36 eV measured by the ONMS is about 10^5 cm^{-2} s^{-1} but that higher fluxes from 10^6 to 10^8 cm^{-2} s^{-1} have been observed about 10% of the time. O^+ fluxes on the order of $\sim 10^5$ are observed by the ONMS in association with the superthermal plasma feature. The peak O_2^+ fluxes above 36 V measured by the ONMS in the superthermal plasma feature sharply increase over an order of magnitude to reach $\sim 5 \times 10^6$. The low-energy ion fluxes measured by the OPA in the plasma feature also show a sharp increase with a maximum flux near 2×10^7. If it is assumed that the ONMS is measuring that portion of the OPA distribution shown in Figure 6 above 36 eV then approximately 20% of the ion flux observed by the OPA is being measured by the ONMS. This assumes an ONMS transmission with energy based on laboratory data [*Kasprzak et al.*, 1987]. A similar ratio of about 25% is observed in the maximum flux ratio. These results are consistent with the ONMS measuring the high-energy tail of a plasma distribution with a lower mean energy as determined by the OPA.

Brace et al. [1987] found a weakened magnetic field in the rays and that a strong steady tailward magnetic field dominates the trough regions surrounding the rays. They also found that an approximate pressure balance existed across ray boundaries, with the static plasma pressure of the rays balanced by the magnetic pressure of the surrounding trough regions. From the available B_z magnetic field data on orbit 4574, B_z appears to peak just before the plasma feature; however, no reliable magnetic field data are available in the feature.

The specific plasma feature we examined is a patch of enhanced plasma densities. It could be associated with a tail ray.

Conclusions

In this paper we conclude the following:

1. A plasma event occurred in the nightside Venus ionosphere on June 14, 1992. The event occurs rarely or only rarely can be seen if it is quite common since instrument configurations and orbiter location were rarely optimal for its detection.
2. The apparent duration of the event was ~1 min.
3. The event was measured by all five PVO plasma experiments (OETP, OIMS, ONMS, ORPA, and OPA) and the plasma wave experiment (OEFD).
4. The event was associated with a patch of plasma with enhanced thermal and superthermal densities.
5. For thermals the OIMS determined that molecular ions in the 28-32 amu mass range were dominant over atomic ion species.
6. For superthermal (>36 eV) the ONMS found that molecular ions (i.e., O_2^+) were dominant over atomic ions.
7. The molecular ion dominance is suggestive of a source in the deep ionosphere.
8. The molecular ions are flowing from the dawn direction as determined by both the ONMS and OPA.
9. The total ion densities are ~300-500 cm^{-3} based on the OETP, OIMS, and ORPA results.
10. Electron temperatures of 7000K were found by the OETP.
11. Thermal ion temperatures of ~10,000K were obtained by the ORPA and OPA but the OPA temperasture may be low.
12. The temperature measurements are also consistent with an ionospheric source for the feature.
13. The OPA density and temperature estimates may be lower than the ambient values due to the narrowness of the plasma feature.
14. There is general agreement between the superthermal fluxes as measured by the OMNS and the OPA.
15. Plasma wave bursts within and on the equatorward edge of the event appear to be associated with ion acoustic waves and relative ion streaming.

Acknowledgments. We are indebted to the Pioneer Project Office for the success of PVO. This work was supported in part by NASA Ames Research Center under contract NAS2-12912, by NASA Headquarters Venus Data Analysis Program under contract NASW-4815, and by Carmel Research Center. We are grateful to C. T. Russell for providing the magnetometer data. Hanchen Huang ran the OPA simulations after David Miller modified the simulation program developed by Ken Intriligator and James Intriligator. We thank D. Hunten and two referees for constructive comments.

The Editor thanks three referees for their assistance in evaluating this paper.

References

Brace, L. H., R. F. Theis, W. R. Hoegy, J. H. Wolfe, J. D. Mihalov, C. T. Russell, E. C. Elphic, and A. F. Nagy, The dynamic behavior of the Venus ionosphere in response to solar wind interactions, *J. Geophys. Res.*, *85*, 7663. 1980.

Brace, L. H., W. T. Kasprzak, H. A. Taylor, R. F. Theis, C. T. Russell, A. Barnes, J. D. Mihalov, and D. M. Hunten, The ionotail of Venus: Its configuration and evidence for ion escape, *J. Geophys. Res.*, *92*, 15, 1987.

Grebowsky, J. M., W. T. Kasprzak, R. E. Hartle, K. K. Mahajan, and T. C. G. Wagner, Superthermal ions detected in Venus' dayside ionosheath, ionopause and magnetic barrier regions, *J. Geophys. Res.*, *98*, 9055, 1993.

Intriligator, D. S., Observations of mass addition to the shocked solar wind of the Venusian ionosheath, *Geophys. Res. Lett.*, *9*, 727, 1982.

Intriligator, D. S., Results of the first statistical study of PVO plasma observations in the distant Venus tail: Evidence for a hemispheric asymmetry in the pickup ionospheric ions, *Geophys. Res. Lett.*, *16*, 167, 1989.

Intriligator, D. S., and F. L. Scarf, Wave-particle interactions in the Venus wake and tail, *J. Geophys. Res.*, *89*, 47, 1984.

Intriligator, D. S., J. Wolfe, and J. Mihalov, The Pioneer Venus orbiter plasma analyzer experiment, *IEEE Trans. Geosci. Remote Sens.*, *GE-18*, 39, 1980.

Kar, J., R. E. Hartle, J. M. Grebowsky, W. T. Kaprzak, T. M. Donahue, and P. A. Cloutier, Evidence of electron impact ionization on the nightside of Venus from PVO/OIMS measurements near solar minimum, *J. Geophys. Res.*, *99*, 11351, 1994.

Kasprzak, W. T., H. A. Taylor Jr., L. H. Brace, and H. B. Niemann, Observations of energetic ions near the Venus ionopause, *Planet. Space Sci.*, *30*, 1107, 1982.

Kasprzak, W. T., H. B. Niemann, and P. Mahaffy, Observations of energetic ions on the nightside of Venus, *J. Geophys. Res.*, *92*, 291, 1987.

Kasprzak, W. T., J. M. Grebowsky, H. B. Neimann, and L. H. Brace, Superthermal >36-eV ions observed in the near-tail region of Venus by the Pioneer Venus Orbiter neutral mass spectrometer, *J. Geophys. Res.*, *96*, 11,175, 1991.

Knudsen, W. C., K. L. Miller, K. Spenner, M. Novak, P. F. Michelson and R. C. Whitten, Suprathermal electron energy distribution within the dayside Venus ionosphere, *J. Geophys. Res.*, *85*, 7754, 1980.

Mihalov, J. D., and A. Barnes, The distant interplanetary wake of Venus: Plasma observations of Pioneer Venus, *J. Geophys. Res.*, *87*, 9034, 1982.

Niemann, H. B., J. R. Booth, J. E. Cooley, R. E. Hartle, W. T. Kasprzak, N. W. Spencer, S. H. Way, D. M. Hunten, and G. R. Carignan, Pioneer Venus orbiter neutral gas mass spectrometer, *IEEE Trans. Geosci. Remote Sens.*, *GE-18*(1), 60, 1980.

Scarf, F. L., W. W. L. Taylor, and P. F. Virobik, The Pioneer Venus orbiter plasma wave investigation, *IEEE Trans. Geosci. Remote Sens.*, *GE-18*, 36, 1980.

Slavin, J. A., D. S. Intriligator, and E. J. Smith, Pioneer Venus orbiter magnetic field and plasma observations in the Venus magnetotail, *J. Geophys. Res.*, *94*, 2383, 1989.

Taylor, H. A., Jr., H. C. Brinton, S. J. Bauer, R. E. Hartle, P. A. Cloutier, and R. E. Daniell Jr., Global observations of the compression and dynamics of the ionosphere of Venus: Implications for the solar wind interaction, *J. Geophys. Res.*, *85*, 7765, 1980.

Vaisberg, O. L., S. A. Romanov, V. N. Smirnov, I. P. Karpinskii, B. I. Khazanov, B. V. Polenov, A. V. Bogdanov, and N. M. Antonov, Structure of the region of interaction of solar wind with Venus inferred from measurement of ion-flux characteristics on Venera 9 and Venera 10, *Cosmic Res.*, *14*, 709, 1977.

D. S. Intriligator, Carmel Research Center, Post Office Box 1732, Santa Monica, CA 90406. (e-mail: dsintriligator@nasamail.nasa.gov)

L. H. Brace, Space Physics Research Laboratory, University of Michigan, Ann Arbor, MI 48109.

P. A. Cloutier, Space Physics, Rice University, Box 1892, Houston, TX 77251.

J. M. Grebowsky, R.E. Hartle, and W.T. Kasprzak, NASA Goddard Space Flight Center, Greenbelt, MD 20771. (e-mail: pacf::grebowsky;pacf::kasprzak)

W. C. Knudsen, Knudsen Geophysical Research, Inc., 18475 Twin Creek Rd., Monte Sereno, CA 95030.

R. J. Strangeway, IGPP, University of California, Los Angeles, Los Angeles, CA 90024. (e-mail: brunet::strangeway)

(Received June 20, 1993; revised May 13, 1994; accepted May 17, 1994.)